CORA Cork Open Research Archive
Cartlann Taighde Oscailte Chorcaí

Title	Dense wavelength division multiplexing at 2 μm for future optical communications
Authors	Kavanagh, Niamh
Publication date	2019
Original Citation	Kavanagh, N. 2019. Dense wavelength division multiplexing at 2 μm for future optical communications. PhD Thesis, University College Cork.
Type of publication	Doctoral thesis
Rights	© 2019, Niamh Kavanagh. - http://creativecommons.org/licenses/by-nc-nd/3.0/
Download date	2026-11-04 14:48:20
Item downloaded from	https://hdl.handle.net/10468/9617



UCC
University College Cork, Ireland
Coláiste na hOllscoile Corcaigh

Dense wavelength division multiplexing at 2 μm for future optical communications

Niamh Kavanagh
BSc
110344367

Thesis submitted for the degree of Doctor of Philosophy



NATIONAL UNIVERSITY OF IRELAND, CORK

COLLEGE OF SCIENCE, ENGINEERING AND FOOD SCIENCE

DEPARTMENT OF PHYSICS

TYNDALL NATIONAL INSTITUTE

PHOTONICS SYSTEMS GROUP

December 2019

Head of Department: Prof. John McInerney

Supervisor: Dr Fatima Gunning

Research supported by the Irish Research Council (GOIPG/2014/637)

Contents

List of Figures . . . iii
List of Tables . . . vii
List of Symbols . . . ix
List of Acronyms . . . xi
Abstract . . . xv
Acknowledgements . . . xvii

1 Introduction **1**
1.1 Context . . . 2
1.2 Motivation . . . 5
1.3 Overview . . . 6

2 Opening a new transmission window at 2 μm **9**
2.1 History of optical communication . . . 9
2.1.1 Trapping light by total internal reflection . . . 10
2.1.2 Transatlantic communication . . . 14
2.1.3 The first optical fibres . . . 16
2.2 Transmission windows . . . 18
2.2.1 First window at 0.85 μm . . . 19
2.2.2 Second window at 1.33 μm . . . 20
2.2.3 Third window at 1.55 μm . . . 22
2.3 A new transmission window at 2 μm . . . 25
2.3.1 Semiconductor materials . . . 25
2.3.2 Fibres . . . 33
2.3.3 TDFAs . . . 38

3 Optical communication systems **41**
3.1 Generating optical signals . . . 42
3.1.1 Direct modulation . . . 43
3.1.2 Modulation formats . . . 46
3.1.3 External modulation . . . 51
3.2 System performance parameters . . . 54
3.2.1 Bit error rate . . . 55
3.2.2 Signal-to-noise ratio . . . 55
3.2.3 Eye diagram . . . 56
3.3 Wavelength division multiplexing . . . 57
3.3.1 WDM systems . . . 59
3.3.2 Importance of WDM . . . 60
3.3.3 WDM at 2 μm . . . 61

4 Increasing system capacity **65**
4.1 WDM system design . . . 65
4.1.1 WDM transmitter . . . 68
4.1.2 HC-PBGF transmission . . . 70
4.1.3 WDM receiver . . . 72

4.2 81 Gbit/s WDM at 2 μm 76
4.3 100 Gbit/s WDM at 2 μm 78
4.3.1 Optimisation 78
4.3.2 SCF transmission 80
4.3.3 System analysis 81

5 Improving spectral efficiency **87**
5.1 DWDM system design 88
5.1.1 Challenges 88
5.1.2 Mux and demux methods 90
5.1.3 Power budget 95
5.2 100 GHz DWDM at 2 μm 101
5.2.1 Experiment 102
5.2.2 System analysis 102
5.2.3 105 Gbit/s system capacity 102
5.3 50 GHz DWDM at 2 μm 105
5.3.1 System design 105
5.3.2 Experiment 109
5.3.3 System analysis 109

6 Injection Locking **123**
6.1 Origins and key concepts 124
6.1.1 From clocks to crickets 124
6.1.2 Brief history 125
6.1.3 Key concepts 126
6.2 OIL experiment 128
6.2.1 Selecting 2 μm lasers 128
6.2.2 Experiment design 132
6.2.3 Observing OIL 133
6.3 Stable OIL at 2 μm 136
6.3.1 Tuning the primary laser 136
6.3.2 Tuning the secondary laser 141
6.3.3 Further OIL analysis 144

7 Conclusion **151**
7.1 Summary 151
7.2 Future Work 153
7.3 Main contributions 154
7.4 Discussion on 2 μm applications 154
7.5 Conclusion 156

A OIL images **159**

B Publications **165**

C Awards **171**

List of Figures

1.1 The electromagnetic spectrum. 3

2.1 The Chappe coding system and optical telegraph. 10
2.2 Colladon's fountain. 11
2.3 Replication of the Colladon/Tyndall fountain with a laser pointer. 12
2.4 Refraction, critical angle and total internal reflection. 13
2.5 The wave vector and propagation constant. 13
2.6 Commemoration of the first transatlantic cable in Valentia Island. 15
2.7 Light guidance by total internal reflection in an optical fibre. . . 17
2.8 Optical fibre transmission windows. 19
2.9 Erbium energy diagram. 23
2.10 Oscillation wavelength regions of semiconductor materials. . . 26
2.11 Emission wavelength of InGaAs. 28
2.12 A Fabry-Pérot cavity. 29
2.13 Standing waves on a string. 30
2.14 Emission spectrum of a Fabry-Pérot laser. 31
2.15 Optical spectrum of a multi-mode Fabry-Pérot laser. 32
2.16 Optical spectrum of a single mode Fabry-Pérot laser. 32
2.17 HC-PBGF image. 33
2.18 Optical fibre transmission windows. 34
2.19 Simplified cross section of a HC-PBGF. 35
2.20 Illustration of Bragg's law. 36
2.21 Photograph of a Blue Morpho butterfly. 37
2.22 Thulium energy diagram. 39

3.1 Tin can telephone. 41
3.2 Communication system. 42
3.3 LI curve of a slotted Fabry-Pérot laser. 44
3.4 Optical spectrum of a slotted Fabry-Pérot laser. 45
3.5 Optical spectrum indicating SMSR and OSNR. 46
3.6 OOK modulation applied to a CW wave. 48
3.7 4ASK. 49
3.8 RZ and NRZ. 50
3.9 Direct and external modulation. 51
3.10 MZM transfer function and configuration. 52
3.11 Constructive and destructive interference. 53
3.12 Eye diagram. 57
3.13 Illustration of a WDM point-to-point link. 58
3.14 WDM filter profile. 60

4.1 Wavelength division multiplexing system. 66
4.2 2 μm WDM transmitter schematic. 69
4.3 Optical spectrum of eight WDM transmitted signals. 71
4.4 2 μm WDM system schematic. 73
4.5 Tunable bandpass filter profile. 74

4.6 BER vs. OSNR for 81 Gbit/s 2 μm WDM system. 75
4.7 Eye diagram for a NRZ-OOK externally modulated channel. . . 77
4.8 4ASK fast-OFDM constellation diagram. 78
4.9 3 dB bandwidth vs. bias current for a directly modulated channel. 79
4.10 Frequency response of a directly modulated channel. 79
4.11 Frequency response of an externally modulated channel. 80
4.12 Optical spectrum WDM channels B2B, over HC-PBGF or SCF. . 81
4.13 BER vs. OSNR for 4 x 9.3 Gbit/s 4ASK fast-OFDM directly modulated channels. 82
4.14 BER vs. OSNR for 4 x 15.7 Gbit/s NRZ-OOK externally modulated channels. 84

5.1 An arrayed waveguide grating (AWGr). 91
5.2 AWGr characterisation setup. 92
5.3 Thermal characterisation of the transmitter AWGr. 93
5.4 Thermal characterisation of the receiver AWGr. 94
5.5 Optical spectrum for AWGr only, and AWGr + bandpass filter. . 95
5.6 Power budget schematic for the DWDM transmitter. 96
5.7 Optical spectrum MZM-TDFA vs. TDFA-MZM in transmitter. . . 97
5.8 Optical spectrum of the 100 GHz DWDM transmitted signals. . 98
5.9 Power budget schematic for the DWDM receiver. 99
5.10 BER vs. OSNR measurement for different power levels to the PD. 100
5.11 Full 2 μm 100 GHz DWDM schematic. 101
5.12 BER vs. OSNR to analyse transmission penalty for 100 GHz DWDM. 103
5.13 BER vs. OSNR for 7 x 15 Gbit/s NRZ-OOK externally modulated channels with 100 GHz spacing. 104
5.14 Proposed interleaved channels to create 50 GHz channel spacing. 105
5.15 Available lasers in the 2 μm waveband. 106
5.16 Temperature vs. wavelength characterisation of two lasers. . . . 107
5.17 50 GHz DWDM experiment setup. 110
5.18 Transmitter spectrum for the 50 GHz experiment. 111
5.19 BER vs. OSNR measurements for CUT (#7) (single channel). . 112
5.20 Average BER vs. OSNR measurements for CUT (#7). 113
5.21 OSNR optical spectra. 114
5.22 Optical spectra of CUT (#7) at the end of the receiver for the four scenarios of the 50 GHz experiment. 115
5.23 Received DWDM spectrum with filter profiles overlaid. 117

6.1 Injection locking of metronomes on a rolling board. 126
6.2 Free-running optical spectra of both lasers used for OIL. 130
6.3 Wavelength and power characterisation of the OIL lasers 131
6.4 Optical injection locking setup. 132
6.5 Optical spectra of coupled primary and secondary lasers. 134
6.6 OSA and ESA spectra of coupled primary and secondary lasers. 135
6.7 False colourplots for increasing primary wavelength sweep. . . 137
6.8 False colourplots for increasing secondary wavelength sweep. . 142

6.9 False colourplots for decreasing injection ratio. 146
6.10 Snapshots of OIL stability test over 24 hours. 148

A.1 False colourplots for decreasing primary wavelength sweep. . . 160
A.2 False colourplots for increasing secondary wavelength sweep. . 161
A.3 False colourplots for increasing primary wavelength sweep. . . 162
A.4 False colourplots for decreasing secondary wavelength sweep. . 163

List of Tables

4.1 First generation of 2 μm lasers. 66
4.2 Second generation of 2 μm lasers. 67
4.3 HC-PBGF details. 72
4.4 SCF details. 81

5.1 Third generation of 2 μm lasers. 89
5.2 2 μm DWDM ~100 GHz grid. 90
5.3 Gain and noise figure of TDFAs used. 101
5.4 DWDM laser and AWGr (demux) settings used 102
5.5 50 GHz DWDM grid 108

6.1 Free-running settings for the OIL lasers. 129
6.2 OIL SMSR and OSNR results. 144
6.3 Summary of the results from the four OIL scenarios. 145
6.4 Relation between injection ratio and OIL bandwidth. 147

List of Symbols

α: Alternative angle of incidence
β: Propagation constant
Δ: Difference in ...
Λ: Period
λ: Wavelength
θ_i: Angle of incidence
θ_r: Angle of reflection/refraction
ν: Frequency
ω: Angular frequency
ϕ: Phase
$_0$: Value in a vacuum
$_1$: Value in medium 1
$_2$: Value in medium 2
$_c$: Critical value
$_g$: Band gap value
B: Bit rate
c: Speed of light in vacuum
E: Energy
E_A: Wave amplitude
E_g: Band gap energy
g: Gain
h: Planck's constant
I: Current
k: Wave number
L: Length
N: Integer
n: Refractive index
R: Reflectivity
P: Power
P_{in}: Power in
P_{out}: Power out
t: Time
V: Voltage
v: Speed

List of Acronyms

ASE: Amplified Spontaneous Emission
ASK: Amplitude Shift Keying
ATT: Attenuator
AU: Arbitrary Units
AWG: Arbitrary Waveform Generator
AWGr: Arrayed Waveguide Grating
B2B: Back-to-Back
BER: Bit Error Rate
CW: Continuous Wave
CUT: Channel Under Test
DAC: Digital to Analogue Converter
DPO: Digital Phosphor Oscilloscope
DSP: Digital Signal Processing
DWDM: Dense Wavelength Division Multiplexing
EA: Error Analyser
ED: Error Detector
EDFA: Erbium Doped Fibre Amplifier
E/O: Electro-Optic
ESA: Electrical Spectrum Analyser
FEC: Forward Error Correction
IM/DD: Intensity Modulation with Direct Detection
ITU: International Telecommunication Union
ITU-T: ITU Telecommunication Standardization Sector
HC-PBGF: Hollow-Core Photonic Band gap Fibre
LDC: Laser Diode Controller
LI: Light Current
MUX: Multiplex
MZM: Mach-Zehnder Modulator
NRZ: Non-Return-to-Zero
O/E: Opto-Electric
OFDM: Orthogonal Frequency Division Multiplexing
OIL: Optical Injection Locking
OOK: On-Off Keying
OSA: Optical Spectrum Analyser
OSNR: Optical Signal to Noise Ratio
PC: Polarisation Controller

PD: Photodetector
PPG: Pulse Pattern Generator
PRBS: Pseudo Random Bit Sequence
RF: Radio Frequency
RI: Relative Intensity
Rx: Receiver
RZ: Return-to-Zero
SCF: Solid Core Fibre
S/N: Serial Number
SNR: Signal to Noise Ratio
SMF: Single Mode Fibre
SMO: Single Mode Operation
SMSR: Side Mode Suppression Ratio
SCF: Solid Core Fibre
TDFA: Thulium Doped Fibre Amplifier
TEC: Thermo-Electric Cooler
Tx: Transmitter

Please note that the text of this thesis has been formatted with left-justification (as per UCC recommendations) for optimal comprehension, readability and legibility, especially for those with dyslexia.

I, Niamh Kavanagh, certify that this thesis is my own work and has not been submitted for another degree at University College Cork or elsewhere.

_____

Niamh Kavanagh

Abstract

The internet is ubiquitous in our lives today, enabling instantaneous access to information, increased international collaboration, and even real-time remote surgery. It has changed how we socialise and how we see the world. From 2017 to 2022, global internet traffic is forecasted to triple, creating severe pressure on optical communication systems. Delivering the capacity required to support this traffic presents significant challenges in terms of system design, device performance, and optical fibre capabilities. Novel solutions are needed now, if we are to meet the demands of the near future. While solutions to increase system capacity and bandwidth efficiency of optical communication systems at 1.55 μm is widely discussed in the literature, shifting transmission to the 2 μm wavelength window could open possibilities to new discoveries in optical components, improved bandwidth efficiency, innovative optical fibres, and other applications transcending beyond optical communications.

This thesis explores opening the 2 μm transmission window for optical communications. The focus of this work investigates the feasibility of implementing dense wavelength division multiplexing (DWDM) systems at 2 μm, with key enabling technologies developed recently. Strained III-V materials can produce foundry-compatible 2 μm lasers and detectors. Hollow-core photonic band gap fibres (HC-PBGFs) can guide 2 μm light through air, offering potentially lower losses, reduced latency and higher power-handling capabilities (in comparison to standard silica fibre). Also, thulium doped fibre amplifiers (TDFAs) could offer bandwidth of up to $\sim$30 THz in the 2 μm waveband ($\sim$double that of EDFAs at 1.55 μm).

Contributions of this thesis include the demonstration of a 2 μm DWDM system with channel spacing of 100 GHz and system capacity above 100 Gbit/s, for the first time in this new transmission window. Further increasing the capacity of 2 μm DWDM systems requires improving the spectral efficiency, which can be accomplished by reducing the spacing between channels. While 50 GHz channel spacing is shown to be achievable with current technologies in the transmitter, insufficient filtering can be a barrier for implementation in the receiver. With this in mind, novel filtering technologies are required and optical injection locking (OIL) is investigated as a possible filtering solution. The first study of OIL using two slotted Fabry-Pérot lasers at 2 μm is demonstrated, achieving a stable OIL bandwidth of $\sim$7 GHz and OIL-induced single mode operation over a 15 GHz range.

Acknowledgements

The last five years have been incredible. I changed, Ireland changed, and I hope the work that I have done will change the world in some way. Above all else, these past five years have taught me the true value of community. I am very lucky to be in the privileged position that I have so many people to thank.

To Fatima Gunning, thank you for your empathy, honesty and guidance. You reignited my passion for physics, opened my eyes to a whole new world of opportunities and supported me every step of the way. You enabled me to go above and beyond what I thought was possible for myself. I don't think I would have done a PhD if it wasn't for you and I know I couldn't have done what I did with this PhD without you. I am so lucky to have had such an amazing supervisor, mentor and confidant throughout this journey.

To my Dad (Pascal Kavanagh), Mam (Elizabeth Kavanagh), brother (Andrew Kavanagh) and sister (Aoife Kavanagh), you are the pillars of my life. Thank you for being my safe haven. Thank you for showing me the value of hard work, fun holidays, reading, music, exploring the world and sitting around the kitchen table chatting. Mam and Dad, thank you for always supporting the three of us to find what we liked and to stick with what we loved. Thank you for making me believe I could do anything, as long as I tried my best.

To my partner, Michael O'Sullivan, I'm so lucky I found you. Thank you for helping me in every way I asked for and more over the past five years (but especially the last one). Thank you for picking me up when I felt fed up, exhausted or full of doubt. Thank you for always reminding me about what really matters. Thank you for all the good morning texts, late night conversations, many dinners, (too many desserts) and the daily supply of cute cat videos. You are a constant source of joy, support and surprise in my life. I'm so grateful for you and I'm so excited for all our adventures together ahead.

To Mairead Spillane and Michael O'Sullivan, you are amazing people that have done so many amazing things (most of which I'll probably never find out about). Thank you for always trying to feed me whenever I turned up, supporting me in every way you could, and welcoming me into your family with open arms. Thank you also for raising such an amazing son!

To Jessie Doherty, Eamonn O'Neill, Sean Goveas, Niamh Furlong and everyone in my 2010-2014 Physics class, I was so lucky to be part of your year. Taking a year out before college was the best decision I ever made, because it meant I got to find you all as friends. Thank you for always being able to talk about anything and everything so openly. Thank you for all the help you've given me over the years. Thank you for being my fireworks, when I felt like locking myself in a bathroom. To Brian Murray, Shane Duggan, Steve Murphy, Alison Perrott and all the lunch crew, thank you for all the distractions, tea breaks, solidarity, help and funny GIFs. I'm very lucky to have gained such a fantastic group of friends over the past ten years.

To Shaun O'Boyle, House of STEM brings me so much pride in every sense of the word and it's one of the best things been involved in during my PhD. LGBT STEM day is amazing. Thank you for helping me find my community, for all the uplifting voice messages and for inviting me to be part of something so special in the first place. Thank you also to Pride in STEM, LGBTQ+STEM, UCC LGBT+ Staff Network, and Bi+ Ireland for the amazing work they do.

Thank you to everyone working to improve the culture of STEM (Science, Technology, Engineering and Maths) to be more diverse, inclusive and supportive of people from all walks of life. Thank you, especially, to everyone at Teen-turn, UCC Athena Swan and Empowering Women at Tyndall. I feel so honoured to have had the opportunity to work alongside so many amazing advocates, inspirational leaders and committed change-makers. I hope we can all keep working together to make the culture of STEM better.

Thank you to Eoin Russell, Natalia Canas-Estrada, Amandeep Kaur, Yuliya Verbishchuk and everyone in Fatima Gunning's group. I am really lucky to have been part of such a supportive team. Thank you for all your assistance, encouragement and solidarity throughout this PhD. Thank you to all my colleagues at Tyndall National Institute and University College Cork. Thank you to Hongyu Zhang for introducing me to the intricacies of the 2 μm system. Thank you to my thesis committee for their counsel.

Thank you to everyone at the IEEE Photonics Society (especially Lauren Mecum-Smith), the Optical Society and the Institute of Physics for connecting me with a wonderful global community of friends. I am especially grateful to have been part of the IEEE Photonics Society Diversity Oversight Committee for all the opportunities I've had to share my passion, meet other passionate people and make real change in the photonics community worldwide.

Thank you to everyone working in science communication (in Ireland and beyond), especially Liz McBain at Famelab, Jessamyn Fairfield at Bright Club, Sheila Gilheany when she was at the Institute of Physics, Eric Fitzpatrick at ARK Speaking and Training, and Ann O'Dea, Elaine Burke and all the team at Siliconrepublic.com. Thank you for all the training, opportunities and visibility you have given me over the past few years. More importantly, thank you for making science more accessible, relevant and enjoyable to so many people.

Thank you to Karen McCarthy, Aoife O'Brien and Magaly Mora for all the encouraging chats, advice and all the times you cheered me up.

Thank you to Arti Agrawal, Gabrielle Thomas and Greg Quarles for all the guidance, support and encouragement you have given me.

Thank you to all the organisations that have funded the work of this thesis including the Irish Research Council (GOIPG/2014/637), Science Foundation Ireland under IPIC (12/RC/ 2276) and (13/CDA/2103), and the EU FP7 IP project MODEGAP (258033).

Thank you to everyone who has read this thesis.

For all the women in my life that led the way.

To Agnes Kavanagh, Joan Doyle,
Fatima Gunning, Mairead Spillane
and, my Mam, Liz Kavanagh.

Thank you.

"*Stand in awe of all mná.*"

From "Heartbreak" by Emmet Kirwan, 2016.

Chapter 1

Introduction

Optical communication systems have enabled high-speed, high-capacity, international communication, thus creating an increasingly globalised society that is more connected than ever before. Thanks to the advances of optical communication systems, people today can communicate with family and friends all over the world, with much greater ease and convenience than those in previous decades. Not only can people communicate with one another almost instantaneously, through text messages or voice calls, but video calling is becoming increasingly popular. People can now see the faces of their loved ones as they swap stories, blow out candles on birthday cakes, or share the view from their part of the world. This is especially meaningful, for example, in a country like Ireland, which has a long history of emigration. There is a massive Irish diaspora in the United States, England and Australia [1]. A 2014 study showed that nearly a fifth (17.5%) of people over the age of 15 who were born in Ireland were residing overseas (the highest percentage of the 34 countries surveyed) [2].

In my own family history, my grandmother's brother emigrated to America in the 1960s. They communicated once a month by letter. In the 1980s, my mother's brother moved to London. Although phones had become more popular by then, they were not yet common in most households. Every fortnight my mother and her family would visit a relative who owned a phone so that they could speak to her brother. With the invention of the telegram, same-day communication was possible by this time, but it was prohibitively expensive and reserved for emergencies. Today, my own brother lives in Canada. We communicate almost every day and I can see his face at the click

of a button. While this thesis focuses on the facts, figures and physical principles of optical communication systems (with particular focus on how to implement those systems at the 2 μm waveband), it is important to remember the social impact of these technological advances in just a few generations. This paragraph serves to highlight one small aspect of that impact on one family in particular.

Today, real-time video calling is possible to most cities around the world. In fact, mobile video traffic now accounts for more than half of all mobile data traffic and is predicted to increase to almost four-fifths by 2022 (representing a nine-fold increase since 2017) [3]. This, along with the rise of augmented reality, artificial intelligence, self-driving cars, high-definition multimedia streaming, cloud storage and increased connectivity through the 'internet of things', requires preparation for a future of big data, with increasingly bandwidth-hungry applications and rapidly growing capacity demands. Current forecasts project global internet traffic to triple from 2017 to 2022, along with the number of internet-connected devices becoming three times larger than the world's population [3].

1.1 Context

Historically, the frequencies at which we communicate information have shifted if more bandwidth/capacity was required and the technology allowed. The electromagnetic spectrum is shown in Figure 1.1. Coaxial cables operate with frequencies from 1 KHz (10^3 Hz) to 1 GHz (10^9 Hz), including the AM and FM radiowave range. Terrestrial and satellite transmission operate in the microwave range, with frequencies from 1 GHz to 1 THz (10^{12} Hz). However, optical communication systems operate at the highest frequencies in the range of 100 THz (10^{14} Hz) to 1000 THz (10^{15} Hz). The optical carrier frequency yields a far greater potential transmission bandwidth than radiowave or coaxial cable systems. For example, by the year 2000, the typical bandwidth for an optical fibre link (incorporating fibre amplifiers) was 50,000 times greater than that of coaxial cables at the time, while also providing superior information-carrying capacity over much longer transmission distances [4].

Optical communication systems transmit information around the world using pulses of light travelling through optical fibres. These fibres are threaded across our whole planet; beneath our feet and under our oceans; connecting

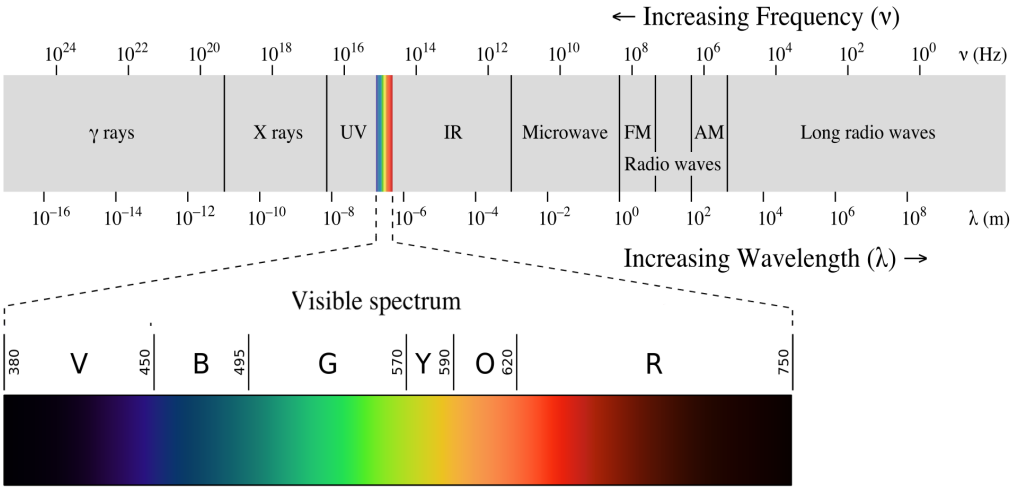


Figure 1.1: The electromagnetic spectrum. *This file is licensed under the Creative Commons Attribution-Share Alike 3.0 Unported license.*

cities, countries and continents. This optical physical layer forms the basis of the internet. The wavelength of light that is used to transmit information is usually within a certain wavelength range, or transmission window. These transmission windows have been primarily determined by the available lasers, optical fibres and, later, optical amplifiers. The first transmission window for optical communication systems was opened in the 1970s. This was done using the first Corning fibres, and Gallium Arsenide (GaAs) semiconductor lasers which operated around 0.85 μm [5]. The second window followed in the 1980s using InGaAs lasers operating at 1.33 μm [6]. Systems in this window were developed for commercial use for the first time. In the 1990s, the third window was opened using low-loss standard single mode fibre (SMF) operating at 1.55 μm, called the conventional band (or C-band from 1.53 μm to 1.56 μm) [6]. Today this transmission window is commonly used in metro, long-haul, and submarine optical transmission systems [7]. The popularisation of the 1.55 μm wavelength region for optical communications over the past three decades has been made possible primarily due to the three key elements mentioned previously; the availability of semiconductor materials for lasers (in transmitters) and detectors (in receivers), low-loss (~0.2 dB/km) standard SMF as a transmission medium [8], and erbium doped fibre amplifiers (EDFAs) to enable transmission over long distances with high-gain and low-noise [9].

Dense wavelength division multiplexing (DWDM) is a method of combining a

number of optical carriers onto a single optical fibre by using different wavelengths (or frequencies) to carry different signals, increasing the capacity of the overall system. Currently, commercial DWDM systems at 1.55 μm can operate up to 100 channels at data rates of 100 Gbit/s (with a spacing of 50 GHz between channels), resulting in spectral efficiency of ~2 (bit/s)/Hz and total capacities in the order of 10 Tbit/s [10]. However, the available bandwidth in the 1.55 μm wavelength region for optical communications is fundamentally limited by physical effects in silica optical fibres. These fundamental effects include unavoidable losses (such as Rayleigh scattering) at shorter wavelengths, infrared absorption at longer wavelengths, and nonlinear optical phenomena that are excited in the fibre at high powers [4]. The bandwidth is also limited by the gain region of EDFAs which extends from 1.48 μm to 1.61 μm (or ~15 THz), covering the C-band and the long-wavelength band (or L-band from 1.56 μm to 1.62 μm) [11], [6].

As the readily available bandwidth becomes more increasingly occupied, capacity demands require much more efficient utilisation of optical bandwidth (through advanced digital signal processing techniques) [10]. Currently, the growth in network traffic, coupled with observed trends in commercial practice, will result in a requirement for optical communication systems which can support channels operating at data rates of 1 Tbit/s and, therefore, total capacities in the order of 100 Tbit/s by 2020. Terabit single-channel bit-rates are difficult to achieve and complex within current technological capabilities [10].

Today, with ever-increasing capacity demands, enabling the capability for transmission in other wavelength regions to increase the available bandwidth is being investigated. Currently, researchers are working on technologies for ultra-wideband optical communication systems beyond the C+L bands [12],[13]. In fact, the Journal of Lightwave Technology is due to publish a special issue on ultra-wideband wavelength division multiplexing (WDM) systems in February 2020 [14]. Now is the time for new and radical solutions. Opening the transmission window at 2 μm and enabling optical communication systems in this new waveband could supplement the available bandwidth and provide alternatives for future internet traffic growth.

1.2 Motivation

Shifting transmission to longer wavelengths was considered as far back as the 1980s, due to the reduction of Rayleigh scattering. For this purpose, new fibre materials were investigated, including chalcogenide, germanate and fluoride (e.g. ZBLAN), glass fibres [15]. The first transmission in the 2 μm waveband took place in 1987 (to the best of our knowledge), over ZBLAN fibre [16]. However, ZBLAN fibres proved to be brittle and highly nonlinear, restricting propagation over long distances [17], [18]. Today, other novel types of optical fibres are available in the 2 μm wavelength window, such as hollow-core photonic band gap fibres (HC-PBGFs).

HC-PBGFs are especially interesting as they have a unique 'cladding' region that consists of a honeycomb-like microstructure which confines light in the hollow core [19]. The transmission of light through air offers significant advantages compared to silica transmission, such as the potential to reach losses as low as 0.1 dB/km around 2 μm [20], near-vacuum latency [21] and a reduction in the nonlinear coefficient by up to three orders of magnitude (i.e. greater power-handling capabilities) [22]. The extended nonlinear threshold and lower loss could enable capacities three to four times greater than the current limits [23]. Shifting transmission to 2 μm has the added advantage that signals can be transmitted over HC-PBGF, without the need to upgrade the electronics complementary to the optical system.

In the 1.55 μm window, III-V semiconductor materials are generally preferred for optical communication applications because of their compact size, relative efficiency and suitable emission wavelengths [24]. When shifting transmission to 2 μm, it would be desirable to choose compounds that are also used in the C-band (i.e. foundry-compatible compounds), as these semiconductor processes are mature, cost-effective and widely available. At 2 μm, photon emission and detection can be achieved by straining the layers of indium gallium arsenide (InGaAs) semiconductors [25], a III-V material used for 1.55 μm applications. Therefore, foundry-compatible semiconductor materials are available at 2 μm.

Amplification at 2 μm can be achieved with thulium doped fibre amplifiers (TDFAs). Thulium offers a potentially broad amplification range from 1.7 μm to 2.1 μm, with similar gain and noise figures to EDFAs [26]. This ~30 THz bandwidth makes TDFAs especially attractive, compared to the current

~15 THz (1.48 μm to 1.61 μm) offered by EDFAs [27]. If TDFAs are also used in conjunction with holmium doped fibre amplifiers, optical amplification around the 2 μm transmission window can be extended to over 40 THz, nearly three times more than the current bandwidth available at 1.55 μm [28].

Moreover, there is also a wide range of applications for technologies in the 2 μm waveband beyond optical communication systems, such as medical sensing (detecting blood glucose and carbon dioxide) [29], [30], [31], [32] greenhouse gas detection (such as methane) [33], [34], gravitational-wave observation (LIGO), and eye-safe LIDAR systems to detect air turbulence, measuring water content for humidity sensors and agricultural purposes [35], [36]. While these technologies are outside the focus of this work, these applications mean that some commercial components are already available in the 2 μm wavelength range [33].

1.3 Overview

The objective of this thesis is to investigate the feasibility of implementing a DWDM system at 2 μm for the first time. The work of this thesis aims to show that opening a new wavelength transmission window for optical communications is possible at 2 μm, using the potential technologies available.

Chapter 2 begins with the history of optical communication, how it has developed into what we know today, and what the key enabling technologies were along the way. The core concepts of fibre-optic transmission are introduced, such as light confinement in optical fibres. The development of optical transmission windows (from 0.85 μm, to 1.33 μm, and 1.55 μm) is discussed and historically contextualised, with the key principles explained. Ultimately, this chapter aims to answer the question - how can we enable optical data transmission at 2 μm?

Chapter 3 discusses the fundamentals of optical communication systems. In general, a communication system consists of a transmitter, a receiver and a transmission medium carrying information. This chapter discusses the physical principles of these key elements. At the transmitter, the focus is on generating the light carrier and converting the electrical signal into optical using various modulation formats [37]. In the receiver, the focus is on converting the optical data back to electrical for data processing or re-transmission, as required. A brief overview of the development of WDM systems at 2 μm is also presented

at the end of Chapter 3.

The main challenge of implementing a DWDM system at 2 μm is the lack of commercially-available telecom-grade components that are needed in order to implement a DWDM system at this waveband. For example, the bandwidth of components like modulators and photodetectors is limited by immature manufacturing technologies, in comparison to those established in the 1.55 μm window over the past three decades. Many of the components used in the experiments throughout this thesis are first generation and non-optimal. Many components suffer impairments such as low power, high insertion loss, thermal fluctuations or poor frequency response. While some commercial products are available, they tend to be more expensive than 1.55 μm equivalents, with poorer performance in comparison. Designing these components to work together in a cohesive DWDM system presents a non-trivial challenge that this thesis aims to address.

Hence, Chapter 4, Chapter 5 and Chapter 6 discuss these challenges in more detail and describe the experimental work in this thesis. The capacity of a WDM system can be maximised by enabling a greater number of transmission channels and optimising the spectral efficiency. As such, Chapter 4 focuses on increasing the WDM system capacity at 2 μm beyond 30 Gbit/s by enabling a greater number of channels, with a capacity of 105 Gbit/s ultimately achieved [38]. Chapter 5 addresses the spectral efficiency of optical communication systems at 2 μm. The experiments in Chapter 5 were designed to investigate the feasibility of implementing DWDM at 2 μm with reduced spacing of 50 GHz between channels (as opposed to >100 GHz channel spacing in previous demonstrations). However, while 50 GHz channel spacing was readily achievable in terms of the 2 μm transmitter, the results of these experiments indicated that current filtering techniques do not provide sufficient channel isolation at 2 μm [39]. Optical injection locking (OIL) is a technique that has been employed for filtering purposes at 1.55 μm and, as such, provides a promising candidate for the same purpose at 2 μm [40], [41], [42]. The first study of stable OIL at 2 μm using two slotted Fabry-Pérot lasers is presented in Chapter 6 [43], [44]. Finally, Chapter 7 presents the conclusions from this thesis.

In order to continue connecting, communicating, and sharing content with friends and family around the world, we need to stay ahead of increasing capacity demands. Novel solutions are needed in order to provide alternatives

for future internet growth. Despite the challenges associated with experimental implementation of 2 μm DWDM technologies, this thesis demonstrates the development of optical communication systems at this waveband. Opening a new transmission window at 2 μm could supplement the available bandwidth and increase capacity for future optical communication systems.

Chapter 2

Opening a new transmission window at 2 μm

The origins of optical communication systems are presented in this chapter. The historical discovery of key elements such as total internal reflection, transatlantic communication, and the first optical fibres are highlighted. These elements combined to enable terrestrial optical communication systems as we know them today. Optical data is transmitted through such systems using a certain range of wavelengths, called a transmission window. This transmission window is primarily determined by the region of minimum optical fibre attenuation, maximum transmission capability (supported by amplifiers and available semiconductor materials for transmitters/receivers), and this is no different for the transmission window at 2 μm.

2.1 History of optical communication

Light and communication have long been intertwined throughout human history. The ability to send information as far as needed, as fast as possible has been sought-after since ancient times. One of the earliest and most well-known examples is smoke signals, which were used by people of many cultures including the Native American and Aboriginal Australian indigenous communities. Also, in ancient China (~900 BC), soldiers guarding the Great Wall would warn others of an incoming attack by signalling from beacon towers using smoke signals in the daytime or a fire at night. Using this method, warnings could be transmitted as far as 750 km in a few hours.

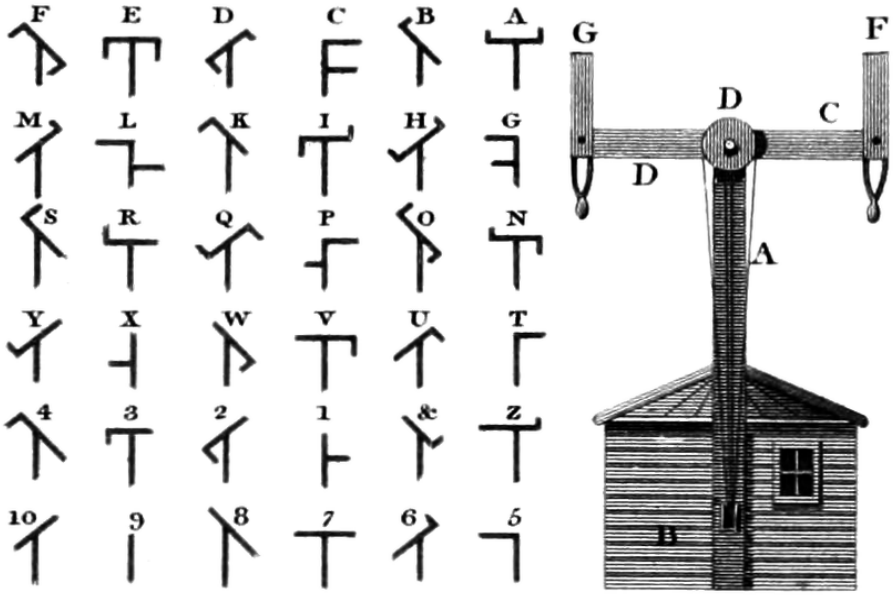


Figure 2.1: The Chappe coding system and optical telegraph, or semaphore. An early example of a complex optical communication system. *This work is in the public domain. Source Rees's Cyclopædia, Plates Vol. IV, TELEGRAPH, Fig. 4.*

Around 150 BC, a Greek historian called Polybius, created a system of smoke signals based on numeric combinations of two torches which corresponded to letters of the alphabet [7]. In this way, more intricate messages could be communicated via smoke signals.

Beyond smoke signals, visual communication systems gradually became more complex. In the 1790s, during the height of the French revolution, the Chappe brothers created the semaphore. Illustrated in Figure 2.1, this optical telegraph system consisted of a series of tower stations that could transmit messages to one another by means of an operator pivoting the arms or shutters on the top of the tower. France was soon covered with a network of 556 of these stations. This system was used for military and national communications until the 1850s [7]. However, from smoke signals to the semaphore, the shared disadvantage of these systems was that messages could only be transmitted via line of sight. Any obstacles that blocked the view, such as inclement weather, could prevent the communication of information.

2.1.1 Trapping light by total internal reflection

It would be more advantageous, therefore, if communication was not dependent upon line-of-sight transmission and instead could be 'trapped' and directed to navigate various paths over long distances. In the 1840s, the Swiss

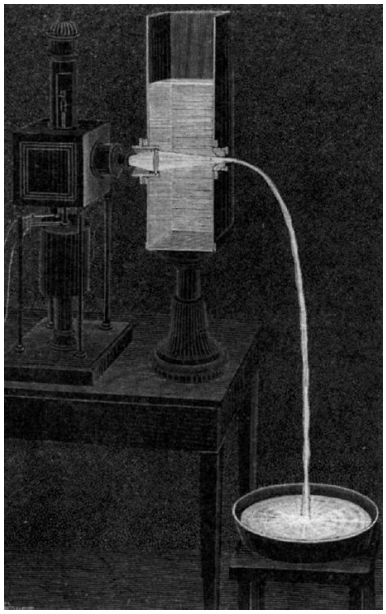
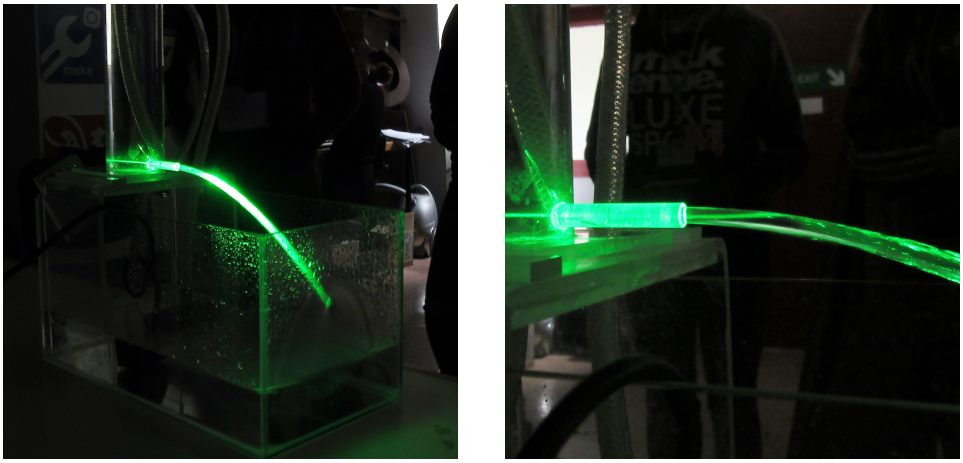


Figure 2.2: Colladon's fountain demonstrating light following the curve of water, later made famous by John Tyndall. *This work is in the public domain. Author: Jean-Daniel Colladon (1802-1893). Source: This illustration appeared first in La Nature magazine in 1884.*

physicist Jean-Daniel Colladon showed that light could be directed along streams of water from a fountain, as shown in Figure 2.2, [45]. This effect was popularised by another physicist; John Tyndall, who was born in Carlow and after whom the Tyndall National Institute (in Cork, Ireland) is named. In May 1854, Tyndall presented the "total reflection of light at the common surface of two media of different refractive indices" - water and air, during a lecture at the Royal Institution in London [46], [47]. This effect can easily be replicated today with a laser pointer, water dispenser (such as a bottle with a hole in the bottom) and basin, as shown in Figure 2.3.

To understand the physics of this light-trapping phenomenon, consider the laws of reflection and refraction. The law of reflection states that if a ray of light is incident on a plane mirror (or reflective surface), then the angle of the reflected light ray will be equal to the angle of incidence. The law of refraction (or Snell's law, Equation 2.1) dictates that if a light ray travels from one medium with refractive index (n_1) to another medium with a different refractive index (n_2), then the ratio of these refractive indices will be equal to the sines of the angles of incidence (θ_i) and refraction (θ_r), with all angles measured from the normal of the boundary. These fundamental laws predict the path that a light ray will take at various boundaries between different media.



(a) (b)

Figure 2.3: (a) The Colladon/Tyndall fountain experiment can be easily replicated using a laser pointer, water dispenser and container. (b) The total internal reflection of the laser beam in the water stream can be seen. *Source: Photo, N. Kavanagh, 2018.*

$$\frac{n_1}{n_2} = \frac{sin(\theta_r)}{sin(\theta_i)} \qquad \textit{Snell's law} \tag{2.1}$$

However, consider Snell's law (Equation 2.1) in the case where $n_1 > n_2$ and the light ray travels from a denser medium (such as water) to a rarer medium (such as air). In this case, Snell's law would require that the sine of the angle of incidence could extend to be greater than one. Since this is not mathematically possible, it implies the existence of an upper limit for the angle of refraction. The angle corresponding to this upper limit is called the critical angle, given in Equation 2.2. Above this critical angle, light from the denser medium (with refractive index n_1) will be completely reflected at the boundary. This phenomenon is called total internal reflection and is illustrated in Figure 2.4.

$$\theta_c = sin^{-1}(\frac{n_2}{n_1}) \qquad \textit{critical angle} \tag{2.2}$$

In order to obtain a mathematical expression for this critical angle, consider a propagating light wave which can be represented by a wave vector($\hat{k}$) whose component of propagation (in the $\hat{z}$ direction) is called the propagation constant (β). The light wave also has a wave number (k), which corresponds to the wavelength λ, according to the relation in Equation 2.3.

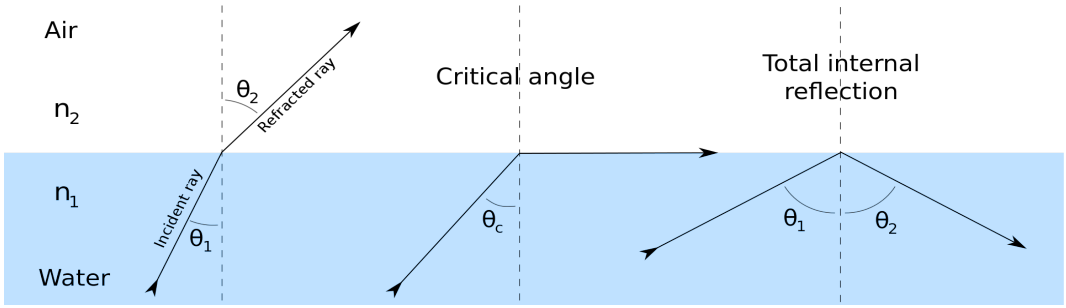


Figure 2.4: Image on the left shows the refraction of a light ray travelling from a denser to a rarer medium. Central image depicts the critical angle. Image on the right demonstrates total internal reflection. In these figures, θ_1 is the angle of incidence, and θ_2 is the angle of refraction/reflection. *This file is licensed under the Creative Commons Attribution-Share Alike 3.0 Unported license. Author: Josell7*

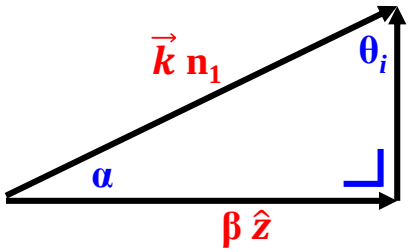


Figure 2.5: A light wave (travelling in medium with refractive index n_1) can be represented by a wave vector $\hat{k}$ and propagation constant β.

$$k = \frac{2\pi}{\lambda} \qquad \textit{wave number} \tag{2.3}$$

If, instead of measuring the angle of incidence from the normal to the surface (θ_i), the alternative angle α is used (as defined in Figure 2.5 and Equation 2.4), the critical angle can then be redefined in terms of β and k, as per Equation 2.5.

$$sin(\theta_i) = cos(90 - \theta_i) = cos(\alpha) \tag{2.4}$$

$$cos(\alpha) = \frac{\beta}{kn_1} \tag{2.5}$$

The propagation constant β is then defined as per Equation 2.6 and an alternative definition for the critical angle, in terms of α, is given in Equation 2.7.

$$\beta = kn_1 cos(\alpha) \qquad \textit{propagation constant} \tag{2.6}$$

$$sin(\theta_c) = cos(\alpha_c) = \frac{n_2}{n_1} \qquad \textit{critical angle} \tag{2.7}$$

For $0 < \alpha < \alpha_c$, then

$$1 > \frac{\beta}{kn_1} > \frac{n_2}{n_1} \tag{2.8}$$

Equation 2.8 gives the condition for light guidance in a medium of refractive index n_1, bordering another medium of refractive index n_2, in terms of the wave number and propagation constant [48].

$$kn_1 > \beta > kn_2 \qquad \textit{guidance condition} \tag{2.9}$$

Equation 2.9 is the guidance condition for a light ray to be trapped by total internal reflection in a medium (of refractive index n_1) when surrounded by another medium (of lower refractive index n_2). If $kn_1 < \beta$ then α is imaginary and the light will be evanescent, i.e. decaying exponentially into the surrounding medium. When the guidance condition is satisfied (for $kn_1 > \beta$), light will propagate, confined within the central medium via total internal reflection. The condition will hold for an integer number of wavelengths, determining a discrete set of light waves that can propagate [48]. It was in this way that light could be 'trapped' inside streams of water for Tyndall's famous fountain experiment (however, some light was scattered from the imperfect streams). Today, this concept of total internal reflection is the conventional guiding mechanism in standard optical fibres.

2.1.2 Transatlantic communication

In 1854, the same year as Tyndall's demonstration of total internal reflection, the installation of the first transatlantic telegraph cable began. The cable connected Valentia Island in Kerry (Ireland) to Heart's Content in Newfoundland (Canada). The installation of this cable finished in 1866 and represented the first time the continents of Europe and North America were physically connected. The first communication occurred in August 1858, using



Figure 2.6: Photo of the author at the commemoration of the first transatlantic cable in Valentia Island, Ireland. Plaque reads: "This marine bollard, made from native stone, stands to commemorate the first successful physical connection between Europe and North America in 200 million years. On July 27, 1866 the Great Eastern completed the laying of the transatlantic cable between Valentia Island, Ireland and Heart's Content, Newfoundland. The cable changed the world by revolutionising global communications and pioneering the information highway we know today."

radio frequency waves. While the initial Morse code messages in 1858 took over 17 hours to transmit, by 1866 the connection was 80 times faster and could transmit eight words a minute. In the 20th century, transmission speeds extended to 120 words per minute. While this may seem slow by today's standards, prior to the transatlantic cable installation, communication between Europe and America was possible only by ship and could take several weeks. The transatlantic telegraph cable enabled messages to be sent and received within the same day. This had significant impact on the economy. For example, a 2018 study from the American Economic Review found that the transatlantic telegraph substantially increased trade across the Atlantic and reduced prices [49]. A new era of global connection had begun. The installation of the first cable is commemorated today by a pair of matching marine bollards in Heart's Content and Valentia Island, as shown in Figure 2.6 [50], [51].

Today, most transatlantic communication systems are based on optical fibres or satellite communications. In the case of terrestrial systems, the main enablers for communications are not only the transmission medium (from the telegraph copper cable to optical silica fibres, for example), but also the terminals which convert the desired data into signals that can be transmitted and received (using radio frequency waves for copper cables and THz frequency waves for optical fibres). It is the convergence of all these key enablers that heralds the invention of a new communication system.

2.1.3 The first optical fibres

Along with the first transatlantic connection, the turn of the century saw bent glass rods being used for the first time. These were used by Viennese doctors Roth and Reuss to illuminate body cavities in 1888 [52], and by French engineer Henry Saint-Rene to guide light images in 1895 [53]. In the 1920s, Englishman John Logie Baird and American Clarence W. Hansell patented the idea of using arrays of transparent rods to transmit images for television and facsimiles, respectively [53]. A German medical student, Heinrich Lamm, was the first person to transmit an image through a batch of optical fibres in 1930 [53]. In the 1950s, nearly 100 years after Tyndall's popular demonstration of total internal reflection, Danish scientist Hogler Moeller proposed cladding glass fibres with a transparent material of lower refractive index to transport images optically, as shown in Figure 2.7 [53]. By the late 1950s, glass-clad fibres had attenuation of ~1 dB per metre. As a result, 90% of light was lost (or attenuated) over only a few metres. This was suitable for medical imaging, but much too high for communications over several kilometres [7], [53]. However, in 1960, the invention of the first laser (emitting red light at 694 nm) renewed researchers' interest in optical fibres as a means to transmit this new coherent light over long distances [54], [55].

In the early 1960s, optical fibre attenuation was ~1000 dB/km, in comparison with 5 dB/km to 10 dB/km in the coaxial cables traditionally used for communications. In 1964, Charles Kao theoretically demonstrated that the light loss in existing glass fibres was due to impurities and was not a feature of the fibre itself. In 1966, Kao and George Hockham predicted that fibre losses could be reduced to below ~20 dB/km and said that optical fibre "represents a possible medium for the guided transmission of energy at optical frequencies" [56]. This prediction inspired a race to reduce losses and produce

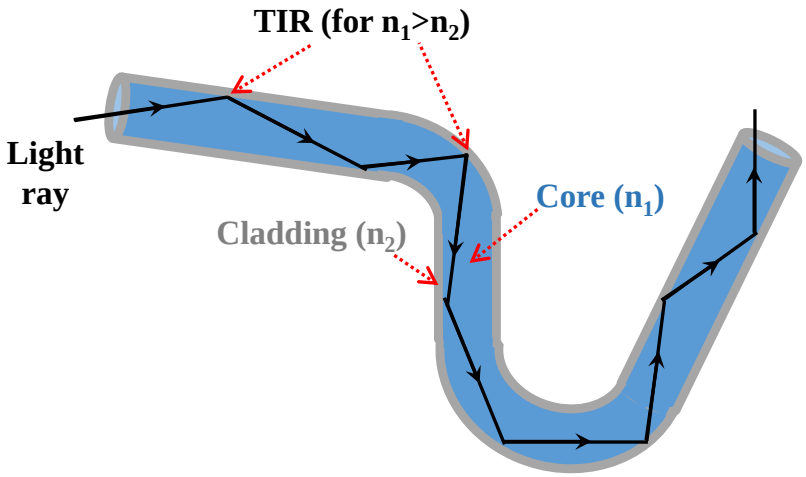


Figure 2.7: Light guidance by total internal reflection (TIR) in an optical fibre.

purer glass fibres. In 2009, Kao won the Nobel prize for groundbreaking achievements concerning the transmission of light in fibres for optical communications. The low loss of today's optical fibres is one of the primary reasons they have become the backbone of global terrestrial communications.

The dominant loss mechanisms in optical fibres include absorption, Rayleigh scattering, and bend losses. Absorption is a loss mechanism related to the material composition and fabrication process of the fibre. It occurs due to the interaction of transmitted light with silica and impurities within the fibre. All materials will absorb energy at certain wavelengths. In the wavelength region $\sim$1.3 μm to 1.6 μm, absorption losses are only $\sim$0.03 dB/km. Water contamination during the fabrication process also contributes loss, resulting in narrow absorption peaks in the fibre attenuation profile [57], [58], [4], [8].

Rayleigh scattering is the greatest source of loss in optical fibres. It is also the reason for the blue colour of the sky. Rayleigh scattering in silica fibres arises from inhomogeneities that are on a smaller scale than the wavelength. These inhomogeneities form when the fibre is heated during fabrication. During this process, the silica moves randomly in the molten state and is subsequently frozen in place when fabrication is finished. This results in local microscopic density (i.e. refractive index) fluctuations on a scale smaller than the optical wavelength. While compositional variations may be reduced by improved fabrication methods, these small scale inhomogeneities are fundamental and cannot be eradicated. The subsequent scattering produces attenuation that is

proportional to $1/\lambda^4$ [59]. Therefore, Rayleigh scattering reduces as the operating wavelength increases. This reduction in Rayleigh scattering provides motivation to shift transmission to longer wavelengths. However, the longer-wavelength limit for transmission is determined by absorption, which becomes stronger in silica fibre as the operating wavelength increases. At 1.55 μm, attenuation due to Rayleigh scattering is ~0.12 dB/km to 0.16 dB/km, making it the dominant attenuation contribution in most C-band glass-based fibres [58], [4].

Bend loss becomes more of a concern when the fibre is implemented into a system. Bend loss is a result of the fundamental speed of light. When light travels through an optical fibre, the wavefront must remain perpendicular to the direction of propagation for optimal guidance. When light travels through a bent optical fibre, the part of the wavefront on the outside of the bend has a longer path length than light on the inside. Losses are incurred when the bend is sufficiently tight that the light in the outer section would need to travel faster than the fundamental speed of light in that medium. Since this is not possible, the energy associated with that part of the wavefront is lost. For this reason, communications fibre is installed in smooth large-radius bends so that bend losses are negligible [57], [4].

2.2 Transmission windows

> "*For nearly a century, scientists had dreamed of using light to "talk" over long distances. They had long recognised that light carries a great deal of information, but it needed a mechanism or a vehicle to guide it. Many people investigated techniques by which this could be accomplished. Nevertheless, by the late 1960s the practical technique had not been found - neither the transmission medium nor the modulatable light source. At the same time, the telecommunication service providers were facing the need for dramatically increased capacity.*"
> From "A Future Full of Light" by D. Keck, 2000. [60]

Figure 2.8 shows an illustration of optical fibre attenuation taking into account Rayleigh scattering and absorption, including the water absorption peaks at 0.95 μm and 1.39 μm (peak-heights are for illustration purposes

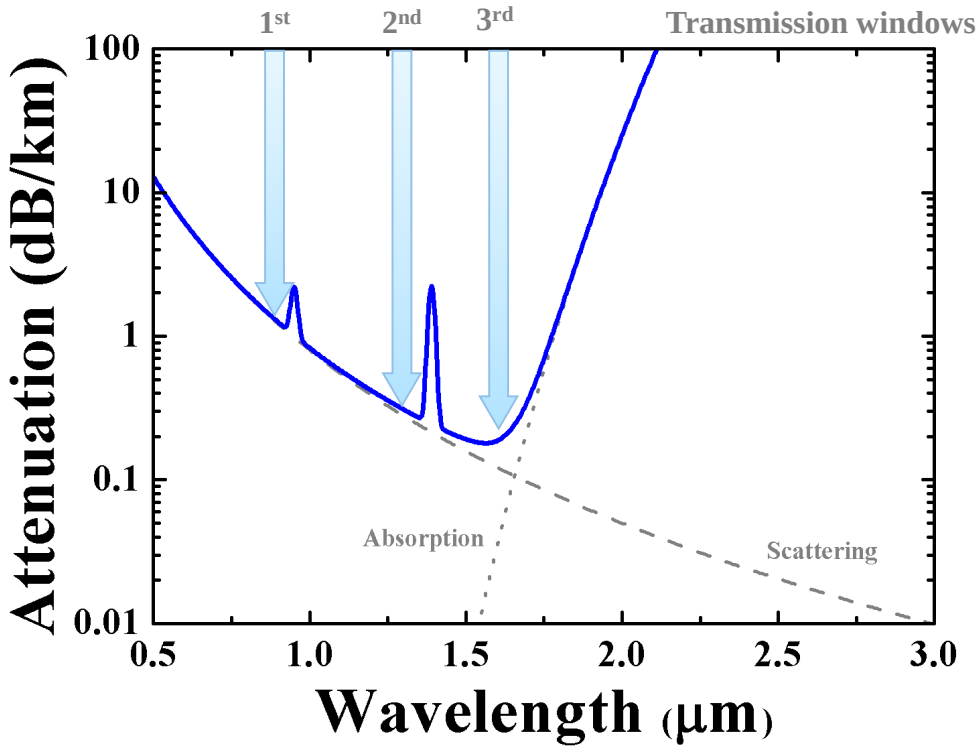


Figure 2.8: Illustration of optical fibre attenuation vs. wavelength taking into account Rayleigh scattering, absorption and the water peaks. The historical transmission windows are indicated with arrows [61].

only) [61], [62], [63]. The historical transmission windows are indicated with arrows and will be discussed in the following sections.

2.2.1 First window at 0.85 μm

> "*The realisation by Corning Glass, in 1970, of the first low-loss fibres which had been predicted in 1966 by K.C. Kao and G. Hockham, and the parallel invention of semiconductor laser diodes and photo-detectors may be seen as the two parents of a newborn field, optical telecommunications.*"
> From "Science and technology challenges in XXIst century optical communications" by E. Desurvire et al., 2011. [64]

In 1970, soon after the revelation by Kao and Hockham that fibre losses could be reduced, Corning produced fibres with attenuation less than 20 dB/km in

the wavelength region near 630 nm [60]. In the same year, the first semiconductor laser diodes were developed which could operate continuously at room temperature, along with photodetectors [5]. These lasers were based on gallium arsenide (GaAs) and emitted light in the region of ~0.85 μm. The simultaneous availability of compact, coherent optical sources and low-loss optical fibres as a transmission medium led to a global effort to develop optical systems for long-distance communications.

In 1973, optical fibres were developed with an attenuation (4 dB/km at 0.85 μm) lower than copper coaxial cables (~5 dB/km) for the first time [65], [66], [67]. This led to the first telecommunications transmission window which was centred at 0.85 μm. The first non-experimental optical fibre link was installed in 1975 by the Dorset police (in the UK) [7], [45]. In April 1977, the General Telephone and Electronics company transmitted the first live telephone traffic through optical fibre in Long Beach, California [7], [45]. After these field trials, commercial optical communication systems became available in 1980 [6].

2.2.2 Second window at 1.33 μm

The bit rate of a system is defined as the number of bits (the smallest unit of information in a binary system, e.g. on/off, 1/0) that can be transmitted in one second, written as bit/s. In 1975, the most advanced coaxial cable communication system operated at a bit rate of 274 Mbit/s (274 million bits per second) [7]. A key disadvantage of coaxial systems used at this time was the small repeater spacing (~1 km), which led to excessive signal regeneration over long distances. While microwave systems generally allowed for longer repeater spacings, their bit rate was limited to ~100 Mbit/s. Optical fibre loss in the transmission window of 0.85 μm was ~3 dB/km at the time, necessitating repeaters every ~10 km [7]. This repeater spacing was ten times larger than the spacing in existing coaxial systems (~1 km) and provided an important motivator for system designers due to reduced installation and maintenance costs [6].

It became clear to system designers that repeater spacing could be increased even further if optical transmission systems were shifted to a longer wavelength of 1.33 μm, where fibre loss was lowest at ~1 dB/km. This realisation led to a worldwide effort for the development of semiconductor lasers and detectors operating near 1.33 μm. In the early 1980s, this resulted

in the second transmission window, which was developed for commercial use with InGaAsP lasers operating at 1.33 μm. In 1987, commercial systems were operating at bit rates of up to 1.7 Gbit/s (i.e. 1.7 billion bits per second) with a repeater spacing of ~50 km for signals transmitting in the 1.33 μm waveband [7], [6].

In 1988, 130 years after the first transatlantic telegraph cable from Valentia Island to Heart's Content, the first transatlantic cable based on optical fibres was completed, called TAT-8 (as it was the 8th transatlantic telecommunications cable) [68]. TAT-8 was a joint venture of AT&T (in the US), France Telecom, and British Telecom to connect the communication systems of their three countries. It was capable of handling 40,000 telephone calls simultaneously [7]. Interestingly, AT&T encountered an unexpected issue around the Canary Islands with the connection being severed, due to sharks biting the cable. This surprising problem resulted in publications in 1989 with titles such as "Sharkbite on the Submarine Lightwave Cable System: History, Causes, and Resolution" and sections of the cable being wrapped in a kevlar-like material in high risk areas to minimise disruption [69].

The race for lower attenuation in optical fibres continued during the 1980s. Researchers at the time were particularly interested in shifting transmission to longer wavelengths in order to minimise the effect of Rayleigh scattering (proportional to $1/\lambda^4$). For this purpose, new fibre materials were investigated, including chalcogenide, germanate, and fluoride (e.g. ZBLAN), glass fibres [15]. In fact, the first 2 μm transmission experiment (to the best of our knowledge) took place in 1987, with the first demonstration of 34 Mbit/s single-channel data transmission over 10 m of ZBLAN fibre [16]. In this demonstration, the transmitter comprised an externally-modulated, helium–neon laser operating at a wavelength of 2.4 μm and the receiver was based on an InGaAs/InP photodiode. However, ZBLAN fibres proved to be brittle and highly nonlinear, restricting propagation over long distances [17], [18]. Investigations into mid-IR transmission experiments were soon abandoned because the same year (1987) saw the invention of the first erbium doped fibre amplifier (EDFA), which operated from 1.48 μm to 1.61 μm, and would serve to revolutionise capacity capabilities in optical communication systems [70].

2.2.3 Third window at 1.55 μm

In the 1990s, the third transmission window was opened. This is the transmission window in which most global optical communications operate today. It is called the conventional band (C-band) and has a spectral range of ~30 nm (1.53 μm to 1.56 μm) [6]. The key elements for success of this transmission window were primarily the availability of semiconductor lasers and detectors for transmitters and receivers, low-loss fibre (~0.2 dB/km at 1.55 μm [8]) as a transmission medium, and EDFAs to enable transmission over long distances [9].

Prior to the invention of the EDFA, optical fibre connections over long distances would require complicated opto-electric (O/E) and electro-optic (E/O) conversion for signal regeneration. Optical amplifiers amplify light signals solely in the optical domain, eliminating the need for such conversion and significantly simplifying the optical communication systems [6]. This was especially impactful for transoceanic transmission systems, where more than one hundred EDFAs may be needed to support an optical fibre link.

EDFAs

> "*It is noteworthy that the two founding technologies of optical communications, namely the laser and the fibre, could be conjoined into the EDFA, a laser-pumped, doped-fibre amplifier.*"
> From "Science and technology challenges in 21st century optical communications" by E. Desurvire et al., 2011. [64]

An optical amplifier operates on the same principles as a laser, with the key difference being the lack of feedback (i.e. no reflections). Doped fibre amplifiers are optical amplifiers that use a length of doped optical fibre as a gain medium to amplify the optical signal. In EDFAs, as the name suggests, the core of a silica fibre is doped with ions of the element erbium (Er^{3+} ions). Erbium is the dopant of choice for optical communications because, if pumped with enough energy, EDFAs will produce emission over a ~35 nm bandwidth (from 1.530 μm to 1.565 μm) coinciding with the third transmission window and the minimum loss region for standard SMF.

The operation of an EDFA is dependent upon the absorption and emission

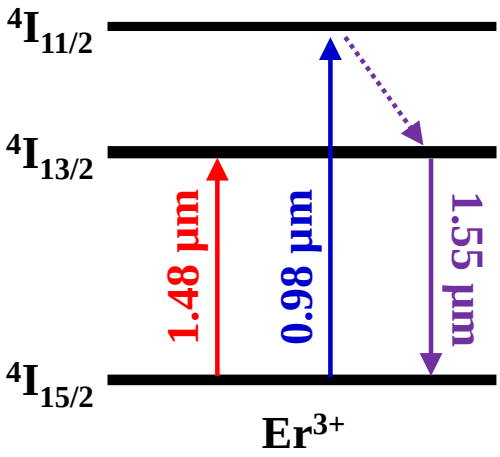


Figure 2.9: Erbium energy diagram [71].

spectra of the erbium ions. A schematic energy diagram for erbium is shown in Figure 2.9. Energy is introduced into the doped fibre via an external laser, called a pump laser. The energy (and therefore wavelength) of the pump laser is determined by the difference between the energy bands. In the case of erbium, pump wavelengths of either 0.98 μm or 1.48 μm are required for excitation to the $^4I_{11/2}$ and $^4I_{13/2}$ energy bands, respectively. The energy and wavelength of the pump photons are inversely related by the Planck-Einstein relation in Equation 2.10.

$$E = \frac{hc}{\lambda} \qquad \textit{Planck-Einstein relation} \tag{2.10}$$

The pump laser at 0.98 μm has greater energy than that of the 1.48 μm pump and excites ions to the higher energy band $^4I_{11/2}$. The lifetime of ions in this $^4I_{11/2}$ band is ~1 μs, after which the ions decay to the $^4I_{13/2}$ band through a non-radiative process (releasing phonons i.e. vibrations, rather than photons i.e. light). The ions can also be stimulated directly to the $^4I_{13/2}$ band with a pump laser of wavelength 1.48 μm. The average lifetime of an Er^{3+} ion in the $^4I_{13/2}$ band is ~10,000 μs. The transition of an Er^{3+} ion from the $^4I_{13/2}$ band to the $^4I_{15/2}$ band is a radiative process that results in the emission of a photon with energy equivalent to $|^4I_{13/2}$ - $^4I_{15/2}|$. This radiative process is a result of either stimulated or spontaneous emission.

Stimulated Emission: If optical signals with wavelengths of 1.53 μm to

1.56 μm enter the doped fibre, they will induce stimulated emission of additional photons that are coherent (i.e. same directionality and phase) with the incoming signal, amplifying the signal as it travels through the doped fibre. Once the rate of stimulated emission becomes greater than the pump rate, the amount of signal amplification (or gain) will reduce due to saturation.

Spontaneous Emission: Spontaneously emitted photons are incoherent, with random direction and phase. As with all emitting devices, optical fibre amplifiers also have spontaneous emission. Ions in the excited states may decay spontaneously and these transitions result in photons that are incoherent with the incoming signal. These incoherent photons can also then become amplified through the length of the doped fibre. This process is called Amplified Spontaneous Emission (ASE). It results in a broad emission spectrum from the amplifier, mimicking the emission band of Er^{3+} ions. ASE contributes to the overall noise of an optical communication system and must be taken into account. The quality of an amplifier is hence primarily defined by its ability to amplify the signal, quantified by the gain, but also by its ability to minimise the noise in the system, quantified by the noise figure.

Beyond TAT-8

In 1996, the first transatlantic optically amplified systems went into operation. These were TAT-12 and TAT-13 which operated in a ring network initially capable of carrying 10 Gbit/s at 1.55 μm (2 x 5 Gbit/s on the fibre pair) [72], [73]. This was the first TAT cable to use a ring structure (involving two stretches of cable across the ocean floor). Wavelength-division multiplexing (WDM) is a technique used to transmit multiple channels at different wavelengths through the same fibre. The combination of EDFAs and WDM enhanced the capacity of optical communication systems so dramatically that data transmission at 1 Tbit/s was also realised in 1996 [7]. In terms of transoceanic communications beyond TAT-8 (which was capable of 280 Mbit/s total capacity in 1988), technological evolution resulted in WDM systems on transoceanic links with total capacity of 128 x 10 Gbit/s per fibre pair by 2009 [74].

Soon commercial systems could operate 100 channels at data rates of 100 Gbit/s and total capacities in the order of 10 Tbit/s in 2010 [10]. However, the rise of augmented reality, artificial intelligence, self-driving cars, high-definition video streaming, cloud storage and increased connectivity

through the 'internet of things' requires preparation for a future full of big data, increasingly bandwidth-hungry applications and high-capacity demands. Current forecasts project global internet traffic to triple from 2017 to 2022, with monthly global mobile data traffic exceeding 77 exabytes (77 million TB) by 2022 and annual traffic reaching almost one zettabyte (one billion TB) [3]. The future is more connected, automated and autonomous than ever before.

Within the given EDFA bandwidth and the third transmission window of SMF, all possible physical parameters are currently being explored by the research community to increase capacity [75]. But the question persists - will this be enough to stay ahead of the ever-increasing demands? Now is the time for innovative solutions. As such, this thesis explores how the 2 μm transmission window can be effectively utilised to extend the available bandwidth. There are several promising advantages of enabling transmission at 2 μm and these will be discussed in the following sections.

2.3 A new transmission window at 2 μm

As per Section 2.2.3, the success of opening the third window required a series of key enabling technologies, primarily semiconductor lasers, optical amplifiers and low-loss fibres. Therefore, the first step in investigating if the 2 μm transmission window could prove feasible for future high-capacity optical communication systems is to search for these same key enablers.

2.3.1 Semiconductor materials

In order to find suitable lasers and detectors at 2 μm, the semiconductor band gap must be considered. In the case of direct band gap transitions, a semiconductor will only detect or emit light with photon energy larger than the band gap (within certain energy bands permitted by the material). In Equation 2.11, E_g represents the band gap energy, h is Planck's constant and ν is the photon frequency. This implies a minimum photon frequency for transitions to occur (Equation 2.12), which in turn corresponds to a minimum wavelength (λ_g, Equation 2.13). In Equation 2.13 and Equation 2.12, c represents the speed of a photon in vacuum. Thus, given the fact that c and h are constant, this results in the approximate 1.24 inverse relationship between the band gap energy and band gap wavelength given in Equation 2.13. In this approximation, the units are eV for E_g and μm for λ_g. Photons with this

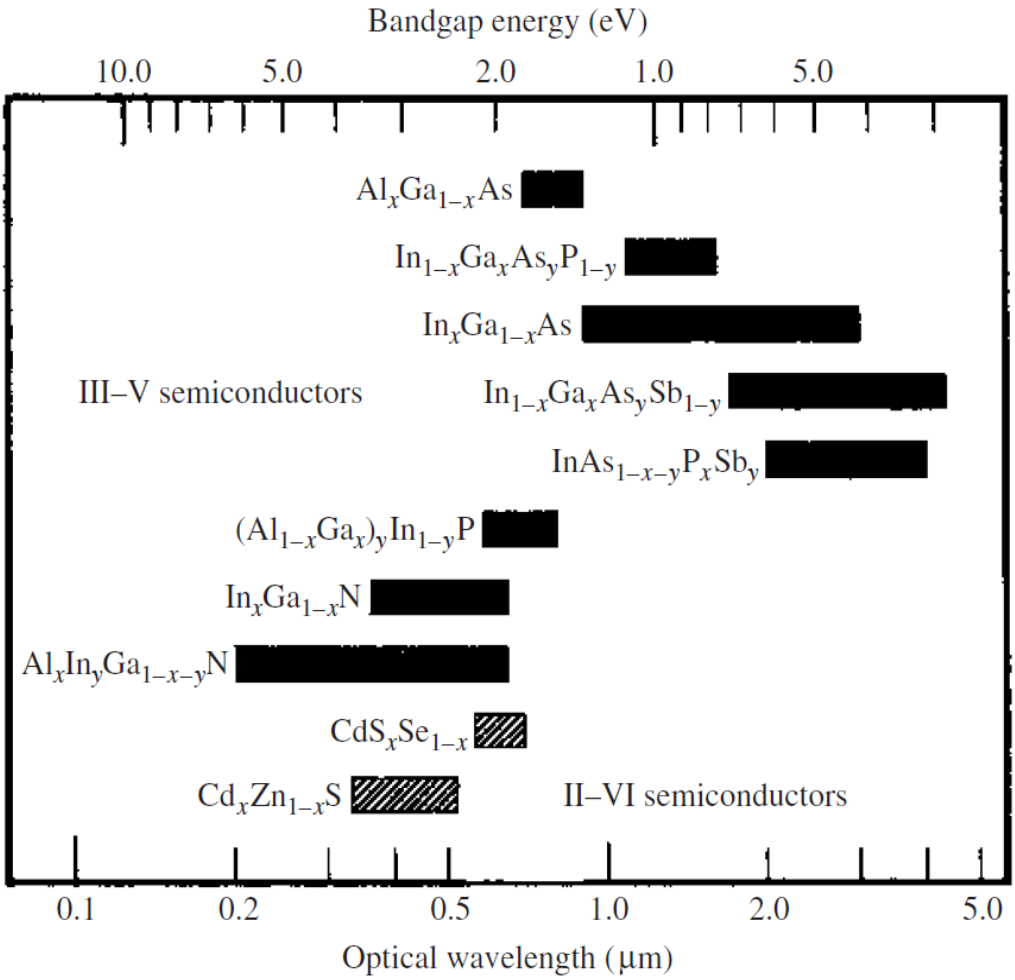


Figure 2.10: Oscillation wavelength regions of semiconductor materials. Image reproduced with permission of CRC PRESS LLC via Copyright Clearance Center [76].

wavelength (or shorter) are able to overcome the band gap. If a particular wavelength is required, the most suitable semiconductor materials can be determined via this relation (Equation 2.13).

$$E_g = h\nu \qquad \textit{band gap energy} \tag{2.11}$$

$$c = \nu\lambda \tag{2.12}$$

$$\lambda_g = \frac{hc}{E_g} \approx \frac{1.24}{E_g} \qquad \textit{band gap wavelength} \tag{2.13}$$

The band gap wavelength and associated band gap energies are illustrated in Figure 2.10 for a range of semiconductor materials. Elemental semiconductors

(such as silicon and germanium) are important in electronics [76]. These materials are not typically used for photon generation due to their indirect band gaps, hence they are not listed here [76]. Compound, or binary, semiconductor alloys can be formed by combining an element in group III of the periodic table (such as gallium, indium or aluminium) with an element in group V (such as phosphorus, arsenic or antimony). Ternary and quaternary alloys can also be formed by mixing two or more of the binary semiconductor compounds. This results in a range of semiconductor materials that can be tuned over a wide range of wavelengths for photonic applications. Elements from group II and group VI of the periodic table can also be used. Unlike their III-V counterparts, II-VI alloys are widely found in nature, but photon sources fabricated from these materials commonly suffer from limited lifetimes. Hence, III-V materials are generally preferred for photonic applications [24].

In the 2 μm wavelength range, there are several options for III-V semiconductor materials, as shown in Figure 2.10, such as InGaAs, InGaAsSb and InAsPSb (where P is the symbol for phosphorus and Sb for antimony). It is desirable to choose compounds that are used in the conventional waveband of 1.55 μm, as these semiconductor processes are mature, cost-effective and widely available. Therefore, it is preferable to avoid compounds that include antimony (Sb), since is not used in the C-band. $In_xGa_{1-x}As$ alloys are an attractive option because they offer a wide range of wavelengths that can be varied depending on the indium content x and are direct band gap for all values of x from 0 to 1. At room temperature (300 K), the dependency of the band gap (in eV) on the indium content x can be calculated using Equation 2.14 from reference: [77]. In Equation 2.14, E_g is the direct energy band gap of $In_xGa_{1-x}As$ and x is the indium fraction of the $In_xGa_{1-x}As$ alloy [78]. As can be seen from Figure 2.11, emission around 2 μm can be achieved with an $In_xGa_{1-x}As$ alloy and an indium fraction of $x \approx 0.7$.

$$E_g(x) = 1.425 \ - 1.501 \ x \ + 0.436 \ x^2 \tag{2.14}$$

In order to fabricate compact devices, thin films of the alloy are required. While it is possible to fabricate thin films of $In_xGa_{1-x}As$, a supporting substrate is required. Ideally, the atomic spacing (or lattice constant) of this substrate and the successive alloy layers should be the same. Failure to effectively match these lattice constants can result in defects which can degrade the performance of photonic devices. For this reason, the most

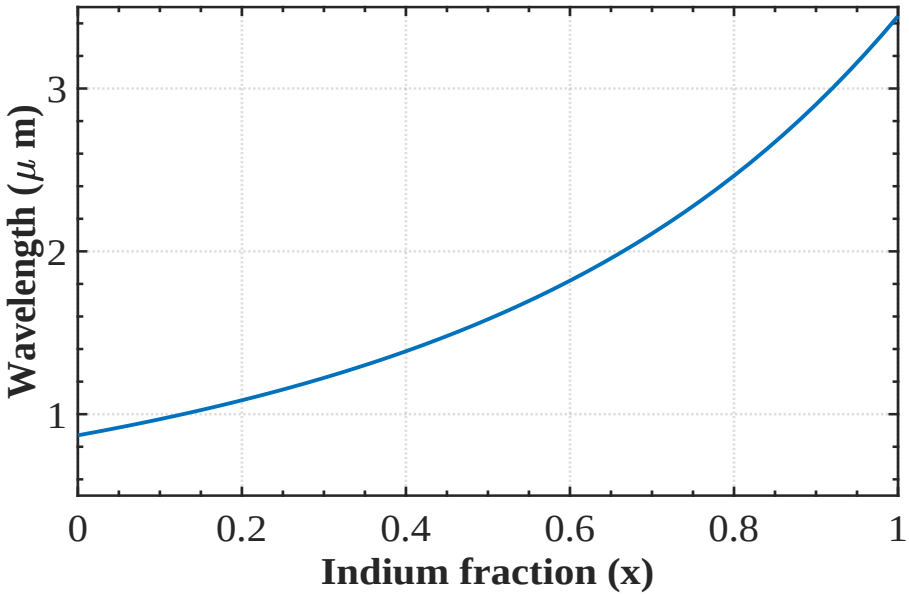


Figure 2.11: Emission wavelength of InGaAs varying with the fraction of indium in the alloy [78], [77].

convenient substrate for $In_xGa_{1-x}As$ is indium phosphide (InP) because the lattice constant is similar and quality InP substrates are available with diameters as large as 100 mm [79].

However, rather than being lattice-matched to neighbouring layers, sometimes regions are deliberately chosen to have a different lattice constant. Introducing strain in this way can have a positive effect on laser performance by reducing the laser threshold current density, making the device more efficient [80]. However, the laser may only be strained to a certain point, beyond which the structure may begin to crack.

With the semiconductor material chosen (as InGaAs/InP), the next step is to select lasers at 2 μm. Most semiconductor materials have natural cleaving planes. These are crystal planes along whose atomic bonds are most easily broken, creating atomically flat mirrors. An emission cavity can be constructed by cleaving two parallel ends of a semiconductor along the crystal axis, creating reflective facets with the semiconductor gain medium in-between. Uncoated, these semiconductor cleaved planes have reflectivity of 30% to 50%. The maximum output power of the device can be optimised by modifying the reflectivity of the facets with optical coatings. This is typically achieved by making the back facet with high reflectivity (90%) and the front

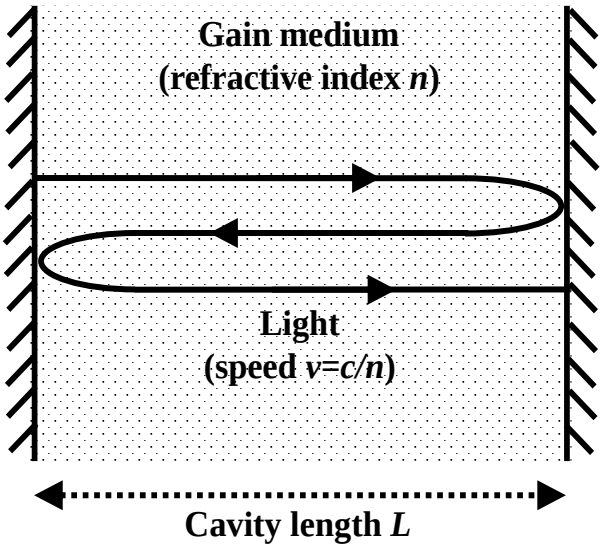


Figure 2.12: A Fabry-Pérot cavity with two mirrors and a gain medium in between [82].

facet with lower reflectivity (10%). The latter allows light to escape [81].

A Fabry-Pérot cavity with two reflecting surfaces (parallel to one another at a distance L apart) and a medium of refractive index n is shown in Figure 2.12. An integer number (N) of wavelengths will be resonant within the Fabry-Pérot cavity, determined by Equation 2.15 [82]. In this equation, λ_0 represents the wavelength of light in vacuum. Equation 2.15 dictates that when the distance between the mirrors is an integer multiple of half wavelengths, light will interfere constructively and undergo resonance within the cavity. Light of other wavelengths will interfere destructively and be dissipated. For this reason, a Fabry-Pérot cavity is also called a resonator.

$$L = \frac{N\lambda_0}{2n} \qquad \textit{resonance condition} \tag{2.15}$$

Multi-mode semiconductor lasers

The resonant wavelengths supported within the cavity (called modes) are analogous to standing wave patterns on a string, see Figure 2.13. If the rope is provided with energy, many modes can oscillate (i.e. resonate). If one end of the rope is held slightly open, some of the oscillation energy will escape, this is representative of the lower reflectivity facet in the Fabry-Pérot cavity. In this

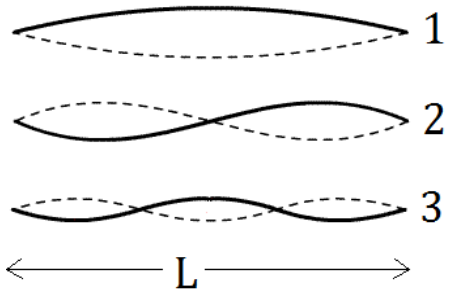


Figure 2.13: Standing waves on a string. *This file is licensed under the Creative Commons Attribution-Share Alike 3.0 Unported license.*

analogy, the higher reflectivity facet is represented by the fixed end of the rope, which reflects almost all energy incident upon it.

In the case where the mirrors do not have 100% reflectivity, the amplitude of the light will experience losses during a round-trip in the cavity and will inevitably fall to zero with repeated reflections. These losses may be mitigated if the cavity is filled with an optical gain medium, enabling the light to be amplified as it bounces back and forth [82]. This is the case in a semiconductor laser. Photon emission is generated by exciting the active medium inside the cavity, by applying a voltage across the device, triggering stimulated emission. The energy within the resonator is then amplified by reflections between the parallel mirrors. In this way, wavelengths fulfilling the resonance condition will be amplified, while other wavelengths are strongly attenuated. This results in an integer number of wavelengths (called modes), given by Equation 2.15, which can be emitted through either mirror (if made partially reflective). Since wavelength and frequency are related (by $c = \nu\lambda$), the frequency separation between the resonant modes within the Fabry-Pérot cavity is given by Equation 2.16.

$$\Delta\nu = \frac{c}{2Ln} \qquad \textit{frequency separation} \tag{2.16}$$

The number of modes that are observed is limited by the existence of optical gain over a finite frequency range, or gain bandwidth of the semiconductor laser. This is indicated by the dashed-line envelope in Figure 2.14. Conventional Fabry-Pérot lasers are multi-mode devices. Since the wavelengths of light are typically small compared to the cavity length, often a complete round trip of the cavity will be equivalent to many hundreds of wavelengths being amplified. This is exemplified by Figure 2.15 which shows

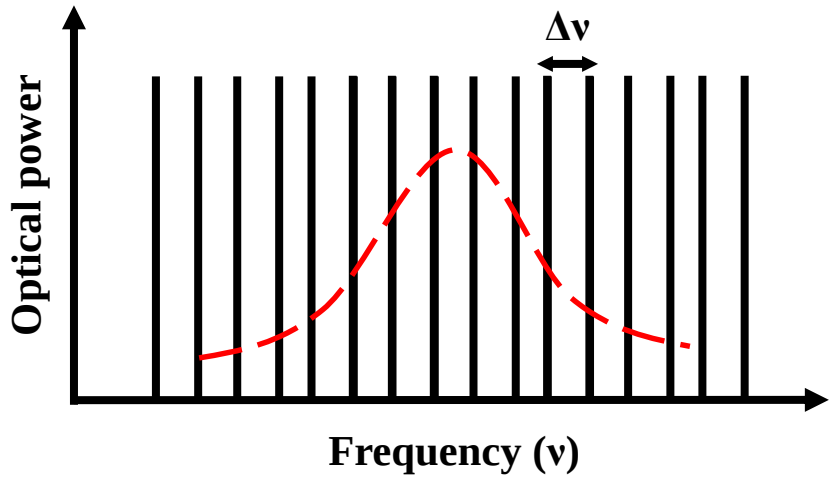


Figure 2.14: Emission spectrum of a Fabry-Pérot laser with resonant frequencies indicated by the vertical lines and gain profile represented by the red dashed line [82].

the optical spectrum for a Fabry-Pérot laser with a cavity length of 400 μm.

Single mode semiconductor lasers

For optical communication purposes, it is desirable to have a single mode laser upon which to encode information. One method to induce single mode operation in Fabry-Pérot lasers is to introduce slots into the cavity. These slots act as a series of smaller Fabry-Pérot cavities within the overall cavity, gradually selecting one individual mode or wavelength, which is then transmitted through the lower reflectivity facet. A typical single mode spectrum of a slotted Fabry-Pérot laser is shown in Figure 2.16, for a cavity length of 400 μm. The effect of adding slots can be seen by comparing Figure 2.16 and Figure 2.15.

In the design of a slotted Fabry-Pérot laser, it is the slot width and spacing that have the most influence on reflectivity of light within the cavity. Narrower slots are desirable in order to keep the cavity length as small as possible (with typical slot width ≥ 1 μm). A greater number of slots increases reflectivity, but reduces transmission. This is because the scattering loss increases with the number of slots and reduces the optical power. Considering the slot depth; shallow slots reduce reflectivity (thus less feedback and gain), requiring more slots to compensate optical power, leading to a longer cavity and increased lasing threshold. Conversely, deeper slots increase scattering losses and the number of slots must be increased to maintain output power, which also

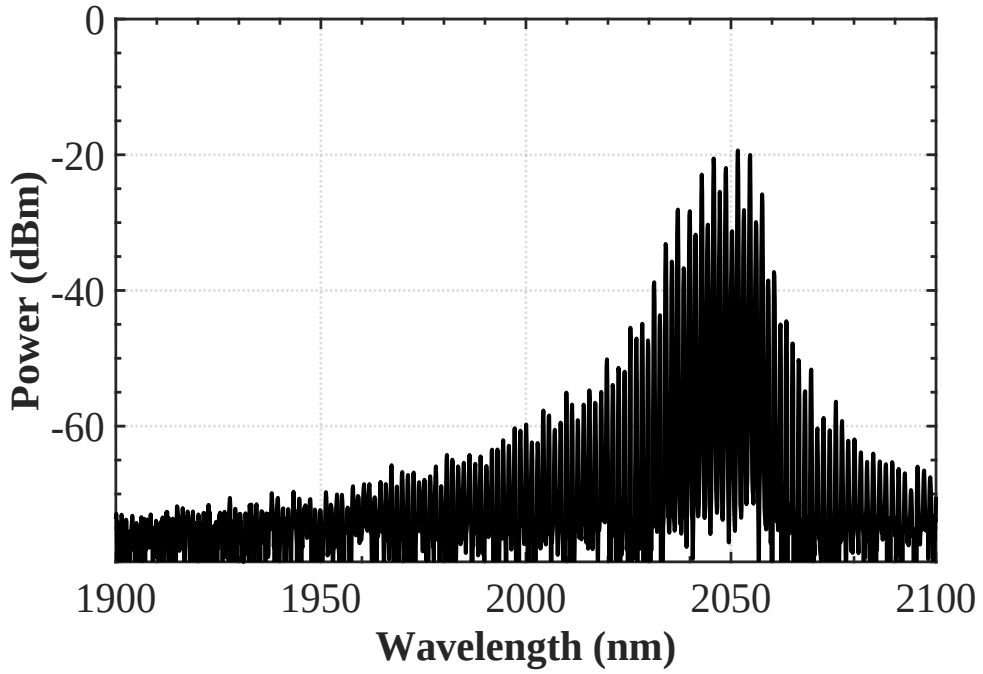


Figure 2.15: Optical spectrum of a multi-mode Fabry-Pérot laser. *Data courtesy of Brian Kelly, Eblana Photonics.*

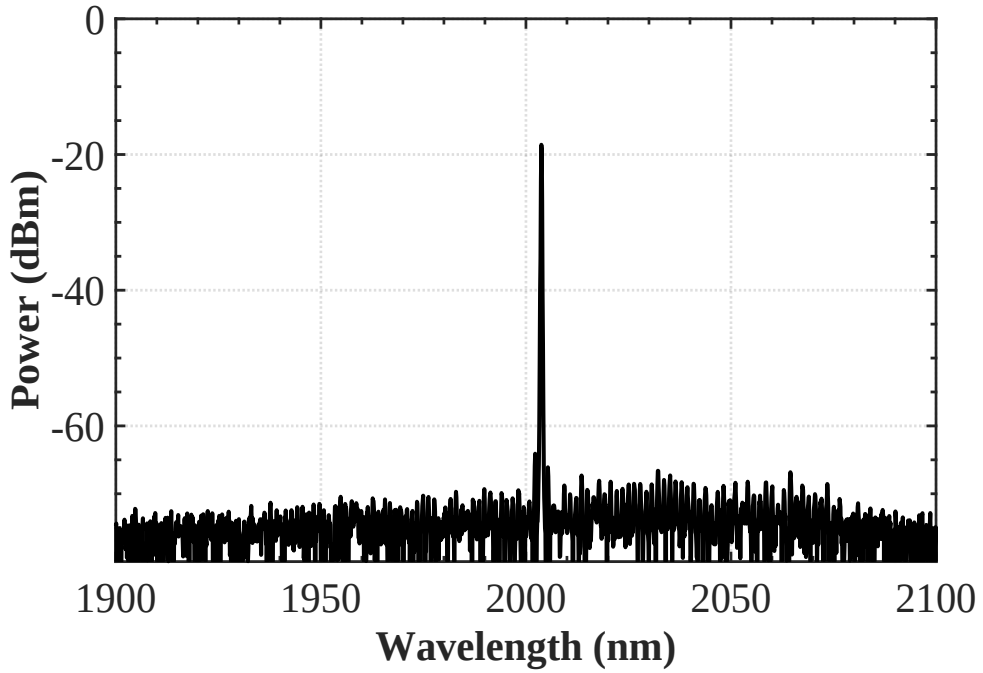


Figure 2.16: Optical spectrum of a single mode Fabry-Pérot laser. *Data courtesy of Brian Kelly, Eblana Photonics.*

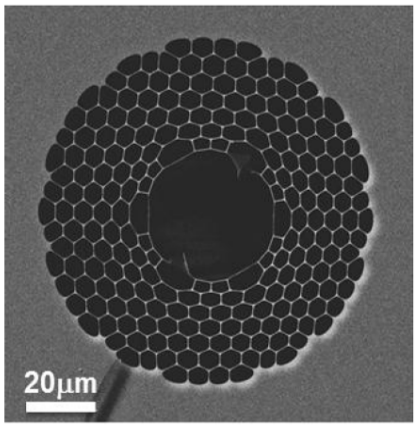


Figure 2.17: SEM micrograph of a 19 cell hollow core fibre cross section. *This image is courtesy of Prof. David Richardson, ORC, University of Southampton [83].*

results in a longer cavity, as before. Desirable features in a laser include low threshold current and high slope efficiency (which indicates a laser's ability to convert electrical current into optical power). A longer cavity length results in a lower slope efficiency and higher threshold current. Therefore, in the case of slotted Fabry-Pérot lasers, it is a compromise between maintaining sufficient reflectivity and minimising the cavity length to maximise single mode operation [25].

2.3.2 Fibres

In terms of optical fibres suitable for transmission at wavelengths longer than 1.55 μm, there are several mid-IR glass-based fibres such as chalcogenide, germanate and fluoride (e.g. ZBLAN), glass fibres. However, another type of fibre, namely hollow-core photonic band gap fibre (HC-PBGF), offers more promising improvements that warrant investigation. A cross section of HC-PBGF is shown in Figure 2.17. The reduced interaction of light with the silica material of the fibre results in several encouraging advantages (over standard SMFs), such as the potential to reach losses as low as 0.1 dB/km around 2 μm [20]. The low-loss region is shifted (in comparison with standard SMF) due to the reduction of Rayleigh scattering in HC-PBGFs.

Silica glass fibre has a refractive index of $\sim$1.5 causing light to propagate 31$\%$ slower than it would in vacuum. In comparison, light in the core of HC-PBGFs can travel at speeds up to 99.7$\%$ of the speed of light in vacuum (since the refractive index of air is close to 1) [84]. This offers a way to reduce the propagation delay over long distances (which gained interest in HC-PBGFs

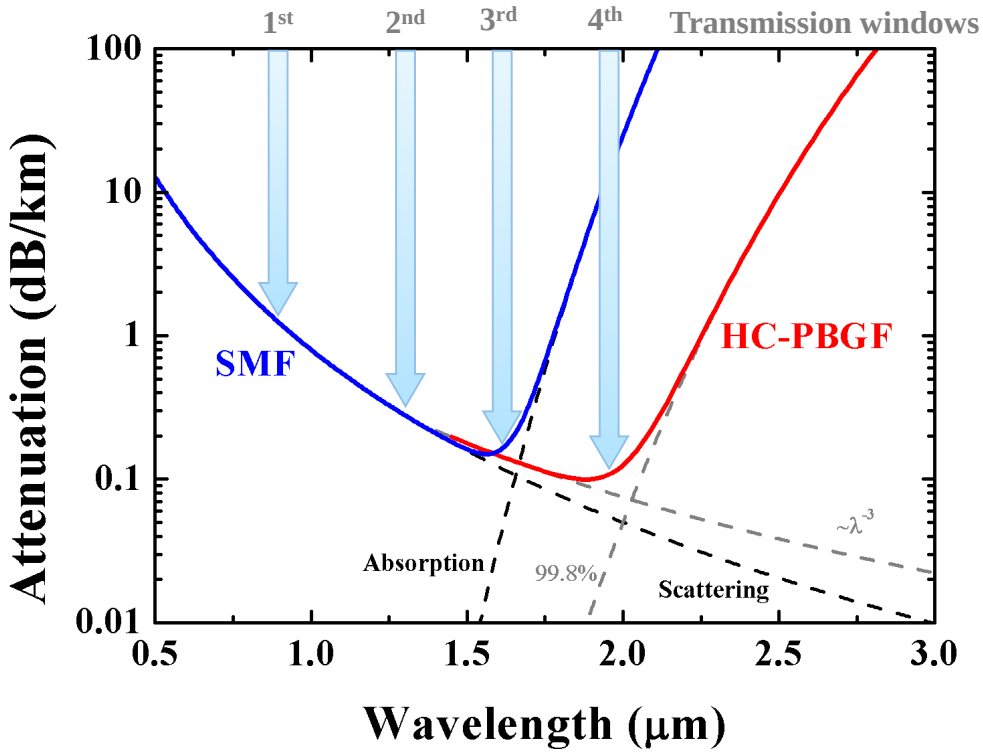


Figure 2.18: Approximate illustration of the predicted HC-PBGF attenuation vs. wavelength for HC-PBGF (in red) and attenuation vs. wavelength for standard SMF (in blue). The transmission windows are indicated with arrows [61].

from the financial sector in 2013 [85]). This delay is known as latency [21]. Perhaps most importantly, guidance in air results in ultra-low nonlinearity (~1000 times less than silica [22]). In standard SMF, most nonlinear effects are the result of the inherently disordered nature of silica in the fibre [86]. The reduced interaction of the light signal with silica material lowers the amount of these effects, allowing for much higher power-handling capabilities and higher capacities [23].

Figure 2.18 shows an illustrative schematic of optical fibre attenuation taking into account losses due to scattering and absorption. In comparison with Figure 2.8, current SMF (blue curve) has greatly reduced water absorption and a record low loss of ~0.149 dB/km [87]. HC-PBGF (red curve) has a predicted minimum loss of ~0.13 dB/km at 1.9 μm [20]. The historical transmission windows are indicated with arrows, along with the proposed new window at 2 μm [62], [63].

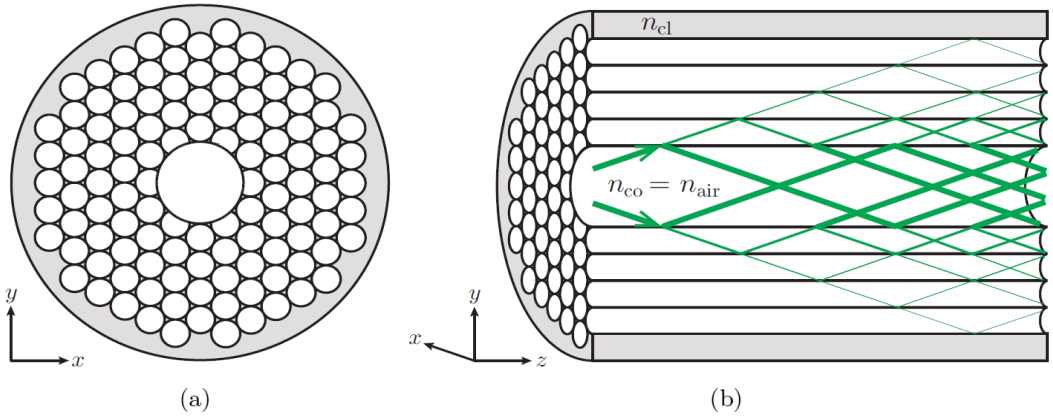


Figure 2.19: Simplified cross section of a HC-PBGF in (a) the x-y plane and (b) three dimensions exhibiting band gap guidance. Green lines represent light rays, with thickness corresponding to intensity. Light grey regions are silica; white regions are air. Axis coordinates are inset. Image reproduced with permission of the author [48].

While light propagation in solid-core fibres obeys the principle of total internal reflection (as per Section 2.1.1), the same guidance mechanism cannot be employed for HC-PBGFs. Since total internal reflection occurs when light travels from a denser (higher refractive index) medium to a rarer (lower refractive index) medium, this is not possible in the case of an air core because the refractive index of the cladding will always be greater than the core. Instead, guidance in HC-PBGF relies upon periodicity that permits light propagation through the low-index defect that forms the hollow core [19], [88], [89], [90].

The cladding of HC-PBGFs consists of a series of longitudinal capillaries in the +z direction (in fact, hollow core fibres earned an entry in the Guinness World Book of Records for the World's Longest Hole in 1999 [91]). These capillaries result in a lattice-like periodic microstructure in the x-y plane of the fibre cladding, as per Figure 2.19. In the centre of this structure is a defect which constitutes the hollow core. When light from the core is incident upon the periodic structure of the cladding, it will be reflected and transmitted at each air/silica interface. The interaction of these reflections contribute to constructive and destructive interference along the +z direction. The result of this interference is that certain wavelengths can propagate along the fibre while other wavelengths are not supported for propagation within the HC-PBGF structure.

One way these wavelengths can be determined is using a modified form of

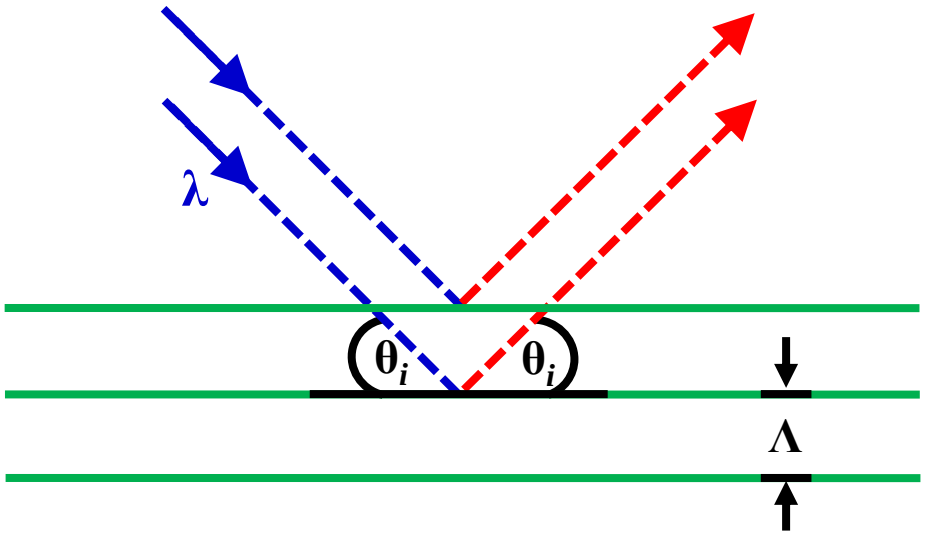


Figure 2.20: Illustration of Bragg's law.

Bragg's law, called the Bragg-Snell law, which takes into account refraction of light in the composite structure and the incident angle of the incoming light [92], [48], [93]. The Bragg-Snell law can be derived from an application of Snell's law (Equation 2.1) and Bragg's law of diffraction, Equation 2.17. Bragg's law is illustrated in Figure 2.20.

$$N\lambda = 2\Lambda Sin(\theta_i) \qquad \textit{Bragg's law} \tag{2.17}$$

In Equation 2.17, N represents the integer order of diffraction, λ is the wavelength of light, Λ is the period of the microstructure and θ_i is the angle of incidence of light with respect to the normal. Beginning from Bragg's law (Equation 2.17) and using Snell's law (Equation 2.1), the Bragg-Snell law, Equation 2.18 can be obtained.

$$\lambda_{max} = \frac{2\Lambda}{N}\sqrt{n_{eff}^2 - sin^2(\theta_i)} \qquad \textit{Bragg-Snell law} \tag{2.18}$$

In Equation 2.18, n_{eff} is the effective refractive index of the system. n_{eff} can be determined by various approaches and one of these is the effective medium approach, as per Equation 2.19. In Equation 2.19, n_i and f_i are the refractive index and volume fraction of each portion of the photonic structure, i.e. air and silica in the case of HC-PBGFs [92].



Figure 2.21: Photograph of a Morpho butterfly whose blue colour is a result of the photonic band gap effect. *This file is licensed under the Creative Commons Attribution-Share Alike 3.0 Unported license.*

$$n_{eff}^2 = \Sigma n_i^2 f_i = n_{air}^2 f_{air} + n_{silica}^2 f_{silica} \tag{2.19}$$

Wavelengths that do not satisfy the Bragg-Snell law (Equation 2.18) can tunnel through the cladding and be dissipated, while wavelengths that satisfy this condition will be consistently reflected. Consequently, light incident on the periodic structure in the cladding is either reflected, or tunnels through to the other side; it cannot exist freely in the periodic medium itself, leading to a 'photonic band gap' for light of certain wavelengths or frequencies [92], [48], [93].

Photonic band gaps can also be seen in nature, for example in gemstones such as opal or in the scales of butterfly wings, as shown in Figure 2.21. In the case of the Morpho butterfly, the brilliant colours are a result of a naturally occurring periodic microstructure in its wings. This periodic microstructure results in a photonic band gap which prevents propagation of certain wavelength bands. In this case, blue light (~450 nm to 490 nm) is strongly reflected, resulting in the vibrant colours of the butterfly's wings in Figure 2.21, [93], [94], [95].

In the case of HC-PBGFs, the photonic band gap prevents propagation transversely and light is confined to travel within the central core, along the +z direction. The core can essentially be considered a cavity surrounded by reflecting walls. This is the basis of the HC-PBGF guidance mechanism.

Considering the 19-cell HC-PBGF used in the experiments of this thesis, the period (Λ) was 5.5 μm, and the volume fractions of silica and air were $f_{silica} = 0.04$ and $f_{air} = 0.96$, with refractive indices of $n_{silica} = 1.542$, $n_{air} = 1.000$, respectively [96]. Equation 2.18 can be maximised for $N = 1$ and θ_i = 90 °, which results in a λ_{max} value of 2.5 μm. Thus indicating that light around 2.5 μm will be confined within the hollow core of the fibre due to the photonic band gap.

While Rayleigh scattering (which is proportional to $1/\lambda^4$) and infrared absorption are the dominant loss mechanisms in conventional solid core fibres, the dominant loss mechanisms in HC-PBGFs are scattering from the glass/air interfaces (which is proportional to $1/\lambda^3$) and infrared absorption. In the case of HC-PBGFs, the absorption curve is shifted due to the reduced interaction of the optical field with the silica material (<0.2%) [61], [97], [20] [98], [99]. These combine to define the minimum-loss transmission window at 2 μm, predicted to be as low 0.1 dB/km (less than the best conventional fibres) [20]. Additional losses may also arise in HC-PBGFs due to atmospheric contamination during fabrication, resulting in small amounts of carbon dioxide and water vapour in the fibre. These contaminants can be reduced significantly or even eliminated by purging the fibre with dry gas [100].

HC-PBGFs offer exciting possibilities such as low nonlinearity, ultra-wide bandwidth, reduced latency, high damage threshold and ultra-low losses. These fibres have applications in gas sensing, nonlinear optics, high peak intensity pulse delivery, mid-IR radiation delivery and data transmission. Particularly for data transmission, HC-PBGFs have the potential to increase capacity through increased bandwidth, higher power-handling capability and reduced OSNR [101], [102].

2.3.3 Optical fibre amplifiers at 2 μm (TDFAs)

Amplifiers can be found at 2 μm in the form of thulium doped fibre amplifiers (TDFAs). Thulium and erbium have been closely linked since their discovery together in 1787, when a strange black rock was found in Ytterby, Sweden. It took over 100 years to analyse the rock completely, during which nine new elements (including erbium and thulium) were revealed [103]. Thulium offers a large energy level transition that can produce coherent photons extending from 1.7 μm to 2.1 μm. This potential broad amplification range of ~30 THz makes TDFAs especially attractive, compared to the current ~15 THz (1.48 μm

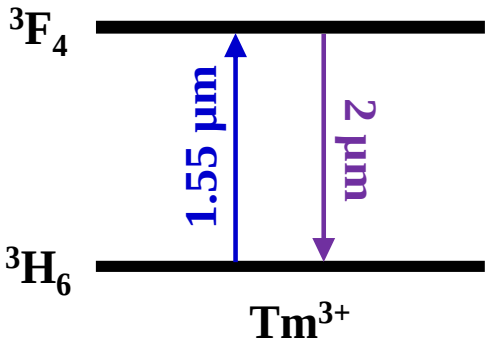


Figure 2.22: Thulium energy diagram [104].

to 1.61 μm) offered by EDFAs [27].

A schematic energy diagram of thulium is shown in Figure 2.22. Thulium ions can be pumped from the $^3H_6$ band to the $^3F_4$ with a 1.55 μm pump to produce emission around the 2 μm waveband. Other pumps can also be used, but 1.55 μm pumps are typically preferred because C-band optical sources are cheaper and more powerful (in general), making this an attractive pump option [18]. TDFAs have been developed with high gain (>35 dB) and low noise figures (<5 dB), similar to EDFAs [26], [27].

Also, if holmium is used in conjunction with thulium, optical amplification from 1.7 μm to 2.2 μm could be achieved. This corresponds to ~40 THz bandwidth, three times more than the current C+L-band capabilities [105], [28], [106], [107].

Chapter summary

In this chapter, the historical context of the work in this thesis is presented, from past optical communication systems (such as smoke signals and the semaphore) to the first transatlantic cable and the first optical fibres. The first telecommunications transmission window was opened in the 1970s using early Corning fibres and GaAs semiconductor lasers operating around 0.85 μm. The second window followed in the 1980s, which was developed for commercial use with InGaAs lasers operating at 1.33 μm. In the 1990s, the third window was opened using low-loss standard SMF operating at 1.55 μm.

The popularisation of the 1.55 μm wavelength region for optical

communications over the last three decades was made possible primarily due to three key enabling technologies; the availability of semiconductor lasers and detectors, low-loss (~0.2 dB/km) standard SMF as a transmission medium, and EDFAs to enable transmission over long distances with high-gain, low-noise and minimal O/E-E/O conversion. However, moving away from standard SMF and the 1.55 μm window was considered as far back as the 1980s (before the EDFA's revolution) due to fundamental losses such as Rayleigh scattering (which is reduced at longer wavelengths). Moving to other fibres operable at longer wavelengths could allow for lower losses and fundamentally higher capacities. Therefore, it is proposed in this thesis to re-investigate this possibility with today's technologies and open the 2 μm transmission window in order to extend the available bandwidth.

Novel solutions are needed and there are several applicable technologies with promising advantages at 2 μm. Lasers for transmitters can be fabricated by straining the layers of InP-based materials to shift the band gap and these same semiconductor processes can enable the fabrication of photodetectors. Mid-infrared fibres are also available, such as chalcogenide, germanate and fluoride (e.g. ZBLAN) glass fibres and HC-PBGFs. HC-PBGFs, in particular, could offer promising potential because of their unique 'cladding' region which consists of a honeycomb-like microstructure that confines light in the hollow core. The transmission of light through air could have significant advantages over SMFs such as theoretical losses lower than 0.1 dB/km, near-vacuum latency and a 1000-fold reduction in the nonlinear coefficient, resulting in higher achievable capacities. Finally, amplification at 2 μm can be found in the form of TDFAs, which have been shown to operate over a broad bandwidth (typically from 1.7 μm to 2.1 μm), double that of EDFAs. It is the convergence of all these key enabling technologies that heralds the opening of a new transmission window. Therefore, with the key elements identified, the next step is to investigate how to combine these elements into a fully-functioning optical communication system at 2 μm.

Chapter 3

Optical communication systems

In this chapter, the core elements of optical communication systems are discussed, with particular focus on the elements relevant to 2 μm transmission experiments. A communication system can be defined as the combination of a transmitter (which sends information) and a receiver (which receives the information), connected via a transmission medium or communication channel. A communication system can be as simple as two tin-cans connected by a string, as per Figure 3.1, or a complex network which contains multiple transmitters, receivers, switching technologies, as is the case in current optical communication systems.

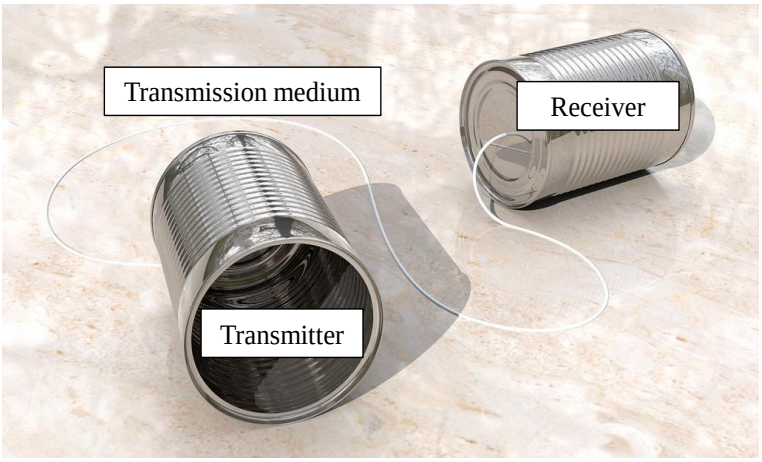


Figure 3.1: A tin can telephone consists of three key components to deliver information from one place to another; a transmitter, receiver and a transmission medium connecting the two. *Image courtesy of ccPixs.com under creative commons licensing (CC BY 2.0)*.

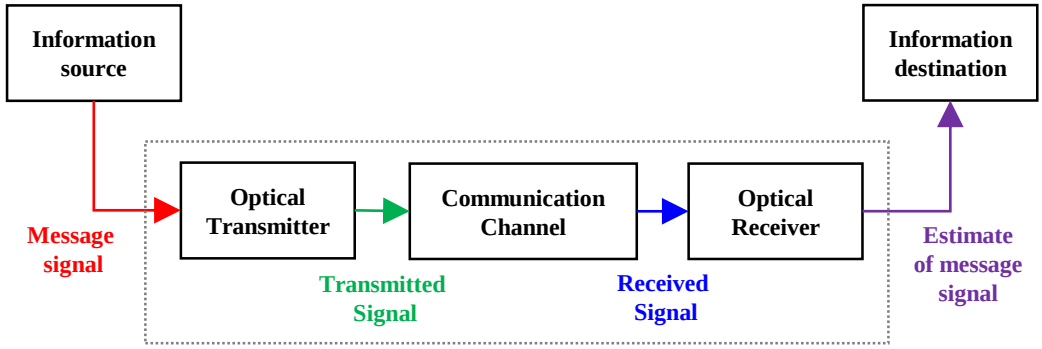


Figure 3.2: Schematic of a simple communication system [108].

Point-to-point links constitute the simplest kind of optical communication system for consideration. Their role is to convert the digital bit stream into optical data and to transport that information from one point to another, as accurately as possible. Figure 3.2 shows a schematic version of information flow in a simple point-to-point system. In the case of optical communication systems, there is additional E/O conversion (via a modulator) and O/E conversion (via a detector) needed in order to apply the baseband signal (actual data) to the optical carrier (laser light) and vice-versa.

These are also the key elements that are needed to establish an optical communication system at 2 μm, as briefly explored in Chapter 2. This chapter presents a review of the main characteristics and building blocks required to implement optical communication systems at 2 μm. In terms of the transmitter, core concepts such as modulation are discussed. The factors for evaluating system performance at the receiver are presented, including the bit error rate, eye diagram and signal-to-noise ratio. The design of a WDM system at 2 μm is discussed, concluding with the state-of-the-art for 2 μm WDM systems in 2014, prior to the beginning of this thesis work.

3.1 Generating optical signals

The purpose of an optical transmitter is to generate an optical carrier, which will carry the baseband information and launch the resulting optical signal into the transmission medium. In modern optical communication systems, the carrier frequency is chosen according to a grid of frequencies that is internationally standardised (this will be covered in more detail in Chapter 5). As discussed in Chapter 2, semiconductor lasers are a suitable contender for

these carrier frequencies because of their compact size, efficiency and emission wavelengths that correspond to the low-loss regions of silica optical fibres. Therefore, semiconductor lasers emitting at 2 μm are required. In order to apply the baseband signal (actual data) to these 2 μm carriers, data modulation is also required (either through direct modulation or via an external optical modulator).

3.1.1 Direct modulation

Direct modulation in its simplest form is a technique which modulates the intensity of laser light to represent information. For example, turning a laser on or off to represent 1s and 0s, respectively (similar concept to Morse code). This binary format is the most common representation of digital signals. For direct modulation, 1-bits and 0-bits correspond to whether an optical carrier is considered to be on or off, respectively. While the word bit originated as a contracted form of the words 'binary digit', today it has taken on a broader definition to mean the smallest unit of information in a system. The amount of time that each bit takes is called the bit period and the bit rate is defined as the inverse of the bit period. This bit rate corresponds to the number of bits transferred per unit time (i.e. per second). It is written as bit/s and is often associated with an SI prefix such as mega (Mbit/s), giga (Gbit/s) and even tera (Tbit/s) denoting factors of a million (10^6), billion (10^9) and trillion (10^{12}) bits per second, respectively. Most optical communication systems employ digital signals due to their reliability, flexibility and sensitivity.

If the laser is to be turned on and off, the laser threshold must first be considered. The laser threshold is the lowest excitation level at which a laser's output is dominated by stimulated emission rather than by spontaneous emission, i.e. the point at which a device 'lases'. An example of a typical light-current (LI) curve for a slotted Fabry-Pérot laser operating at the 2 μm waveband is shown in Figure 3.3, with threshold current indicated by a dotted yellow line. As can be seen in Figure 3.3, below the threshold current ($<$18 mA), the output power rises slowly with increasing current as spontaneous emission dominates. Above the threshold current ($>$18 mA), the laser is said to be lasing, as stimulated emission becomes the dominant mechanism, causing the slope of the LI curve to rapidly increase. This is because, as the current is increased, more carriers are injected into the conduction and valence bands of the semiconductor material, subsequently

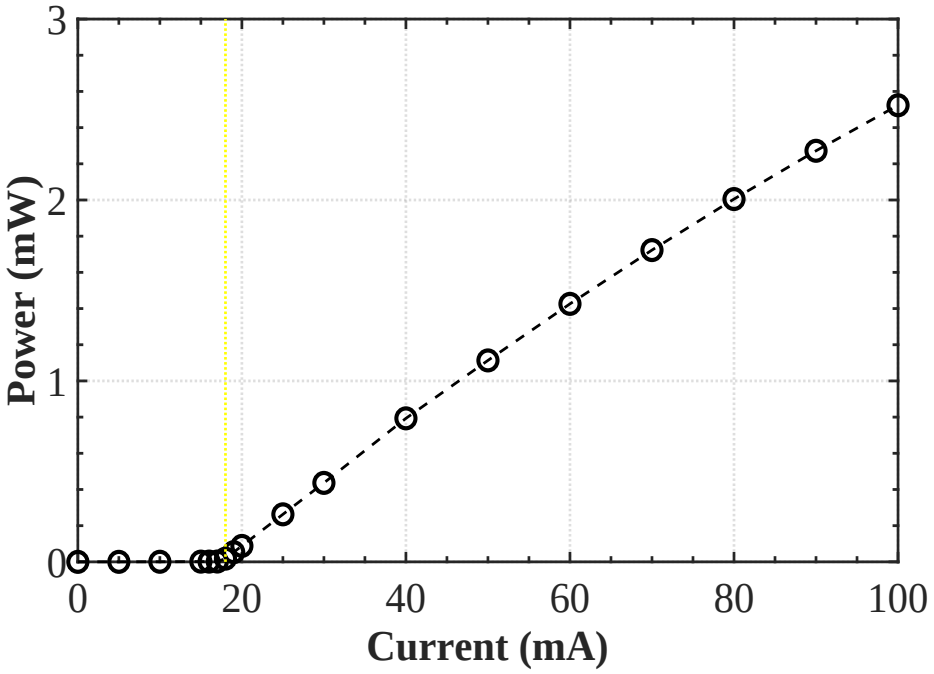


Figure 3.3: LI curve of a slotted Fabry-Pérot laser (module S/N YE1918 at 25°C). Dotted yellow line indicates the threshold current.

recombining and releasing more photons. Operating below this threshold corresponds to turning the laser 'off' and operating above the threshold turns the laser 'on'. Ideally, a low threshold current and a high slope efficiency are desirable features in a transmitter for optical communication applications, as this indicates a more efficient system that will need less power to operate while converting as much current to light as possible.

Another way to visualise the laser threshold is via the optical spectrum, which is a measure of the optical power density as a function of wavelength, as shown in Figure 3.4. This is recorded via an optical spectrum analyser (OSA) which measures the optical power per unit bandwidth (defined by the resolution). Below the laser threshold, spontaneous emission produces incoherent light in random directions, shown below in red in Figure 3.4. This broad emission spectrum has a periodic spectral structure which indicates the permitted modes or wavelengths within the Fabry-Pérot cavity but with no peak dominating below the threshold point. Above the laser threshold, stimulated emission produces coherent light at a certain wavelength that experiences gain (against the other potential resonant wavelengths or modes within the cavity) as shown in blue in Figure 3.4. The wavelength value of this

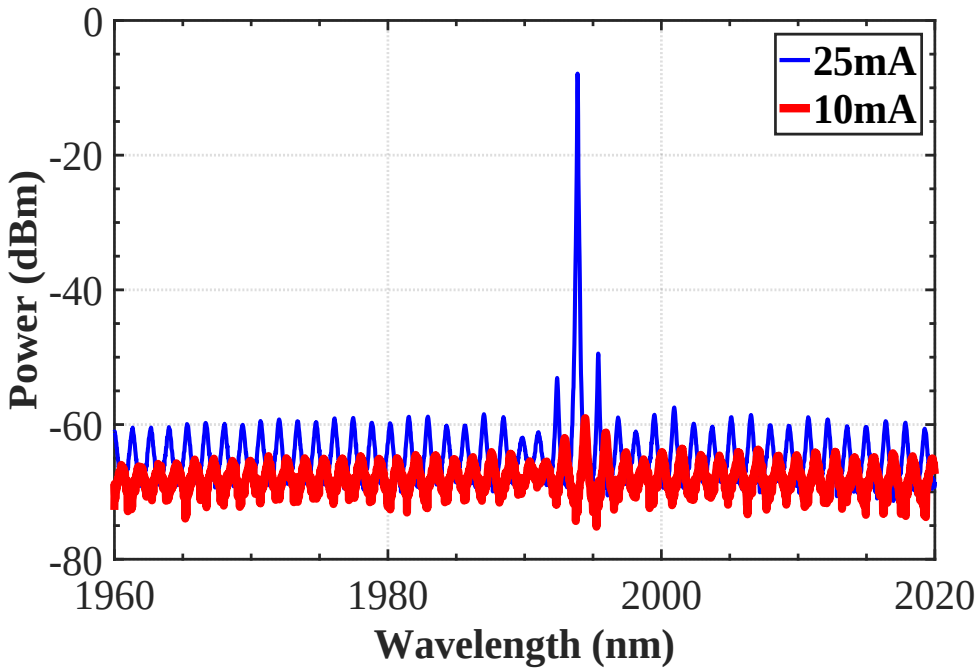


Figure 3.4: Optical spectrum of a slotted Fabry-Pérot laser (module S/N YE1922 at 25°C) below threshold (at 10 mA, red, below) and above threshold (at 25 mA, blue, above) (0.05 nm resolution, 3334 sampling points, 70 nm span).

peak determines the emission wavelength, the defining feature of a laser. This emission wavelength can be slightly tuned via the temperature (and to a lesser extent, current) of the laser. In terms of the slotted Fabry-Pérot lasers used in the experiments in this thesis, for example, the emission wavelength was found to tune linearly with temperature at a rate of ~0.1 nm/°C (and ~0.01 nm/mA with current).

Other characteristics of the laser that can be identified via the optical spectrum include the side mode suppression ratio (SMSR) and the optical signal-to-noise ratio (OSNR), as per Figure 3.5. The SMSR is a measure of the power difference between the laser emission peak and the next highest side mode, thus giving an indication of the degree of single mode operation of the laser device. The OSNR is a measure of the power difference between the laser emission peak and the noise level of the laser. These are important parameters in direct modulation schemes where well-defined single mode devices are desired for optimal spectral efficiency [109].

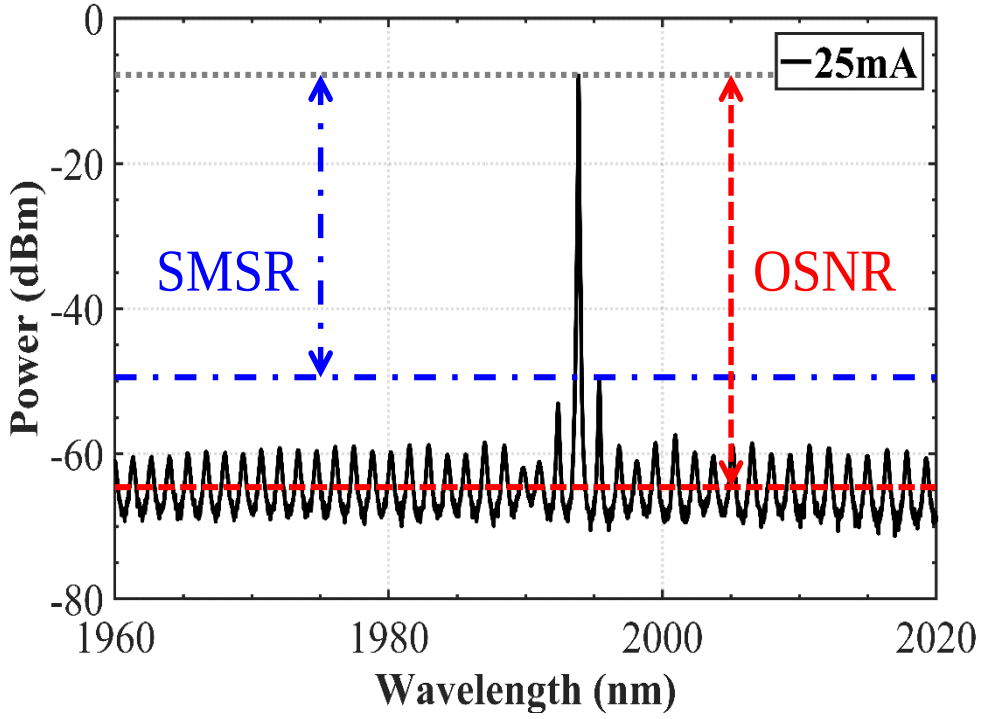


Figure 3.5: Optical spectrum of a slotted Fabry-Pérot laser indicating the SMSR (in blue) and OSNR (in red) (0.05 nm resolution, 3334 sampling points, 70 nm span).

3.1.2 Modulation formats

The optical data signal is created by modulating the optical carrier wave, i.e. encoding the carrier with information. The optical carrier before modulation is in the form of a continuous wave (CW) and its electric field can be written as Equation 3.1. In this equation, $\mathbf{E}(t)$ is the electric field vector, $\hat{\mathbf{e}}$ is a unit vector representing the state of the polarization of the optical field, E_{A0} is the amplitude, ϕ is the phase, ω_0 is the angular frequency which is related to the carrier frequency through $\omega_0 = 2\pi\nu_0$. Equation 3.1 indicates the possible physical parameters that can be modulated, with $\hat{\mathbf{e}}$ representing each polarisation [109], [110].

$$\mathbf{E}(t) = \hat{\mathbf{e}}\, E_{A0}(t)\, exp\,(-i\,(\,\omega_0(t)\,t + \phi_0(t)\,)\,) \tag{3.1}$$

Consequently, in order to modulate the carrier wave, the characteristics of the light wave that one may vary are the amplitude E_{A0}, frequency ν_0, or phase ϕ_0. Therefore, for digital signals, the three modulation formats are called amplitude-shift keying (ASK), frequency-shift keying (FSK), and phase-shift keying (PSK), depending on whether the amplitude, frequency, or phase of the

carrier wave is shifted between the two levels of a binary digital signal. The most common modulation scheme in optical communications is ASK, in which only the amplitude of the carrier wave is modified in modulation. The simplest version of ASK is called on-off keying (OOK). This two-level scheme essentially operates as a switch. The amplitude takes one of two fixed values during each bit period, depending on whether a 1-bit or 0-bit is transmitted. Most often, the amplitude is set to zero during transmission of 0-bits so that the presence of a carrier wave indicates a binary one and its absence indicates a binary zero, hence the name on-off keying (OOK).

Most optical communication systems employ OOK [109], [110]. Figure 3.6 shows several voltage vs. time plots. The digital bit stream using two voltage levels representing 1s and 0s is depicted in Figure 3.6(a). Figure 3.6(b) illustrates the continuous carrier wave before modulation. In Figure 3.6(c), OOK modulation has been applied to the waveform. For cyclical processes, such as rotation, oscillations, or waves, the frequency is defined as a number of cycles per unit time, measured in Hertz (Hz), i.e. $t = 1/\nu$, where ν is the carrier frequency in this case. Therefore, while the carrier frequency for lasers is in the THz range, the modulation frequency (or bit slot, as indicated by white/grey shading in Figure 3.6) is in the GHz range for modulation schemes such as OOK.

The modulated carrier wave can take one of two different states in OOK modulation to represent either a 1-bit or 0-bit. These different carrier states are known as symbols. If there are more than two possible carrier states (i.e. more than two symbols available), then it is possible for each symbol to represent more than one bit. Figure 3.7 shows ASK with four possible amplitude levels, or four symbols, called 4ASK. With four symbols available, each symbol can be uniquely represented with a two-bit binary number. This is because there are four possible two-bit binary numbers: 11, 10, 01 and 00. The relationship between the number of available symbols (N) and the number of bits that can be represented by a symbol x is $N = 2^x$. Therefore, if there were eight symbols, each could represent three data bits, and so on. The bit rate measures the number of bits that are transmitted per unit time. However, a symbol rate, known as the baud rate, is used in the case of modulation formats like 4ASK to measure the number of symbols that are transmitted per unit of time [111].

In the case of the OOK, there are two main choices with regards to optical bit

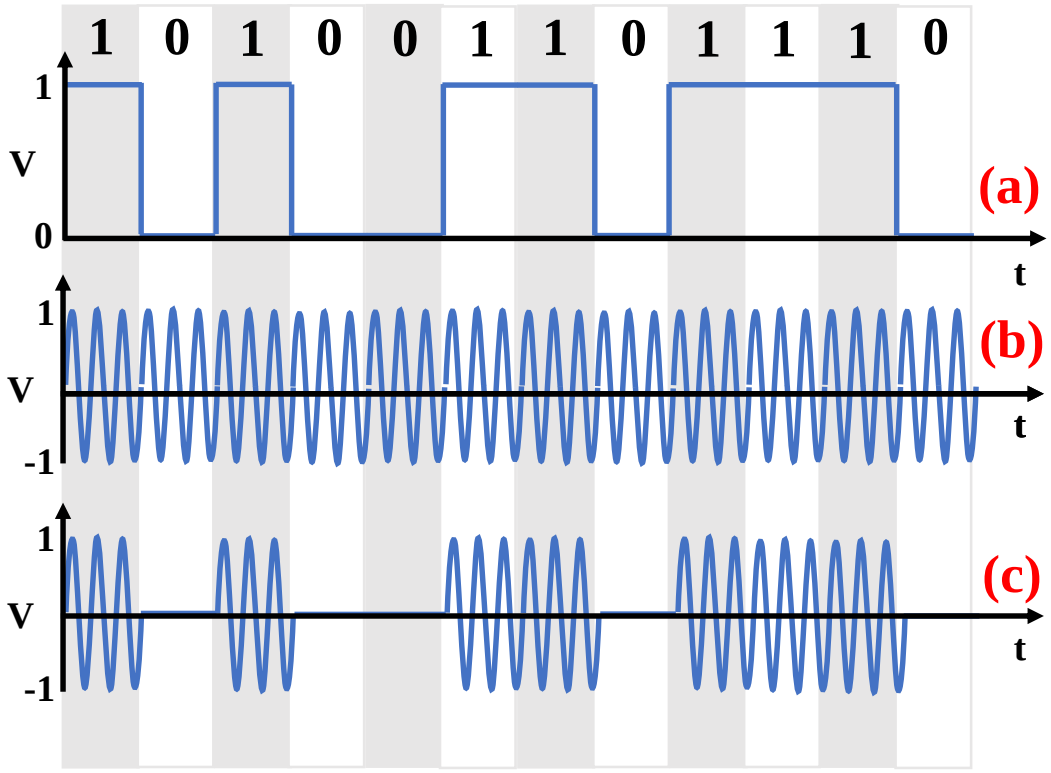


Figure 3.6: (a) bit stream of 1-bits and 0-bits, (b) unmodulated continuous carrier wave, (c) on-off keying (OOK) modulated signal [111].

stream formats, these are known as the return-to-zero (RZ) and non-return-to-zero (NRZ), shown in Figure 3.8. In the RZ format, each optical pulse representing a 1-bit is shorter than the bit period, and its amplitude returns to the zero level before the end of the bit period. All the pulses are identical in a RZ optical bit stream, but the spacing between them will depend upon the digital bit pattern. In the NRZ format the optical pulse for a 1-bit remains on (i.e. at the one level) for the full duration of the bit period and its amplitude does not drop to zero between two or more successive 1-bits, resulting in a pattern of optical pulses that vary in length depending on the digital bit pattern, as shown in Figure 3.8. For the NRZ format, the optical receiver must be able to extract an electrical clock from the bit stream in order to correctly sample and analyse the signal.

The main advantage of the NRZ format is that the bandwidth associated with this format is smaller than that of the RZ format by about a factor of two. The reduced bandwidth of an NRZ signal can be understood qualitatively from

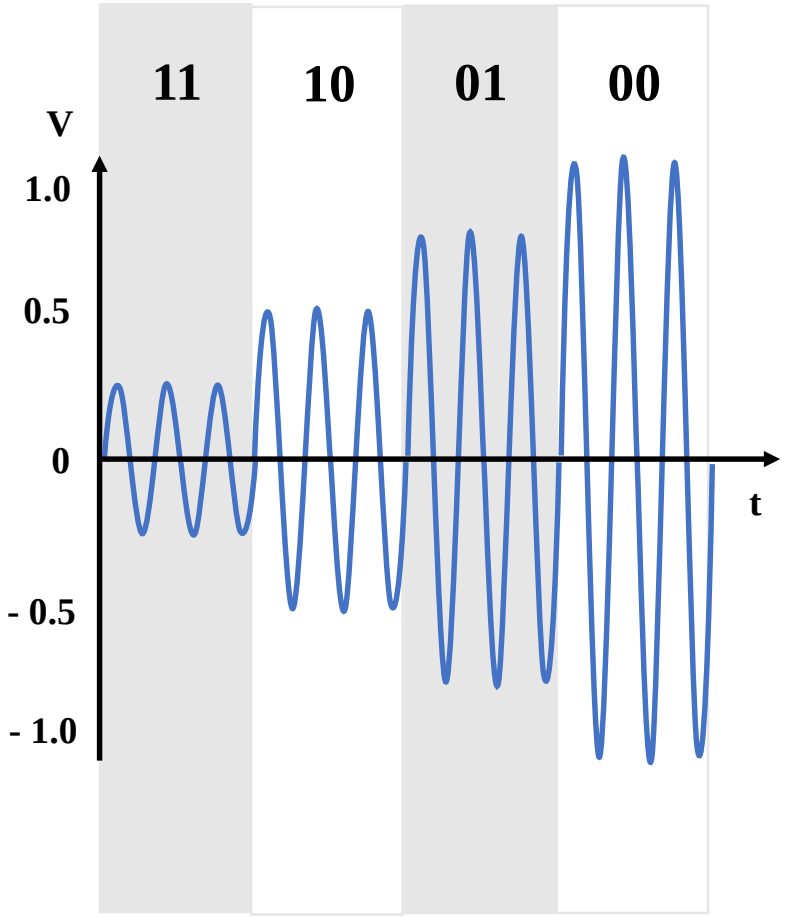


Figure 3.7: ASK with four amplitude levels (4ASK) [111].

Figure 3.8 by noting that on-off transitions occur much less often for an NRZ signal. This is the reason why the NRZ format is used extensively in the case of microwave and coaxial-cable systems for which the bandwidth should be economized as much as possible. However, the use of NRZ format for optical communication systems is not always the right choice because of the dispersive and nonlinear effects that can distort optical pulses during transmission and spread them outside their assigned bit slot. Since the pulse occupies the entire bit slot, the NRZ format cannot tolerate even a relatively small amount of pulse broadening and is quite vulnerable to intersymbol crosstalk. Moreover, a long sequence of 1 or 0 bits contains no information about the bit duration and makes it difficult to extract the clock electronically with a high accuracy. In spite of these difficulties, the NRZ format is still often used for optical communication systems, especially at low bit rates. The use of

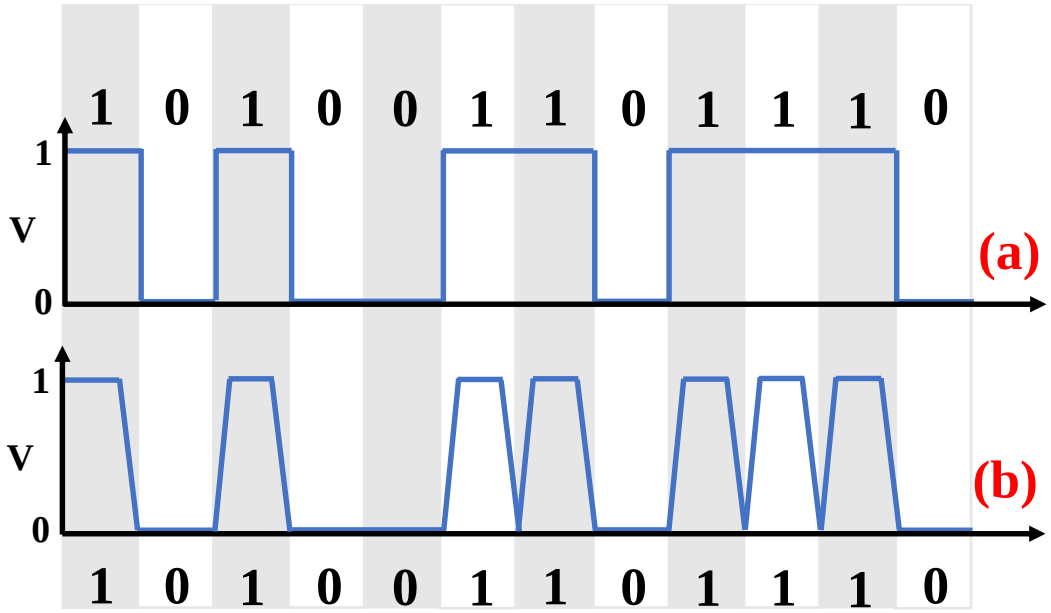


Figure 3.8: (a) NRZ bit stream, (b) RZ bit stream.

NRZ format becomes questionable at bit rates higher than 10 Gbit/s [110].

Optical modulation can be applied either directly or externally to the optical source, as shown in Figure 3.9. Direct modulation takes place before the optical carrier has been generated by applying an electrical signal (representing the information) directly to the drive current of the laser, resulting in a modulated light output from the optical source. The laser can be biased at a lower current to represent each 0-bit. For the 1-bits, the drive current of the laser can then be set to higher value, resulting in the emission of an optical pulse whose duration is similar to that of the electrical pulse. The advantage of direct modulation (over external) is that it simplifies the transmitter design and is generally more cost-effective because no other components are required for modulation other than the optical source. However, such an approach requires that the laser can be turned on and off as fast as the bit rate of the signal to be transmitted [110]. For higher bit rates, indirect (or external) modulation is often needed. External modulation takes place after the light has been generated by employing a component called an optical modulator which is used to encode information onto a CW optical carrier.

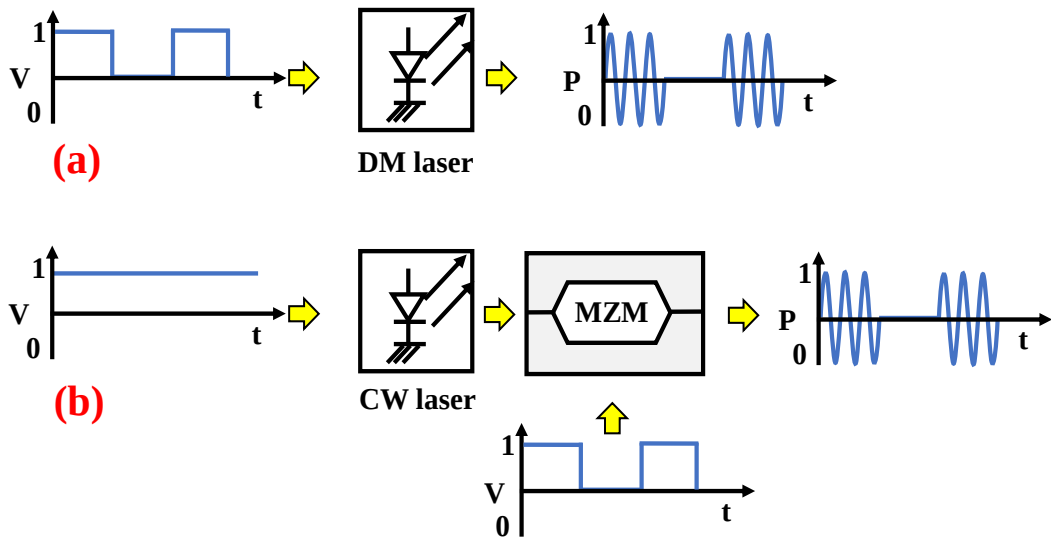


Figure 3.9: (a) Direct modulation (DM), (b) External modulation.

3.1.3 External modulation

A commonly used external modulator is based on electro-optic waveguides in a Mach–Zehnder configuration. The basic configuration of a Mach Zehnder modulator (MZM) is a splitter and a combiner connected by a pair of matched waveguide arms (as shown in the inset of Figure 3.10). These waveguides are made of a material, such as lithium niobate ($LiNbO_3$), whose optical properties can be varied by applying an electric field (called the electro-optic effect). An electric field is obtained by applying a voltage across the waveguide between two electrodes. In the case of $LiNbO_3$, an applied electric field will increase the refractive index (n). Increasing the refractive index (n) will decrease the speed of light in the medium v since they are inversely related through the equation $v = c/n$ (where c is constant). Naturally, this will increase the amount of time it takes for the light to travel through the medium (since speed is equal to distance over time $v = L/\Delta t$). For a modulator of fixed length (L) if there is a difference in the electric field applied to either arm of the modulator, then this will mean that the light will take longer to travel through one arm, compared to the other, due to Equation 3.2. This relative delay corresponds to a phase difference between the two signals in the arms of the MZM.

$$\Delta t = \frac{Ln}{c} \tag{3.2}$$

When the two light signals are recombined, the phase difference is then

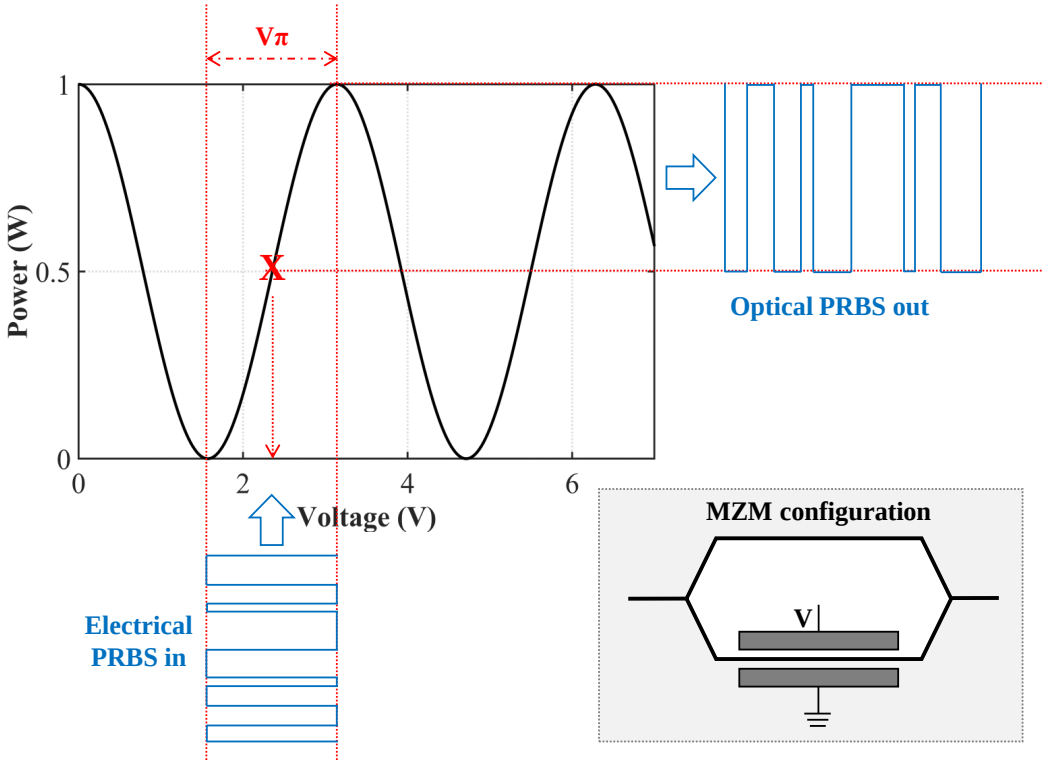


Figure 3.10: Transfer function of a MZM indicating how E/O conversion occurs. V_π and the quadrature point (X) are shown in red. The inset (in grey) shows a typical MZM configuration, with a voltage applied to one arm of the modulator.

converted into amplitude variations, due to interference. As shown in Figure 3.11, if two waves are in phase, constructive interference will occur when they are combined. Conversely, if two waves are out of phase, destructive interference will occur when they combine and the resulting wave will have smaller amplitude (or no amplitude if the waves are completely out of phase). In this way, phase difference is converted to amplitude variations through interference. The phase shift (and, therefore, output intensity) is controlled by changing the delay through one or both of the optical paths by means of the electro-optic effect. This forms the basis of the MZM mechanism; the incoming signal is split and transmitted through the two different arms of the MZM. After a few centimetres, the two signals are recombined, causing the optical waves to interfere with each other, resulting in amplitude modulation.

The performance of external modulators is generally characterised by the on-off ratio, the modulation bandwidth and the modulation voltage required for a π phase change (V_π). The on-off ratio is the difference between the optical power at maximum and minimum transmission. A higher on-off ratio allows for greater definition between the on and off states of the modulator.

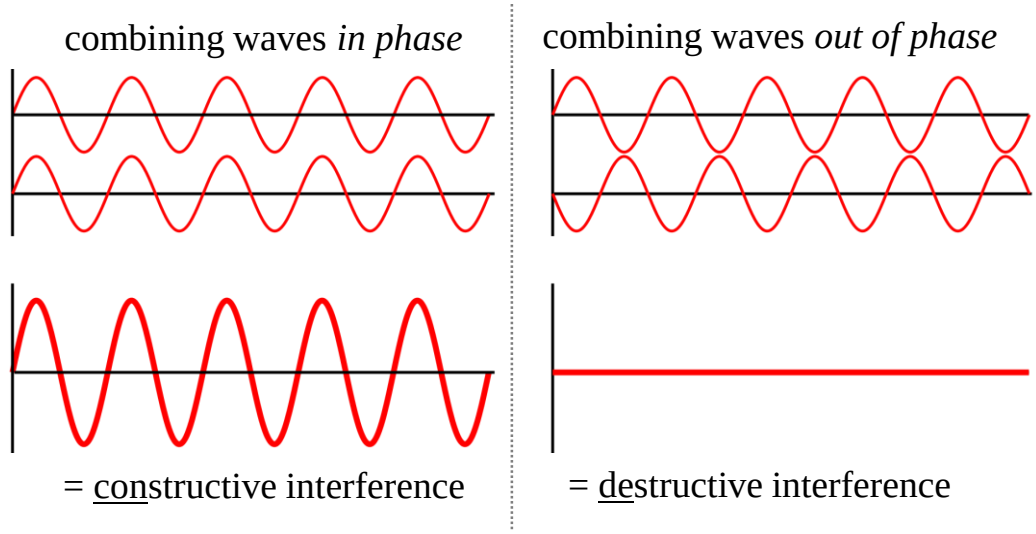


Figure 3.11: Interference occurs when two waves are combined, this can be constructive (as shown on the left) or destructive (as shown on the right) depending on the relative phase of the two waves when they combine.

For OOK, this would mean greater definition between the 1-bit and 0-bit. $LiNbO_3$ modulators generally provide an on-off ratio >20 dB. In terms of modulation bandwidth, many $LiNbO_3$ C-band modulators are operable up to ~40 GHz, whereas 2 μm modulators are currently operable up to ~10 GHz [112]). Finally, a smaller V_π is preferable as this indicates a stronger electro-optic response and a more efficient modulator, with V_π of ~5 V being typical for $LiNbO_3$ modulators (this has been achieved at 2 μm [113]). An additional consideration for systems implementation would be the insertion loss of the device, since all external modulators will add some loss to the system (typically 3 dB to 7 dB) [114].

Figure 3.10 shows a typical example of a MZM transfer function. The transfer function is a measure of the output power from the MZM with respect to the applied bias voltage and provides an indication as to how the bias voltage is transferred to optical power. V_π can be measured via this transfer function as the bias voltage that corresponds to a π phase change (i.e. from minimum to maximum amplitude). In Figure 3.10 V_π, for example, would be about 1.5 V. The red X in Figure 3.10 marks the quadrature point. If the bias of the MZM is set at this value, the E/O conversion will be approximately linear since it is within the linear regime of the transfer function.

After the signal has been generated, the purpose of the transmission medium is to transport the signal from the transmitter to the receiver, preferably with as little signal power loss and distortion as possible. In the case of a

point-to-point optical communication system, the transmission medium takes the form of an optical fibre link. Ideally the optical fibre would not modify the signal in any way as the signal is transmitted. In reality, the signal will lose power as it is transmitted through the fibre due to the losses as discussed in Section 2.1.3. Current standard SMF has loss up to 0.2 dB/km in the 1.55 μm wavelength region. Even at this low loss level, the optical power of a signal will be reduced to only 1% of its original value after travelling through 100 km of this fibre, and would hence require repeaters or amplification to achieve longer lengths, which in turn introduces additional impairments (and cost). Loss is not the only impairment through which the light can be distorted - dispersion and nonlinearities can also cause distortions in the field as it propagates through the fibre [110],[109],[7]. However, little of these effects were observed during the experimental work of this thesis.

3.2 System performance parameters

The primary purpose of an optical receiver is to detect an incoming optical signal from the transmission medium and decode the data within that signal (by converting the optical signal to an electrical signal). The information can be distributed to its final destination or, in the case of this thesis, further processed to determine the performance of the system. Firstly, O/E conversion is needed in order to extract the baseband signal data from the optical carrier, and this is done using a photodetector and demodulator.

The function of the photodetector is to detect the optical signal, i.e. absorb light of a certain wavelength and convert this optical input to electrical output. Semiconductor detectors are the most common photodetectors because of their reliability, flexibility and sensitivity at absorption wavelengths that correspond to the low-loss regions of silica optical fibres. Assuming a linear response, the slope efficiency (or responsivity) of the photodetector can be calculated. This responsivity will be different depending on the wavelength of the input light. Once the signal has been extracted by the photodetector and converted into electronic pulses, the signals are processed at the electrical level, helping to generate a suitable square wave that can then be administered at the logic level. Therefore, one of the key considerations in the performance of the optical receiver (and, hence, the overall system) is the photodetector itself, because the response time of the detector determines the speed of the data that can be recovered.

The original encoded information is recovered through a process called demodulation. The design of the demodulator depends on the modulation format used in the transmitter. Most optical communication systems employ a digital binary scheme called intensity modulation with direct detection (IM/DD) [4]. Demodulation in this case is performed by a decision circuit that identifies bits as a 1-bit or a 0-bit, depending on the intensity of the electric field. It is almost impossible to recover the original bit stream with 100% accuracy. For this reason, the performance of an optical communication system is characterised in terms of the bit-error rate (BER).

3.2.1 Bit error rate

In a digital transmission system, the BER is defined as the ratio between the number of bit errors received in a certain time interval and the total number of bits transferred during the same time. The BER can also be defined as the average probability of identifying a bit incorrectly. If p_1 is the probability of incorrectly identifying a 1-bit and p_0 is the probability of incorrectly identifying a 0-bit (i.e. mistaking a 1-bit for a 0-bit and vice versa), and if the two bits are equally likely to be transmitted, then the BER in this case is given by Equation 3.3.

$$BER = \frac{1}{2}(p_1 + p_2) \tag{3.3}$$

BER is usually expressed as 10 to a negative power. A BER of 1×10^{-6} corresponds to an average of one error per million bits transmitted. Optical communication systems are generally designed to operate in such a way that the error probability in the digital receivers is smaller than a specified value. A common acceptance level for NRZ systems operating at 40 Gbit/s or below is a BER less than 1×10^{-9} [109], [110]. In an OOK system, 1-bits and 0-bits are represented by the presence and absence of an optical pulse, respectively. The receiver electronics then include a comparator to the data expected, and the BER is calculated [6].

3.2.2 Signal-to-noise ratio

The accuracy of identifying a 1-bit or a 0-bit depends on the signal-to-noise ratio (SNR) of the electrical signal generated by the photodetector. A higher SNR will correspond to a larger difference between the 1-bit level and the 0-bit

level, leading to higher accuracy in distinguishing if a bit is 1 or 0. Even in the case of an ideal optical receiver, some inherent noise is introduced by the process of photodetection itself. Due to these fundamental noise fluctuations, there is always a finite probability that a bit will be incorrectly identified at the decision circuit [6].

Two fundamental noise mechanisms that contribute to current fluctuations in all optical receivers (even in the presence of an incident optical signal with constant power) are shot noise and thermal noise. Shot noise is a result of the random generation of charge carriers under interaction with an external field. Therefore, even if the current to a photodetector is constant when photons are absorbed, electron-hole pairs may be generated at random time intervals. Thermal noise is a result of the thermal motion of charge carriers, which, at a finite temperature, will move randomly within any conductor. In a resistor, this spontaneous motion will result in a fluctuating current, regardless of the voltage applied. Resistors within the circuitry of the photodetector add such fluctuations to the current emitted.

Both thermal and shot noise affect the SNR for the decision circuitry. However, noise is defined as any distortion that is added to a signal, thereby making it more difficult to accurately determine the bit value at the receiver. As such, in an optical communication system, additional noise sources such as that from amplifiers must also be considered, as per Chapter 2. Amplified spontaneous emission, or ASE, is the primary source of noise prior to detection, and hence the optical signal-to-noise ratio (OSNR) is often the parameter measured to determine the quality of the signal arriving at an optical receiver. The influence of ASE noise is essentially characterised by the OSNR. A degraded OSNR will also correspond to a degradation in SNR. In the experimental work of this thesis, a measurement of the BER vs. OSNR is presented in order to analyse the performance of the optical communication system.

3.2.3 Eye diagram

Another performance indicator used in this thesis is the eye diagram, which is formed when consecutive combinations of two or more bits are overlapped on an oscilloscope, resulting in a pattern which resembles an open eye (in the ideal case). Visualisation of the eye diagram is of interest as it gives a qualitative analysis of the signal reaching the detector and hence informs expectations about the performance of the transmission link. This is commonly

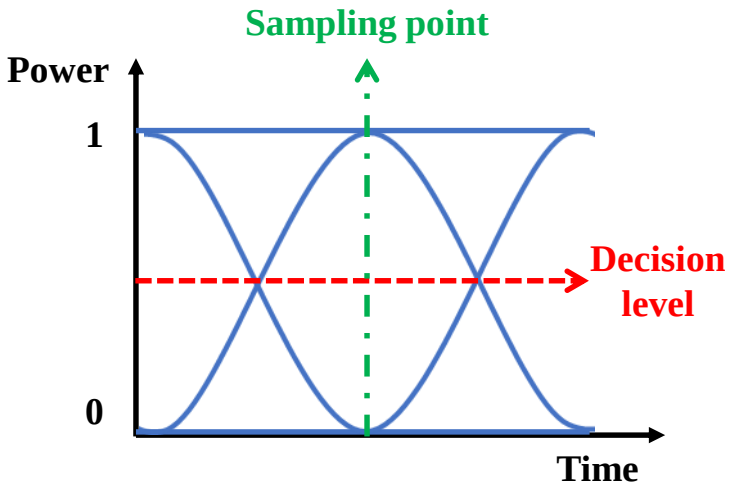


Figure 3.12: Illustration of an eye diagram.

used in optical communications as a qualitative monitoring scheme enabled by a fast photodetector and a sampling oscilloscope.

An illustration of an eye diagram for a NRZ-OOK bit stream is represented by the blue lines in Figure 3.12. The decision threshold and optimal sampling time can be visualised via the eye diagram. The decision threshold (Figure 3.12, red dashed line) is the power level which corresponds to the centre of the eye opening and the optimal sampling time (Figure 3.12, green dash-dotted line) corresponds to the maximum opening of the eye. As such, any reduction in eye opening indicates an increase in the BER and the eye diagram provides a visual way of monitoring the performance of the optical communication system [109], [110], [4].

An overview of optical signal generation has been discussed and some of the key performance indicators that are used in this thesis have been presented (namely, BER, OSNR and the eye diagram). With these fundamental conventions established, the next section will expand beyond the single channel example to discuss the concept of multiplexing many channels over a point-to-point link.

3.3 Wavelength division multiplexing

Channel multiplexing is a technique used to send many signals through a transmission medium at the same time. Multiplexing enables greater use of the transmission medium bandwidth and increases the overall data-carrying

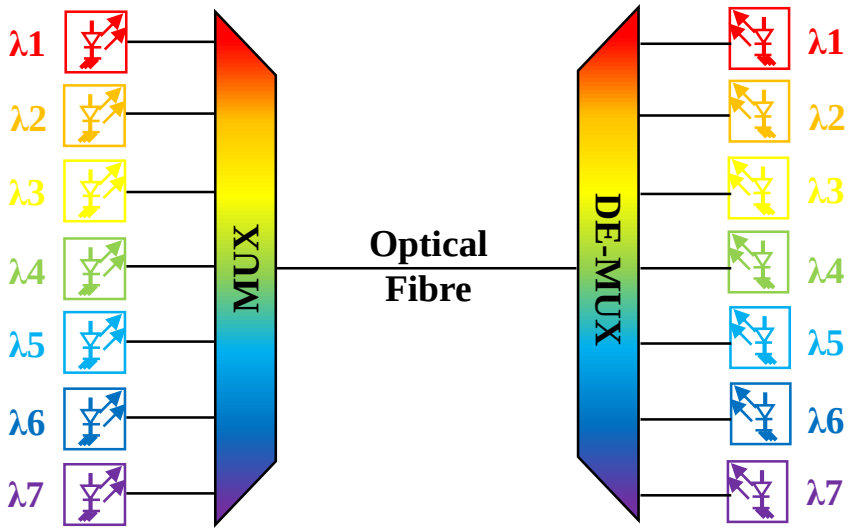


Figure 3.13: Illustration of a WDM point-to-point link where λ_1, λ_2 etc. refer to the different wavelengths.

capacity of the communication system. An everyday example of multiplexing is television channels. In Ireland, SaorView is the digital terrestrial television service which broadcasts channels over frequencies from 470 MHz to 780 MHz (FM radio channels are below 470 MHz and above 780 MHz is reserved for 4G broadband) [115]. Using these frequencies, different channels are simultaneously transmitted to your television and, by selecting each individual channel (i.e. tuning your receiver to the desired frequency), you can receive different signals on your screen and view different content.

One of the most common multiplexing techniques is frequency division multiplexing (FDM). First developed in the early 20th century for radiowave broadcast, FDM was then adapted to microwaves for the television industry and today it is used for lightwaves in optical communications. As the name suggests, the different channels propagate with different frequencies. Each channel consists of a carrier wave, oscillating at a certain frequency, that is used to transmit one signal. These channels are combined using a device, known as a multiplexer, and sent through the transmission medium together, after which the channels are then separated (or demultiplexed). Similar to microwave transmission, multiple frequencies (or wavelengths) can be used for multiplexing in optical communication systems. However, in the case of optical communications it is more commonly referred to as Wavelength Division Multiplexing (WDM). The concept of WDM was first published in the 1970s, with WDM systems being realised in the lab soon after [116], [117], [118], [119].

3.3.1 WDM systems

Wavelength division multiplexing (WDM) is a technique used to increase the transmission capacity of an optical fibre. In a WDM system, multiple optical channels, each operating at a different wavelength (λ), are combined in a single fibre by an optical multiplexer (mux) and then transmitted over the same optical fibre. At the receiver, the WDM signals are demultiplexed by an optical demultiplexer (demux) into separate optical channels, as shown in Figure 3.13. In current optical communication systems, many wavelength channels are used (sometimes summing up to a hundred channels within the C-band) in order to meet capacity demands.

Multiplexers (and demultiplexers) are essentially wavelength-dependent filters. Hence, filters are essential components in WDM systems. A simple filter selects one wavelength and rejects all others. The fundamental mechanism of most optical filters is based on the property of interference (as discussed in Section 3.1.3). Figure 3.14 shows a representation of a filter profile (in dotted lines) overlaid with a WDM optical spectrum. The filter profile for the two channels on the right (purple and blue) shows ideal channel isolation with a narrow passband and sharp 'passband skirts' enabling only data from the selected channel to be transmitted.

In comparison, the filter profile on the left in Figure 3.14 (yellow) has poor channel isolation in comparison, as it allows for adjacent channel leakage, resulting in crosstalk between the WDM channels. Optical crosstalk is an important issue in the design of WDM systems. The system performance degrades whenever crosstalk leads to transfer of power from one channel to another. Optical crosstalk can occur in a perfectly linear channel due to the imperfect nature of various WDM components, such as optical filters or demultiplexers, which often allow a fraction of the power from adjacent channels to leak into one another. Crosstalk is exacerbated when channels are more tightly spaced and acts as a noise source to the signal being detected in WDM transmission systems [6].

Some key parameters to consider in a WDM system are the number of channels (N), the bit rate of each channel (B) and the spacing between two neighbouring channels (in wavelength $\Delta\lambda$ or frequency $\Delta\nu$). These parameters determine the overall communications capabilities of the WDM system, such as the capacity ($N \times B$), bandwidth ($N \times \Delta\nu$) and spectral efficiency ($B/\Delta\nu$). As can be seen from these relations, the capacity of a WDM

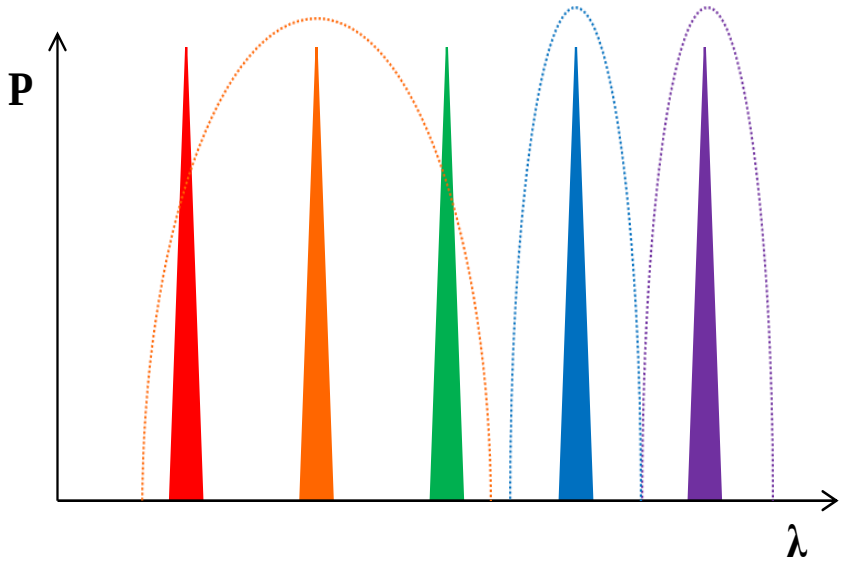


Figure 3.14: Representation of a filter profile (in dotted lines) overlaid with a WDM optical spectrum.

system depends on how closely optical channels can be packed in the wavelength domain. Ideally, the channel spacing should be minimised and the spectral efficiency should be maximised. However, this is limited by crosstalk and is related to many factors including the channel bit rate, the modulation format, the filter pass-band, and central wavelength variations (due to laser manufacturing and temperature variations).

There are two main types of WDM technologies used in optical communication systems today: Coarse Wavelength Division Multiplexing (CWDM) and Dense Wavelength Division Multiplexing (DWDM). CWDM systems are used primarily for metro and access network applications (typically 40 km to 80 km from the service switching centre) [4]. CWDM systems are cost-effective over shorter distances; they have wider channel spacing (1000 GHz) and do not require precise wavelength control for transmitter lasers [120]. In comparison, a conventional DWDM system typically uses 40 channels at 100 GHz spacing or 80 channels with 50 GHz frequency spacing and is used primarily in high-capacity, long-haul networks [110].

3.3.2 Importance of WDM

If one optical channel can transmit ~0.5 million telephone conversations over a single optical fibre, by employing WDM to transmit 100 channels at different

wavelengths, then that same fibre can transport more than 50 million telephone conversations at once [7]. Hence, the latter part of the 1990s saw dramatic increases in the capacity-carrying capabilities of optical communication systems brought about through the use of WDM and enabled by EDFAs [10]. This technological revolution ignited massive investment in system development and the capacity of optical communication systems increased from less than 100 Mbit/s, when they debuted in the 1970s, to roughly 1 Tbit/s by 2000 [121]. This represents an increase by a factor of more than 10,000 in 30 years. The introduction of WDM contributed to a factor of 1,000 increase in only 10 years [10]. By 2001, a WDM experiment with 273 channels operating at 40 Gbit/s was demonstrated, reaching a total capacity of 11 Tbit/s [122]. During these decades, the rapid growth in system capacity exceeded the requirements of network traffic.

However, this was before the days of YouTube (2005), Netflix (2007) and other high-capacity streaming services which dominate capacity demands today. Therefore, while commercial WDM systems were capable of operating 100 channels at data rates of 100 Gbit/s and total capacities in the order of 10 Tbit/s in 2010, progress soon slowed as the readily available bandwidth in the C-band became increasingly occupied and capacity demands required much more efficient utilisation of optical bandwidth [10]. Currently, the growth in network traffic, coupled with observed trends in commercial practice, will result in a requirement for WDM systems which can support channels operating at data rates of 1 Tbit/s and, therefore, total capacities in the order of 100 Tbit/s by 2020 [10]. Terabit single-channel bit-rates are difficult to achieve and complex within current technological capabilities [10]. Therefore, opening the transmission window at 2 μm and enabling WDM systems in this new waveband could extend the available bandwidth and provide alternatives for future high-capacity optical communication systems.

3.3.3 WDM at 2 μm

As per Section 2.2.2, the first 2 μm transmission experiments took place in 1987 and were motivated by the reduction of Rayleigh scattering at longer wavelengths which could allow for fundamentally higher capacity. However, as described above, the invention of the EDFA and implementation of WDM soon followed. This enabled much greater capacities and ultimately lead to the halt of 2 μm investigations. Then, in the 2010s, interest in the 2 μm wavelength

region was reinvigorated due to the ever-increasing traffic on the world's optical networks and global demands for more capacity, leading to the first data transmission experiments at this waveband in nearly 30 years.

Establishing data transmission in the 2 μm region involved the development of a vast array of optical components and the collaboration of many research groups internationally. This was made possible through a collaborative R&D project called MODEGAP (2010-2014), which was supported under the European Union 7th Framework programme. The goal of MODEGAP was to develop disruptive technology to enhance optical communication infrastructure and reduce energy consumption. The establishment of a new wavelength window is primarily governed by the availability of semiconductor materials for lasers in the transmitter (and detectors in the receiver), low-loss optical fibre for a transmission medium and amplifiers to enable transmission over long distances. The MODEGAP experiments combined advances in semiconductor laser technologies (Section 2.3.1), along with novel HC-PBGF (Section 2.3.2), and custom-built high-gain, low-noise TDFAs (Section 2.3.3) to establish an optical communication system in this new waveband.

The first demonstration of 2 μm data transmission over HC-PBGF was reported in 2012 [123]. This experiment comprised a single CW laser emitting at 2.08 μm which was externally modulated using a MZM at a bit rate of 8 Gbit/s NRZ-OOK. The signal was amplified using a custom-built TDFA, before transmission over 290 m of HC-PBGF. The first WDM data transmission at 2 μm was simultaneously reported, resulting in two post-deadline papers at ECOC 2012 [123], [124]. In this WDM experiment, a total capacity of 16 Gbit/s was achieved using three channels directly modulated at 2.5 Gbit/s and one channel that was externally modulated at 8.5 Gbit/s (all NRZ-OOK), over 290 m of HC-PBGF [124]. This experiment demonstrated that both direct and external modulation can be implemented in the 2 μm wavelength region. The bit rate of the directly modulated channels in this demonstration was fundamentally limited by the 3 dB RF bandwidth of the lasers (which was $\sim$3 GHz at 50 mA) and the bit rate of the externally modulated channel was limited by the 3 dB bandwidth of the 2 μm photodetector (which was $<$9 GHz). The capacity of the 2 μm optical communication system was then pushed further by implementing advanced modulation formats resulting in a total capacity in excess of 20 Gbit/s by 2013 [124] and 30 Gbit/s in 2014 [125].

By 2014, an operational testbed was in place at Tyndall National Institute. However, many of the components involved in this system represented the first steps into this new wavelength region. Device options were limited and those that were available were first generation and/or non-optimal (compared to more mature technologies at 1.55 μm). These 2 μm devices presented challenges such as limited operation speeds (as described above), thermal fluctuations and high insertion losses, which compounded when combined in a system with other non-optimal components. Due to these limitations, increasing the capacity beyond 30 Gbit/s was a non-trivial challenge. This thesis project (which began in 2014) aims to build upon these discoveries and address the issues therein, such as increasing capacity, improving spectral efficiency and enabling transmission over longer distances. Chapter 4 will discuss some of the early experiments of this thesis project which focused on these three key challenges.

Chapter summary

This chapter provides an introduction to optical communication systems in terms of the building blocks, parameters and key considerations that are needed in order to establish a DWDM system in the new transmission window of 2 μm. While the concept of shifting transmission to 2 μm was previously considered in the 1980s, it resurfaced 30 years later during the 2010s when global demands for capacity rapidly increased. The ability to branch out into this new wavelength region was made possible through the EU project MODEGAP, which developed key enabling technologies such as optical components and fibre. The first 2 μm WDM system was demonstrated with four optical sources, and a record capacity of 30 Gbit/s was achieved, but with enormous challenges in terms of non-optimal devices, limited device options and restricted transmission distances. This thesis will explore these challenges further and propose novel solutions.

Chapter 4

Increasing system capacity

As discussed in Section 3.3.2, the adoption of WDM (along with the invention of the EDFA) revolutionised the capacity-carrying capabilities of optical communication systems during the 1990s and resulted in the system capacity increasing by a factor of 1,000 in 10 years [10]. It is clear from these trends that, in order to establish the 2 μm transmission window for optical communications, it is necessary to increase the system capacity well beyond the previous record of 30 Gbit/s. This chapter focuses on experimental efforts to push beyond that record, with the ultimate aim of increasing system capacity by an order of magnitude.

In demonstrations prior to this thesis, a maximum of four WDM channels were implemented in 2 μm transmission experiments, with a maximum data rate per channel of 8.5 Gbit/s [96], [124]. In order to increase system capacity, a 2 μm WDM system was designed with a greater number of channels that could be modulated at higher bit rates, resulting in a total system capacity of 100 Gbit/s ultimately achieved. The design, implementation and analysis of this system forms the basis of this chapter.

4.1 WDM system design

Figure 4.1 illustrates the schematic of a WDM system (as per Section 3.3). From this figure, it is clear that one way to increase the capacity of a WDM system would be to increase the number of WDM channels. Another way would be to improve the bit rate of these WDM channels. This section focuses on the design of a 2 μm system to increase the capacity in these two ways.

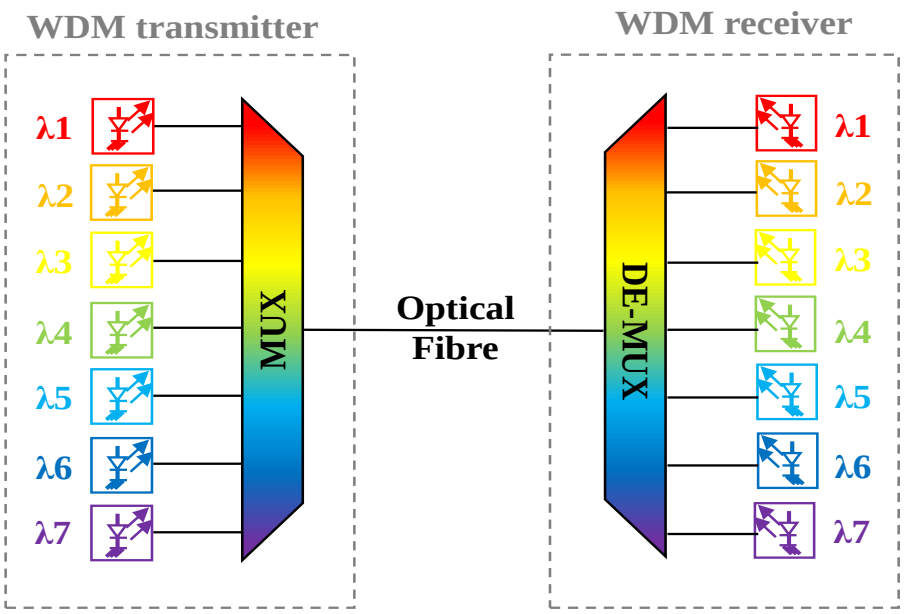


Figure 4.1: Wavelength division multiplexing system.

Table 4.1: First generation of 2 μm lasers (at 25°C and 80 mA).

Module S/N	**Centre λ**
-	***(nm)***
YE1699	1997.40
YE1698	2003.70
YE1696	2004.00
YE1697	2005.60
YE1694	2006.00

More channels

Considering the WDM channels first, the lasers used to generate optical carriers were highly-strained, InGaAs, InP-based, slotted Fabry-Pérot lasers designed for single mode operation at 2 μm (as per Section 2.3.1) [25]. As described in Section 3.3.3, device options were limited, with only five lasers initially available. These five lasers are listed in Table 4.1, with the module serial number (S/N) and emission wavelength (λ) at 25°C and 80 mA. For the purpose of this thesis, the set of lasers listed in Table 4.1 is referred to as the 'first generation' of slotted Fabry-Pérot lasers at 2 μm, as they were the lasers used in the first 2 μm WDM experiments (pre-2014 [96], [124]).

In order to enable a greater number of WDM channels, additional lasers were required. Thus, a second set of 2 μm lasers was developed in conjunction with

Table 4.2: Second generation of 2 μm lasers (at 25°C and 80 mA).

Module S/N	**Centre λ**
-	***(nm)***
YE1919	1876.20
YE1916	1886.40
YE1918	1905.75
YE1917	1913.43
YE1984	1953.20
YE1920	1956.79
YE1985	1963.85
YE1921	1968.28
YE1922	1992.83
YE1928	2002.35
YE1923	2019.92
YE1924	2045.10

MODEGAP partners, Eblana Photonics. In order to maximise the use of available bandwidth, the emission wavelengths of these lasers were designed to fill the broad spectrum of the TDFA, which operates over a wide bandwidth extending from ~1.7 μm to 2.1 μm [26]. This set of 12 lasers is listed in Table 4.2 and is referred to in this thesis as the 'second generation' of slotted Fabry-Pérot lasers at 2 μm. By combining the first and second generation of lasers, a greater number of channels could be incorporated into the 2 μm WDM system. With the WDM channels identified, the next step was to apply the baseband data to these optical carriers, either directly or externally (via a MZM, for example), which will be discussed in the following section.

Higher data rates

The second step in achieving greater system capacity was to enable the WDM channels to be modulated at higher data (or bit) rates. This presented challenges due to restricted device options (in terms of the number of modulators available) and device limitations (with regards to non-optimal performance).

Consider, first of all, the bandwidth of modulation components. For directly modulated channels, it is the 3 dB bandwidth of the lasers that is of primary concern when determining the maximum data rate. For this reason, the second generation lasers were developed with a higher bandwidth. The first generation of lasers were reported to have 3 dB bandwidths of ~3 GHz [96], [124], whereas the second generation of lasers were measured to have

3 dB bandwidths of >5 GHz [126]. This improved 3 dB bandwidth (of >5 GHz compared to ~3 GHz) enabled higher achievable bit rates for directly modulated channels in the 2 μm WDM transmitter. However, these capabilities are still limited in comparison to the bandwidth of other slotted Fabry-Pérot lasers available at 1.55 μm, for example, in which 10 GHz is standard (extendable up to ~20 GHz today) [127].

For other channels, an external modulator was applied in order to enable higher data rates (as per Section 3.1.3). In this case, a commercial $LiNbO_3$ MZM, suitable for operation from 1.9 μm to 2.2 μm, was used (Photline MX2000-LN-10). This MZM had a V_π of 9.5 V, insertion loss of ~8 dB and a bandwidth of ~12 GHz. In previous WDM demonstrations, a commercial InGaAs photodetector was used which was measured to have a bandwidth less than ~9 GHz [96], [124]. In order to at least match the capabilities of the MZM, a new InGaAs photodetector with a 3 dB bandwidth of ~12.5 GHz (EOT ET-5000) was implemented in the 2 μm WDM receiver. Incorporating these improved components enabled a 2 μm system that could operate at higher data rates.

4.1.1 WDM transmitter

Taking device limitations into account, an improved WDM system was designed by combining a greater number of channels at higher data rates, in order to push the capacity of 2 μm optical communication systems further than previous records. Accordingly, a 2 μm transmitter was designed which increased the number of WDM channels to eight (double the previous maximum of four channels), as shown in Figure 4.2. In this WDM transmitter, four directly modulated lasers were combined with four externally modulated lasers.

Fast-OFDM is a variant orthogonal frequency division multiplexing (OFDM). It was originally labelled as “fast” because the subcarrier spacing is more compact than in conventional OFDM [128], [129]. For the directly modulated channels, four lasers (with emission wavelengths at 1967.6 nm, 1977.8 nm, 1986.9 nm and 1992.5 nm) were modulated using two independent 4ASK fast-OFDM signals, together with their delayed versions. Each 4ASK fast-OFDM used 128 discrete cosine transform point size, among which 106 subcarriers were used for data modulation. Double side-band 4ASK fast-OFDM signal provides a spectral efficiency of 2 bit/s/Hz, so the total data rate per

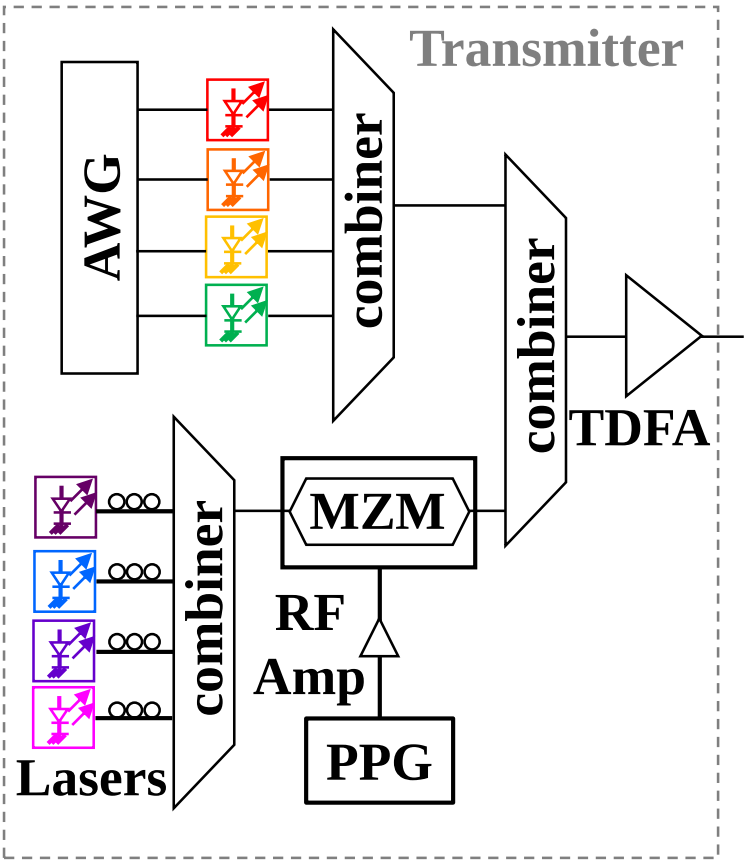


Figure 4.2: 2 μm WDM transmitter schematic with eight channels (four directly modulated and four externally modulated).

channel was 8.3 Gbit/s (or 7.7 Gbit/s taking into account overheads for forward error correction (FEC) at 7%). Each fast-OFDM frame consisted of one start-of-frame symbol for synchronization and 100 payload symbols [130], [131]. These signals were generated using a 5 GS/s arbitrary waveform generator (AWG) and performance was monitored, via direct detection, with a real-time oscilloscope. 4ASK and OFDM were described in Section 3.1.2. Fast-OFDM is an attractive version of OFDM for this application, in particular, because it can directly generate a real-valued signal suitable for intensity modulation with direct detection (whereas OFDM generates imaginary components which would be unsuitable in this case) [132], [133], [134], [135], [136].

For the externally modulated channels, four lasers (with emission wavelengths at 1995.7 nm, 1998.4 nm, 2001.9 nm, and 2003.9 nm) were NRZ-OOK

modulated using the commercial MZM, driven with a pseudo-random bit sequence (PRBS) of length $2^{31} - 1$ from a pulse pattern generator (PPG), at a bit rate of 12.5 Gbit/s. This represented a higher bit rate per channel than previous experiments (which demonstrated 8.5 Gbit/s maximum per channel). Polarization controllers (PC) were added after the lasers to align polarization with the MZM.

In a WDM transmitter, the channels must be multiplexed before being launched into the optical fibre. While 1x4 and 1x8 couplers were purchased specifically for multiplexing channels at 2 μm, the excess loss was significantly larger than using standard 2:1 couplers (designed for 1.55 μm). Therefore, optical fibre couplers were used to multiplex the channels, with an average loss of 4 dB per channel. However, scaling to further channels using such couplers was non-viable due to the additional loss per channel. For example, to multiplex two channels, a standard 2:1 coupler would introduce a minimum of 3 dB loss per channel. To multiplex four channels another 2:1 coupler would be needed, this would then add up to 6 dB loss and so on. Therefore, the number of channels was reasonably restricted. In terms of the directly modulated channels, the AWG had two outputs. In order to directly modulate the maximum number of channels, two independent signals were generated, together with their delayed versions in order to decorrelate the data between the different channels, giving a maximum of four directly modulated channels. As a result of these restrictions, eight was the maximum number of WDM channels that could be supported in the 2 μm transmitter at the time. Thus, using four 12.5 Gbit/s NRZ-OOK externally modulated channels and four 7.7 Gbit/s 4ASK fast-OFDM directly modulated channels, a total capacity of 81 Gbit/s was transmitted.

4.1.2 HC-PBGF transmission

Prior to the channels being launched into the fibre, a TDFA was implemented to compensate for transmitter losses (such as those from couplers, for example) and to pre-compensate for transmission losses. Figure 4.3 shows the spectrum of all eight channels after this TDFA, with channel output powers up to -1 dBm. The non-uniformity in channel power levels can be attributed to the unbalanced losses of passive components in the transmitter for different wavelengths. The SMSR was measured to be >40 dB for most channels. However, the SMSR of some lasers (e.g. 1977.8 nm and 1986.9 nm) was

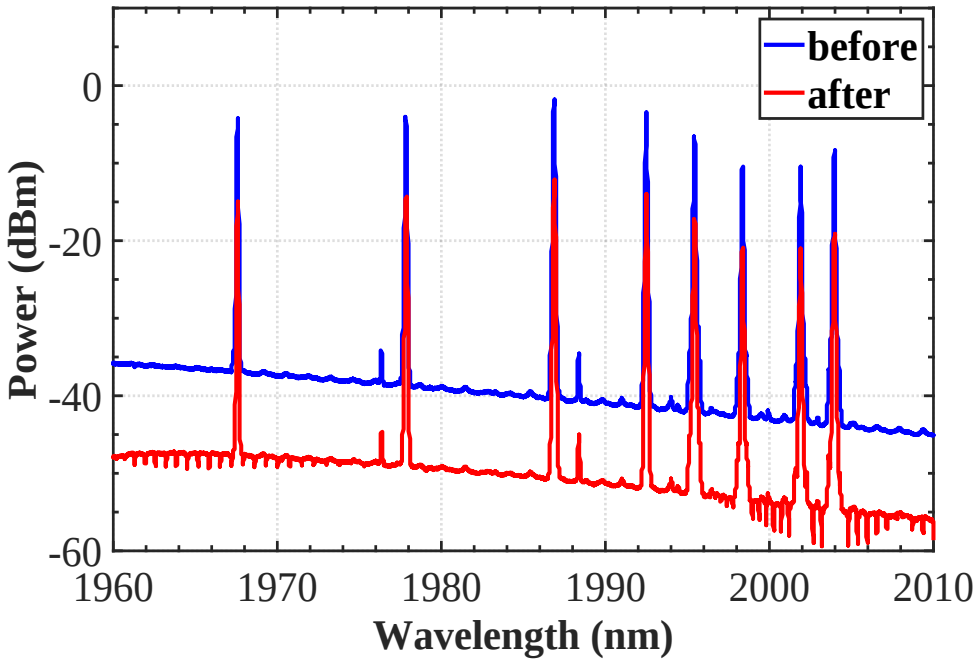


Figure 4.3: Optical spectrum of eight WDM transmitted signals (amplified by a TDFA), before the HC-PBGF (blue) and after transmission over 1.15 km of HC-PBGF (red).

poorer and this is likely due to the slots in the laser not sufficiently selecting a single mode in the Fabry-Pérot cavity (as per Section 2.3.1). The gain of the TDFA reduces at longer wavelengths and this roll-off can be seen by the downward slant of the spectrum floor in Figure 4.3 [130].

The eight WDM channels were then transmitted over 1.15 km of HC-PBGF, nearly four times further than the previous maximum transmission distance of 290 m reported in references: [123], [83], [125], [96]. The spectrum after transmission can also be seen in Figure 4.3. The details of the HC-PBGF used are given in Table 4.3 [130], [126]. The difference in the attenuation loss versus the insertion loss values in this table can be attributed to mode mismatch between the HC-PBGF and the spliced SMF/buffer fibre for standardised connection with other components [137], [126].

Another source of loss in the HC-PBGF transmission medium is due to atmospheric contamination within the fibre. Small amounts of carbon dioxide (CO_2) and water vapour (H_2O) can contaminate the hollow core of the fibre, especially in a lab environment which is not sealed and solely controlled with air conditioning (as was the case for the experiments in this thesis). This contamination can either be removed (by purging the fibre with dry gas) or

Table 4.3: HC-PBGF details, as per reference: [100].

Description	Details
Type	HC-PBGF
Design	19-cell core
Length	1.15 km
3 dB bandwidth	85 nm
Min. attenuation	2.8 dB/km (at 1990 nm)
Total insertion loss	11.5 dB (at 1987 nm)

avoided (by tuning the wavelengths of the WDM channels not to overlap with the discrete loss peaks, in this case no more than 0.4 nm tuning was required). The red line in Figure 4.3 shows the spectrum of the eight channels after transmission, in comparison to before transmission (which is shown in blue). The power difference between these spectra illustrates the excess loss due to transmission in this case. The absorption features of CO_2 and H_2O are characterised by the narrow dips that can be seen in the spectrum after transmission [126], [138], [139].

4.1.3 WDM receiver

The implementation of WDM systems for optical communications requires demultiplexing to split the received signal into individual channels (each operating at its own carrier frequency or wavelength). After demultiplexing, these channels are then sent to different receivers for further distribution or analysis, as per Figure 4.1. In the case of the 2 μm WDM receiver, it was not possible to incorporate multiple receivers for the different WDM channels (due to device limitations). Instead, a receiver was designed that could be tuned to demultiplex each incoming WDM signal in turn. The full schematic of the 2 μm WDM system, including the receiver, is shown in Figure 4.4.

The system included an optically pre-amplified receiver (for the first time at 2 μm) by employing a TDFA after the fibre. The purpose of an optical pre-amplifier is to increase the signal level prior to photodetection in order to improve the receiver sensitivity. Therefore, optical pre-amplification is commonly used in optical receivers to amplify low-power signals [109], [110], [4]. Ideally, a pre-amplifier should have a low noise figure and a high gain for optimal receiver performance.

Prior to the pre-amplifying TDFA, a variable attenuator was used to control the input power and hence vary the OSNR to the receiver. The OSNR was

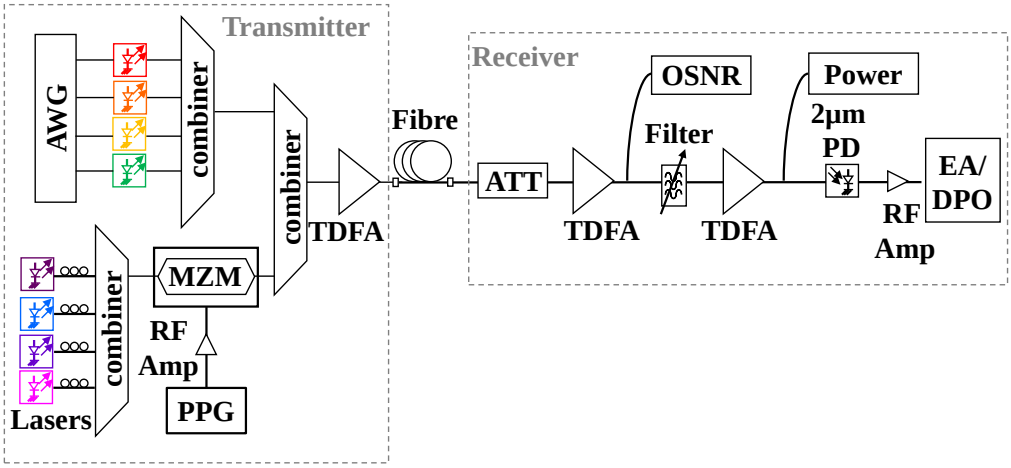


Figure 4.4: 2 μm WDM system schematic with eight channels (four directly modulated and four externally modulated), transmitted over 1.15 km of HC-PBGF.

monitored using a 10% tap which was connected to an OSA. In order to demultiplex the WDM channels at the receiver, a commercial (Agiltron) tunable bandpass filter was used (whereas a Bragg grating filter had been used in previous demonstrations [96], [124]). A bandpass filter transmits (or passes) wavelengths within a certain range (or band) and attenuates other wavelengths outside this range (as per Section 3.3.1). The 3 dB bandwidth and 20 dB bandwidth of such a filter indicates the shape of the filter profile and the width of the wavelength range that it will transmit. These filters are often made to be tunable, such that the central wavelength can be chosen by the user (within a certain range). If several filters are used in series, the passband will get narrower [140]. The 2 μm commercial (Agiltron) tunable bandpass filter used in the experiments in this thesis had 3 dB bandwidth of 1.6 nm and a 20 dB bandwidth of 4.5 nm, as shown by the filter profile in Figure 4.5. In comparison, other 1.55 μm Agiltron tunable bandpass filters have a 3 dB bandwidth of 0.25 nm and a 20 dB bandwidth of 0.75 nm [141], indicating the limitations of technologies in the 2 μm region.

A third TDFA was incorporated to compensate for the reduced gain of the channels between 1900 nm and 2000 nm (due to TDFA gain roll-off). The gain of the two TDFAs in the receiver was measured to be ~26 dB (for the pre-amplifying TDFA) and ~22 dB, respectively. The gain of the final TDFA was adjusted to ensure that the total optical power to the PD was constant for all WDM channels and OSNR values. It is important that the power into the receiver PD should be consistent for all conditions in order to ensure that it is

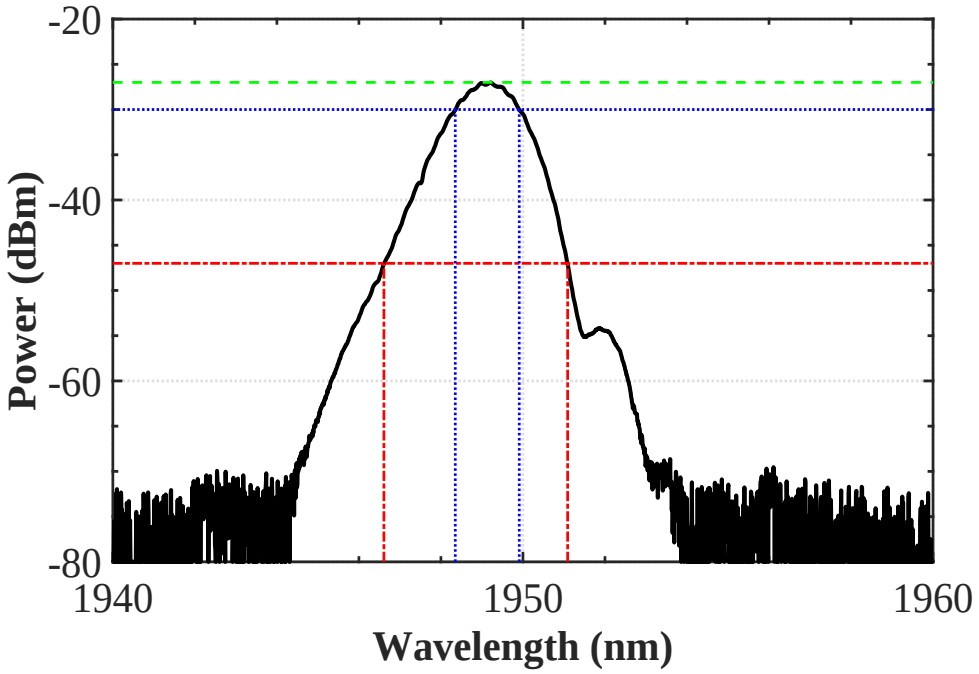
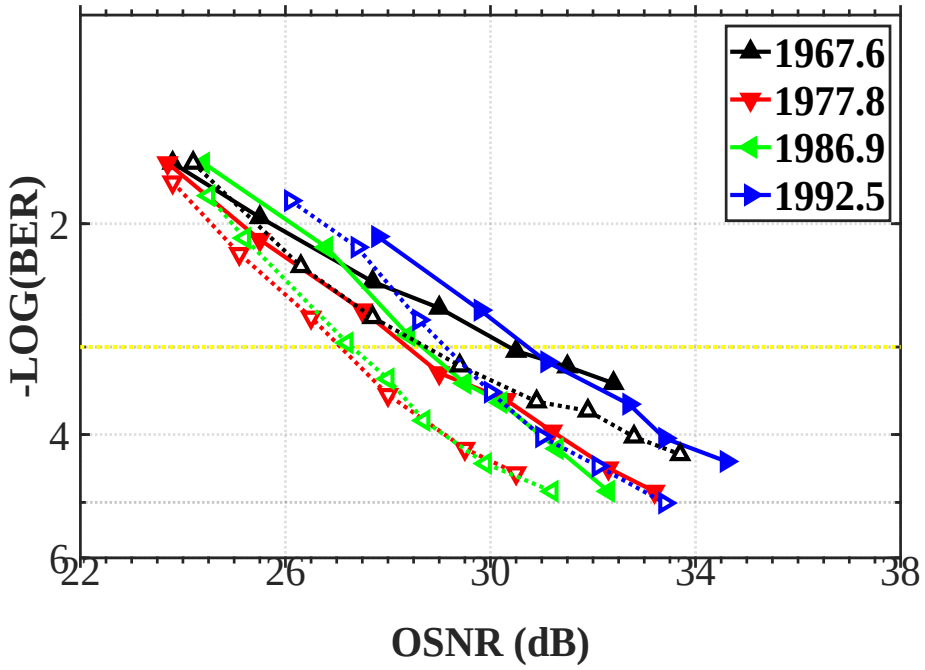
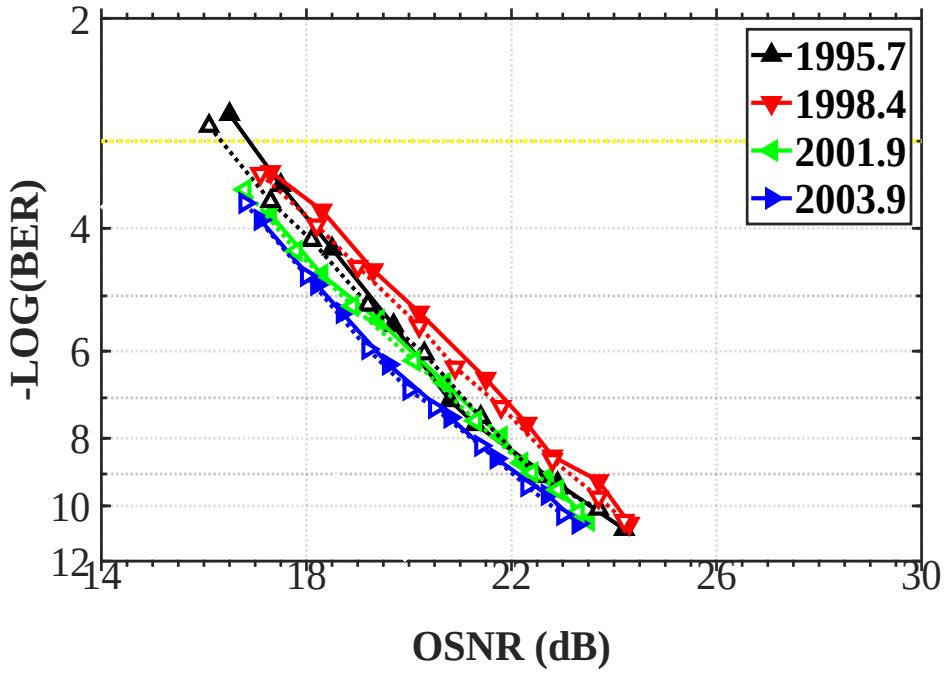


Figure 4.5: Tunable bandpass filter profile (characterised with ASE), with a 3 dB bandwidth of 1.6 nm (blue dotted lines) and a 20 dB bandwidth of 4.5 nm (red dash dotted lines).

the performance of the WDM system that is being characterised, independent of the detector performance. This fixed power level to the PD was monitored using a 10% tap which was connected to a low-speed (DC to 15 MHz) InGaAs PD (Thorlabs PDA10DT) and a 60 MHz oscilloscope (1 GS/s Tektronix TDS 1002). The oscilloscope recorded the input power in voltage, which could then be converted to dBm. In this way, the attenuator and power meter configuration enabled power monitoring and control to ensure that the power to the PD was fixed for different conditions of systems testing. In this experiment, the power level was fixed at -2 dBm for optimal performance considering the constraints of the system. Finally, the PD electrical signal was amplified and analysed with a 16 GHz, 100 GS/s digital phosphor oscilloscope (DPO), or an error detector (ED) depending on the channel measured [130]. The sampled data was then processed off-line and recovered using Matlab-based digital signal-processing (DSP) techniques [136].



(a) 4 x 8.3 Gbit/s 4ASK fast-OFDM directly modulated.



(b) 4 x 12.5 Gbit/s NRZ-OOK externally modulated.

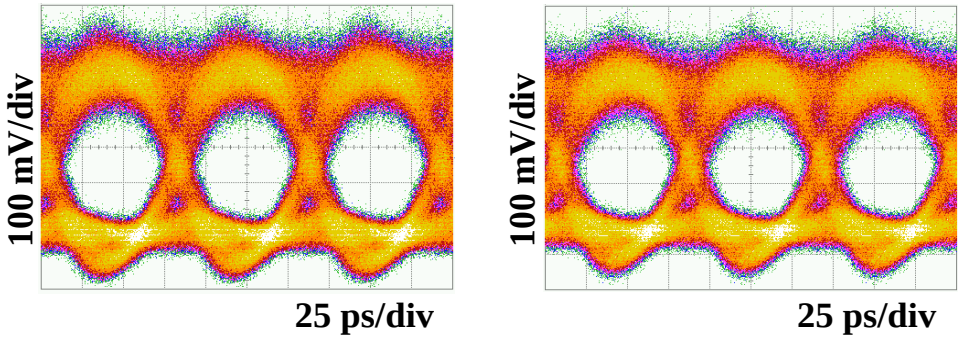
Figure 4.6: BER vs. OSNR for 81 Gbit/s 2 μm WDM system at back-to-back (open symbols, dashed lines) and after transmission over 1.15 km of HC-PBGF (closed symbols, solid lines). Yellow dotted line BER = 1×10^{-3}.

4.2 81 Gbit/s WDM at 2 μm

As per Section 3.2, the performance of an optical communication system is typically tested by analysing the BER with respect to the received optical power, via the OSNR, as well as the OSNR penalties after fibre transmission. The performance of the 2 μm system was analysed both at back-to-back (B2B, i.e. direct from transmitter to receiver with no fibre) and after transmission (over 1.15 km of HC-PBGF). OSNR values were measured using an OSA, with a 0.1 nm bandwidth. Transmission penalties were calculated at a BER of 1×10^{-3} (FEC limit) for directly modulated channels, and at BER of 1×10^{-9} for externally modulated channels.

Figure 4.6a shows the BER vs. OSNR performance for the four directly modulated channels (at wavelengths 1967.6 nm, 1977.8 nm, 1986.9 nm and 1992.5 nm). These lasers were directly modulated using 4ASK fast-OFDM, at a data rate of 8.3 Gbit/s. The open symbols indicate the back-to-back data (with dashed lines as a guide) and closed symbols indicate the data recorded after transmission (with solid lines as a guide). To achieve a BER of 1×10^{-3}, an average OSNR of 29.6 dB was measured after transmission, with a spread in OSNR requirement of 2.3 dB measured between all channels. As an indicator of transmission penalties, this is then compared to the back-to-back scenario. Before transmission, an average OSNR of 28.1 dB was required, with a spread of 2 dB between channels. The OSNR transmission penalty was 1.5 dB in this case. The OSNR spread is likely due to the different frequency responses (S21) for each of the lasers used with direct modulation, with better BER values recorded for those with larger bandwidths.

Figure 4.6b shows the performance of the four externally modulated channels. These lasers were modulated using a MZM at a data rate of 12.5 Gbit/s. In this case, an average OSNR of 22.7 dB was recorded to achieve a BER of 1×10^{-9}, with a spread in OSNR requirement of 1.3 dB measured between channels. The OSNR spread is likely due to the TDFA gain roll-off, as per Section 4.1.2. For all four externally modulated channels, the transmission power penalty was found to be negligible (<0.3 dB) over the HC-PBGF. In terms of comparison, one of the key differences between NRZ-OOK and 4ASK fast-OFDM is that 4ASK offers higher (double) spectral efficiency of OOK, thus doubling the data rate if baud rates are the same. 4ASK is a high-level modulation format and transmits 2 bits/symbol. In contrast, OOK has only 1 bit/symbol. Therefore, to deliver the same symbol rate, 4ASK requires more



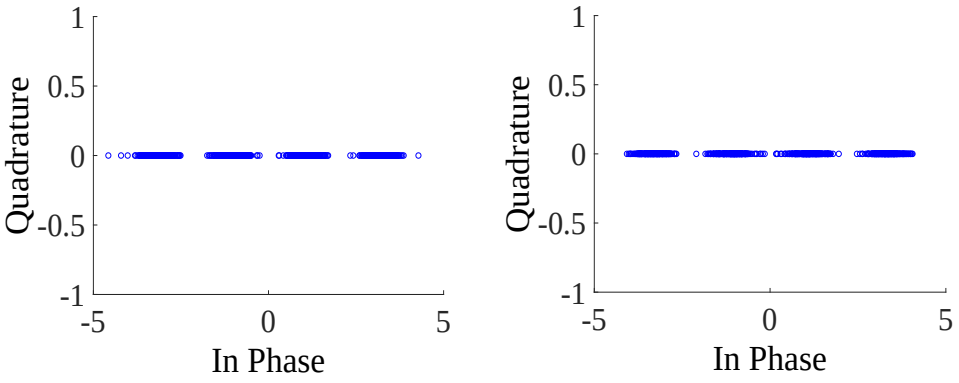
(a) Back-to-back. (b) After transmission.

Figure 4.7: Eye diagram for a 12.5 Gbit/s NRZ-OOK externally modulated channel (at 1998.4 nm, OSNR 24 dB).

than double the power of OOK. In turn, to achieve the same BER, 4ASK requires more than double the SNR (>3 dB) of OOK or, for a given OSNR, 4ASK will have worse BER in comparison.

In order to visualise the transmission penalty in another way, consider the eye and constellation diagrams. Figure 4.7 shows the eye diagram for a NRZ-OOK externally modulated channel (1998.4 nm) both at back-to-back (Figure 4.7a) and after transmission (Figure 4.7b). As can be seen by comparing the two, the eye diagram for the externally modulated channel was quite open and remained so after transmission. Figure 4.8 shows the constellation diagram for a 4ASK fast-OFDM directly modulated channel (at 1986.9 nm). Despite a transmission power penalty of 1.3 dB recorded for this channel, the constellation diagram was still clear after transmission over 1.15 km of HC-PBGF, showing little distortion after transmission.

In summary, in this section a 2 μm WDM system with total capacity of 81 Gbit/s was presented, which is almost three times greater than previous system capacity records [125]. This total capacity was achieved using four 12.5 Gbit/s NRZ-OOK externally modulated channels and four 7.7 Gbit/s 4ASK fast-OFDM directly modulated channels. These eight WDM channels were transmitted over 1.15 km of HC-PBGF, nearly four times further than previously reported [130].



(a) Back-to-back. (b) After transmission.

Figure 4.8: Constellation diagram for a 4ASK fast-OFDM directly modulated channel (at 1986.9 nm).

4.3 100 Gbit/s WDM at 2 μm

In order to push the system capacity even further, the 2 μm WDM system was optimised, with the goal to achieve 100 Gbit/s. This section will focus on that optimisation process.

4.3.1 Optimisation

The same system design was used with four NRZ-OOK externally modulated channels (at wavelengths 1995.7 nm, 1998.4 nm, 2001.9 nm and 2003.9 nm) and four 4ASK fast-OFDM directly modulated channels (at wavelengths 1967.6 nm, 1977.8 nm, 1986.9 nm and 1992.5 nm). By optimising the laser settings (such as the current and temperature), channel output powers of up to 2 dBm were recorded (in comparison to -1 dBm previously).

For the systems tests, the drive current of the directly modulated channels was optimised in order to guarantee best performance. In order to modulate the lasers with fast-OFDM coding, the modulation depth needs to be maximised, while maintaining the laser response in a linear regime. The current needs to be high enough to allow high power and high modulation depth, but low enough to allow switching. As such, the lasers were characterised in terms of drive current and BER. This was performed at back-to-back (laser + PD), with the bias current varied and the BER recorded for a 1 V 4ASK fast-OFDM signal applied. The result of this characterisation showed better BER performance for bias current below 33 mA at 2.5 Gbaud/s, hence this drive current was chosen for system tests.

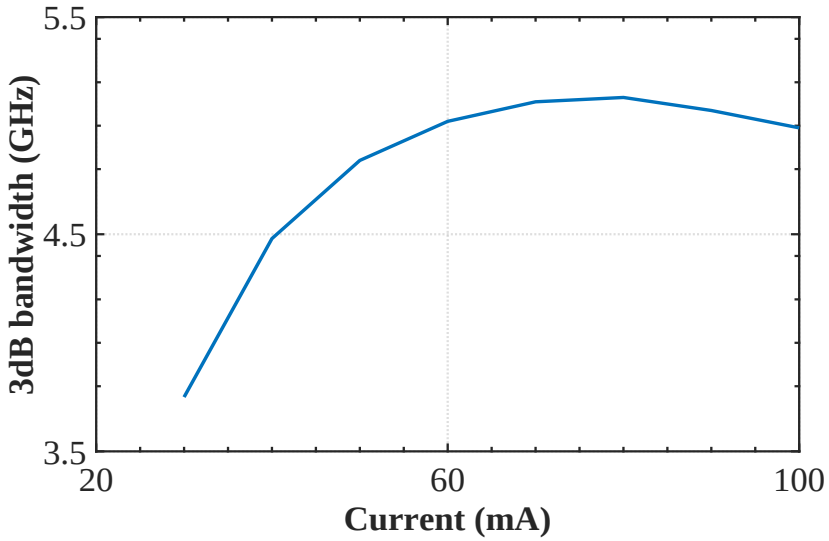


Figure 4.9: 3 dB bandwidth vs. bias current for a directly modulated channel (at 1992.5 nm).

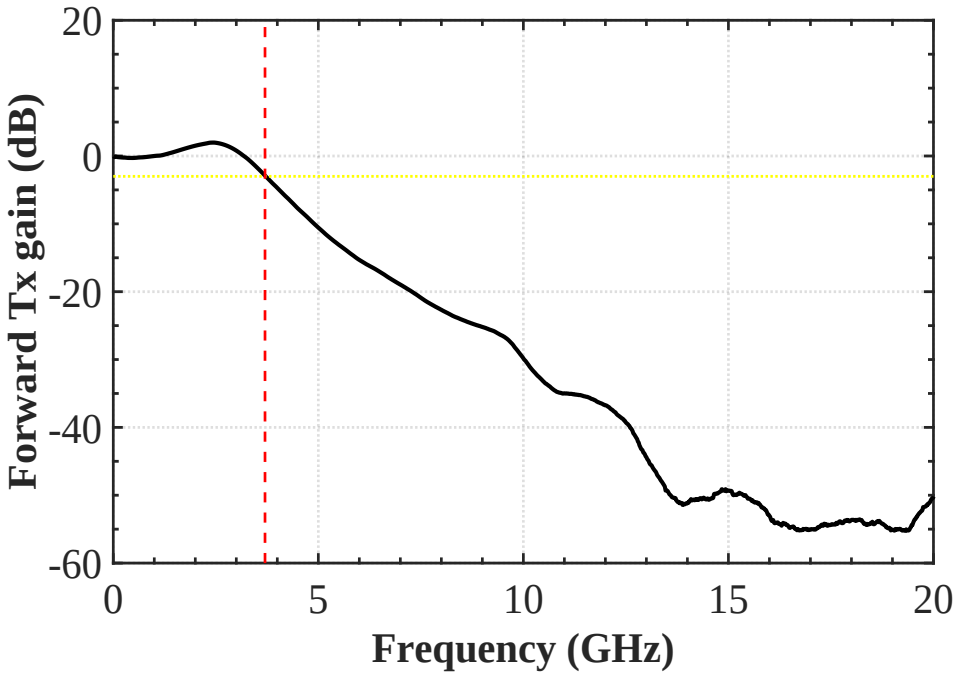


Figure 4.10: Frequency response of a directly modulated channel (at 1992.5 nm) at a bias current of 32.5 mA, with a 2 μm PD. Yellow dotted line = - 3 dB, which corresponds to 3.7 GHz (red dashed line).

Figure 4.9 shows the frequency response measurement for the 1992.5 nm laser. Higher drive currents (up to ~80 mA in this device) corresponded to a

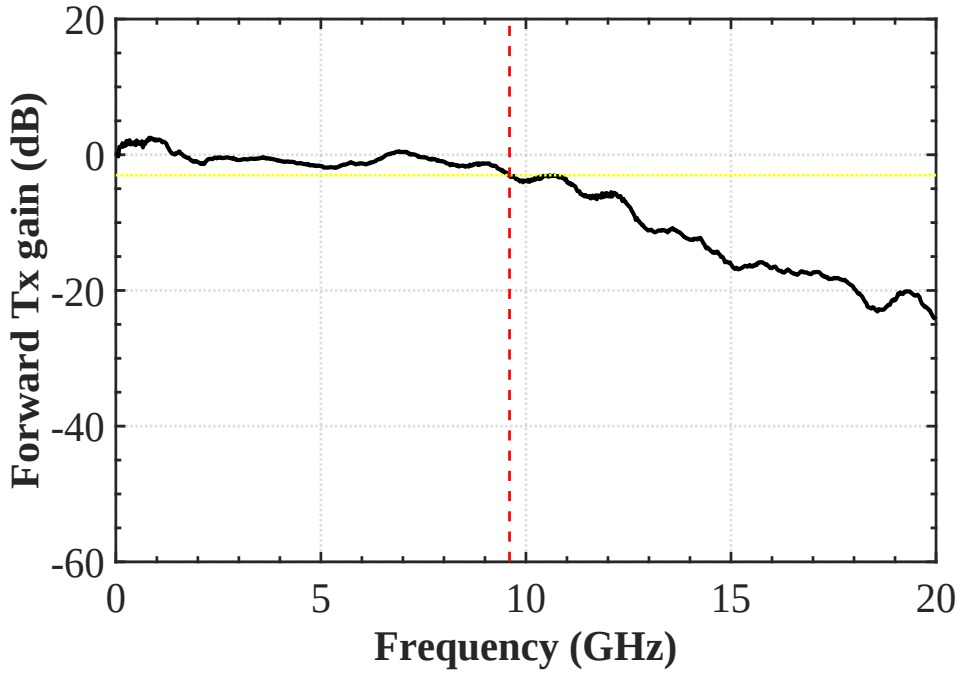


Figure 4.11: Frequency response of a laser (at 1998.4 nm) externally modulated with a MZM at a bias voltage of -5.3 V and measured with a 2 μm PD. Yellow dotted line = - 3 dB, which corresponds to 9.6 GHz (red dashed line).

greater 3 dB bandwidth, with results of >5 GHz recorded. However, Figure 4.10 shows the frequency response for the same laser (1992.5 nm), this time at a fixed bias point current of 32.5 mA, with guidelines indicating that the -3 dB point corresponds to 3.7 GHz. The 3 dB bandwidth of the other directly modulated lasers was similar at this current. In terms of the externally modulated channels, the data rate was ultimately limited by the combined 3 dB bandwidth of the MZM and PD, which was measured to be ~10 GHz, as shown in Figure 4.11.

4.3.2 SCF transmission

The system design was the same as shown in Figure 4.4. Two types of transmission media were tested in this experiment: 1.15 km of HC-PBGF and 1 km of solid-core fibre (SCF) designed (by OFS Denmark) to have low bend-loss at 2 μm. The details of the SCF fibre (ClearLite1700 20) are given in Table 4.4. The additional loss of SCF in the 2 μm wavelength range (in comparison to HC-PBGF) can be seen in Figure 4.12, which shows the same spectrum as Figure 4.3 but with the SCF transmitted channels overlaid for

Table 4.4: SCF details.

Description	**Details**
Fibre type	SCF (OFC ClearLite 1700 20)
Design	SMF step index
Length	1 km
Attenuation	18 dB/km (at 1985 nm)
Operating Wavelength	1700 nm – 2100 nm

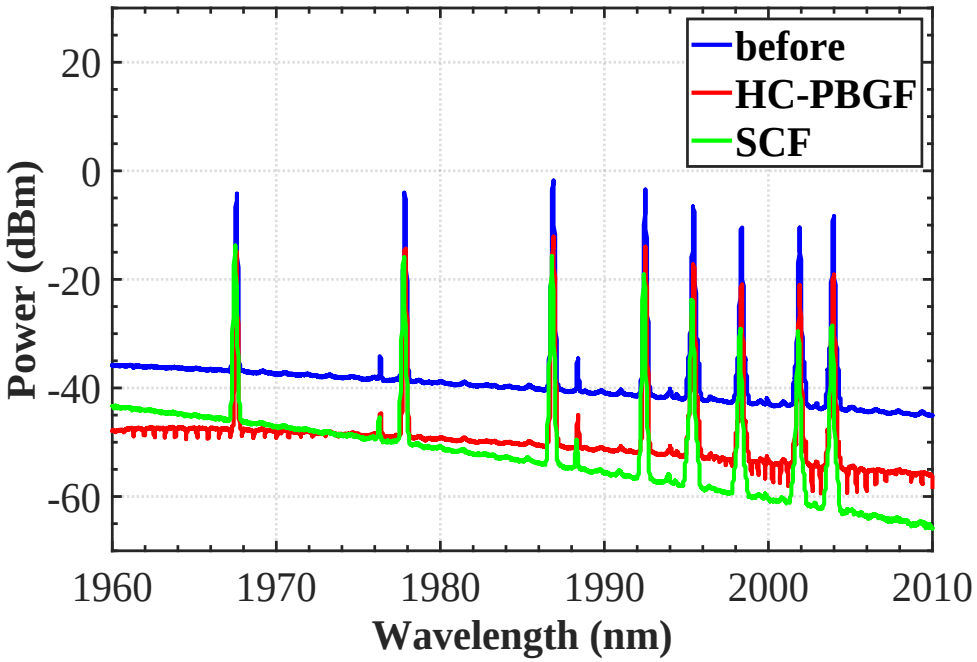


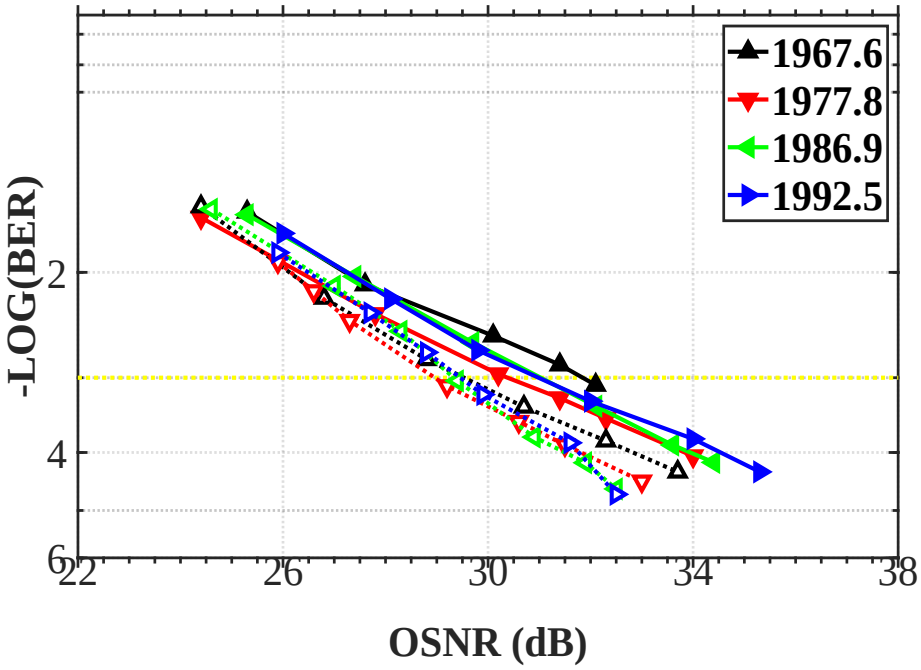
Figure 4.12: Optical spectrum of the eight WDM transmitted signals (amplified by a TDFA) before transmission (blue), after transmission over 1.15 km of HC-PBGF (red), or after transmission over 1 km of SCF (green).

comparison in this case. It is notable that the absorption dips do not appear in the SCF spectrum, further confirming that these can be attributed to contamination in the HC-PBGF.

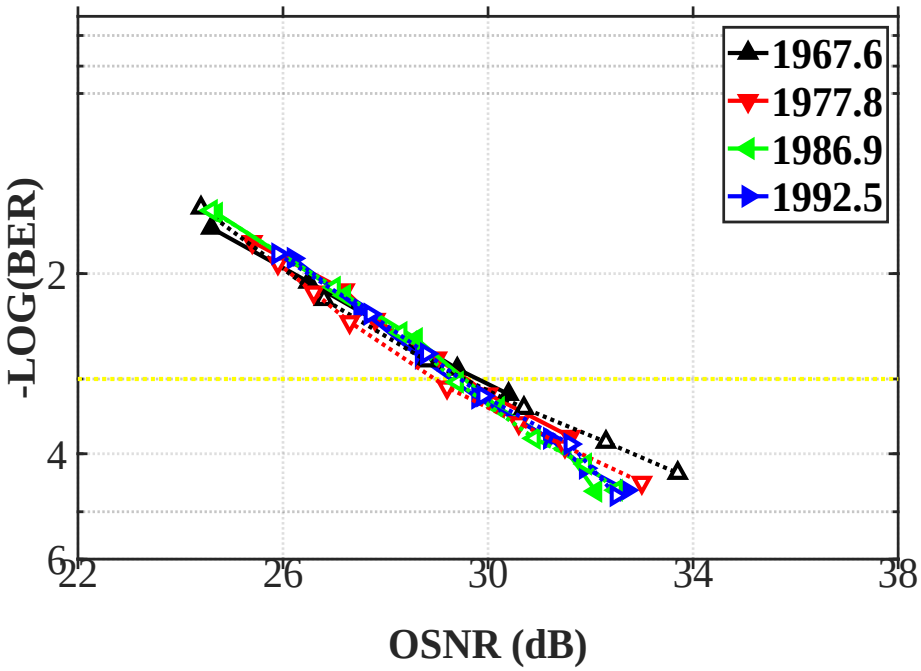
4.3.3 System analysis

The performance of the WDM system was analysed as before, in terms of BER vs. OSNR and transmission penalties (calculated at a BER of 1×10^{-3} for direct modulation and 1×10^{-9} for external modulation).

Figure 4.13 shows the performance of the four directly modulated channels at back-to-back and after transmission over either HC-PBGF (Figure 4.13a) or



(a) 1.15 km HC-PBGF.

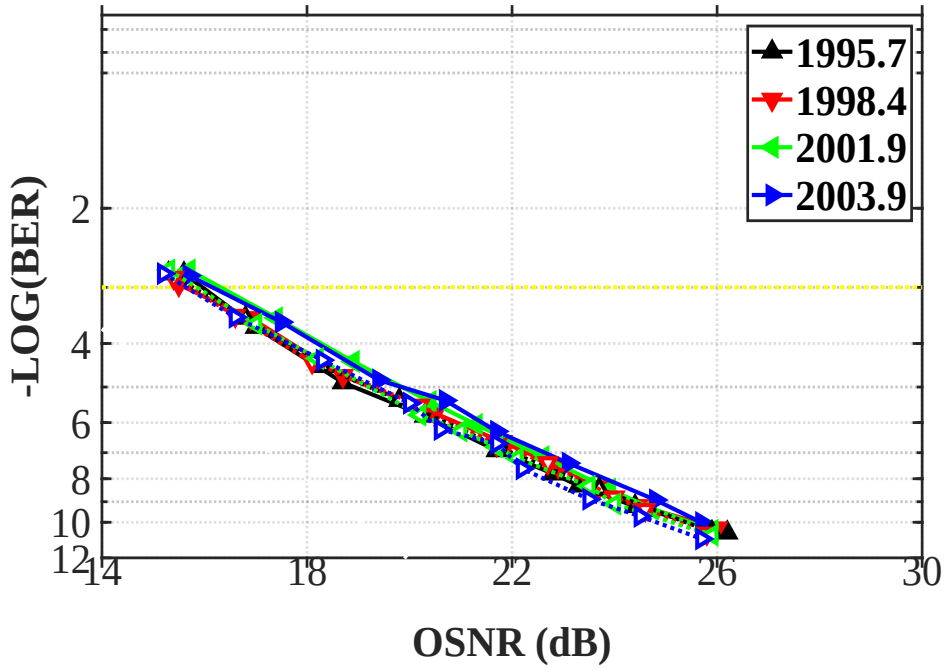


(b) 1 km SCF.

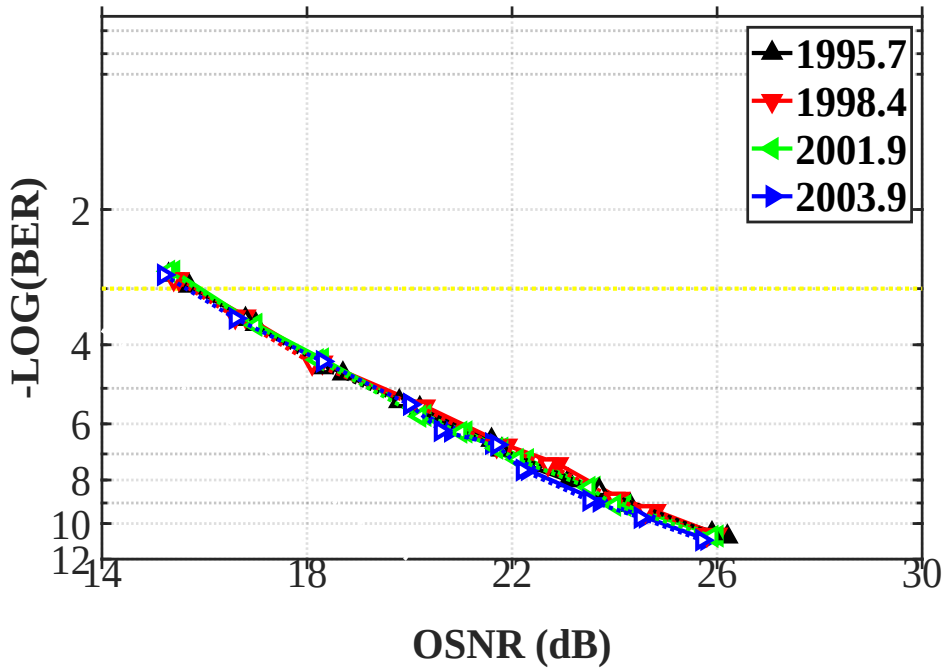
Figure 4.13: BER vs. OSNR for 4 x 9.3 Gbit/s 4ASK fast-OFDM directly modulated channels at B2B (open symbols, dashed lines) and after transmission (closed symbols, solid lines). Yellow dotted line BER = 1×10^{-3}.

SCF (Figure 4.13b). These lasers were directly modulated using 4ASK fast-OFDM, at a data rate of 10 Gbit/s (or 9.3 Gbit/s taking into account 7% FEC overheads) and analysed at a BER of 1×10^{-3}. Before transmission, the average OSNR required to achieve a BER of 1×10^{-3} was 29.3 dB, with a spread in OSNR requirement of 0.7 dB measured between channels. This OSNR requirement is similar to the back-to-back demonstration in the previous section (Section 4.2 in which 28.1 dB average was recorded for the same BER) but the OSNR spread is smaller in this case (0.7 dB, compared to 2.0 dB) perhaps due to optimising the laser settings. For transmission over 1.15 km of HC-PBGF, the average OSNR required to achieve a BER of 1×10^{-3} was measured to be 31.1 dB, with a spread of 1.4 dB. The transmission power penalties varied from 2.2 dB, in this case, to 1.5 dB minimum (average 1.7 dB). These results are similar to the previous demonstration of HC-PBGF transmission (1.5 dB OSNR penalty). For transmission over 1 km of SCF, an average OSNR of 29.6 dB was measured, with a spread of 0.6 dB. It was observed that, while the transmission penalties varied from 1.5 dB to 2.2 dB for HC-PBGF, the maximum transmission power penalty for SCF was measured to be 0.3 dB. As the HC-PBGF is not strictly single-mode, it is possible that the additional penalty may be caused by the asynchronicity between fast-OFDM symbols, which arises from the modal dispersion and mode coupling to higher-order modes in the HC-PBGF [126].

Figure 4.14 shows the performance of the four externally modulated channels, again at back-to-back and after transmission over either HC-PBGF (Figure 4.14a) or SCF (Figure 4.14b). These lasers were modulated using a MZM at a bit rate of 15.7 Gbit/s. Before transmission, the average OSNR required to achieve a BER of 1×10^{-9} was 24.0 dB, again with a spread in OSNR requirement of only 0.7 dB between channels for back-to-back (same as previous HC-PBGF measurement). For transmission over 1.15 km of HC-PBGF, the average OSNR was 24.4 dB, with a spread of 0.8 dB. The maximum transmission power penalty was 0.5 dB, similar to the previous transmission of externally modulated channels over HC-PBGF (in Figure 4.6b). For transmission over 1 km of SCF, the average OSNR requirement was 24.1 dB, with a spread of 0.6 dB. The transmission power penalty was negligible (<0.2 dB). While the BER vs. OSNR performance was slightly better for the SCF compared to HC-PBGF in both cases (direct modulation and external), it is the high loss of SCF at this wavelength region (~18 dB/km) that is the main inhibiting factor.



(a) 1.15 km HC-PBGF.



(b) 1 km SCF.

Figure 4.14: BER vs. OSNR for 4 x 15.7 Gbit/s NRZ-OOK externally modulated channels at B2B (open symbols, dashed lines) and after transmission (closed symbols, solid lines). Yellow dotted line BER = 1×10^{-3}

Chapter summary

The goal of the experiments in this chapter was to increase the capacity of 2 μm WDM systems beyond the previous demonstrated record of 30 Gbit/s [124], [125] in order to further the 2 μm wavelength region for optical communications applications. A total capacity of 100 Gbit/s was achieved using four 9.3 Gbit/s 4ASK fast-OFDM directly modulated channels and four 15.7 Gbit/s NRZ-OOK externally modulated channels. These 2 μm WDM channels (spanning an extended waveband of 36.3 nm) were transmitted over 1.15 km of HC-PBGF (nearly four times further than previous records) and also 1 km of SCF, with error-free performance in both cases. This factor-of-three capacity increase was enabled by improving the system design (for example, doubling the number of WDM channels and implementing a pre-amplified receiver), incorporating improved components (such as lasers and a PD with better frequency response) and optimising the devices throughout the setup to operate at highest-possible data rates. This chapter illustrates the growth in maturity of technologies at 2 μm for optical communications applications. However, within a given bandwidth, the capacity of a WDM system depends on how closely optical channels can be packed in the wavelength domain. Therefore, the next chapter focuses on minimising the channel spacing to implement dense WDM (DWDM) at 2 μm and maximising the spectral efficiency of optical communication systems in this new transmission window.

Chapter publications

1. H. Zhang, **N. Kavanagh**, Z. Li, J. Zhao, N. Ye, Y. Chen, N. V. Wheeler, J. P. Wooler, J. R. Hayes, S. R. Sandoghchi, F. Poletti, M. N. Petrovich, S. U. Alam, R. Phelan, J. O'Carroll, B. Kelly, L. Grüner-Nielsen, D. J. Richardson, B. Corbett, and F. C. Garcia Gunning, **"100 Gbit/s WDM transmission at 2 μm: transmission studies in both low-loss hollow core photonic bandgap fiber and solid core fiber," in Optics Express**, vol. 23, no. 4, pp. 4946–4951, 2015.
doi:10.1364/OE.23.004946

2. H. Zhang, Z. Li, **N. Kavanagh**, J. Zhao, N. Ye, Y. Chen, N. V. Wheeler, J. P. Wooler, J. R. Hayes, S. R. Sandoghchi, F. Poletti, M. N. Petrovich, S. U.

Alam, R. Phelan, J. O'Carroll, B. Kelly, D. J. Richardson, B. Corbett, and F. C. Gunning, **"81 Gb/s WDM transmission at 2 μm over 1.15 km of low-loss hollow core photonic bandgap fiber," at the European Conference on Optical Communication (ECOC)**, pp. 1–3, 2014. doi:10.1109/ECOC.2014.6964083

3. **N. Kavanagh**, H. Zhang, J. Zhao, N. Ye, B. Corbett, and F. C. Garcia Gunning, "**Dense Wavelength Division Multiplexing at 2 μm", at Photonics Ireland**, Cork, Ireland, 2015, Poster.

Technical acknowledgements

The author's contribution to this chapter was the laser characterisation, systems demonstration and all OOK measurements presented. The author would like to acknowledge:

- F. C. Garcia Gunning (Tyndall National Institute, University College Cork) for supervision and technical guidance.
- H. Zhang (Tyndall National Institute, University College Cork) for 2 μm experiment design, frequency response characterisation and 4ASK fast-OFDM measurements.
- J. Zhao and X. Ouyang (Tyndall National Institute, University College Cork) for fast-OFDM and digital signal processing.
- N. Ye and B. Corbett (Tyndall National Institute, University College Cork) for 2 μm semiconductor devices.
- Z. Li, Y. Chen, N. V. Wheeler, J. P. Wooler, J. R. Hayes, S. R. Sandoghchi, F. Poletti, M. N. Petrovich, S. U. Alam and D. J. Richardson (Optoelectronics Research Centre, University of Southampton) for the use of TDFAs, 1.15 km of HC-PBGF tailored to 2 μm, and splicing to SMF.
- R. Phelan, J. O'Carroll and B. Kelly (Eblana Photonics Ltd) for the 2 μm $In_{0.74}Ga_{0.26}As$ slotted Fabry-Pérot lasers.
- L. Grüner-Nielsen (OFS Denmark) for the speciality ClearLite1700 20 SCF with low bend-loss at 2 μm.

Chapter 5

Improving spectral efficiency

In the 1990s, early WDM systems combined four to eight channels at data rates of 2.5 Gbit/s, resulting in total capacities of ~20 Gbit/s. When multiplexed, these channels were spaced ~200 GHz apart, corresponding to spectral efficiency of ~0.0125 (bit/s)/Hz [10]. Over the following decade, WDM systems rapidly advanced to encompass 100 channels at data rates of 10 Gbit/s and total capacities of nearly 1 Tbit/s by the year 2000. These systems had reduced channel spacing to 50 GHz, resulting in spectral efficiency of ~0.2 (bit/s)/Hz. As the optical bandwidth within the 1.55 μm transmission window (primarily dictated by minimum SMF loss and maximum EDFA gain) became increasingly occupied, globally-growing capacity demands required much more efficient utilisation of available bandwidth [10]. By 2010, commercial systems could operate the same number of channels (100), at data rates of 100 Gbit/s and channel spacing of 50 GHz, resulting in spectral efficiency of ~2 (bit/s)/Hz and total capacities in the order of 10 Tbit/s [10].

This global commercialisation of WDM systems in the C-band was made possible due to international workgroups, and agreements between various component and sub-system manufacturers, to set international standards. The ITU Telecommunication Standardization Sector (ITU-T) (one of the three sectors of the International Telecommunication Union (ITU)) develops international technical standards to ensure that these networks and technologies can seamlessly interconnect [6]. In terms of dense WDM (DWDM) applications, recommendation number G.694.1 from the ITU-T defines the frequency grid for DWDM channels. This grid is anchored at 193.1 THz and primarily covers the C to L wavebands (1.53 μm to 1.63 μm).

Currently, DWDM channel spacings are specified in multiples of 12.5 GHz, up to a maximum of 100 GHz. The second edition of this ITU-T recommendation also allows for a flexible DWDM grid [6]. While some DWDM technologies in the C-band are capable of 12.5 GHz spacing, most conventional DWDM systems typically use 40 channels at 100 GHz spacing or 80 channels with 50 GHz frequency spacing [110].

$$\frac{\Delta\lambda}{\Delta\nu} = \frac{\lambda^2}{c} \tag{5.1}$$

Conversion between frequency and wavelength separation can be calculated via Equation 5.1, where $\Delta\lambda$ = wavelength spacing, $\Delta\nu$ = frequency spacing, c = speed of light in vacuum and λ is the wavelength of choice. While 100 GHz corresponds to ~0.80 nm at λ = 1.55 μm, the same wavelength spacing (0.80 nm) at 2 μm corresponds to ~60 GHz in the frequency domain. It was one of the goals of this thesis work to replicate current DWDM channel spacing standards, with the ultimate aim of increasing system capacity at 2 μm and improving spectral efficiency. Therefore, this chapter focuses on the design, implementation and analysis of a 2 μm DWDM system with channel spacing determined by the ITU-T standards, i.e. 100 GHz and, subsequently, 50 GHz DWDM.

5.1 DWDM system design

This section addresses the design of a 100 GHz DWDM system at 2 μm in terms of challenges, improved methods to multiplex (mux) and demultiplex (demux) the DWDM channels, and an in-depth power budget.

5.1.1 Challenges

As discussed previously, high-quality, commercial-grade lasers are not widely available at 2 μm. Therefore, in conjunction with MODEGAP partners, Eblana Photonics, new lasers were developed specifically for the purpose of this DWDM demonstration. Following the convention adopted in Chapter 4, the set of lasers listed in Table 5.1 is referred to as the 'third generation' of slotted Fabry-Pérot lasers at 2 μm. These lasers were designed with the goal of denser ~0.5 nm spacing between adjacent laser wavelengths, in comparison to previous generations. However, as can be seen from Table 5.1, the emission

Table 5.1: Third generation of 2 μm lasers (at 25°C and 60 mA).

Module S/N	**Centre λ**
-	***(nm)***
YE2263	1990.00
YE2258	1990.68
YE2261	1992.00
YE2259	1992.16
YE2262	1992.28
YE2260	1992.48
YE2272	1993.08
YE2274	1993.48
YE2271	1994.64
YE2269	1994.76
YE2273	1995.00
YE2270	1995.08
YE2264	1996.92
YE2268	1997.00
YE2266	1998.36
YE2265	1998.44
YE2267	1998.80

wavelengths of these lasers were not regularly spaced. Therefore, the lasers were fully characterised in order to select the devices that were best suited for a 100 GHz demonstration in terms of optimal emission wavelength (determined by the 100 GHz grid), peak power, and OSNR.

The emission wavelength of a laser can be tuned primarily via the temperature and fine-tuned via the drive current. Typical values for temperature tuning coefficients are ~0.4 nm/°C for 1.55 μm devices [142]. The tunability of the 2 μm slotted Fabry-Pérot lasers was ~0.1 nm/°C, with a typical tuning range of 2 nm, as per reference: [25]. However, when the temperature of the lasers was changed, the output power of the device was also affected, as increasing temperature resulted in decreasing the output power of the laser. On the other hand, the power could be increased by raising the current, but this also affects the emission wavelength and the maximum current was capped at 100 mA for this set of devices (as per manufacturer recommendation). Therefore, achieving the desired emission wavelengths (with 100 GHz spacing between channels) while also optimising the OSNR and maintaining uniform power-per-channel proved a challenging balance. Taking into account the available lasers and respective tuning ranges, an approximate 100 GHz channel grid was designed at 2 μm. This grid is listed in Table 5.2.

Table 5.2: 2 μm DWDM ~100 GHz grid.

Module S/N	λ	$\Delta\lambda$	$\Delta\nu$
-	*nm*	*nm*	*GHz*
YE2263	1989.35	-	-
YE2259	1990.60	1.25	93.75
YE2272	1992.00	1.40	105.00
YE2271	1993.32	1.32	99.00
YE2270	1994.65	1.33	99.75
YE2268	1996.00	1.35	101.25
YE2267	1997.33	1.33	99.75

5.1.2 Mux and demux methods

In a DWDM transmitter, the channels must be multiplexed before being launched into the optical fibre. In previous 2 μm system demonstrations, optical fibre couplers were used to multiplex the channels, with an average loss of 4 dB per channel. Scaling to further channels using such couplers was non-viable due to the additional loss per channel. For example, to multiplex two channels, a standard 2:1 coupler would introduce a minimum of 3 dB loss per channel. To multiplex four channels another 2:1 coupler would be needed, this would then add up to 6 dB loss and so on. Previously, this restricted the number of channels that could be implemented in the 2 μm transmitter. As an alternative to using fibre couplers, a multi-channel Arrayed Waveguide Grating (AWGr) can be used to multiplex the DWDM channels. This experiment marked the first time an AWGr was implemented in a 2 μm optical communication system.

An arrayed waveguide grating is commonly used as an optical multiplexer/demultiplexer in WDM systems. It consists of two multi-port couplers connected by a large number (or array) of waveguides. The key elements of an AWGr are indicated in Figure 5.1: (1) an optical fibre input channel, (2) an input coupler, (3) an array of waveguides (or grating), (4) an output coupler and (5) a set of output channels. The grating consists of an array of waveguides with different lengths. The length of these waveguides is chosen such that the optical path-length difference between adjacent waveguides is equal to an integer multiple of the transmission wavelength, as this results in constructive interference (as per Section 3.1.3). By manipulating this interference pattern, light of different wavelengths can be focused onto the different output channels. In this way, an AWGr can be used in the receiver as a demultiplexer to separate individual channels with different wavelengths

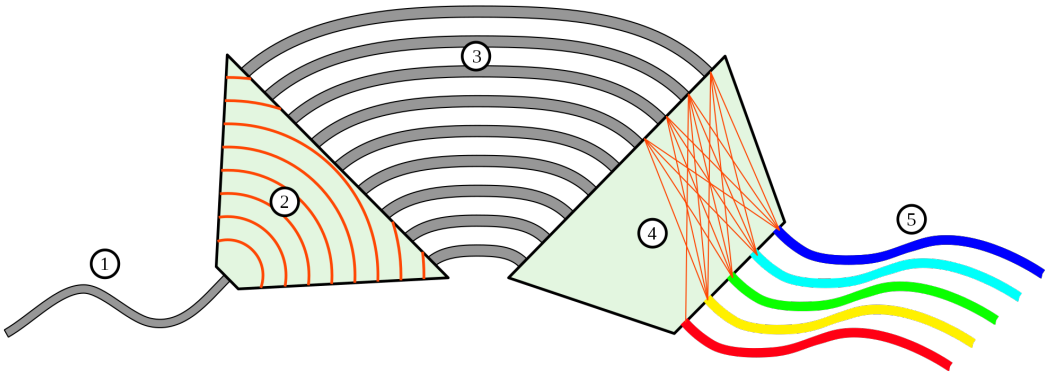


Figure 5.1: An AWGr consists of two multi-port couplers ((2) and (4)) which are connected by a waveguide array (3). It can be used as a demultiplexer (path (1) to (5)) or a multiplexer (path (5) to (1)). *This file is licensed under the Creative Commons Attribution-Share Alike 3.0 Unported license.*

(in which case the light follows the path from (1) to (5) in Figure 5.1), or vice versa, the AWGr can be used in the transmitter to multiplex channels of several wavelengths onto a single optical fibre (light path from (5) to (1) in Figure 5.1) [143], [109], [110].

An InGaAsP/InP-based AWGr was developed in collaboration with the device integration and packaging teams at Tyndall National Institute [100], [38]. A 20-channel cyclical AWGr was designed, with the precise 100 GHz wavelength spacing required for a DWDM demonstration at 2 μm. The AWGr chip was packaged in a housing with a single-channel lensed fibre input and a 10-channel fibre output array (with speciality ClearLite 1700 20 fibre from OFS used). The fibre-packaged sub-assembly was then enclosed in a metal casing, which included an integrated Peltier device for temperature control. As the specifics of the AWGr design, fabrication and packaging was not the focus of this thesis, more details can be found in references: [100], [38].

The most important performance parameters for an AWGr in an optical communication system are the insertion loss, crosstalk and temperature dependence. In terms of the loss, the dominant loss contribution in the 2 μm AWGr originated from coupling losses at the input and output (due to the mode mismatch between the optical fibre and the InP-based AWGr) which resulted in a high insertion loss of $\sim$18 dB per channel on average (compared to $<$5 dB typical for AWGrs at 1.55 μm). This coupling loss could be reduced by using optical mode converters on the AWGr chip, which would improve the total loss of the fibre coupled device. Also, during the design process, the bend loss was overestimated, leading to a larger device and greater waveguide

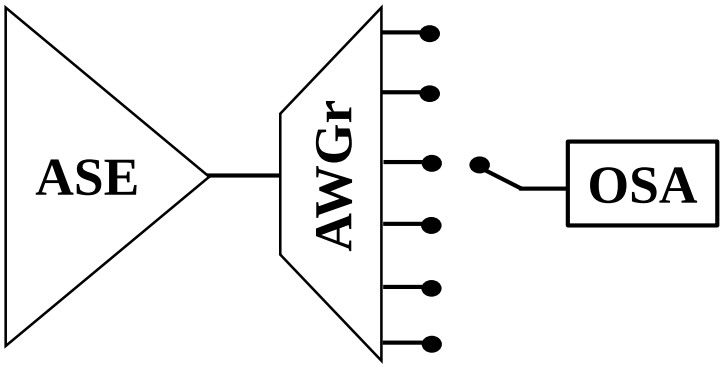


Figure 5.2: AWGr characterisation setup.

losses [100]. Another important parameter to consider when designing WDM systems is crosstalk. As discussed in Section 3.3.1, the term 'crosstalk' is used to describe the transfer of power from one channel to another, usually within a specified bandwidth (for example, 100 GHz). Counter-intuitively, crosstalk is defined in such a way that higher values of crosstalk are preferable (corresponding to higher channel isolation), with 'good' devices demonstrating crosstalk >35 dB [143], [109], [110]. In the case of the 2 μm AWGr, limited crosstalk of ~18 dB was measured between channels. These limited performance parameters indicate some of the challenges associated with implementing first-generation devices in to DWDM systems at 2 μm.

The main effect of temperature dependence in an AWGr is a shift in the emission wavelength. Typically, InP-based AWGrs have a temperature dependence in the order of 0.12 nm/°C (so they can be tuned over a wavelength range of a few nanometres with a temperature change of 30°C to 40°C) [143]. In order to optimise the multiplexing, the 2 μm AWGr was thermally tuned to best match the 100 GHz frequency grid. A thermo-electric cooler (TEC) was used to adjust the wavelengths of the AWGr channels. In order to characterise the spectral response of the AWGr, the ASE of a TDFA was used as a broadband source. ASE was launched into the AWGr and the output spectrum was measured with an OSA, as per Figure 5.2. Figure 5.3 shows the spectrum of the DWDM channels (black trace) with the resulting spectra of the AWGr overlaid. The traces of different colours in this figure correspond to the different AWGr channels (channels 3 to 8). Note that the symbol markers along the curves in this figure do not represent data points measured, they are only included as an additional distinguishing factor between the different colour traces. Through this characterisation process, a thermal dependence of 0.108 nm/°C was recorded and it was determined that

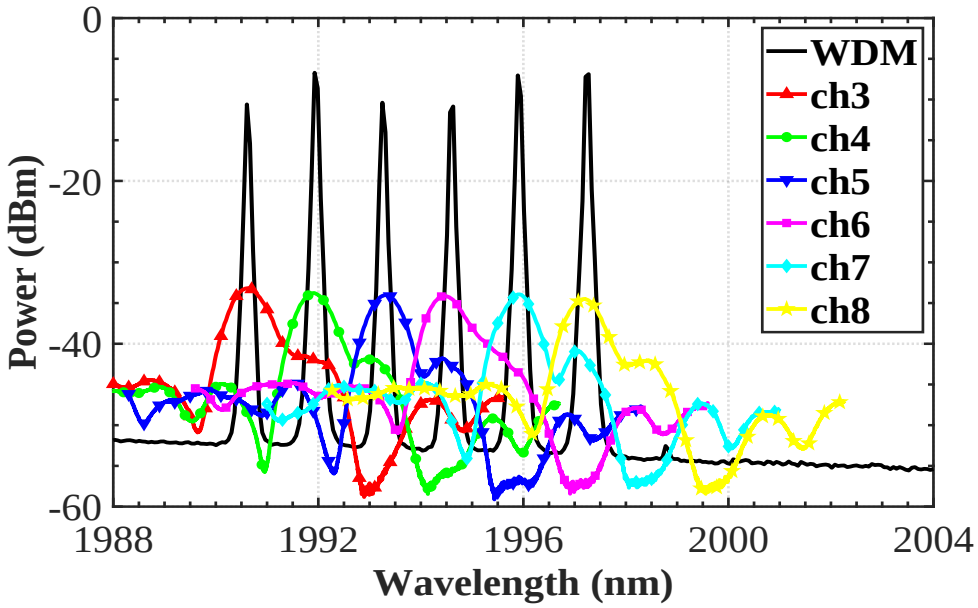


Figure 5.3: Thermal characterisation of the transmitter AWGr, with channels 3 to 8 fixed at 25.6°C. Black trace shows the DWDM transmitter spectrum. (0.05 nm resolution, 3334 sampling points, 10 nm span).

a temperature of 25.6°C gave the best alignment with the DWDM channels. In this case, best alignment was determined by matching the AWGr channel peak (from ASE) with the DWDM channel peak (from the lasers). In this way, the thermal characterisation of the AWGr was fine-tuned and temperature dependence was strictly maintained to best match with all the DWDM channels.

Of course, multiplexing channels that are more closely spaced in the transmitter requires improved demultiplexing techniques at the receiver to sufficiently filter each DWDM channel for testing and this is not trivial at 2 μm. Previously, to demonstrate WDM at 2 μm, channel selection was performed via a tunable bandpass filter which had a 3 dB bandwidth of ~1.6 nm (discussed in Section 4.1.3). However, since 100 GHz corresponds to ~1.33 nm at λ = 2 μm, this filter was not sufficient for this DWDM demonstration (Section 5.3.3 will cover this in more detail). To improve channel isolation in the 2 μm 100 GHz receiver, the tunable bandpass filter was used in conjunction with another AWGr (from the same batch as the transmitter AWGr). While the AWGr had adjacent-channel crosstalk of ~18 dB, cascading both devices enabled improved channel isolation and increased OSNR at the receiver PD (in comparison to using the bandpass filter only). With this cascading

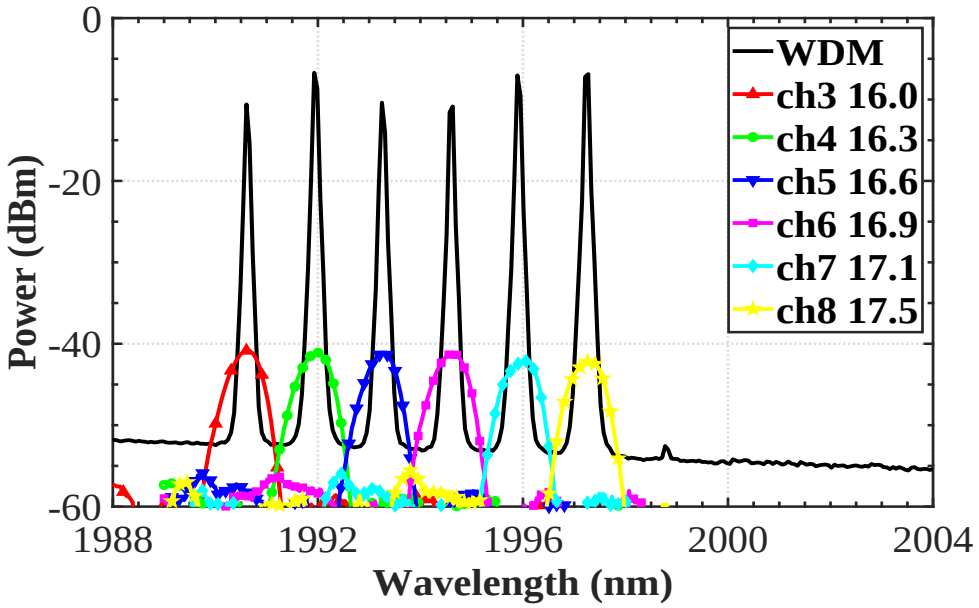


Figure 5.4: Thermal characterisation of the receiver AWGr (overlaid with the transmitted WDM spectrum, in black) with each channel tuned from from 16.0°C to 17.5°C to maximise demultiplexing (0.05 nm resolution, 3334 sampling points, 10 nm span).

configuration, channel isolation was measured to be ~26 dB, closer to typical DWDM demultiplexing standards at 1.55 μm (~35 dB) [143], [109], [110].

The receiver AWGr was thermally tuned to ensure optimal demultiplexing for each of the DWDM channels. The setup for the thermal characterisation was the same as that for the transmitter AWGr (Figure 5.2). In Figure 5.4, the black line depicts the DWDM wavelengths, separated by 100 GHz. Each coloured line represents adjacent channels of the AWGr output array, set at different temperatures (ranging from 16.0°C for channel 3 to 17.5°C for channel 8). Note that the symbol markers along the curves in this figure do not represent data points measured, they are only included as an additional distinguishing factor between the different colour traces. By adjusting the temperature for each channel, the AWGr was accurately aligned with the desired DWDM channel to optimise demultiplexing at the receiver. This AWGr was first implemented in reference: [100], with the receiver comprising the bandpass filter, followed by the AWGr. This receiver configuration was later modified to optimise the OSNR at the receiver PD. It was found that placing the AWGr before the bandpass filter resulted in OSNR values that were improved by ~3 dB (compared to the reverse configuration). In this way, the AWGr was used to demultiplex the 100 GHz DWDM channels and the tunable

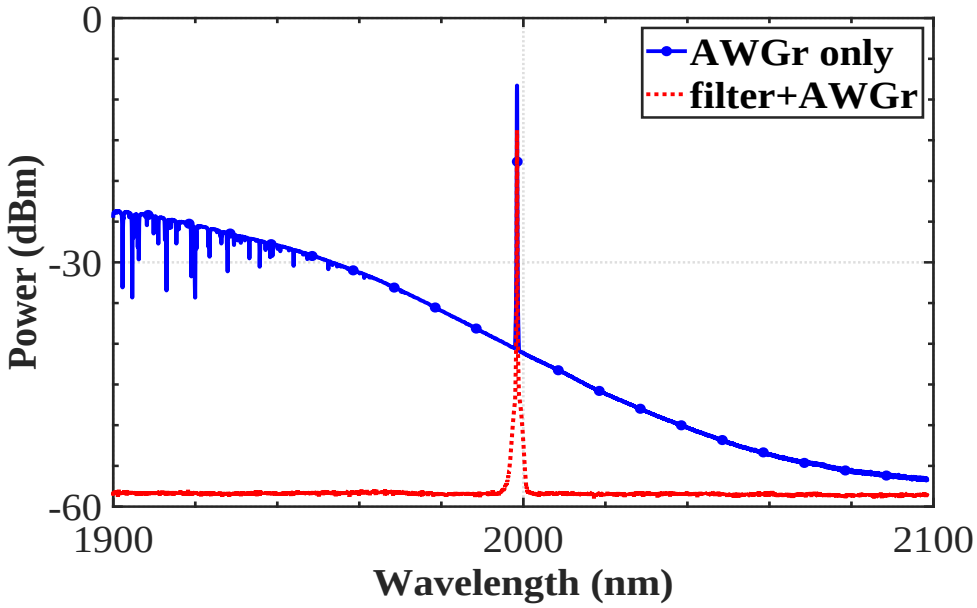


Figure 5.5: Optical spectrum for a single channel (at the end of the receiver) comparing (i) the AWGr only (blue) to (ii) cascading both the AWGr and tunable bandpass filter (red) (0.05 nm resolution, 10000 sampling points, 200 nm span).

bandpass filter was used to remove the out-of-band ASE, as can be seen in Figure 5.5. Note that the symbol markers along the blue curve in this figure do not represent data points measured, they are only included as an additional distinguishing factor between the different colour traces.

5.1.3 Power budget

In order to implement high-capacity 100 GHz DWDM at 2 μm, an improved system needed to be designed, chiefly from a power budget perspective. The purpose of an optical power budget is to ensure that adequate signal strength will reach the receiver to achieve reliable performance over time. In an ideal system (assuming no margin and no additional gain) the power required from the transmitter can be calculated as the power required at the detector minus the loss of the transmission medium. The total loss of the 1.15 km of HC-PBGF in this case (including the ~3.2 dB fibre attenuation and all splice losses) was measured to be ~9.2 dB at 2 μm [100]. However, most DWDM systems are non-ideal and will consist of various optical sources and amplifiers, as well as several loss-producing mechanisms beyond the fibre, such as bend losses, splice losses, and connector losses. Therefore, with the aim of ensuring

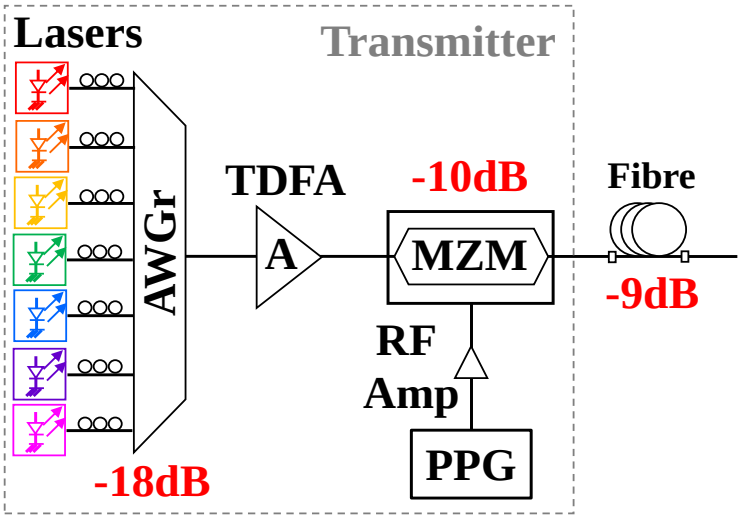


Figure 5.6: Power budget schematic for the DWDM transmitter.

sufficient optical power at the receiver, it is necessary to evaluate all sources of loss and gain when considering the power budget of an optical communication system. Calculating the power budget is the focus of this section.

Transmitter

The transmitter had many configurations (as listed in reference: [38]), but ultimately the transmitter comprised (i) the DWDM channels, (ii) an AWGr multiplexer, (iii) a MZM, and (iv) an amplifier. Considering the DWDM channels first, the output power of the available lasers was low at ~2 dBm (~1.6 mW) on average, whereas lasers with ~20 dBm (~100 mW) power are available at 1.55 μm [144]. The challenge of low-power lasers was then compounded by subsequent high-loss components in the system. As discussed in the previous Section 5.1.2, the channels were multiplexed using an AWGr which introduced a high insertion loss of ~18 dB per channel. The DWDM channels were then externally modulated using a commercial MZM (Photline MX2000LN-10 MZM). In this case, the MZM was measured to have a loss of ~10 dB. To compensate, a TDFA (with maximum gain ~15 dB and noise figure ~8 dB) was introduced to compensate for the transmitter losses and pre-compensate for the fibre losses. The dynamics of the amplifier differ depending on the input power and it was found that adding the amplifier (TDFA) before the modulator (MZM) resulted in an OSNR improvement of ~3 dB (in comparison to the reverse configuration), this comparison between the two configurations for a single channel can be seen in Figure 5.7. Note

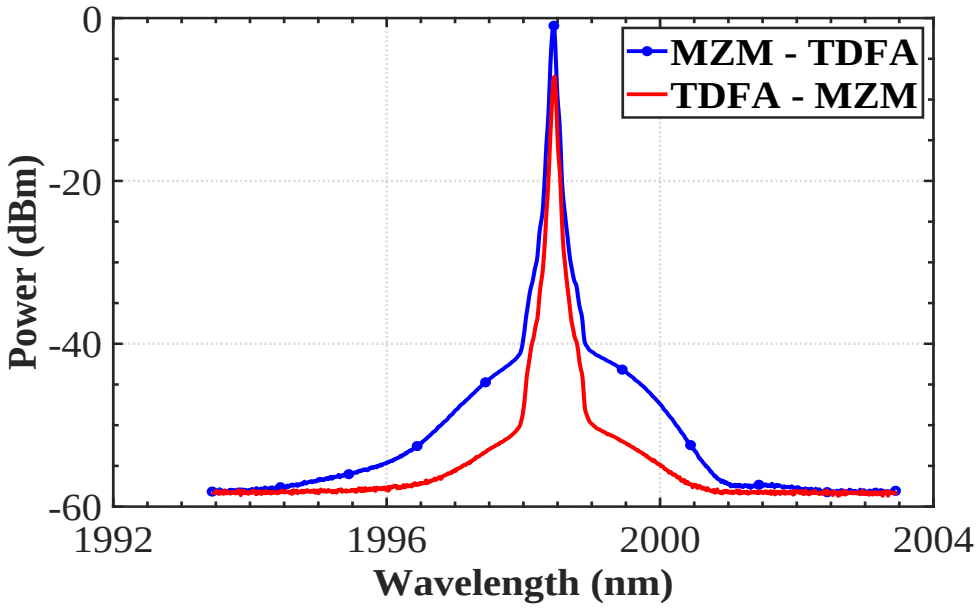


Figure 5.7: Optical spectrum for a single channel with (i) the modulator followed by the amplifier (blue dotted line), compared to (ii) the reverse configuration (amplifier then modulator, red line) (0.05 nm resolution, 1001 sampling points, 10 nm span).

that the symbol markers along the blue curve in this figure do not represent data points measured, they are only included as an additional distinguishing factor between the different colour traces. The final configuration of the transmitter consisted of (i) the DWDM channels (+2 dBm), (ii) an AWGr multiplexer (-18 dB), (iii) a TDFA (+15 dB) and (iv) a MZM (-10 dB), as shown in Figure 5.6, resulting in an optical power of ~ -11 dBm output from the transmitter.

As per Section 3.2, the performance of a DWDM system is typically tested by analysing the BER vs. OSNR measurements. In this process, the power into the receiver PD should be consistent for all conditions. Fixing the power level in this way is necessary to ensure that it is the performance of the system being characterised, independent of the detector performance. In practice, after all other components are accounted for, the fixed power to the PD will be determined by the 'worst-performing' laser in the transmitter, i.e. the maximum power achievable for the lowest desired OSNR value of that channel. The 'weakest' channel, in the case of this 100 GHz grid, was the channel with the longest wavelength (module S/N YE2265) at $\lambda =$ 1998.63 nm (32.6°C and 80 mA). The peak power of this device was recorded to be -0.38 dBm when measured at the OSA (from the output of the fibre

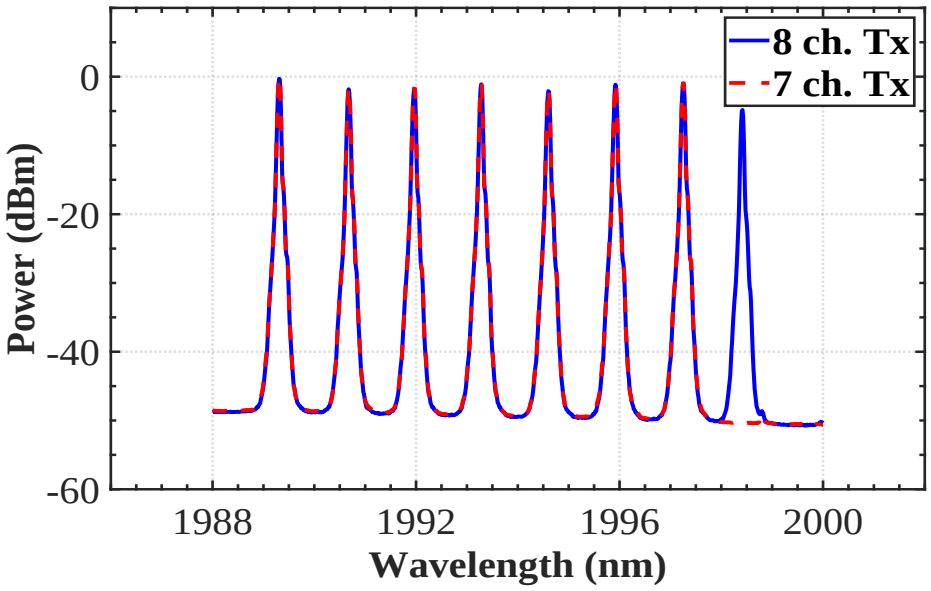


Figure 5.8: Optical spectrum of the 100 GHz DWDM transmitted signals, originally eight channels (blue), with seven channels ultimately used (dotted red), measured after TDFA and before MZM (0.05 nm resolution, 1001 sampling points, 12 nm span).

coupled to the laser device). In comparison, its neighbour channel had a peak power of 3.35 dBm (λ = 1997.33 nm, module S/N YE2267 at 14.0°C and 95 mA). When the 1998.63 nm channel was added to the transmitter system, this power issue was then compounded due to the TDFA gain roll-off at longer wavelengths, which meant that this channel was amplified less in comparison to other channels, as can be seen from the transmitter spectrum in Figure 5.8. For this reason, it was decided to cap the DWDM channels at this upper wavelength ~1998 nm limit for the purposes of this 100 GHz DWDM demonstration.

Receiver

As in Section 4.1.3, a pre-amplified receiver was implemented by using a variable attenuator (with 3 dB insertion loss) to control the input power to the TDFA, enabling adjustment of the OSNR (which was measured at the OSA). This attenuator was followed by an amplifier, which should have a low noise figure, in order to ensure it has minimal impact on performance measurement. The TDFA used in this case had ~22 dB maximum gain and ~6 dB noise figure (best noise figure of the TDFAs measured). As per Section 5.1.2, two filters were required to ensure high channel isolation, the insertion loss of the

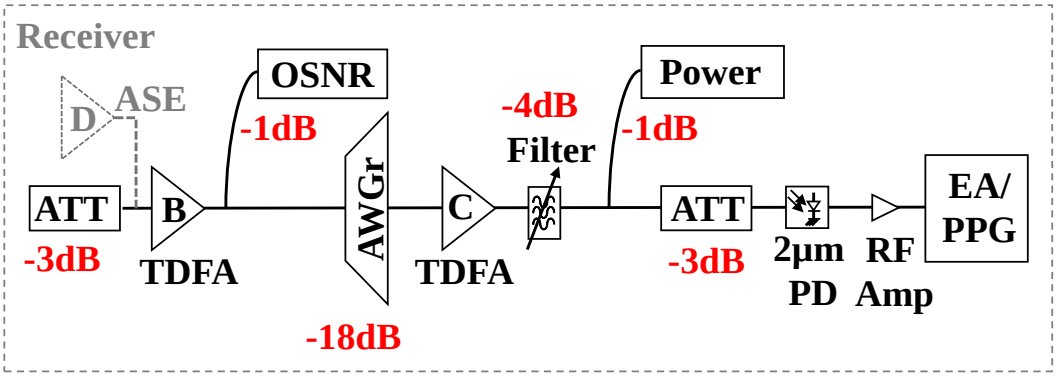


Figure 5.9: Power budget schematic for the DWDM receiver.

tunable bandpass filter was ~4 dB per channel and the average insertion loss of the AWGr per channel was ~18 dB. A TDFA was employed between both filters to compensate for this loss. Moreover, the design of the full receiver was optimised such that it minimised losses, and maximised the OSNR at the PD. Therefore, the highest-gain TDFA (~26 dB maximum gain, with a noise figure of 8 dB) was chosen for this position in order to boost the signal as much as possible prior to the PD. A high-speed (12.5 GHz) InGaAs 2 μm commercial PD was used (EOT ET-5000). The power to the PD was monitored by a 10% tap connected to a low-speed (DC to 15 MHz) InGaAs PD (Thorlabs PDA10DT) and a 60 MHz oscilloscope (1 GS/s Tektronix TDS 1002). The oscilloscope recorded the incoming power in voltage, which could then be converted to dBm. The total power going into the PD was controlled using a variable attenuator. The attenuator had a 3 dB insertion loss and the 10% tap introduced a 1 dB loss. This attenuator and power meter configuration enabled power monitoring and control to ensure that the power to the PD was kept constant for different conditions of system testing.

Noise load receiver

In order to deliver sufficient power to the PD, amplification is required due to the compound losses of all devices and optical fibre attenuation in an optical communication system. This is particularly evident in the case of the first/second generation 2 μm systems, which have much higher losses in general, leading to additional amplifiers being required throughout the system. When all the approximate losses in the proposed system (as per Figure 5.6 and Figure 5.9) were summed, they totalled negative ~67 dBm. Taking into account the power from the lasers (~2 dBm) and the gain of all

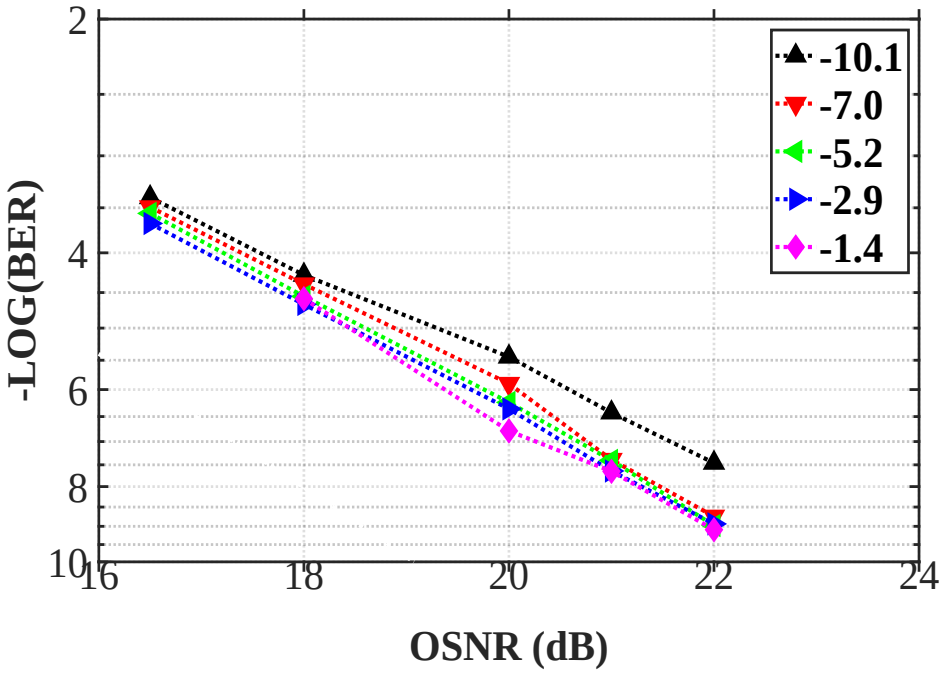


Figure 5.10: BER vs. OSNR measurement for five different power levels (given in dBm in the legend) to the PD.

TDFAs (A=∼15 dB, B=∼22 dB, and C=∼26 dB), this resulted in negative ∼2 dBm power to the PD. However, even this relatively low power level was difficult to achieve, especially at lower OSNR values. As such, the 2 μm PD was characterised to determine the penalty on BER for power values <-2 dBm. The BER vs. OSNR measurement was repeated for the same channel at five different power levels to the PD. The plot resulting from this characterisation is shown in Figure 5.10. Based on this measurement, it was decided that a power level of -7 dBm, for example, was too low and would impact the BER measurements. However, it was decided that operating in the range of $-$ 3 dBm to 0 dBm (optical power to the PD) was suitable and would have minimal impact on the BER measurements.

The challenge remained that even the $-$ 3 dBm to 0 dBm power range was difficult to achieve, especially at lower OSNR values, and this restricted the range of OSNR values available for system testing. For example an OSNR of ∼20 dB corresponded to below -7 dBm at the PD for $\lambda = 1997.7$ nm (the longest-wavelength channel). Initially, the OSNR was varied by changing the signal power via the variable attenuator located at the beginning of the receiver. As a solution that could provide more power (and a greater range of

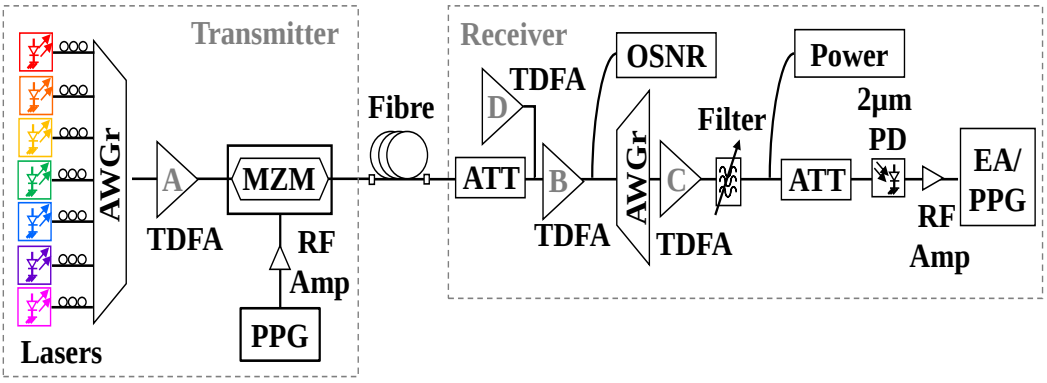


Figure 5.11: Full 2 μm 100 GHz DWDM schematic.

Table 5.3: Gain and noise figure (NF) of TDFAs used in 100 GHz DWDM experiment.

TDFA *label*	Gain *dB*	NF *dB*
A	15	8
B	22	6
C	26	8
D	21	10

possible OSNR values for testing), a noise load configuration was incorporated into the receiver (see the greyed-out *ASE amplifier D* in Figure 5.9). By adjusting an ASE pump to the TDFA, the noise level was changed thereby enabling the OSNR to be varied. With this method, the noise floor could be increased by ~10 dB maximum, in comparison to the noise-off state. While it did result in a slight OSNR reduction in general (of ~3 dB), the reduced OSNR values recorded more total optical power at the PD. For example, using this method, an OSNR of ~20 dB corresponded to ~ -2.2 dBm at the PD for $\lambda =$ 1997.7 nm (in comparison to < -7 dBm before). For this reason, -2.2 dBm was chosen as the fixed power level for all channels throughout system testing. By incorporating the noise load receiver in this way, a greater range of OSNR values were able to be recorded for system testing.

5.2 100 GHz DWDM at 2 μm

This section provides details of the experiment to demonstrate 100 GHz channel spacing in a 2 μm DWDM system. The goal of this experiment was to demonstrate improved spectral efficiency of 2 μm systems, in comparison to previous records, in order to further establish the potential of this new transmission window for optical communications.

Table 5.4: DWDM laser and AWGr (demux) settings used for 100 GHz demo at 2 μm.

λ	**Module S/N**	**Temp.**	**Current**	**AWGr ch.**	**AWGr Temp.**
nm	-	*°C*	*mA*	-	*°C*
1989.30	YE2263	15.0	94.55	2	15.7
1990.60	YE2259	13.4	94.78	3	16.0
1991.97	YE2272	11.4	94.82	4	16.3
1993.30	YE2271	13.4	94.78	5	16.6
1994.60	YE2270	22.0	94.77	6	16.9
1996.00	YE2268	15.2	94.78	7	17.2
1997.27	YE2267	9.0	95.03	8	17.5

5.2.1 Experiment

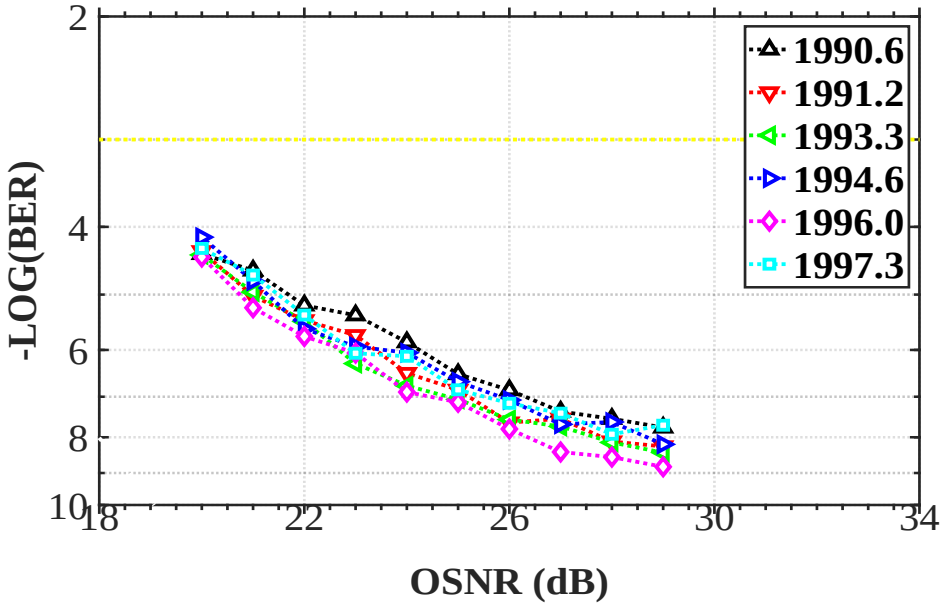
The full schematic of the 100 GHz system is shown in Figure 5.11, with the details of the TDFAs used listed in Table 5.3. This experiment represented the first time such DWDM channels were multiplexed via a 2 μm AWGr. The specific wavelengths, laser modules, temperature/current settings and AWGr settings for this setup are given in Table 5.4. All lasers were operated near maximum current (100 mA) to achieve maximum power in each case. NRZ-OOK modulation was applied to six DWDM channels using a $LiNbO_3$ MZM, which was driven with a PRBS of length $2^{31} - 1$ at a data rate of 12.5 Gbit/s, using a PPG and RF amplifier.

5.2.2 System analysis

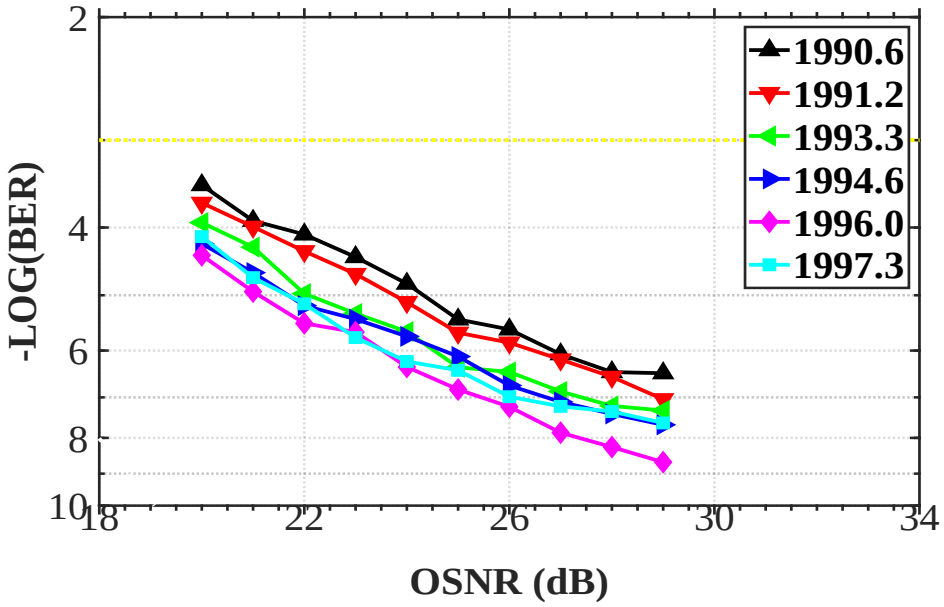
The performance of the 100 GHz DWDM system was analysed in terms of BER vs. OSNR performance and transmission penalty over 1.15 km of HC-PBGF. Figure 5.12a shows the BER results for measurement back-to-back (no fibre). For a BER of 1×10^{-6}, an average OSNR of 23.3 dB was recorded, with a spread of 1.6 dB. Figure 5.12b shows the same results repeated after transmission over 1.15 km of HC-PBGF. The average OSNR for BER of 1×10^{-6} was 24.9 dB, with a spread of 3.4 dB. The observed average OSNR penalty was recorded to be 1.7 dB. This figure is consistent with the additional presence of water or CO_2 in the fibre [100] which can be reduced through a purging process [138].

5.2.3 105 Gbit/s system capacity

With the testbed established, the capacity of the 100 GHz DWDM system at 2 μm was then pushed further by increasing the number of DWDM channels to



(a) Back-to-back.



(b) After transmission over 1.15 km of HC-PBGF.

Figure 5.12: BER vs. OSNR performance to analyse transmission penalty for 100 GHz DWDM. 6 $\times$ 12.5 Gbit/s NRZ-OOK externally modulated channels. Yellow dotted line BER = $1x10^{-3}$.

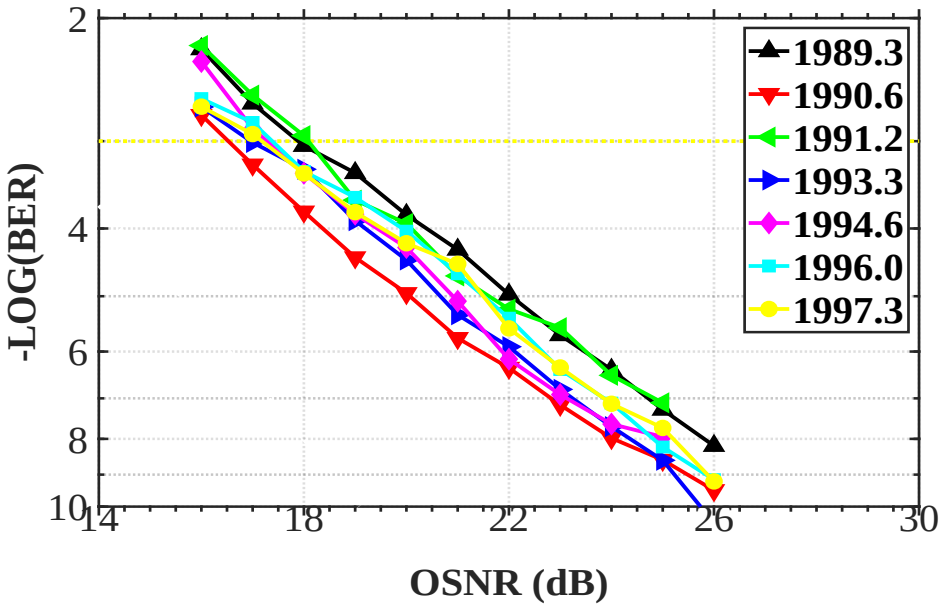


Figure 5.13: BER vs. OSNR performance for 7 x 15 Gbit/s NRZ-OOK externally modulated channels with 100 GHz spacing, multiplexed by an AWGr and transmitted over 1.15 km of HC-PBGF, totalling 105 Gbit/s capacity. Yellow dotted line BER = 1×10^{-3}.

seven and operating at higher data rates. In this case, NRZ-OOK modulation was applied to seven DWDM channels using a $LiNbO_3$ MZM, which was driven with a PRBS of length $2^{31} - 1$ at a data rate of 15 Gbit/s. Thus, a total capacity of 105 Gbit/s was achieved. Figure 5.13 shows the BER performance against OSNR for all seven DWDM channels after transmission over 1.15 km of HC-PBGF. There is also no evidence of an error floor, which would be indicated by the slope of the curve significantly decreasing (or flattening off) for lower -LOG(BER) values, corresponding to a performance limit. In this analysis, the OSNR was measured as the ratio between the signal and the noise (under the signal) for a 0.05 nm bandwidth resolution. For a BER of 1×10^{-6}, the average OSNR required was 22.5 dB, with a spread of 2.1 dB. Therefore, with 7 x 15 Gbit/s channel transmission, a total capacity of 105 Gbit/s was achieved. All BER results recorded were below the FEC limit of 1×10^{-3}. Thus, this experiment established that DWDM with 100 GHz channel spacing is possible at 2 μm.

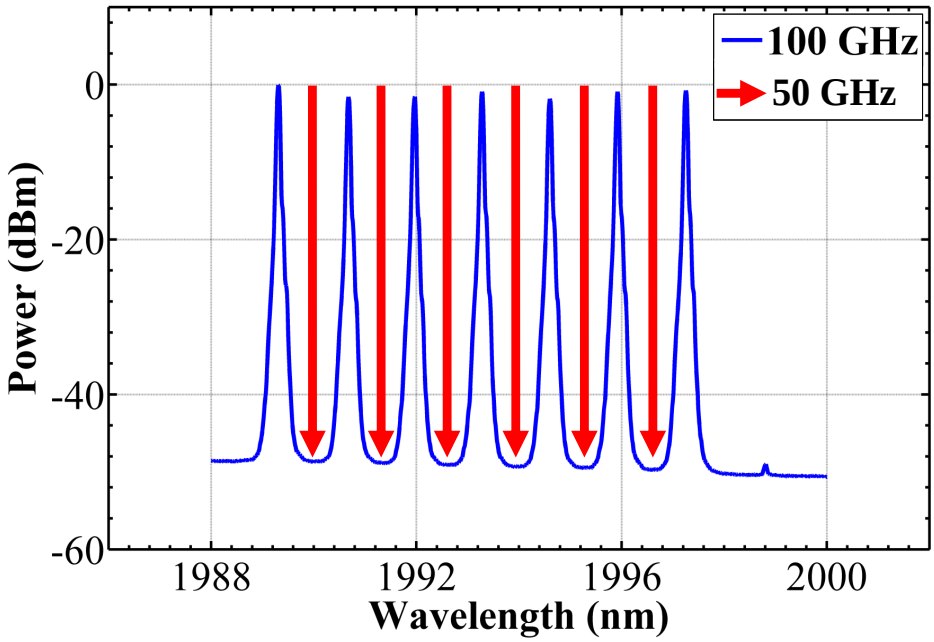


Figure 5.14: Proposed interleaved channels to create 50 GHz channel spacing in the DWDM transmitter (0.05 nm resolution, 1001 sampling points, 12 nm span).

5.3 50 GHz DWDM at 2 μm

Moving to narrower channel spacing is critical to improve spectral efficiency at 2 μm. Therefore, the feasibility of reducing 2 μm DWDM channel spacing from 100 GHz to 50 GHz was investigated and forms the basis of the following section. The aim of the following experiments was to optimise the available bandwidth, increase system capacity at 2 μm, and move closer to replicating current ITU-T DWDM standards.

5.3.1 System design

In order to achieve 50 GHz channel spacing, the 100 GHz system shown in Figure 5.11 was maintained, with the addition of a new set of lasers which was based on a 100 GHz grid that was 50 GHz-shifted from the original. These new laser channels were then interleaved (or tuned to emit in-between) with the original channels using a standard 2:1 coupler, as illustrated in Figure 5.14. The updated channel grid is listed in Table 5.5, with the interleaved channels shaded in grey.

Originally, it was planned that the six new channels would be externally modulated (prior to interleaving) using an InP-based MZM that was developed

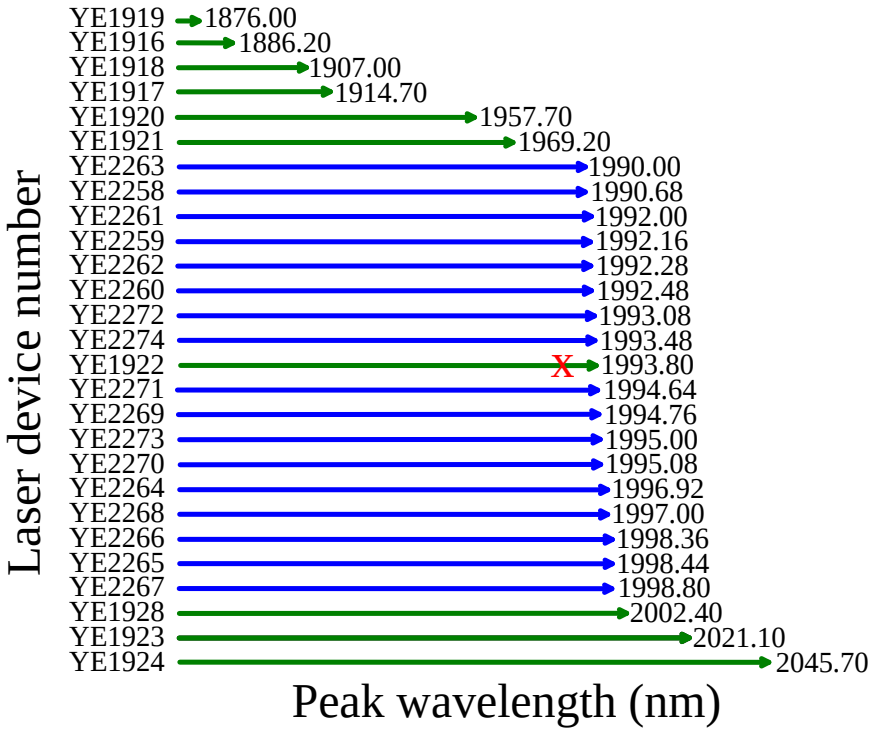


Figure 5.15: Second (green) and third (blue) generation of laser devices designed for the 2 μm waveband, with module S/N on the left and corresponding peak centre wavelength on the right (at 25^{o}C and 50 mA). YE1922 highlighted with a red X.

in parallel by a partner research team at Tyndall National Institute [38],[113],[145]. However, this modulator was not available at the time of system testing, but this did not preclude the 50 GHz DWDM investigation. Given that no other 2 μm modulator was available, the six additional lasers could not be implemented as initially intended (due to their butterfly-packaging which required external modulation). Instead, lasers from the first/second generation (Table 4.1/Table 4.2) had to be selected, with the requirements that they were suitable for direct modulation (determined by packaging) and their emission wavelength could be tuned within the region of the proposed channel grid. These restrictions presented challenges to the systems implementation.

In order to select suitable DWDM lasers, the second generation of laser devices (Table 4.2) were more favourable because the frequency response of these devices was higher, at ~5 GHz (and over 7 GHz recorded in some cases) [126], in comparison to the first generation of lasers which had a limited frequency response of ~3 GHz on average [96], [124]. However, upon

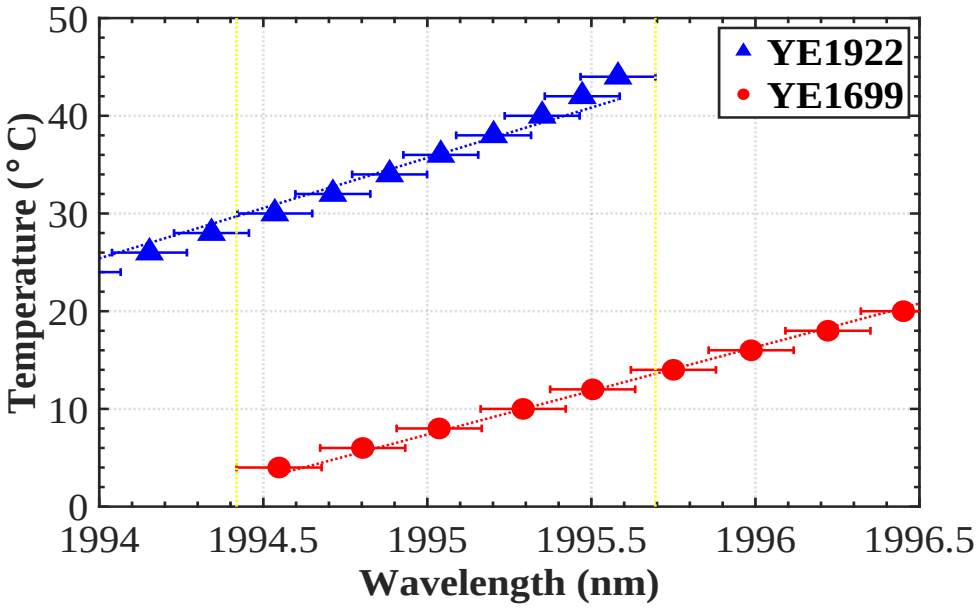


Figure 5.16: Temperature vs. wavelength characterisation for two lasers, illustrating the region of wavelength overlap (between yellow dotted lines). Markers represent wavelength value at 60 mA with the horizontal errors bars indicating the wavelength variation ± 20 mA at each temperature.

characterisation, only one of the lasers from the second generation was within the desired wavelength range, as can be seen from Figure 5.15. The module S/N of this device was YE1922, indicated by a red X. This laser could be tuned to match three of the desired emission wavelengths in the channel grid (1992.68 nm, 1994.02 nm and 1995.35 nm). The thermal characterisation of this device is shown (in blue triangles) in Figure 5.16. In this figure, the data points represent the wavelength value recorded for the laser at 60 mA and the horizontal errors bars indicate the wavelength variation that corresponds to ± 20 mA at each temperature point. Based on this characterisation, the temperature and current settings required for each desired wavelength can be determined.

Finally, with only one suitable device identified for the interleaved channels from the second generation of lasers, the first generation were considered in order to further fill the 50 GHz channel grid. The list of available devices can be seen in Table 4.1 of Chapter 4. One suitable device was identified within the desired wavelength range from the first generation. The module S/N of this device was YE1699. Similar to the YE1922 device, this laser could be tuned to three of the desired wavelengths in the channel grid (1994.02 nm,

Table 5.5: 50 GHz DWDM grid, with interleaved channels shown in grey and check-marks indicating the channels available to be interleaved.

	No.	λ	$\Delta\lambda$	$\Delta\nu$
	-	*nm*	*nm*	*GHz*
×	0	1990.02	0.67	50.00
	1	1990.60	0.58	43.75
×	2	1991.35	0.75	56.25
	3	1992.00	0.65	48.75
✓	4	1992.68	0.68	51.25
	5	1993.32	0.64	47.75
✓✓	6	1994.02	0.70	52.25
	7	1994.65	0.63	47.50
✓✓	8	1995.35	0.70	52.50
	9	1996.00	0.65	48.75
✓	10	1996.68	0.68	51.25
	11	1997.33	0.65	48.50

1995.35 nm and 1996.68 nm). The thermal characterisation of this device is also shown (in red circles) in Figure 5.16. The region of wavelength overlap between the two lasers can be seen by comparing the two characterisations and is indicated by the dotted yellow lines in Figure 5.16.

In Table 5.5, the '×' mark on the left indicates the wavelengths that could not be implemented with available 2 μm lasers and the '✓' mark indicates the wavelengths that were possible to emulate (with lasers YE1922 and YE1699 as described). Both devices could be tuned to overlap at two wavelengths (1994.02 nm and 1995.35 nm) and these are indicated by two '✓' marks beside the table. For convenience from this point forward, the initial 100 GHz channels will be referred to as the **odd** channels and the new interleaved channels (i.e. those shaded in grey in Table 5.5) will be referred to as the **even** channels. By using the two devices specified (YE1922 and YE1699), these lasers could be tuned to emit at either side of each odd channel, hence representing the required even channels in turn and emulating 50 GHz channel spacing in the transmitter for each channel under test (CUT).

- Original (externally modulated) channels = **odd** channels
- Interleaved (directly modulated) channels = **even** channels

5.3.2 Experiment

The experimental setup to investigate 50 GHz DWDM at 2 μm is depicted in Figure 5.17. The components used were the same as previously described in Section 5.2.1, Figure 5.11, with the addition of the two directly modulated even channels. Note that, for the purpose of this 50 GHz investigation, the previous channel at 1989.35 nm was omitted for this demonstration because there were no suitable lasers to emulate 50 GHz adjacent channel spacing (as per Table 5.5), resulting in six odd channels and two even channels (eight in total). NRZ-OOK modulation was applied to the odd channels using the $LiNbO_3$ MZM discussed previously, which was driven with a PRBS of length $2^{31} - 1$ at a data rate of 12.5 Gbit/s, using an independent pulse pattern generator (PPG) and RF amplifier. To our knowledge, this was the first time such a high baud rate (as per Section 3.1.2) was demonstrated for closely-spaced OOK channels at 2 μm, although higher aggregated bit rates have been achieved with advanced modulation formats and digital signal processing [100].

The even channels were directly modulated using a second independent PPG with a PRBS of $2^{31} - 1$. NRZ-OOK modulation was applied at a data rate of 8 Gbit/s. The reduced bit-rate was due to the limited frequency response of the lasers, as per reference: [124]. The two even channels were then amplified using a commercial TDFA (AdValue Photonics 2 μm fibre amplifier) and multiplexed with the six odd channels using a standard 2:1 fibre coupler. The lasers were optimised for modulation in order to ensured that the data from the odd CUT was de-correlated from the two even adjacent channels. As discussed in the previous section, the odd channels (2 x 8 Gbit/s NRZ-OOK) were thermally tuned to emit at wavelengths either side of the even channels (6 x 12.5 Gbit/s NRZ-OOK) in the transmission spectrum, creating 50 GHz channel spacing around each CUT in turn.

5.3.3 System analysis

The aim of this experiment was to investigate the feasibility of implementing 50 GHz DWDM at 2 μm. In order to understand the challenges associated with this implementation, the impact of reduced channel spacing was investigated by measuring the OSNR vs. BER performance of one channel under four different scenarios which will be discussed in the following sections:

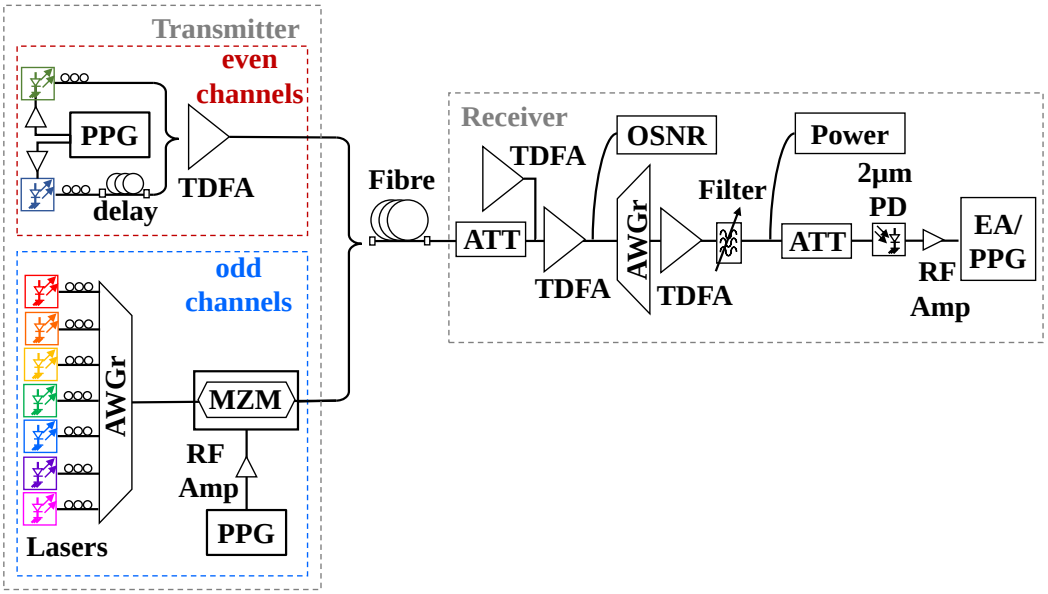


Figure 5.17: Experiment setup to investigate the impact of reduced (50 GHz) DWDM channel spacing using 6 x 12.5 Gbit/s (externally modulated) and 2 x 8 Gbit/s NRZ-OOK (directly modulated) signals.

(a) single channel

(b) 100 GHz spacing (6 channels)

(c) 50 GHz spacing (3 channels)

(d) 50 GHz spacing (all 8 channels)

Channel #7 (1994.65 nm) was selected to be the CUT for this investigation. As per Table 5.5 of Section 5.3.1, the two directly modulated even channels could be tuned to 1994.02 nm (channel #6) and 1995.35 nm (channel #8) to create dense 50 GHz spacing around channel #7 centre wavelength in the 2 μm transmitter, as shown in Figure 5.18. For this configuration, the performance of channel #7 was measured for scenarios (a) - (d).

(a) Single channel

First, the performance of the system was recorded for the single channel case (channel #7 only), in order to obtain a baseline performance for comparison. The BER vs. OSNR measurement was repeated five times. The results of these five measurements are shown by the blue curves in Figure 5.19, with the calculated average overlaid (circles with red lines) and the standard deviation indicated by the vertical error bars. As can be seen by these error bars, the system was highly unstable, especially at low power and low OSNR values.

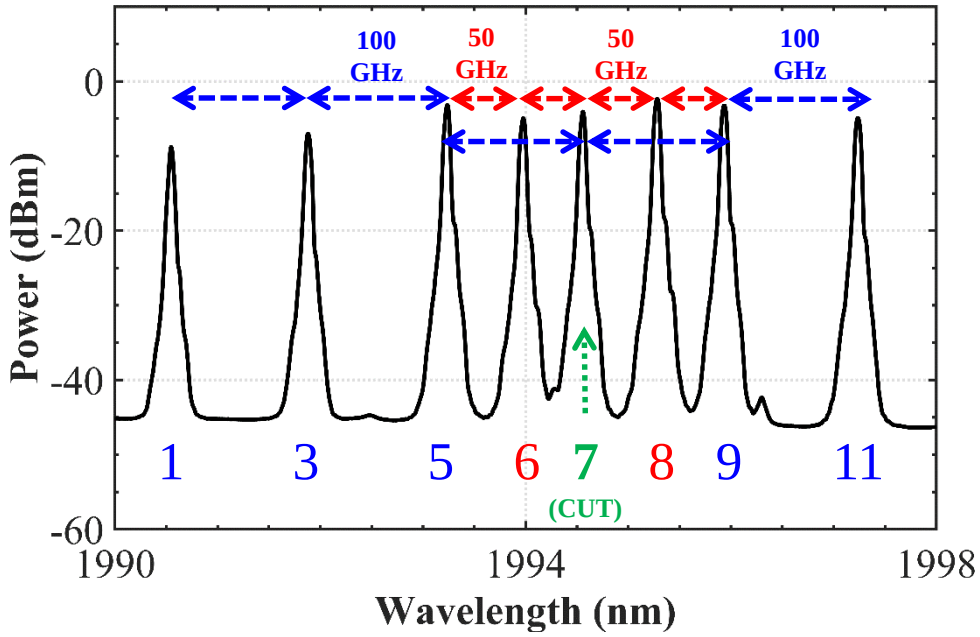


Figure 5.18: Transmitter spectrum for the 50 GHz experiment (without data) with six odd channels and two interleaved even channels (#6 and #8). These two even channels were tuned to emit at either side of the CUT (#7) to emulate 50 GHz channel spacing (0.05 nm resolution, 3334 sampling points, 10 nm span).

This was largely due to the commercial TDFA (AdValue Photonics 2 μm fibre amplifier) used in the system which was observed to have poor temporal stability, especially when the power level and OSNR were reduced. The average OSNR required to achieve a BER of 1×10^{-6} was 25.1 dB, with a spread of 2.6 dB (indicating a conservative error margin of $\pm$ 1.5 dB). This OSNR requirement is somewhat higher than conventional 1.55 μm OOK systems, due to the non-ideal components used.

(b) 100 GHz spacing (6 channels)

Secondly, the performance of channel #7 was measured with the six odd channels at 100 GHz channel spacing. Again this was repeated five times and the results are shown in Figure 5.20 for all four scenarios. The data points in this figure indicate the average BER value (for a certain OSNR) and the vertical error bars indicate the standard deviation. For case (b) (red downward triangles), the average OSNR required for channel #7 to achieve a BER of 1×10^{-6} was found to be 27.9 $\pm$ 1.5 dB, a higher (~2.8 dB) OSNR than the single channel case. This is a repeat of the experiment in Section 5.2.2, Figure 5.12a. In this case, a higher OSNR was required for channel #7

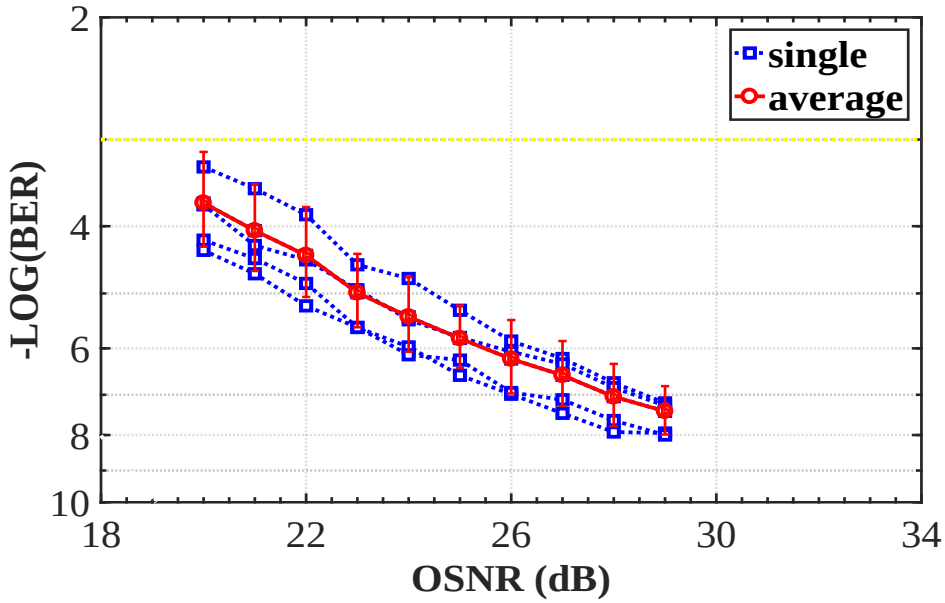


Figure 5.19: Five BER vs. OSNR measurements for CUT(#7) single channel (at 12.5 Gbit/s NRZ-OOK) shown with blue squares and dotted lines. The calculated average is overlaid (red circles with solid lines) and the standard deviation indicated by the vertical error bars. Yellow dotted line BER = 1×10^{-3}.

(1994.65 nm), likely due to the introduction of an extra coupler in the transmitter to multiplex the two odd 50 GHz channels for this experiment.

(c) 50 GHz spacing (3 channels)

Next, the scenario with three DWDM channels at 50 GHz channel spacing was considered. The CUT (channel #7) was recorded, together with the even channels (channel #6 and channel #8). The purpose of this measurement was to investigate the impact of 50 GHz channel spacing, in comparison to the single channel case. The resulting data for case (c) is shown by the green left-pointing triangles in Figure 5.20. One would expect a higher OSNR requirement in this case as the CUT is surrounded by two adjacent channels with de-correlated data acting as noise to the signal under test. For example, if there was a ~50% increase in crosstalk, one would expect the OSNR requirement to be ~3 dB higher. However, the average OSNR required for channel #7 to achieve a BER of 1×10^{-6} was found to be 26.4 $\pm$ 1.5 dB, only slightly higher on average. This measurement will be discussed in more detail in the following sections.

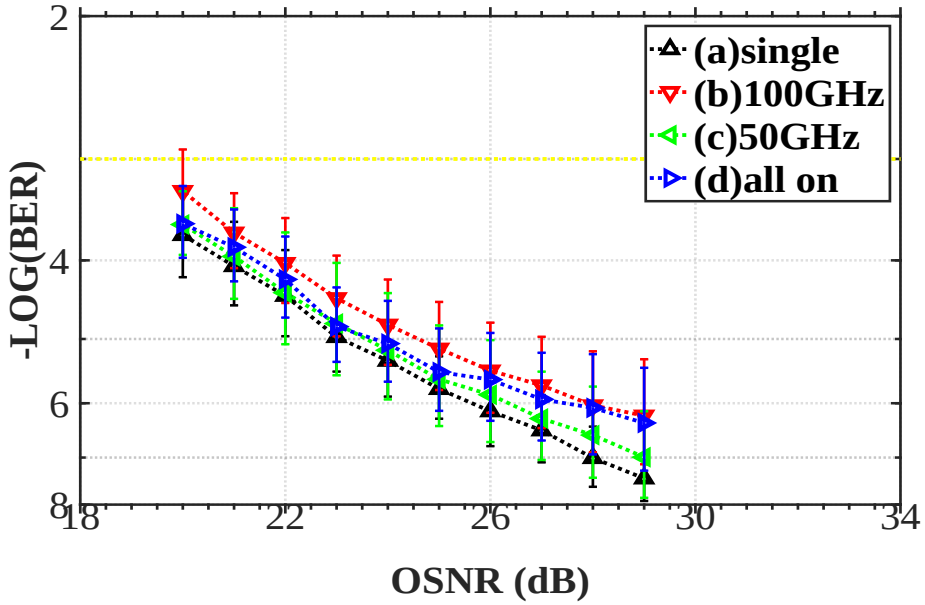


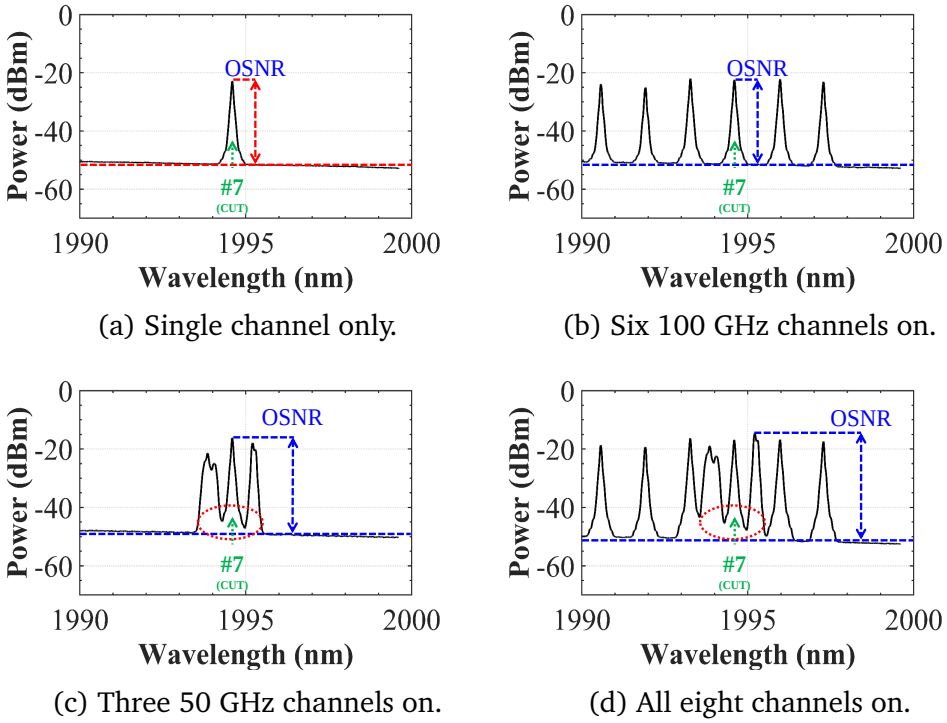
Figure 5.20: Average BER vs. OSNR measurements for CUT(#7) at 12.5 Gbit/s NRZ-OOK. This channel was measured under four different scenarios: (a) single channel only (black △), (b) six 100 GHz channels on (red ▽), (c) three 50 GHz channels on (green ◁) on and (d) all eight channels on (blue ▷). Yellow dotted line BER = 1×10^{-3}.

(d) 50 GHz spacing (all 8 channels)

Finally, all available DWDM channels were switched on, as per Figure 5.18. The data for case (d) is shown by the blue right-pointing triangles in Figure 5.20. The purpose of this measurement was to investigate the impact of 50 GHz channel spacing, in comparison to the 100 GHz case (b). One would expect that this case would be the 'worst case scenario' due to the increased number of channels and reduced channel spacing with de-correlated neighbouring channels. The average OSNR required for channel #7 to achieve a BER of 1×10^{-6} was found to be 27.5 $\pm$ 1.5 dB, which is slightly lower on average than the 100 GHz six-channel case. Therefore, within the margin of error, very little penalty was recorded for increased channel number, increased crosstalk and reduced channel spacing, which is unusual. The discussions that follow will focus on understanding these results.

OSNR

Figure 5.21 shows the optical spectra used for OSNR measurements (indicated in Figure 5.17) for the four scenarios (a) - (d). In order to compare the BER



(a) Single channel only.

(b) Six 100 GHz channels on.

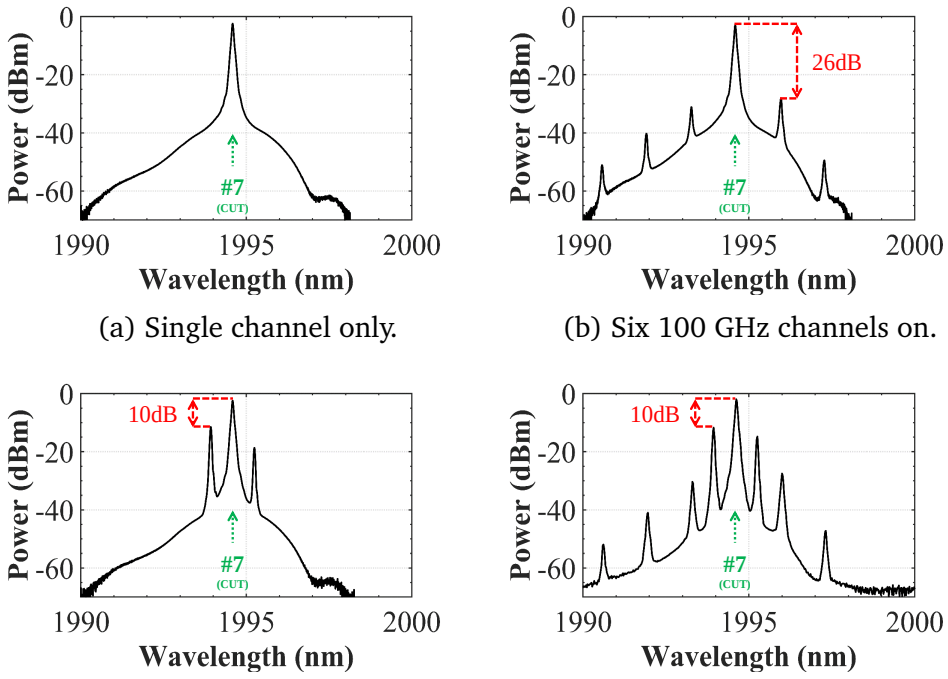
(c) Three 50 GHz channels on.

(d) All eight channels on.

Figure 5.21: Optical spectra recorded during OSNR measurement of the CUT (#7) (0.05 nm resolution, 3334 sampling points, 10 nm span.)

vs. OSNR performance of the CUT for the different scenarios, it was necessary to decide a standardised way to measure OSNR that was common to each case. To do this, the power level of the signal peak was measured against the out-of-band noise floor to calculate the OSNR. As can be seen from Figure 5.21, this was sufficient in the single channel and 100 GHz case (Figure 5.21a and Figure 5.21b). However, in the cases where channel spacing was reduced to 50 GHz (Figure 5.21c and Figure 5.21d), the noise level around the base of the peak (highlighted by the red dotted circle) does not match the out-of-band noise floor.

Therefore, in the scenarios with 50 GHz channel spacing, measuring the OSNR based on the out-of-band noise floor was an overestimation. For example, in Figure 5.21c, an OSNR of ~35 dB was recorded using the out-of-band noise floor as the reference noise level. But, looking at the level of crosstalk with the 50 GHz channels in this case, the OSNR is likely a lower value of ~30 dB. One would expect that the OSNR overestimation should result in a better performance given the BER measured. For example, if an OSNR of ~25 dB was recorded (using the out-of-band noise floor) to achieve a BER of 1×10^{-6}, an OSNR overestimation would imply that the actual OSNR required to achieve



(a) Single channel only.

(b) Six 100 GHz channels on.

(c) Three 50 GHz channels on.

(d) All eight channels on.

Figure 5.22: Optical spectra of CUT (#7) at the end of the receiver (before the PD) for the four scenarios of the 50 GHz experiment (0.05 nm resolution, 3334 sampling points, 10 nm span).

the same BER would be lower, perhaps around 20 dB. Following on from this, if the OSNR was overestimated that would mean that if the BER vs. OSNR curves were to be corrected, they would be shifted to the left, indicating even better system performance for the scenarios with 50 GHz channel spacing. As per case (c), this result further contradicts the expectation of a higher OSNR requirement in the case of reduced channel spacing. However, this measured improvement in performance is likely due to the 100 GHz neighbouring channels falling within the filter bandwidth and constructively interfering with the CUT. As such, the next analysis will discuss the filter profile.

Filtering

In order to investigate the effect of filtering towards BER performance, the optical spectrum just before the detector was recorded (i.e. the OSA was connected instead of the PD in Figure 5.17). Figure 5.22 shows the resulting optical spectra of channel #7, prior to the detector, for the four scenarios (a) - (d). Using these spectra, the channel isolation can be measured for each case by calculating the difference between the peak of the CUT and the next highest

channel peak. For the 100 GHz case (in Figure 5.22b), a channel isolation of ~26 dB was recorded for the CUT. While this value represented an improvement upon previous demonstrations [100] (likely due to fine-tuning of the AWGr), many systems exhibit channel isolation >35 dB at this point to ensure sufficient suppression of neighbouring channels. However, for the cases with 50 GHz channel spacing (Figure 5.22c and Figure 5.22d), the isolation of the CUT deteriorated even further and was reduced to only ~10 dB in both cases.

Figure 5.23 shows both filter profiles overlaid with the CUT. This is an image constructed from three sets of data seen previously. The black trace shows all eight DWDM channels before filtering (from Figure 5.21d). The red trace (with squares) shows the Agiltron commercial tunable bandpass filter profile (as per Figure 4.5). The blue trace (with circles) shows the profile of the receiver AWGr (as per Figure 5.4). Both filter profiles were adjusted in terms of power offset and centre wavelength shift (with no re-scaling) in order to illustrate optimal overlap with the CUT in this case. As per Section 4.1.3, the Agiltron tunable bandpass filter has a 3 dB bandwidth of 1.6 nm and a 20 dB bandwidth of 4.5 nm. These values correspond to ~120 GHz and 340 GHz at 2 μm, respectively. Clearly, this filter is too wide to isolate the CUT in the 100 GHz and 50 GHz scenarios. A second filter is required to improve channel isolation. However, while the AWGr curve shows a narrower profile for the CUT, it would only improve isolation by ~7 dB for the 50 GHz case, which is still poor. Therefore, despite the use of two cascading filters (which increased channel isolation to 10 dB), this configuration was not sufficient to isolate the DWDM CUT.

The results here show that 50 GHz DWDM is possible at 2 μm from the transmitter perspective, as potential lasers to operate at this tight frequency spacing were identified. However, there were challenges associated with the receiver, in particular related to the channel isolation between adjacent 50 GHz channels. Narrow-band tunable bandpass filters at 2 μm are not currently available, although some researchers have utilised micro-ring resonators for this application [146], [147], [148]. Potential solutions to circumvent this problem (if optical filters are not available), is through the use of balanced detectors or coherent detection. But, given that balanced detectors are also not available (or are prohibitively expensive via Discovery Semiconductors Inc., for example), testing such systems is not currently feasible. In previous 2 μm demonstrations, fibre Bragg gratings were employed

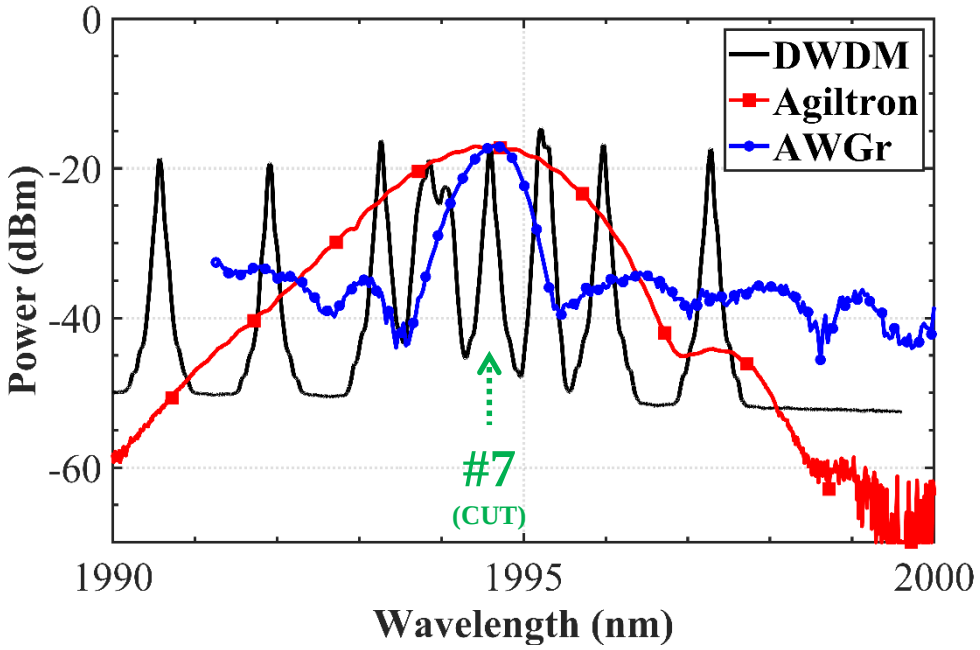


Figure 5.23: Received DWDM spectrum, before filtering, for the 50 GHz experiment with all channels on (black line). Filter profiles of the Agiltron filter (red line, square markers) and AWGr (blue line, round markers) are overlaid for comparative purposes. Both profiles are adjusted in terms of power and wavelength (with no re-scaling).

at the receiver. This presents another solution, but its implementation would require purchasing an expensive system for tunability (e.g. TeraXion) or, alternatively, the construction of a tool which could stretch, twist, heat the gratings in order to enable tuning over sufficiently large bandwidths. Finally, injection locking also may provide a path forward. It is a technique that has been employed for filtering purposes at 1.55 μm [40], [41], [42] and would be compatible with photonic integration. This was the avenue chosen and will be discussed in Chapter 6.

Chapter summary

The capacity of an optical communication system can be maximised by enabling a greater number of wavelength channels with narrower channel spacing. The spacing between these channels is commonly determined by ITU-T standards which dictates 100 GHz or 50 GHz spacing for DWDM systems. Accordingly, one of the aims of this thesis was to demonstrate DWDM transmission at 2 μm, while replicating these ITU-T channel-spacing standards in order to increase the achievable capacity of 2 μm optical communication

systems. Key challenges were addressed such as lack of commercial-grade devices at this waveband, limited tunability and high insertion losses. Nonetheless, a 2 μm DWDM system was designed with 100 GHz channel spacing. This was achieved by implementing, for the first time, a 2 μm AWGr to multiplex the 7 x 15 Gbit/s channels, with 105 Gbit/s total capacity reached.

The feasibility of decreasing the channel spacing from 100 GHz to 50 GHz DWDM using current 2 μm technologies was then investigated. It was found that 50 GHz channel spacing can be readily achieved in the DWDM transmitter. However, there are several challenges in terms of the receiver, the most critical of which are available filtering techniques to sufficiently isolate the DWDM channels and accurately analyse the performance of the CUT. Further filtering developments are required in order to support such dense channel spacing in 2 μm optical communication systems.

Chapter publications

1. **N. Kavanagh**, K. Shortiss, H. Zhang, M. Sadiq, K. Thomas, A. Gocalinska, J. Zhao, E. Pelucchi, P. O'Brien, F. Peters, B. Corbett, and F. Gunning, **"Impact of DWDM at 50GHz spacing in the 2 μm waveband," in 2016 Conference on Lasers and Electro-Optics (CLEO)**, CLEO 2016, (San Jose, California), p. SF1F.5, Optical Society of America, 2016. doi:10.1364/cleo_si.2016.sf1f.5

2. **N. Kavanagh**, M. Sadiq, K. Shortiss, H. Zhang, K. Thomas, A. Gocalinska, J. Zhao, E. Pelucchi, P. O. Brien, F. H. Peters, B. Corbett, and F. C. G. Gunning, **"Exploring a new transmission window for telecommunications in the 2 μm waveband," in 18th International Conference on Transparent Optical Networks (ICTON)**, pp. 1–4, 2016. ***Awarded Best Student Paper.*** doi:10.1109/ICTON.2016.7550279

3. **N. Kavanagh**, K. Shortiss, H. Zhang, M. Sadiq, E. Pelucchi, P. O'Brien, F. H. Peters, B. Corbett, and F. C. Garcia Gunning, "**Opening a New Transmission Window for Telecommunications", in Institute of Physics Spring Meeting**, Belfast, Ireland, 2016, Poster. ***Awarded IOP Rosse Medal.***

4. M. U. Sadiq, H. Zhang, J. O'Callaghan, B. Roycroft, **N. Kavanagh**, K. Thomas, A. Gocalinska, Y. Chen, T. Bradley, J. R. Hayes, Z. Li, S. U. Alam, F. Poletti, M. N. Petrovich, D. J. Richardson, E. Pelucchi, P. O'Brien, F. H. Peters, F. Gunning, and B. Corbett, **"40 Gb/s WDM Transmission over 1.15 km HC-PBGF Using an InP-Based Mach-Zehnder Modulator at 2 μm," Journal of Lightwave Technology**, vol. 34, no. 8, pp. 1706–1711, 2016.
doi:10.1109/JLT.2015.2508941

5. M. U. Sadiq, H. Zhang, M. Gleeson, N. Ye, B. Roycroft, **N. Kavanagh**, C. Robert, H. Yang, K. Thomas, A. Gocalinska, Z. Li, Y. Chen, N. V. Wheeler, J. R. Hayes, S. U. Alam, F. Poletti, M. N. Petrovich, D. J. Richardson, B. Kelly, J. O'Carroll, R. Phelan, E. Pelucchi, P. O'Brien, F. Peters, F. Gunning, and B. Corbett, **"40 Gbps WDM transmission over 1.15 km HC-PBGF using the first InP-based Mach Zehnder modulator at 2 μm," in European Conference on Optical Communication (ECOC)**, vol. 2015-November, pp. 1–3, 2015.
doi:10.1109/ECOC.2015.7341853

6. H. Zhang, M. Gleeson, N. Ye, N. Pavarelli, X. Ouyang, J. Zhao, **N. Kavanagh**, C. Robert, H. Yang, P. E. Morrissey, K. Thomas, A. Gocalinska, Y. Chen, T. Bradley, J. P. Wooler, J. R. Hayes, E. Numkam Fokoua, Z. Li, S. U. Alam, F. Poletti, M. N. Petrovich, D. J. Richardson, B. Kelly, J. O'Carroll, R. Phelan, E. Pelucchi, P. O'Brien, F. Peters, B. Corbett, F. Gunning **"Dense WDM transmission at 2 μm enabled by an arrayed waveguide grating," Optics Letters**, vol. 40, no. 14, pp. 3308–3311, 2015.
doi:10.1364/OL.40.003308

7. E. Russell, **N. Kavanagh**, K. Shortiss, and F. C. G. Gunning, **"Development of thulium-doped fibre amplifiers for the 2 μm waveband," in SPIE Photonics Europe**, vol. 10683, p. 8, SPIE, 2018.
doi:10.1117/12.2306462

8. F. C. Garcia Gunning, **N. Kavanagh**, K. Shortiss, H. Zhang, M. Sadiq, K. Thomas, A. Gocalinska, J. Zhao, E. Pelucchi, P. O'Brien, F. H. Peters, and B. Corbett, **"Enabling technologies for a new wavelength window at 2microns," in IEEE Photonics Conference**, IPC 2016, pp. 546–547, 2016.
doi:10.1109/IPCon.2016.7831223

Technical acknowledgements

The author's contribution to this chapter was the experiment design, device characterisation, and all presented system measurements. The author would like to acknowledge:

- F. C. Garcia Gunning and H. Zhang (Tyndall National Institute, University College Cork) for supervision and technical guidance.
- E. Russell (Tyndall National Institute, University College Cork) for characterisation and understanding of 2 μm TDFAs.
- K. Shortiss (Tyndall National Institute, University College Cork) for characterisation of 2 μm lasers (third generation).
- M. Sadiq (Tyndall National Institute, University College Cork) for development of an InP-based MZM at 2 μm [113], [149].
- F. Peters (Tyndall National Institute, University College Cork) for design of 2 μm semiconductor devices.
- N. Ye, M. Gleeson, B. Roycroft, C. Robert, H. Yang, J. O'Callaghan and B. Corbett (Tyndall National Institute, University College Cork) for 2 μm semiconductor devices.
- K. Thomas, A. Gocalinska and E. Pelucchi (Tyndall National Institute, University College Cork) for epitaxy of 2 μm semiconductor devices.
- P. O'Brien (Tyndall National Institute, University College Cork) for packaging of 2 μm semiconductor devices.
- J. Zhao and X. Ouyang (Tyndall National Institute, University College Cork) for fast-OFDM and digital signal processing.
- Z. Li, Y. Chen, N. V. Wheeler, J. P. Wooler, J. R. Hayes, S. R. Sandoghchi, F. Poletti, M. N. Petrovich, S. U. Alam, T. Bradley and D. J. Richardson

(Optoelectronics Research Centre, University of Southampton) for the use of TDFAs, 1.15 km of HC-PBGF tailored to 2 μm, and splicing to SMF.

- R. Phelan, J. O'Carroll and B. Kelly (Eblana Photonics Ltd) for the 2 μm $In_{0.74}Ga_{0.26}As$ slotted Fabry-Pérot lasers.
- L. Grüner-Nielsen (OFS Denmark) for the speciality ClearLite1700 20 SCF with low bend-loss at 2 μm.

Chapter 6

Injection Locking

For optical communication systems in the 2 μm transmission window, enabling DWDM systems with 50 GHz channel spacing has been identified as the next step towards improving spectral efficiency and increasing system capacity [39]. However, as discussed in the previous chapter, while this can be achieved in terms of the transmitter, current demultiplexing techniques do not provide sufficient filtering to isolate these 50 GHz channels at the DWDM receiver. Optical injection locking (OIL) is a technique that has been employed for these purposes, in addition to other DWDM applications at 1.55 μm. These applications will be discussed in the following section.

The use of OIL as a channel selection mechanism was proposed by Kikuchi and Zah in 1988 [150] and was experimentally demonstrated by using OIL to select particular comb lines from a broadband comb spectrum which included over 100 significant lines (emulating a WDM system) [151]. In 2001, a DWDM system was demonstrated in which tunable lasers were used as narrow-bandwidth, high-tuning-speed, injection-locked filters [152]. Most of these early demonstrations were based on distributed feedback lasers but OIL has been demonstrated with Fabry-Pérot lasers also. In 2000, OIL was employed to induce single mode operation (SMO) in Fabry-Pérot lasers, which were then applied as low-cost WDM sources [153]. OIL with Fabry-Pérot lasers has also been demonstrated to enable DWDM systems with 50 GHz channel spacing [154]. Finally, in terms of slotted Fabry-Pérot lasers (those used in the experiments of Chapter 4 and Chapter 5), OIL has been demonstrated for WDM source applications [155] and, most relevant in this case, OIL with slotted Fabry-Pérot lasers has been used for channel selection and

demultiplexing purposes in the 1.55 μm region [40], [41], [42]. Therefore, OIL with slotted Fabry-Pérot lasers is investigated at 2 μm, with a view to potential applications for demultiplexing in the DWDM receiver.

In this chapter, the discovery, history and key concepts of OIL are presented in Section 6.1. The availability of lasers at 2 μm is limited and the lasers used presented challenges (primarily limited tuning capabilities) which are described in Section 6.2.1, together with their characteristics. In order to perform OIL at 2 μm, an experiment was designed which included monitoring apparatus to ensure OIL was occurring. The setup used for this demonstration is typical for OIL schemes, with one laser (called the primary) being injected into the another laser (called the secondary) via a circulator, this is presented in Section 6.2.2. The dynamics therein were observed using two different methods: optically, with the aid of an Optical Spectrum Analyser (OSA), and electrically, via direct detection and with the aid of an Electrical Spectrum Analyser (ESA), this is discussed in Section 6.2.3. The observed OIL dynamics are discussed in Section 6.3.1 and Section 6.3.2. Finally, in Section 6.3.3, further OIL analysis is presented, with the relationship between injection ratio and OIL bandwidth explored, and the time stability of OIL is investigated. Therefore, in this chapter OIL at 2 μm is discussed and stable OIL is demonstrated between two semiconductor slotted Fabry-Pérot lasers at 2 μm.

6.1 Origins and key concepts

In this section, the origins of injection locking as a physical phenomenon observed throughout nature are presented. Then, the history of optical injection locking (OIL) and the key concepts relevant to this thesis are introduced.

6.1.1 From clocks to crickets

> *"In February 1665 the great Dutch physicist Christiaan Huygens, inventor of the pendulum clock, was confined to his room by a minor illness. One day, with nothing better to do, he stared aimlessly at two clocks he had recently built, which were hanging side by side. Suddenly he noticed something odd: the two pendulums were swinging in perfect synchrony. He watched them for hours, yet they never broke step. Then he tried disturbing them - within half an hour they regained synchrony. Huygens suspected that the clocks must*

> *somehow be influencing each other, perhaps through tiny air movements or imperceptible vibrations in their common support. Sure enough, when he moved them to opposite sides of the room, the clocks gradually fell out of step, one losing five seconds a day relative to the other.*"
> From "Coupled Oscillators and Biological Synchronization" by S. Strogatz and I. Stewart, 1993. [156]

The above quotation tells the story of the first recorded observation of injection locking, described in a letter from Huygens to his father. Based on this observation, Huygens theorised that mechanical vibrations (which were transmitted between the two oscillating clocks via a common beam) induced the locking. A simple demonstration of this phenomenon can be performed with metronomes, a wooden board, and two tin cans, as shown in Figure 6.1. Imagine, at first, the metronomes are placed on the board and set ticking at random rhythms. If the two tin cans are laid on their sides and the board (with the ticking metronomes) is balanced on top, then the metronomes will begin to lock oscillations and will ultimately all tick in unison. When the metronomes are ticking in unison, they are oscillating with the same frequency and phase, i.e. they are injection locked [157].

Beyond ticking clocks, injection locking is a physical phenomenon that is observed in oscillators throughout nature. Injection locking can be seen in the synchronised flashing of tropical fireflies along the tidal rivers of South East Asia [158] (these fireflies can be also locked to an external LED [159]), to snowy-tree crickets chirping in unison [160], and even in our own bodies where pacemaker cells periodically stimulate our hearts to regulate its rhythm [161]. Injection locking is a fundamental feature found in many biological oscillators. Before many of these biological examples were discovered, the fundamental dynamics of injection locking in electrical oscillator circuits were identified and modelled by Adler in 1946 [162].

6.1.2 Brief history

Soon after the invention of the laser in 1960, Steier and Stover demonstrated the locking of laser oscillators by external light injection using HeNe lasers [163]. Their experiment focused on the phase-locking of one laser to another by direct injection of the first laser beam into the cavity of the second

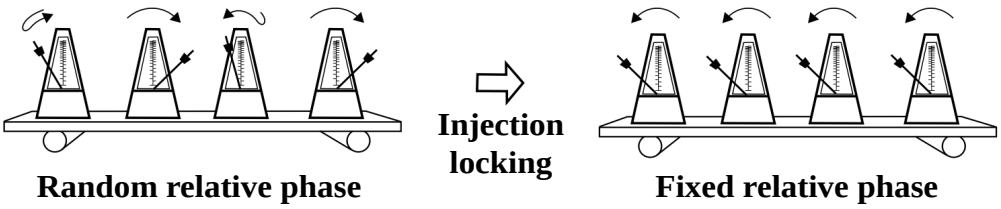


Figure 6.1: Injection locking of metronomes on a rolling board. *Image reproduced with permission of original author* [157].

laser. The resulting paper marked the first reported demonstration of OIL. This was followed, in the 1970s, by a demonstration of OIL using CO_2 lasers by Buczek [164]. The first detailed theoretical and experimental study of OIL with semiconductor (AlGaAs) lasers was performed by Kobayashi and Kimura in the 1980s [165], [166]. It was in this same decade that Lang published the OIL rate equations for semiconductor lasers [167], which were experimentally confirmed with lasers at 0.85 μm and 1.3 μm by Mogensen [168], and with InGaAsP lasers at 1.55 μm by Henry [169]. Demonstrations of OIL have closely followed historical laser developments. This is because OIL has been shown to improve laser performance for a variety of applications [170], [164], [171], [172], [173]. At 2 μm, the only previous demonstration of OIL was used in the transmitter to improve the single mode operation (SMO) of a directly modulated laser and enable advanced modulation formats [125]. Thus, OIL is a key enabling technology for laser applications in optical communication systems and could provide promising improvements for this new transmission window at 2 μm.

6.1.3 Key concepts

OIL occurs when light from one laser p (called the primary laser, with main lasing mode centred at the wavelength λ_p or carrier frequency f_p) is injected into the cavity of another laser s (called the secondary, with main lasing mode at λ_s or f_s). When the light from the primary laser is injected into the secondary cavity, the secondary laser's internal field will be forced to change from its free-running value. This only occurs when the fields are sufficiently close. As such, for a certain range of frequencies, the primary laser can force the secondary laser to oscillate at the same frequency as (and at a fixed phase relative to) the primary. The range of values for which the secondary laser's

frequency is the same as the primary's is called the locking range and the width of this range is often referred to as the OIL bandwidth.

The OIL bandwidth is one of the key figures of merit used to evaluate performance in OIL schemes. In optical communications, the term bandwidth is used in a variety of contexts. Optical bandwidth can be specified in terms of frequency ($\Delta\nu$) or wavelength ($\Delta\lambda$), due to the inverse relationship between the two. It is more commonly stated in frequency units. Generally, bandwidth refers to the maximum width of an optical frequency range in which an optical component, system of components or phenomenon operates. For example, the width of the optical frequency range that can be transmitted by some element (e.g. an optical fibre), the width of the gain region of an optical amplifier (e.g. a TDFA), the width of the frequency range of some other optical phenomenon (e.g. OIL).

In OIL schemes, certain characteristic features are used to identify the OIL bandwidth, or locking range. For instance, near the locking range, f_s is shifted or 'pushed' towards f_p. This frequency influencing is a common feature observed around the boundary of the locking range in most OIL cases. Then, within the locking range, f_s has been pulled enough that it matches f_p and the frequencies become locked, with a fixed relative phase maintained between the primary and the secondary lasers [170]. Inside the locking range, it is commonly said that the primary has 'captured' the secondary and, in this case, if f_p is changed, f_s will follow. This single frequency emission (i.e. $f_p = f_s$) characterises stable OIL. When the detuning (the absolute difference between the main lasing mode of the primary laser and main lasing mode of the secondary laser, (i.e. $|f_p - f_s|$) exceeds a certain value, the lasers will unlock and at this point the secondary no longer follows the primary. This pattern of (i) frequency influencing, (ii) followed by a region of single frequency emission and then (iii) a return to unlocked behaviour, is used to identify regions of OIL in this chapter.

In the case of the experiments in this thesis, different dynamics were observed depending on which laser was tuned (i.e. primary vs. secondary) and also depending on the direction of tuning (i.e. decreasing vs. increasing) towards the region of OIL. Hence, Section 6.3.1 and Section 6.3.2 are divided into four sections:

- Section 6.3.1 OIL by increasing the primary laser λ_p

- Section 6.3.1 OIL by decreasing the primary laser λ_p
- Section 6.3.2 OIL by increasing the secondary laser λ_s
- Section 6.3.2 OIL by decreasing the secondary laser λ_s

6.2 OIL experiment

In order to demonstrate OIL at 2 μm, an experiment was designed to ensure:

(i) one laser could be injected into another laser,

(ii) the emission wavelengths of the lasers could be tuned close enough to investigate OIL dynamics between the two,

(iii) the coupled output of both lasers could be monitored in order to identify and measure regions of OIL.

6.2.1 Selecting 2 μm lasers

Selecting lasers for OIL is not straightforward at 2 μm, as the availability of lasers is limited in this wavelength region. Table 4.1 and Table 4.2 in Chapter 4, and Table 5.1 in Chapter 5, list the full set (first, second and third generation, respectively) of slotted Fabry-Pérot lasers readily available for the 2 μm OIL demonstration [25]. Most of these lasers were unsuitable to operate as a secondary laser. This was because the second and third generation of lasers were developed with dual isolators, which blocked most light input to the laser cavity (as well as preventing any back reflections from the output of the laser back into the laser cavity). These dual isolators made lasers from the second and third generation unsuitable for external injection. In comparison, the first generation of lasers were not developed with an isolator. Therefore, the secondary laser needed to be chosen from the first generation of devices (to fulfil requirement (i) above), further limiting the availability of suitable lasers for the OIL scheme.

Selection of the primary laser did not have the same restrictions (as the primary's role was only to output light, not have light incident upon it). However, it was required for the OIL demonstration that the emission wavelengths of both lasers could be tuned close to one another (to fulfil requirement (ii) above). Based on these requirements, a laser from the first generation was selected to be the secondary (module S/N YE1699) and a laser

Table 6.1: Free-running settings for the OIL lasers.

Module S/N	λ_p	T_p	I_p
-	*(nm)*	*(°C)*	*(mA)*
YE1922	1995.50	41.1	35.0

Module S/N	λ_s	T_s	I_s
-	*(nm)*	*(°C)*	*(mA)*
YE1699	1995.05	10.0	14.3

from the second generation was selected to be the primary (module S/N YE1922). These two lasers were the same as those used for the 50 GHz DWDM investigation in Section 5.3 of Chapter 5. It had been previously established (for example, Figure 5.16 in Chapter 5) that the emission wavelengths of these two lasers could be tuned to overlap with one another with reliable performance (in terms of tunability and stability). In this way, two slotted Fabry-Pérot lasers were chosen as the primary and secondary lasers for the OIL demonstration.

Figure 6.2 shows the free-running optical spectra of the two slotted Fabry-Pérot lasers chosen as the primary and secondary for the OIL demonstration. The settings for these lasers (as they are shown in Figure 6.2) are listed in Table 6.1 in terms of the wavelength (λ), temperature (T) and current (I) values for the primary (p) and secondary (s) lasers. As shown in Figure 6.2, the primary laser was measured to have a free-running $SMSR_p$ = ~35 dB, and an $SMSR_s$ = ~30 dB was recorded for the secondary. Non-lasing side modes of the secondary laser were measured at 1994.03 nm and 1996.05 nm in Figure 6.2. OIL to the side modes is investigated later in the chapter. In this case, the free-running optical spectra serve as a comparative reference for the coupled dynamics.

It was desired that the emission wavelengths of the two lasers could be tuned close enough to investigate OIL dynamics between the primary and secondary (requirement (ii), Section 6.2). In many OIL schemes, a highly tunable laser (e.g. with 100 nm tunability) is used as the primary laser [155]. However, such tunable lasers are not widely available at 2 μm, hence it was necessary to tune the operating wavelength of the lasers by adjusting the temperature. To minimise instabilities when tuning with temperature, a laser controller (ILX LDC 3900) was used, with a stability of $<\pm 0.01$°C. This LDC enabled control of up to four lasers simultaneously, but independently. The lasers were fully characterised in terms of thermal tunability (and power variation) over the

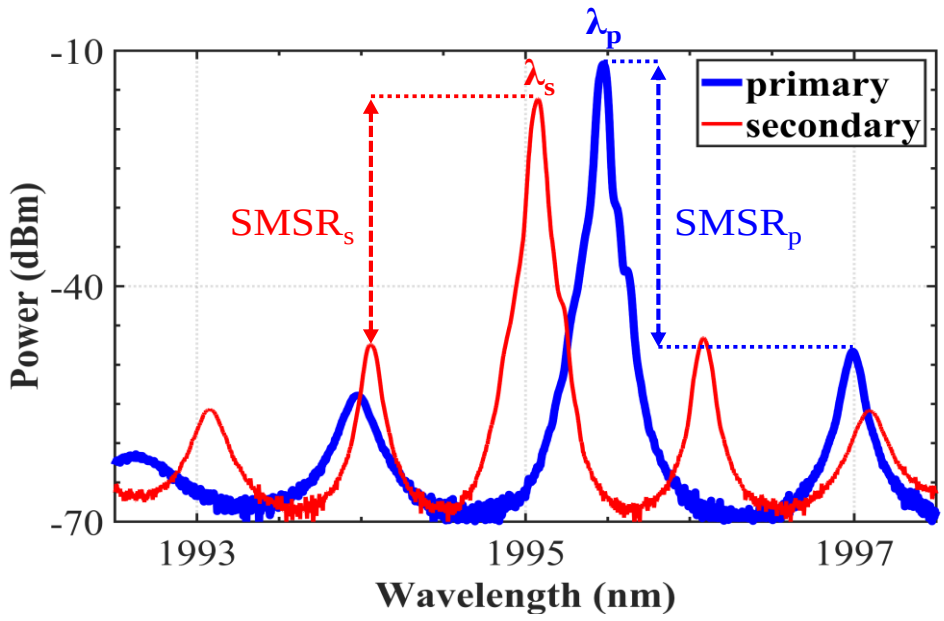
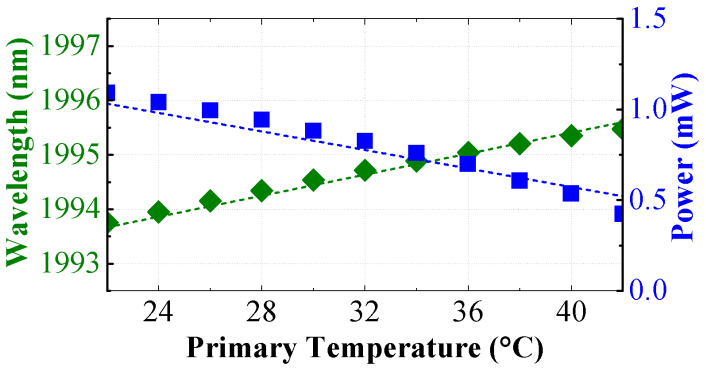


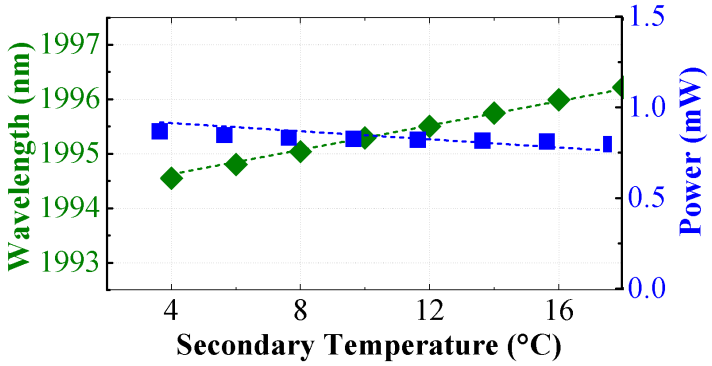
Figure 6.2: Free-running optical spectra of both lasers used for OIL, depicting the primary in blue (thicker line) and the secondary laser in red.

range of temperatures used in this demonstration; 22.0°C to 42.0°C for the primary laser, and 3.5°C to 16.5°C for the secondary laser, (in steps of 2.0°C in each case). These temperature ranges were chosen to ensure that the main mode of each laser could be tuned to overlap with the other around the wavelength of 1995 nm (as shown in Chapter 5, Figure 5.16).

The results of this thermal characterisation are shown in Figure 6.3. In both figures, the green data (diamond points) corresponds to the left y-axis (wavelength in nm) and the blue data (square points) corresponds to the right y-axis (power in mW), with temperature in °C on the x-axis. The scatter points show the data recorded and the dashed lines represent a linear fit to this data. The threshold current for both lasers was ~15 mA at 20°C (this value was reduced at lower temperatures), with 100 mA maximum operational current for both devices. Both lasers were fixed at 60 mA for the thermal characterisation. For the variation of the laser wavelength (λ) with temperature (T), the linear fit to this data shows $\Delta\lambda/\Delta T_p$ =0.10 nm/°C for the primary and $\Delta\lambda/\Delta T_s$ =0.11 nm/°C for the secondary, matching the expectations of $\Delta\lambda/\Delta T$ =0.1 nm/°C, as per [25]. These figures are important because they form the basis of the wavelength sweeps used in the later sections of this chapter. The narrow window of main-mode overlap in the region of 1994.50 nm to 1995.50 nm can be seen here by comparing the green



(a)



(b)

Figure 6.3: Wavelength and power characterisation of the OIL lasers, with respect to temperature (both at 60 mA constant current).

line in both plots.

As first and second generation 2 μm devices, the power of these lasers was low at ~1 mW (in comparison to ~5 mW to 20 mW standard at 1.55μm). The variation of the laser power (P) with temperature is shown by the blue data, corresponding to right y-axis in Figure 6.3a and Figure 6.3b. The blue dashed line represents a linear fit to this data, with $\Delta P/\Delta T_p = -0.03$ mW/°C for the primary and $\Delta P/\Delta T_s = -0.01$ mW/°C for the secondary, indicating that both lasers lose power with increasing temperature. This power penalty, in conjunction with the narrow (~1 nm) window of wavelength overlap and limited 0.1 nm/°C tunability indicates the challenges of using these lasers in an OIL system.

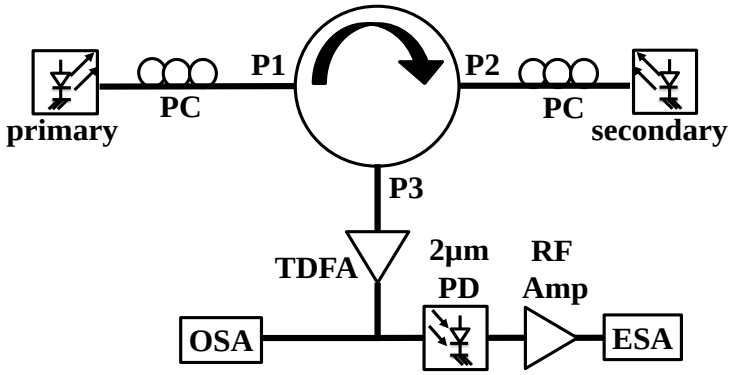


Figure 6.4: Optical injection locking setup.

6.2.2 Experiment design

Once the primary and secondary lasers had been selected, the next step was to design an experiment to enable light injection from the primary into the secondary, monitoring of the coupled output from the lasers, and measurement of any OIL dynamics observed therein. The resulting experiment schematic is shown in Figure 6.4 (and is typical for many OIL schemes [155]). The fibre-coupled outputs of both lasers were spliced with polarisation controllers (PC). The polarisation of both lasers was aligned to ensure optimal OIL was achieved and then not adjusted for the duration of the experiment. The bias current of both lasers was also fixed throughout the demonstration (both lasers were operated above threshold current to ensure lasing), with the primary at 35 mA and the secondary laser biased at 14.3 mA.

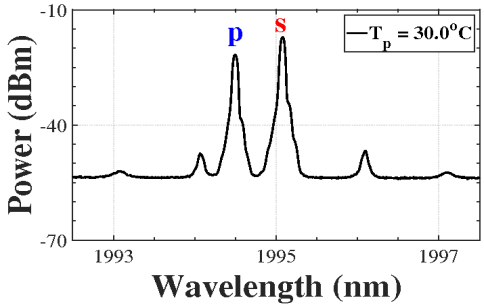
An optical circulator (FCIR-2000 N-L-1) was used to couple the light from the primary laser into the secondary cavity. An optical circulator comprises three ports (P1, P2 and P3) with isolating mechanisms in-between. The circulator allows light to travel in the direction from P1 to P2 and from P2 to P3, but not the other way around. In this way the primary laser is isolated from light injection from the secondary. This circulator had an insertion loss of 1.8 dB for P1 $\rightarrow$ P2, 3.8 dB for P2 $\rightarrow$ P3, and 16 dB of isolation for P3 $\rightarrow$ P2 and P2 $\rightarrow$ P1 (all measured at 1993 nm). The increased insertion loss from P2 $\rightarrow$ P3 was due to the splicing losses between the fibre from the circulator and the fibre connection to the PC. The output from P3 of the circulator was amplified using a TDFA, to increase the output power of the system, prior to detection. Thus, the circulator enabled light injection from the primary laser into the secondary, with the coupled light output at P3. OIL can be monitored via optical spectral analysis. This is achieved by observing the wavelength peaks using an optical

spectrum analyser [155]. Another way to measure OIL is by monitoring the beating frequency between the primary and the secondary lasers, which can be done using a square law detector and ESA [151]. In order to monitor OIL the coupled output of the primary and secondary lasers (from P3 of the circulator) was measured simultaneously on the OSA (Yokogawa AQ6375) and the ESA (Agilient 8565EC). Prior to the ESA, a commercially-available 2 μm InGaAs photodetector (EOT ET-5000F) with a 3 dB bandwidth of 12.5 GHz was used. An electrical amplifier (SHF 804 EA) was added to boost the signal to the ESA. In this way, the coupled light output from the primary and secondary lasers was monitored and recorded in both the optical domain (on the OSA) and the electrical domain (with the PD and ESA).

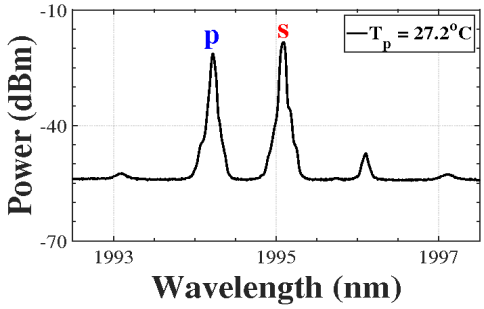
6.2.3 Observing OIL

In the optical domain, OIL is identified by the indicators discussed in Section 6.1.3: frequency influencing around the locking range and single wavelength emission within that range. The optical spectra of the coupled output at P3 of the circulator are shown in Figure 6.5, with λ_p denoted by a blue-coloured *p* for the primary and λ_s by a red *s* for the secondary. Note that, in Figure 6.5 (and the following Figure 6.6) the secondary laser settings were the same as those in free-running Figure 6.2 (i.e. T_s = 10°C and current 14.3 mA). Figure 6.5a shows the spectrum of the coupled output for T_p = 30°C, in which the individual primary and secondary laser peaks are distinct and identifiable. In Figure 6.5b, T_p = 27.2°C, the primary laser sits at the edge of the locking region (and the secondary continues to lase at 1995.05 nm). Then in Figure 6.5c, with an adjustment of 0.1° to T_p=27.1°C, OIL occurs and lasing is at λ_p only. Suppression of the other cavity modes (from the unlocked to locked states) can be seen by comparing Figure 6.5a and Figure 6.5c.

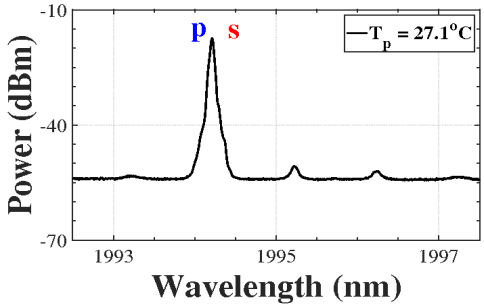
In the electrical domain, the RF power spectrum requires the use of a square-law detector, which enables a beating frequency peak to be measured at the corresponding absolute value of the detuning ($|f_p - f_s|$). As the detuning is reduced, the frequency of this beating tone will decrease up to the point at which the laser fields are sufficiently close so that OIL occurs ($f_s = f_p$), and this single frequency emission corresponds to a “quiet” region in the RF spectrum, characterising stable OIL. The electrical spectra (or RF power spectra) of the coupled output are shown in Figure 6.6. In this figure, the optical spectra are shown on the left and the corresponding electrical spectra



(a) Unlocked.



(b) Edge of locking range.



(c) Locked.

Figure 6.5: Optical spectrum of coupled primary and secondary lasers, showing OIL to the side mode in (c).

are shown to the right in each case, for T_p increasing from 35.0°C to 38.0°C.

In Figure 6.6a and Figure 6.6c, the optical spectra are shown for T_p = 35.0°C and 36.0°C, respectively, as λ_p is red-shifted towards λ_s. In the corresponding electrical spectra, Figure 6.6b and Figure 6.6d, beating frequency peaks at 8.9 GHz and 4.6 GHz, respectively, as T_p increases and the detuning reduces. Figure 6.6e shows injection locking at T_p = 37.5°C, single wavelength emission is observed ($\lambda_p = \lambda_s$) and in Figure 6.6f, no beating peak is recorded inside the locking region. In Figure 6.6g, T_p = 38.0°C and the primary laser

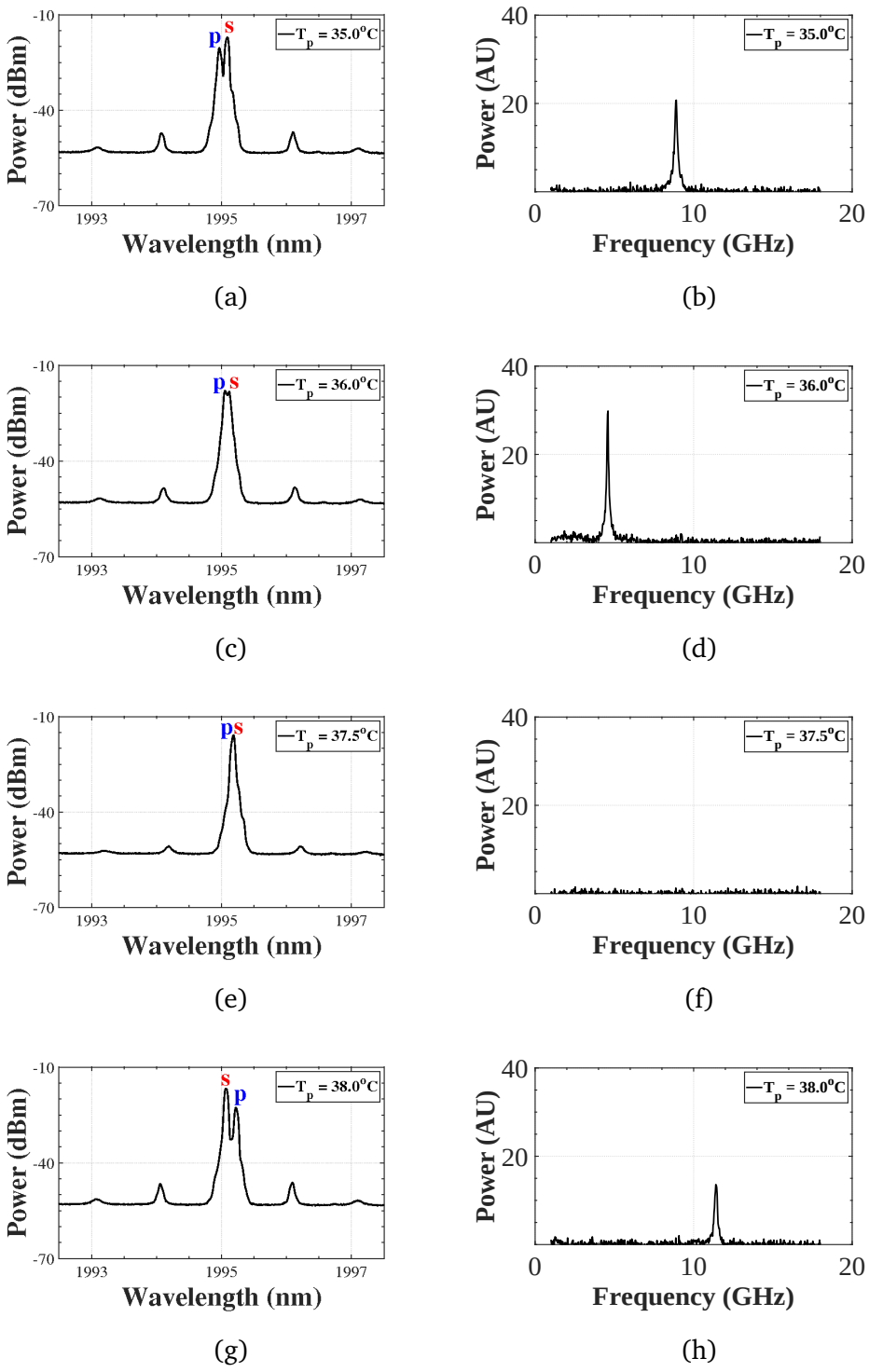


Figure 6.6: Spectra of coupled primary and secondary lasers, showing OIL to the main mode in (e) and (f). Optical spectra are on the left with the corresponding electrical spectra to the right, for increasing T_p from 35.0°C to 38.0°C.

has moved out of the locking region. The lasers have unlocked and, in Figure 6.6h, a beating peak reappears at 11.4 GHz. This 11.4 GHz peak is

relatively weak due to the limited operating range of the PD.

6.3 Stable OIL at 2 μm

This section looks at the OIL dynamics in more detail over larger tuning ranges. As mentioned in the chapter introduction, experimental OIL investigations with the lasers (discussed in Section 6.2.1) revealed different dynamics depending on which laser was tuned (i.e. primary vs. secondary) and also depending on the direction of tuning towards the region of OIL (i.e. decreasing vs. increasing). Hence, in this section, the findings are split between these four different scenarios.

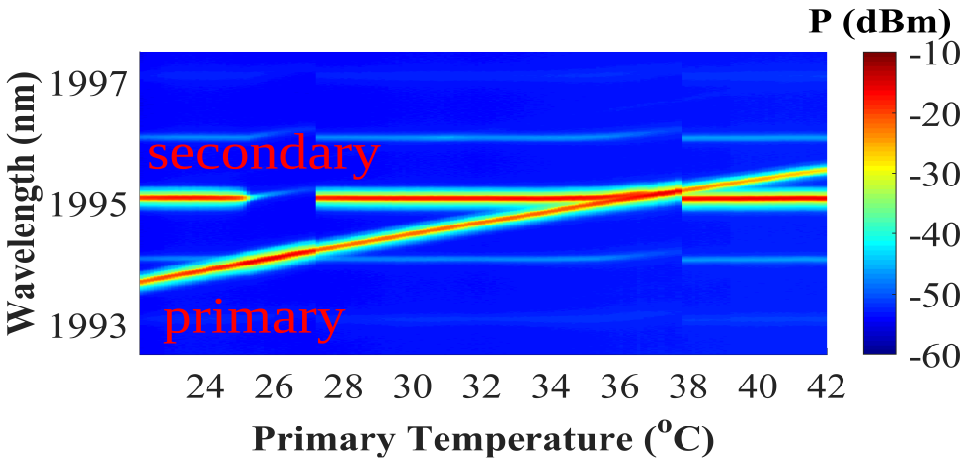
6.3.1 Tuning the primary laser

Increasing λ_p

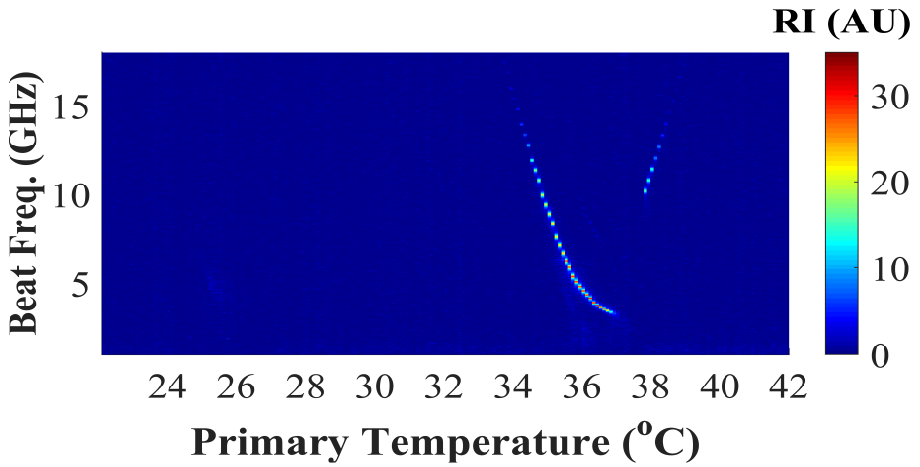
The primary laser wavelength (λ_p) was tuned by increasing temperature (T_p) from 22.0°C to 42.0°C in steps of 0.1°C, while the secondary temperature (T_s) was kept constant at 10.0°C, as per Figure 6.2, with accuracy as discussed in Section 6.2.1.

An optical spectrum of the coupled output from P3 of the circulator was recorded for each 0.1°C increment. Figure 6.7a shows a false colourplot of all these optical spectra combined. Essentially, this figure shows a combination of each optical spectrum (such as those in Figure 6.5 and Figure 6.6), stacked like sheets of paper and colour-coded so the optical power at each point is visible, making the relative peaks clearer. This relative optical power (P) of the peaks is denoted by the colourbar on the right, with red indicating more intense optical power and blue representing less intensity.

These false colourplots enable visualisation of the coupled laser dynamics. Looking from left to right in Figure 6.7a, for example, it can be seen that increasing primary temperature on the x-axis corresponds linearly to increasing primary wavelength on the y-axis, as expected as per Section 6.2.1. The secondary wavelength was fixed at λ_s = 1995.05 nm throughout. OIL of the secondary laser to the primary can be seen when the main lasing mode of the primary overlaps with the side mode of the secondary laser at 1994.05 nm. Within this range, the secondary's main mode is suppressed and lasing occurs at λ_p only. This region of SMO can be observed from T_p = 25.2°C to 27.2°C.



(a) Optical domain. Colourbar = optical power (P) in dBm.



(b) Electrical domain. Colourbar = relative intensity (RI) in arbitrary units.

Figure 6.7: The wavelength of the primary laser was swept across the fixed secondary by increasing T_p from 22.0°C to 42.0°C. Figure 6.7 shows false colour-plot combinations of each 0.1°C measurement overlaid.

The secondary laser is locked to the primary laser and when λ_p is changed, λ_s will follow. The combined injected peak at $\lambda_s = \lambda_p$ is of greater intensity than the secondary or primary peaks previously. It can also be seen that the side modes of the secondary laser are suppressed and following the primary laser, demonstrating that OIL affects the laser cavity as a whole. Outside the locking

region, at T_p = 27.2°C, the secondary laser unlocks, with lasing returning to the secondary's main mode at λ_s = 1995.05 nm and the secondary no longer following the primary. It is in this way that the false colourplots enable identification of the OIL region around the side mode.

Now examining the region around the main mode, as the primary laser λ_p moves towards the main mode of the secondary laser λ_s in Figure 6.7a, the effects of OIL can be observed around 35.9°C to 37.8°C. Again, the characteristic identifiers of an OIL region can be seen: suppression and pushing of the side modes, the secondary laser follows the primary and the injected peak is of greater intensity. At 37.8°C the unlocking boundary is very clear in the optical domain. Note, around the locking boundary, the separate secondary and primary laser peaks may not be distinguishable due to the resolution of the OSA which was 0.05 nm (or ~3.75 GHz at 2 μm), making determination of the locking/unlocking regions around the main mode difficult on the OSA. Hence, it was decided that a more accurate measurement to verify OIL at the main mode would be to utilise the ESA. Thus, while the optical spectrum of the coupled output from P3 was recorded for each ΔT_p = 0.1°C increment from 22.0°C to 42.0°C, the power spectrum was simultaneously acquired via the square law detector.

With the aim of identifying the beating peaks, the ESA trace was set to the 'max hold' mode, which maintains the highest amplitude value in each measurement interval (30 seconds in this case) and displays this value in the trace point. Noise is detected in the same manner using max hold since noise is just another signal. Due to the random nature of noise, one sweep may not be sufficient to capture the noise dynamics. Therefore, by enabling the ESA in max hold mode, an array of random noise events are captured. This raises the apparent overall noise floor of the captured data. But, upon analysis of the data, it was found that the recorded noise floor was higher at lower frequencies and this tilted shape made it difficult to determine the beating peak, especially when the detuning reduced towards zero. In order to distinguish the beating peak at lower frequencies, the noise data was isolated by repeating the experiment with the lasers turned off. This noise data was then subtracted from the data with the lasers turned on. This subtraction resulted in an RF power spectrum with a relatively flat 'noise floor' (now adjusted), from which the beating peak could be clearly distinguished and its value recorded. Figure 6.7b shows a false colourplot combination of all these power spectra, with the adjusted beating frequency on the y-axis and the

temperature of the primary laser on the x-axis, where again the secondary laser was fixed at 10.0°C.

While these false colourplots of the ESA enabled visualisation of the coupled laser dynamics around the main mode, the dynamics at the side mode could not be visualised due to the limited bandwidth of the PD. Also, the power of the side mode was much less than the main lasing mode, making any beating between the two difficult to detect. Looking at from left to right in Figure 6.7b, moving towards the side mode of the secondary laser, no beating peaks were detected around the locking region at T_p = 25.2°C to 27.2°C. This is due to the limited 3 dB bandwidth of 12.5 GHz PD used with the ESA. 12.5 GHz corresponds to 0.17 nm at the 2 μm. Since the detuning between the secondary and laser peaks was >0.17 nm around this locking range, beating frequency peaks were not recorded in this region. So, while there would be beating between the primary laser and the suppressed main mode of the secondary laser in this regime, since the mode separation is around ∼1 nm, this would correspond to a beating signal of approximately 75 GHz, which is significantly outside current limits of detection.

As the primary was tuned towards the main mode of the secondary laser, the detuning was reduced to within the bandwidth of the detector and a beating peak was detected in Figure 6.7b. Initially, the frequency of this beating peak reduced linearly towards zero with increasing primary temperature, as per $\Delta\lambda/\Delta T$ =0.1 nm/°C. However, near the locking region, the relationship no longer followed the linear pattern and the effect of the primary laser influencing the frequency the secondary and pushing the secondary to match its frequency could be seen. When the laser fields were sufficiently close, single frequency emission was observed ($f_s = f_p$) and no beating peak was recorded on the ESA between T_p = 36.9°C to 37.8°C. Thus, stable OIL was observed, with no other frequencies recorded in this region. When the primary laser was tuned beyond the locking region, the beating peak returned and the frequency increased linearly with increasing temperature. In the case of the ESA signal, we have a clearly defined beating peak curve corresponding to the locking region around the main mode. The beating peak curve serves to show a well-defined transition from beating between the primary and secondary, to stable OIL and unlocking/return to beating. These transition points allow for an accurate measurement of the stable OIL bandwidth for injection around the main mode.

However, such an accurate measurement is not as easily obtained at the side mode region. The difference in powers between the primary laser main mode and the non-lasing side mode (such as the case of injection into the non-lasing side mode from T_p = 25.2°C to 27.2°C in Figure 6.7) makes the transition points harder to detect. While the presence of SMO and improved SMSR in the optical spectrum potentially indicate OIL, since the beating signal in the RF power spectrum is beyond the detector bandwidth, it is difficult to accurately determine the OIL bandwidth in the same way. Therefore, in the case of side mode injection (where beating signals could not be recorded), a region of SMO can only be estimated, rather than a classic stable OIL region, or OIL bandwidth. Fortunately, in the intended application of the OIL system investigated here (namely its implementation as a demultiplexer in a DWDM system), it is the width of the SMO region, rather than the OIL bandwidth, which is of primary concern.

The region of SMO at the side mode and OIL bandwidth at the main mode was calculated by converting the width in temperature (for example T_p = 25.2°C to 27.2°C is 2°C width) to wavelength (in nm) using the $\Delta\lambda\backslash\Delta T$ characterisation and then converting this to frequency using Equation 6.1, where $\Delta\lambda$ = wavelength range, $\Delta\nu$ = frequency range, c = speed of light in vacuum and λ = 2 μm. The error value was taken as the temperature step (0.1°C) and this was converted in the same way.

$$\frac{\Delta\lambda}{\Delta\nu} = \frac{\lambda^2}{c} \tag{6.1}$$

Decreasing λ_p

The same experiment was then repeated for decreasing the wavelength of the primary laser (via its temperature). The false colourplot images for this section can be found in Figure A.1 of Appendix A. Similar results were observed in Figure A.1 with the notable difference being that, for decreasing T_p, the region of SMO at the secondary laser's side mode was (12.0 $\pm$ 0.7) GHz, compared to (15.0 $\pm$ 0.7) GHz for increasing T_p. Similarly, the stable OIL bandwidth at the main mode was (3.7 $\pm$ 0.7) GHz for decreasing T_p, compared to (6.7 $\pm$ 0.7) GHz for increasing T_p. This hysteresis is typical in OIL schemes with semiconductor lasers. In semiconductor lasers, the gain spectrum is often asymmetric (with respect to the gain spectrum peak), giving rise to asymmetric tuning characteristics [174], [167], [175], [168], [169].

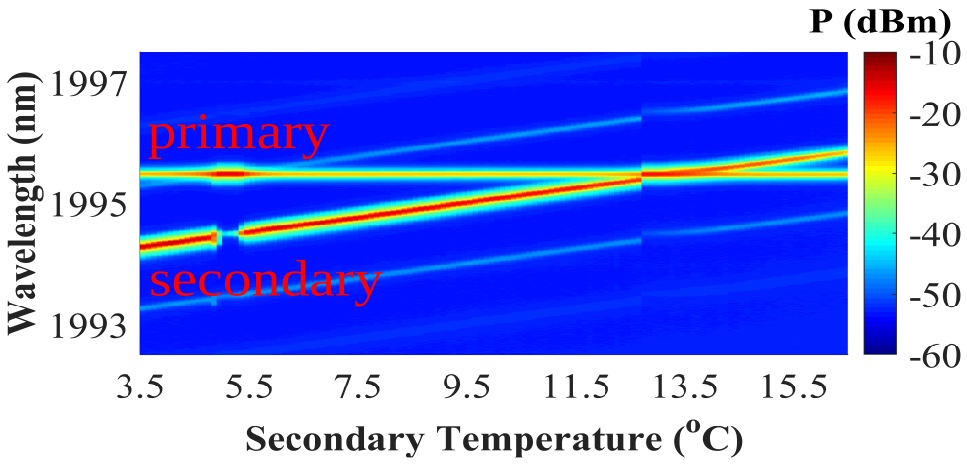
6.3.2 Tuning the secondary laser

In order to implement OIL as a demultiplexing mechanism in a DWDM optical communication system, it would be necessary to tune the secondary laser rather than the primary laser. In such a scenario, the receiver would incorporate a secondary laser that would tune to the incoming DWDM primary signal. Thus, a reversal of the above experiment was performed, this time adjusting the secondary laser, while keeping the primary laser constant, in order to investigate if the performance would be similar.

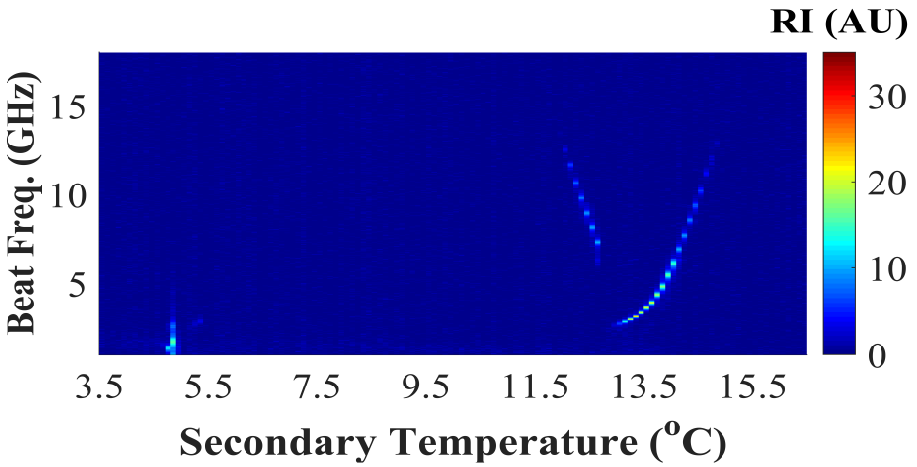
Increasing λ_s

Initially, the secondary laser wavelength was tuned by increasing temperature from 3.5°C to 16.5°C in steps of 0.1°C, while the primary temperature was kept constant, as per Figure 6.2, at 41.1°C (λ_p = 1995.50 nm), with accuracy as discussed Section 6.2.1. The resulting OSA spectrum can be seen in Figure 6.8a. In practical terms, this section: increasing the secondary wavelength (from 1994.30 nm) while holding the primary constant (at 1995.50 nm) in Figure 6.8, can be compared to Section 6.3.1: decreasing the primary (from 1995.60 nm) while keeping the secondary constant (at 1995.05 nm) in Figure A.1, as both methods change the detuning in the same fashion.

However, when comparing the figures for decreasing the primary temperature in Figure A.1 to those for increasing the secondary temperature in Figure 6.8, some differences can be seen. In Figure 6.8, for example, the effects of OIL of the secondary laser to the primary can be observed from T_s = 4.9°C to 5.3°C, when the side mode of the secondary overlaps with the main mode of the primary laser. This region of SMO is significantly reduced to (3.0 $\pm$ 0.7) GHz in comparison to the same region which measured (12.0 $\pm$ 0.7) GHz in Figure A.1. This decrease (in the case of increasing secondary temperature, compared to decreasing primary temperature in Section 6.3.1) may be due to a reduction in the injection ratio. The primary laser has a higher power penalty for temperature tuning ($\Delta P/\Delta T_p$ = - 0.03 mW/°C), in comparison to the secondary laser ($\Delta P/\Delta T_s$ = - 0.01 mW/°C), as per Section 6.2.1. Therefore, the injection ratio for the range in this section: T_s = 3.5°C to 16.5°C with T_p = 41.1°C would likely be lower compared to the range in Section 6.3.1: T_p = 22.0°C to 42.0°C with T_s = 10.0°C. The relation between injection ratio and OIL is investigated in further detail in Section 6.3.3.



(a) Optical domain. Colourbar = optical power (P) in dBm.



(b) Electrical domain. Colourbar = relative intensity (RI) in arbitrary units.

Figure 6.8: The primary was then fixed and the wavelength of the secondary laser swept by increasing T_s from 3.5°C to 16.5°C. Figure 6.8 shows false colour-plot combinations of each 0.1°C measurement overlaid.

Other differences include high intensity features observed in Figure 6.8b in the power spectrum of the laser around 4°C, which may correspond to nonlinear dynamical behaviour close to the OIL boundary of the lower wavelength side mode. The analysis of such features was not in the scope of this thesis and can be found in references: [176], [177], [178]. Another notable difference

between Figure A.1b and Figure 6.8b is the shape of the ESA beating peak curve. However, this beating peak curve for increasing secondary temperature can be mapped almost exactly onto the beating peak curve for decreasing primary temperature if flipped by 180 degrees. In the case of tuning the secondary while fixing the primary (vs. tuning the primary while fixing the secondary), it is proposed that the beating dynamics are similar but the regions of linearity and frequency 'pushing' are reversed.

Decreasing λ_s

Finally, the secondary wavelength was decreased (from 1995.90 nm) while holding the primary constant (at 1995.50 nm). The false colourplot images for this section can be found in Figure A.4 of Appendix A. This scenario for decreasing the secondary while keeping the primary fixed (Figure A.4) can be compared to increasing the primary while keeping the secondary fixed (Figure 6.7). In previous experiments in this chapter, decreasing the primary wavelength to reduce detuning resulted in a reduction in the OIL bandwidth (in comparison to increasing primary wavelength). Less of a reduction in the OIL bandwidth was seen for decreasing the wavelength in this case, with the region of SMO at the side mode measured to be the same in each case, (3.0 $\pm$ 0.7) GHz for both increasing and decreasing T_s. Slight broadening in the OIL bandwidth was recorded at the main mode with (4.5 $\pm$ 0.7) GHz for decreasing T_s and (3.0 $\pm$ 0.7) GHz for increasing T_s. This further demonstrates that when tuning the secondary rather than the primary, the injection dynamics are similar but reversed.

Ideally, for demultiplexing purposes, there would be an improvement in channel isolation in the identified regions of SMO. To investigate the impact of OIL on the channel isolation, the SMSR and OSNR of the primary signal are used as figures of comparison in this section. The OSNR was calculated by analysing the OSA spectrum and the power ratio between the primary signal peak at centre wavelength and the median noise level (~ -53 dBm, across a 5 nm span). The SMSR was taken as the power ratio between the primary signal and the highest power side mode, for consistency between the regions with/without SMO. The results of these calculations can be seen in Table 6.2. The T_s values chosen were those which maximised SMSR and OSNR values in each region. As can be seen from Table 6.2, the SMSR improved from $\sim$20 dB in the region without SMO (at $T_s = 7.5$°C) to $\sim$32 dB in the region with SMO

Table 6.2: SMSR and OSNR results corresponding to T_s values inside and outside the two recorded regions of SMO from Figure A.4a

T_s(°C)	SMO	SMSR (dB)	OSNR (dB)
7.5 ± 0.1	No	20 ± 1	26 ± 1
12.3 ± 0.1	No	22 ± 1	28 ± 1
5 ± 0.1	Yes	32 ± 1	37 ± 1
12.5 ± 0.1	Yes	34 ± 1	36 ± 1

(at $T_s = 5$°C). Likewise, in this case, the OSNR improved from ~26 dB to ~37 dB, respectively, resulting in an improvement of 12 dB in SMSR and 11 dB in OSNR. Similar figures were recorded around the second region of SMO at 12.5°C, with an OSNR improvement of 8 dB in this case. These SMSR and OSNR improvements indicate that implementing OIL techniques into 2 μm DWDM systems could improve laser performance and also increase channel isolation in the receiver.

6.3.3 Further OIL analysis

Table 6.3 summarises the results from the four OIL scenarios depending on increasing/decreasing temperature for the primary or secondary lasers (T_p/T_s). The width of the SMO at the side mode (SM) and OIL bandwidth at the main mode (MM) is given in GHz for each case. Locking bandwidths of ~10 GHz are standard for semiconductor lasers [179]. This summary again shows that, due to the low flexibility of operating conditions of the two lasers, the OIL bandwidth is compromised when the secondary is tuned to the primary rather than vice versa. Nevertheless, stable OIL was observed in all cases.

Injection Ratio

In Section 6.3.2, it was discussed that the observed decrease in OIL bandwidth (when tuning the secondary laser vs. tuning the primary in Section 6.3.1) may be due to a reduction in the injection ratio. For this reason, the relation between injection ratio and OIL bandwidth is investigated in further detail in this section. Typically, the OIL bandwidth will increase if the ratio of injected primary power to secondary power (called the injection ratio) is increased [180], [181].

In the experiments performed here, the primary laser was tuned to higher temperatures (around 40°C) in the region of overlap compared to the

Table 6.3: Summary of the results from the four OIL scenarios depending on increasing/decreasing temperature of the primary/secondary laser (T_p/T_s). The width of the SMO region at the side mode (SM) and OIL bandwidth main mode (MM) is given in GHz for each case.

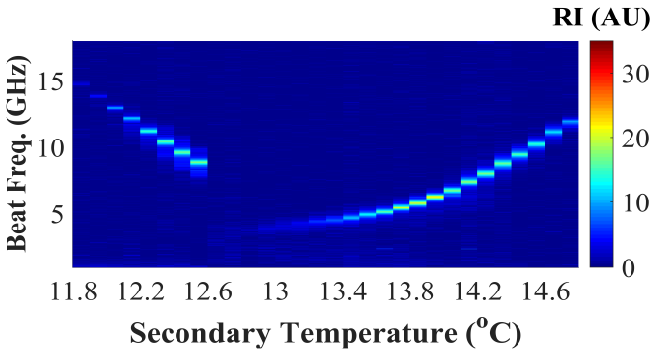
T_p	T_s	**SMO SM (GHz)**	**OIL MM (GHz)**
Increased	Fixed	15.0 ± 0.7	6.7 ± 0.7
Decreased	Fixed	12.0 ± 0.7	3.7 ± 0.7
Fixed	Increased	3.0 ± 0.7	3.0 ± 0.7
Fixed	Decreased	3.0 ± 0.7	4.5 ± 0.7

secondary laser (around 10°C) within this window, which meant that the secondary laser presented higher power (since both lasers suffered power penalty with increasing temperature, as per Figure 6.2). For this reason, it was difficult to obtain an injection ratio >0 dB, where the primary laser was more powerful than the secondary. Therefore, as a proof of principle, decreasing injection ratios were investigated. In this way, one would expect that as the injection ratio is decreased, the OIL bandwidth should also decrease.

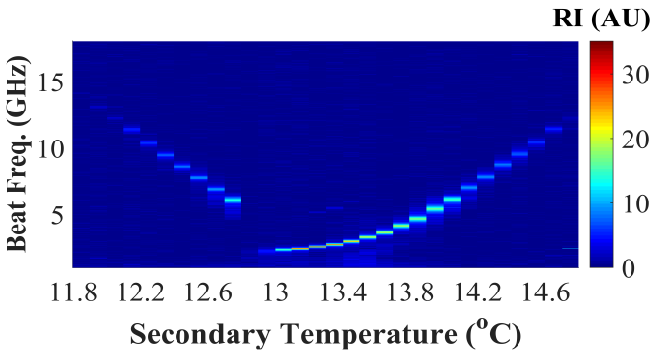
The injection ratio is typically defined as the ratio between the injected power from the primary laser and the optical power of the free-running secondary laser. However, as an initial investigation in this case, the injection ratio was taken as the ratio of the primary laser peak power to the secondary laser peak power at 1 nm distance apart on the coupled optical spectrum, with the secondary wavelength then increased and swept across the region of the primary laser's (fixed) main mode as before.

Using this method, three distinct injection ratio measurements were made with values of approximately -3 dB, -10 dB and -17 dB. As can be seen by comparing Figure 6.9a, Figure 6.9b and Figure 6.9c, reducing the ratio of the primary power to the secondary power did result in a reduction in the stable locking range, as is indicated by the narrowing quiet region in the ESA data. The minimum injection ratio measured was -17 dB because below that value the margin of error became too large.

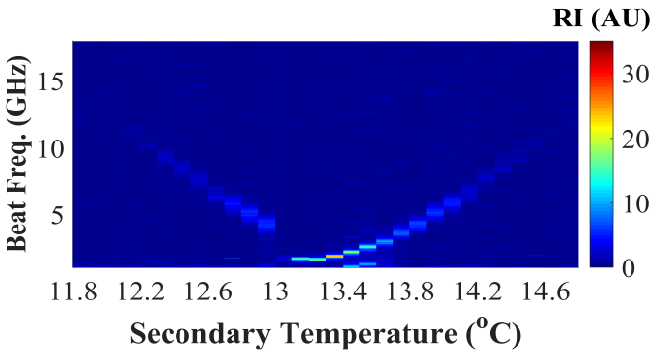
A smaller temperature increment would be needed for a more accurate measurement beyond this point. Nonetheless, a trend was established and the summarised findings are shown in Table 6.4. The injection ratio of the primary to secondary power determines the effective OIL bandwidth for an OIL system.



(a) Injection ratio of - 3 dB.



(b) Injection ratio of - 10 dB.



(c) Injection ratio of - 17 dB.

Figure 6.9: The secondary wavelength was swept across the fixed primary (by increasing T_s) for a set of decreasing injection ratios from (a) to (c).

Table 6.4: Summary of results showing the relation between injection ratio and OIL bandwidth (BW).

Ratio (dB)	**OIL BW (GHz)**
-3	2.2 ± 0.7
-10	1.5 ± 0.7
-17	0.7 ± 0.7

Stability over time

Finally, if this OIL technique were to be implemented in a DWDM transmission system, the lasers must remain locked, and not display thermal drift, over long periods of time to ensure error-free performance. This section presents a preliminary investigation into possible temperature drifts that could affect OIL as part of a DWDM transmission system, where low BERs are sensitive to small drifts in wavelength.

To test suitability for this, OIL was achieved (by decreasing T_s to 12.8°C while T_p was fixed at 41.1°C) and an automatic peak search of the ESA data was performed every 30 seconds for over 24 hours. The peak search was performed after the noise floor was subtracted from the active data. The minimum peak threshold was set to 4 GHz, as this was the approximate minimum beating peak recorded in previous measurements.

Figure 6.10 shows several snapshots of this data acquisition in 6-hour intervals. No beating peaks were detected over 24 hours, thus the lasers remained locked. By comparing the optical spectra at the start and end of this 24-hour measurement, it was also found that the lasing peak of injection locked lasers did not display any thermal drift over the time period, further indicating the suitability of these lasers for potential implementation in an optical communication system.

Chapter summary

Optical injection locking (OIL) is a technique that has been employed for demultiplexing in the 1.55 μm transmission window [40], [41], [42]. In the 2 μm transmission window, insufficient demultiplexing techniques in the receiver has been identified as a barrier to reducing channel spacing and optimising optical bandwidth in 2 μm DWDM systems. In this chapter, it was shown that OIL can effectively lock a local oscillator (secondary laser) to the

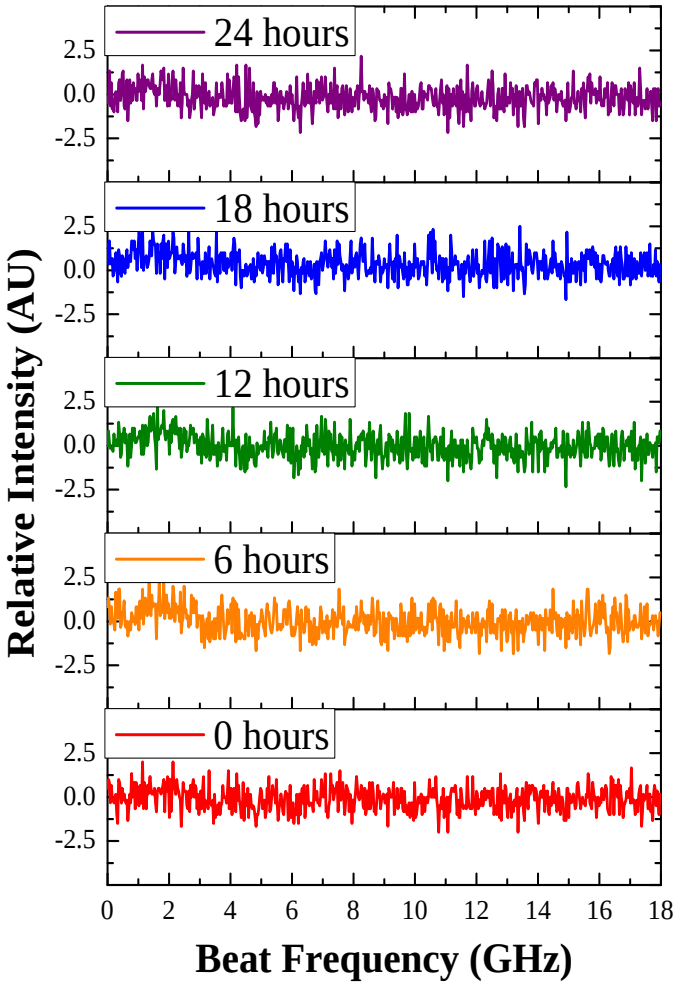


Figure 6.10: Results of stability test showing snapshots of the relative intensity vs. frequency from the ESA data, in 6 hour intervals.

incoming signal (primary laser), which may have potential applications for demultiplexing at 2 μm.

Thus, a study of stable OIL in the 2 μm wavelength region has been presented utilising InGaAs/InP slotted Fabry-Pérot lasers. Common characteristics of OIL were observed in both the optical domain and RF power spectrum, such as injection 'pushing', side mode suppression and the distinctive quiet region in the electrical domain - denoting single frequency emission and stable locking. Two locking regions were observed in each case; a region of SMO around the side mode and stable OIL at the main mode.

A maximum stable OIL bandwidth of 6.7 GHz was measured at the main mode for increasing primary temperature, with a region of SMO of 15 GHz measured

around the side mode in this case. These figures were reduced to 3.7 GHz and 12 GHz, respectively, for decreasing primary temperature, displaying OIL hysteresis. SMSR and OSNR improvements of 12 dB were recorded, indicating suitability for improving DWDM channel isolation at this waveband. In addition, as expected in OIL systems, it was found that decreasing the injection ratio (from –3 dB to –17 dB, for example) corresponded to a reduction in the locking bandwidth (from 2.2 GHz to 0.7 GHz, respectively). Finally, the lasers were shown to remain injection locked, with no thermal drift, for over 24 hours.

Chapter publications

1. **N. Kavanagh**, D. Goulding, and F. C. Garcia Gunning, **"Stable injection locking with slotted Fabry-Pérot lasers at 2 μm," Journal of Physics: Photonics**, vol. 1, p. 015005, January 2019.
   Inaugural Issue.
   doi:10.1088/2515-7647/aae7d9

2. **N. Kavanagh**, B. Murray, D. Goulding, P. E. Morrissey, R. Sheehan, B. Corbett, and F. C. Gunning, **"Enabling photonic technologies at 2 μm," in 19th International Conference on Transparent Optical Networks (ICTON)**, pp. 1–4, 2017.
   doi:10.1109/ICTON.2017.8024868

3. F. C. Garcia Gunning, **N. Kavanagh**, E. Russell, R. Sheehan, J. O'Callaghan, and B. Corbett, **"Key enabling technologies for optical communications at 2000 nm," Applied Optics**, vol. 57, no. 22, p. E64, 2018.
   Special Ireland Issue.
   doi:10.1364/AO.57.000E64

4. **N. Kavanagh**, D. Goulding, and F. C. Garcia Gunning, "**Injection Locking at 2 μm", in Photonics Ireland**, Cork, Ireland, 2018, Presentation.

5. **N. Kavanagh**, B. Murray, D. Goulding, P.E. Morrissey, R. Sheehan, B.

Corbett, and F. C. Garcia Gunning, "**Injection Locking at 2 μm", in Photonics Ireland**, Galway, Ireland, 2017, Poster.

Technical acknowledgements

The author's contribution to this chapter was the experiment design, all measurements and analysis presented.

The author would like to acknowledge:

- F. C. Garcia Gunning (Tyndall National Institute, University College Cork) for supervision and technical guidance.
- D. Goulding (Centre for Advanced Photonics and Process Analysis, Cork Institute of Technology) for technical guidance with regards to understanding OIL, interpreting results and co-authoring the Journal of Physics: Photonics publication.
- P. E. Morrissey and R. Sheehan (Tyndall National Institute, University College Cork) for help understanding OIL.
- B. Murray (Tyndall National Institute, University College Cork) for help with MATLAB visualisation of OIL.
- E. Russell (Tyndall National Institute, University College Cork) for development of 2 μm TDFAs.
- J. O'Callaghan and B. Corbett (Tyndall National Institute, University College Cork) for 2 μm semiconductor devices.
- R. Phelan, J. O'Carroll and B. Kelly (Eblana Photonics Ltd) for the 2 μm $In_{0.74}Ga_{0.26}As$ slotted Fabry-Pérot lasers.

Chapter 7

Conclusion

In this chapter, a summary of the research work presented in this thesis is discussed and the main conclusions are highlighted.

7.1 Summary

Chapter 1 introduced the context, motivation and a brief overview of the work in this thesis. The purpose of this work was to investigate the feasibility of implementing DWDM systems at 2 μm. This purpose was pursued by designing experiments to demonstrate DWDM at 2 μm and, consequently, identify any barriers involved.

Chapter 2 began with the history of optical communication, how it has developed into what we know today, and what the key enabling technologies were along the way. In the historical context, shifting transmission to longer wavelengths is not a new concept. Optical communication transmission windows have shifted from 0.85 μm in the 1970s, to 1.33 μm in the 1980s and then, finally, to 1.55 μm in the 1990s, where the focus of optical communication research and development has remained since [7]. The popularisation of the 1.55 μm wavelength window for optical communications was primarily due to three key enabling technologies; semiconductor materials for lasers and detectors, low-loss ($\sim$0.2 dB/km) standard SMF as a transmission medium, and EDFAs to enable transmission over long distances with high-gain, low-noise and minimal O-E/E-O conversion. It is the convergence of these technologies that heralds the opening of a new transmission window.

Today, these key enablers can also be found in the 2 μm wavelength region. Lasers for transmitters can be fabricated from strained InP materials (similarly, detectors for receivers can be produced) [25]. Mid-IR fibres are available, such as chalcogenide, fluoride (e.g. ZBLAN), and HC-PBGFs. HC-PBGFs are especially interesting as they have a unique 'cladding' region that consists of a honeycomb-like microstructure which confines light in the hollow core [19]. The transmission of light through air offers exciting advantages (compared to transmission through solid silica), such as the potential to reach losses as low as 0.1 dB/km [20], near-vacuum latency [21] and a reduction in the nonlinear co-efficient by up to three orders of magnitude [22]. This could lead to much higher power-handling capabilities and, consequently, higher achievable capacities (up to four times the current limits) [23]. Finally, doped fibre amplifiers based on thulium (rather than erbium) offer a bandwidth of 30 THz in the wavelength region of 2 μm (double that of EDFAs at 1.55 μm) [26].

With key enabling technologies identified in Chapter 2, Chapter 3 provides an introduction to implementing these technologies in an optical communication system at 2 μm. As such, the essential components (in the transmitter and receiver), parameters (such as BER and OSNR) and considerations (for example, choice of modulation format) were discussed. A brief overview of the evolution of 2 μm systems was presented, from single channel (with limited 8 Gbit/s) [123], to increasing the number of channels (employing WDM), implementing advanced modulation formats and pushing the data rate further [124]. In 2014, prior to this thesis, the record capacity for a 2 μm system was 30 Gbit/s [125].

The challenge of increasing capacity at 2 μm was addressed in Chapter 4, with 100 Gbit/s system capacity achieved [126]. This factor-of-three capacity increase was enabled by an improved systems design (doubling the number of WDM channels), incorporating components with better frequency response (such as new lasers, MZM and PD), and optimising the devices throughout the setup to operate at higher data rates. 2 μm transmission was demonstrated over 1.15 km of HC-PBGF (nearly four times further than previous records) and also 1 km of SCF, with error-free performance recorded in both cases [126]. However, within a given bandwidth, the capacity of a WDM system depends on how closely optical channels can be packed in the wavelength domain.

The challenge of improving spectral efficiency was addressed in Chapter 5.

The goal for the experiments in this chapter was to emulate ITU-T standards by reducing channel spacing to 100 GHz, and then 50 GHz. For the first time at 2 μm, 100 GHz DWDM was presented [38]. Reduced 50 GHz channel spacing was also demonstrated in terms of the 2 μm transmitter (with the implementation of a 2 μm AWGr multiplexer for the first time). However, spectral analysis in the receiver revealed that the channel isolation was reduced to only ~10 dB at the detector for 50 GHz channel spacing [39]. Therefore, despite cascading both a tunable bandpass filter and an AWGr, current filtering techniques were insufficient to demultiplex DWDM channels in the case of 50 GHz spacing at 2 μm [39].

OIL has been used for filtering purposes and channel selection at 1.55 μm, along with other applications in DWDM systems [40], [41], [42]. As such, OIL was the focus of Chapter 6. If OIL were to be implemented as a filtering mechanism in a 2 μm DWDM system, the receiver would need to incorporate the secondary laser, which would then tune to the incoming DWDM primary signal. Therefore, in Chapter 6, stable OIL was demonstrated with two slotted Fabry-Pérot lasers at 2 μm, thus demonstrating that the wavelength of a secondary laser can be locked to an incoming primary laser at 2 μm [44]. However, a full system analysis would be required in order to deduce the true efficiency and feasibility of OIL as a filtering mechanism at 2 μm.

7.2 Future Work

The natural next step to this work would be to test if OIL can be used to overcome the DWDM filtering limitations at 2 μm. As described previously, if OIL were to be implemented as a filtering mechanism in the DWDM system, the receiver would incorporate the secondary laser. This secondary receiver laser could then be tuned to lock to the incoming DWDM channel under test (which would take the place of the primary laser). Hence, one immediate suggestion would be to repeat the OIL experiment (as detailed in Section 6.3.2), with data imposed on the primary laser (using the MZM, for example), in order to test if stable OIL is still observed and to measure if the OIL bandwidth is affected. Once this is completed (and assuming a stable OIL bandwidth was still maintained), further work would be required to incorporate the OIL technique into the full DWDM system with 100 GHz channel spacing (as per Section 5.2). The realisation of such a system would require significant work from an experimental viewpoint, along with further

analysis of the phase-locking aspect of OIL. If the OIL technique were to successfully operate as a filter in this case, the final step in this comparative process would be to reduce the channel spacing to 50 GHz in order to measure if the channel isolation is improved in comparison to the measurements in Section 5.3 (with improved OSNR measurement methods also needed).

7.3 Main contributions

Some of the main contributions of the work in this thesis, to the field of optical communication systems, are highlighted below:

- 2 μm system capacity increased, with >100 Gbit/s achieved [38], [126].
- DWDM at 2 μm demonstrated, with 100 GHz spacing between channels [38].
- Spectral efficiency improved, with the first demonstration of a DWDM transmitter at 2 μm using 50 GHz channel spacing [39].
- First study of stable OIL with slotted Fabry-Pérot lasers at 2 μm [43], [44].

7.4 Discussion on 2 μm applications

While the main results presented in this thesis focus on DWDM at 2 μm, it is worthwhile to note that the development of technologies within this waveband may also be relevant to other areas of optical communications. In particular, silicon photonics has been an area of interest for 2 μm applications. Silicon photonics offers potentially lower costs and high compatibility with the CMOS (complementary metal-oxide-semiconductor) industry and presents an attractive option to integrate optical and electronic components onto a single chip. For these purposes, it is desirable to find a material that has low two-photon absorption and a high Kerr coefficient as this presents the best combination between low losses and nonlinear processes. At 2 μm, silicon is transparent, has low two photon absorption, and a high Kerr coefficient [182], [183], [184]. These qualities make the development of silicon photonic devices at 2 μm very promising [185]. Currently, some silicon photonic devices at 2 μm have been demonstrated including arrayed waveguide gratings [186], modulators [187], couplers [188], detectors [189],

filters [190] and more.

Technology at 2 μm (especially OIL [180], for example) also has wide-ranging applications in fields beyond optical communication systems because gases such as water vapour (H_2O), carbon dioxide (CO_2) and hydrochloric acid (HCl) have absorption peaks within the 1700 nm to 2025 nm window [18]. From an environmental viewpoint, water vapour is the most abundant naturally-occurring greenhouse gas in the atmosphere. Greenhouse gases absorb long-wave radiation and radiate it back to the surface, thus contributing to global warming. When it comes to human influences, carbon dioxide is the most dominant anthropomorphic contribution. Therefore, the detection and monitoring of H_2O and CO_2 is very important [191].

Greenhouse gases can be detected via a light detection and ranging (LIDAR) [192], [193], [194]. LIDAR is one of the most useful active remote sensing systems in the detection of atmospheric aerosols, clouds, and molecular species distributions [195]. An advantage of operating LIDAR at 2 μm, in particular, is that it is eye-safe. Eye-safety enables increased transmitter energy, longer operating ranges and higher sensitivities, while simultaneously avoiding interference with aircraft. As a consequence, sophisticated LIDAR methodology, such as differential absorption lidar (DIAL), can be applied at 2 μm [33], [34].

These remote sensing applications also extend to fields such as astronomy, including for example, determining the concentration of water on the surface of Mars. The atmospheric DIAL technique could be utilised to measure the distribution of water on the Martian surface, which in turn could lead to sites where signs of life may be found [196]. Thus, extensive research efforts are focused on developing new technologies at 2 μm. For example, under NASA programs, components including tunable pulsed lasers and optical detectors have been developed at 2 μm [33]. In other areas of astronomy, such as at the Laser Interferometer Gravitational-Wave Observatory (LIGO), 2 μm sources are being considered due to the material properties of silicon at this wavelength which would allow for higher powers, improving signal-to-noise ratio for highly sensitive sensing techniques [197], [28].

In medicine, 2 μm applications include the non-invasive measurement of glucose in the blood stream [29], [30], breath analysis using the exhaled CO_2 level to monitor patients during anaesthesia [31], [32], and laser surgery [198]. Finally, the detection of water content in air is an important

parameter in many other applications such as agriculture, ecology and material storage [35], [36].

7.5 Conclusion

The rise of augmented reality, artificial intelligence, self-driving cars, high-definition video streaming, cloud storage and increased connectivity through the 'internet of things' requires us to prepare for a future full of big data, increasingly bandwidth-hungry applications and high-capacity demands. Current forecasts project global internet traffic to triple from 2017 to 2022, along with the number of internet-connected devices becoming three times larger than the world's population.

Historically, the frequency at which we transmit information has always shifted if increased bandwidth/capacity was on offer and the technology allowed. Shifting transmission to the 2 μm region offers exciting benefits due to the availability of foundry-compatible components, mid-IR silica-based fibres (that could offer lower losses, lower latency and higher power-handling capabilities) and TDFAs (that could offer double the bandwidth of EDFAs). Also, with only-optical conversion required, 2 μm transmission may be especially attractive for high-capacity links, for example between data centres where equipment turnover takes place every 3-5 years.

The wide range of applications for 2 μm technologies serves as both an additional motivator for development in this waveband, and as an advantage - in that some components are already available in this wavelength region, ready to be adapted for optical communications. However, while some commercial products are available, many 2 μm devices are first-generation, non-optimal and expensive (in comparison to their standard off-the-shelf 1.55 μm counterparts). The challenges of these 2 μm components are then further compounded when combined in an optical communication system.

Despite these challenges, the work in this thesis has established a DWDM system at 2 μm with channel spacing of 100 GHz. System capacity has been pushed beyond 100 Gbit/s by enabling a greater number of channels, incorporating improved components and optimising the system to operate at higher data rates. The next step to increase system capacity at 2 μm is to improve the spectral efficiency by reducing the spacing between the DWDM channels further. However, while this is achievable with current technologies

in terms of the transmitter, insufficient filtering techniques have been a barrier in the receiver. The demonstration of OIL within this thesis shows promise as a potential future filtering solution at 2 μm.

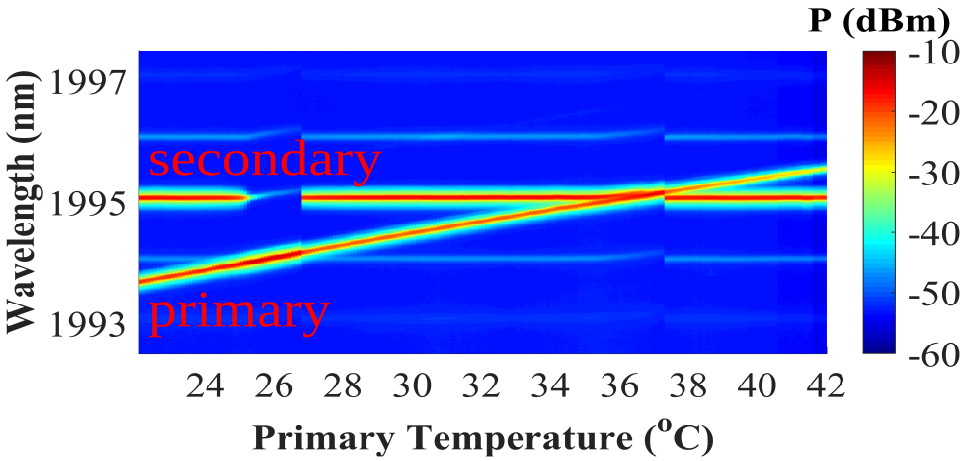
Beyond improved filtering techniques, it is clear that much work is needed if the 2 μm window is to prove competitive to the established 1.55 μm standards. For example, improved integrated-photonic, high-performance devices such as transmitters and receivers will be required to lower insertion losses, improve thermal stability and enable higher data rates. Simultaneously, commercial TDFAs with better stability are needed to compensate for losses, increase optical power and truly test the nonlinear limits of HC-PBGF in this wavelength region. Finally, further optical fibre research and development is needed to enable transmission beyond tens of kilometres.

In a world of ever-increasing capacity demands, novel solutions are needed. The future is more connected, automated and autonomous than ever before. Opening a new transmission window at 2μm could supplement the available bandwidth for future internet growth. This thesis demonstrates the development in optical communication systems at this waveband.

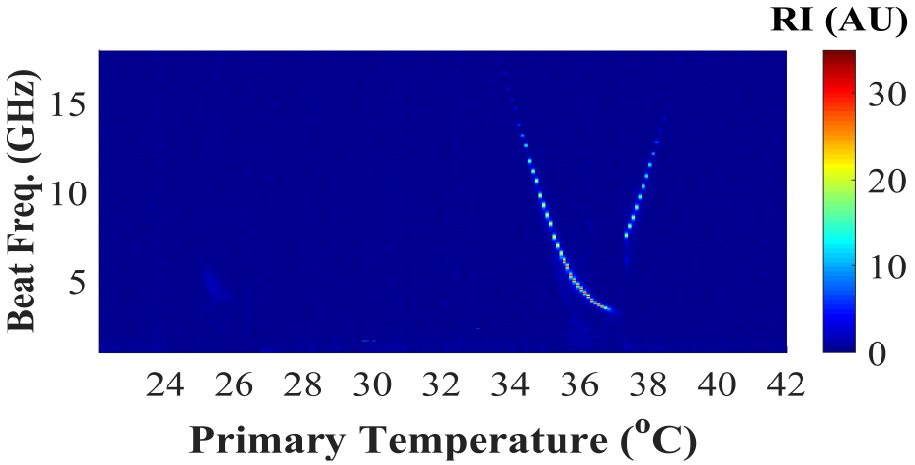
Appendix A

OIL images

In Chapter 6, experimental OIL investigations revealed different dynamics depending on which laser was tuned (i.e. primary vs. secondary) and also depending on the direction of tuning towards OIL (i.e. decreasing vs. increasing). Hence, the findings were split between these four different scenarios. This appendix provides some supplemental images for each case. Figure 6.7 (increasing the primary laser) and Figure 6.8 (increasing the secondary laser) from Chapter 6 are then repeated here (as Figure A.3 and Figure A.2, respectively) for ease of comparison between the different scenarios.

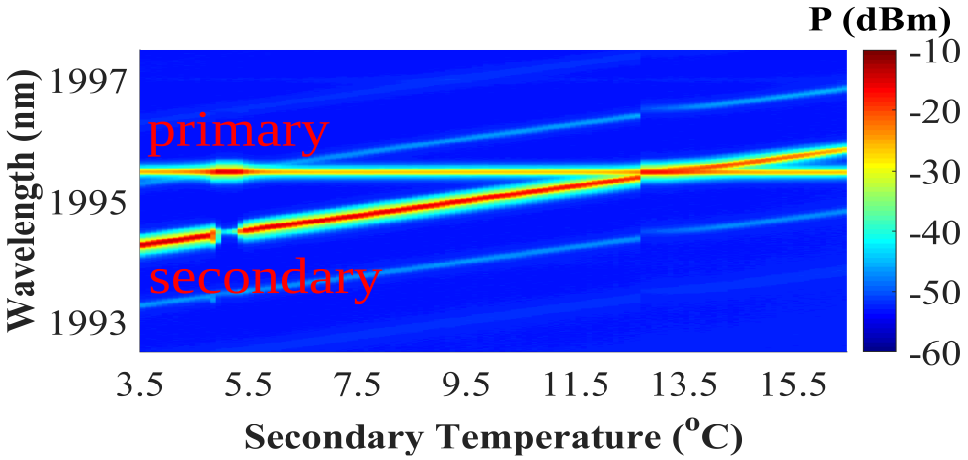


(a) Optical domain. Colourbar = optical power (P) in dBm.

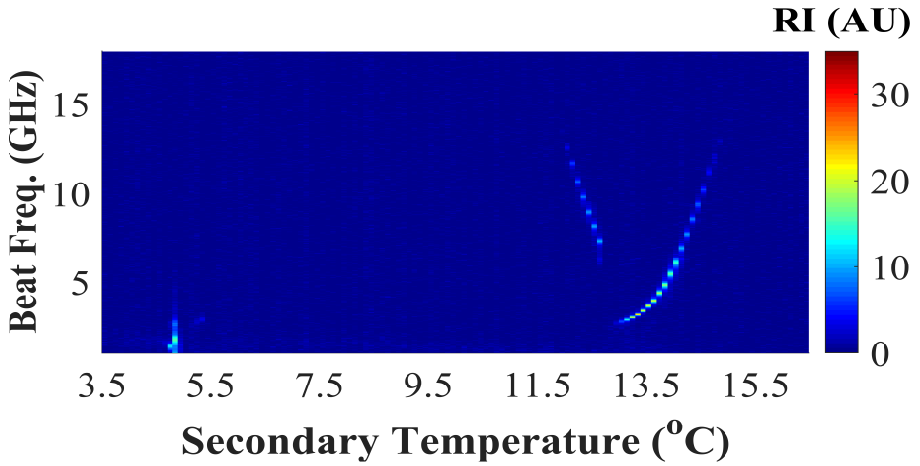


(b) Electrical domain. Colourbar = relative intensity (RI) in arbitrary units.

Figure A.1: The wavelength of the primary laser was swept across the fixed secondary by decreasing T_p from 42.0°C to 22.0°C. Figure A.1 shows false colourplot combinations of each 0.1°C measurement overlaid. In comparison to Figure A.2, the region of SMO around the side mode in the optical domain is reduced in this case. The width of the quiet region corresponding to stable OIL at the main mode is also decreased.

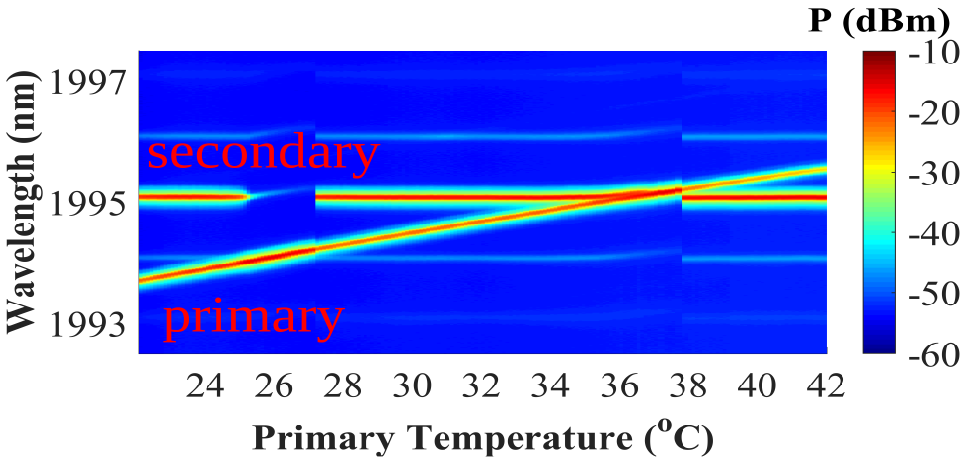


(a) Optical domain. Colourbar = optical power (P) in dBm.

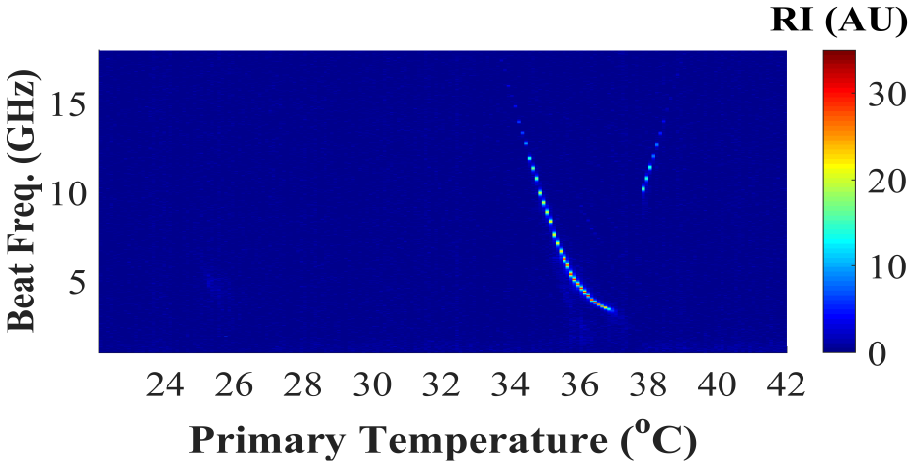


(b) Electrical domain. Colourbar = relative intensity (RI) in arbitrary units.

Figure A.2: The primary was then fixed and the wavelength of the secondary laser swept by increasing T_s from 3.5°C to 16.5°C. Figure A.2 shows false colour-plot combinations of each 0.1°C measurement overlaid. This figure can be compared to Figure A.1, as the detuning is varied similarly in each case (i.e. increasing the secondary ≈ decreasing the primary). Key differences include the decreased region of SMO at the side mode in this case and the different shape of the beating peak curve.

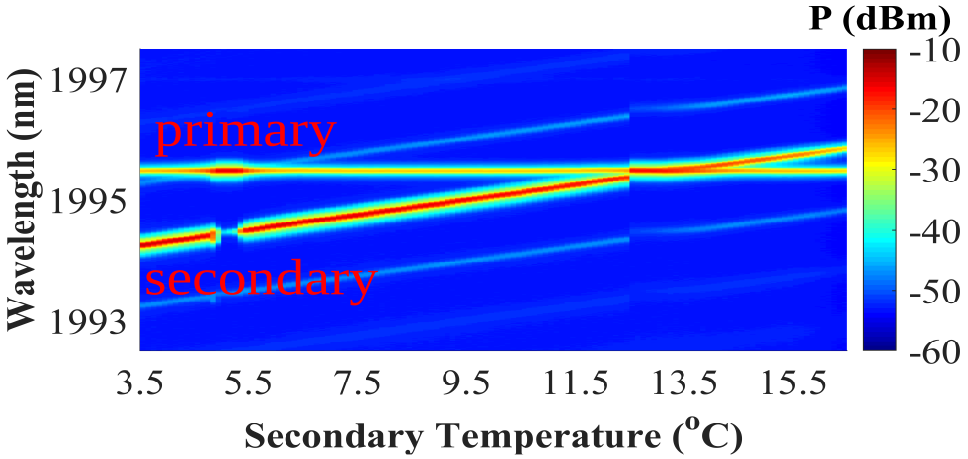


(a) Optical domain. Colourbar = optical power (P) in dBm.

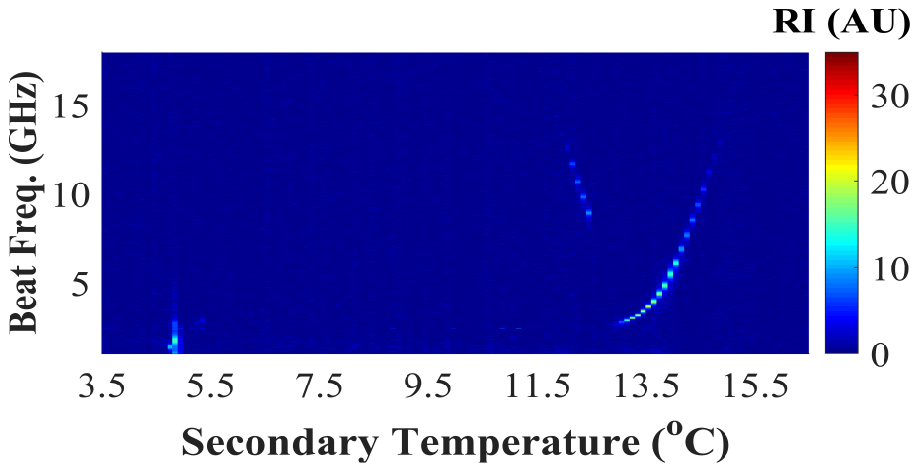


(b) Electrical domain. Colourbar = relative intensity (RI) in arbitrary units.

Figure A.3: The wavelength of the primary laser was swept across the fixed secondary by increasing T_p from 22.0°C to 42.0°C. Figure A.3 shows false colour-plot combinations of each 0.1°C measurement overlaid. SMO around the side mode (from ~25.0°C to 27.0°C) can clearly be seen in the optical domain above and stable OIL to the main mode is signified by the characteristic quiet region in the beating peak curve in the electrical below.



(a) Optical domain. Colourbar = optical power (P) in dBm.



(b) Electrical domain. Colourbar = relative intensity (RI) in arbitrary units.

Figure A.4: The wavelength of the secondary laser was swept across the fixed primary by decreasing T_s from 16.5°C to 3.5°C. Figure A.4 shows false colour-plot combinations of each 0.1°C measurement overlaid. Previously, decreasing the primary wavelength to achieve OIL in Figure A.1 resulted in a reduction in the locking bandwidth. However, in this case, decreasing the secondary caused an increase in the locking bandwidth at the main mode, perhaps indicating that when tuning the secondary rather than the primary, the OIL dynamics are similar but reversed.

Appendix B

Publications

Peer-reviewed journals

1. **N. Kavanagh**, D. Goulding, and F. C. Garcia Gunning, **"Stable injection locking with slotted Fabry–Perot lasers at 2 μm,"** **Journal of Physics: Photonics**, vol. 1, p. 015005, January 2019. ***Inaugural Issue.*** doi:10.1088/2515-7647/aae7d9

2. F. C. Garcia Gunning, **N. Kavanagh**, E. Russell, R. Sheehan, J. O'Callaghan, and B. Corbett, **"Key enabling technologies for optical communications at 2000 nm,"** **Applied Optics**, vol. 57, no. 22, p. E64, 2018. ***Special Ireland Issue.*** doi:10.1364/AO.57.000E64

3. M. U. Sadiq, H. Zhang, J. O'Callaghan, B. Roycroft, **N. Kavanagh**, K. Thomas, A. Gocalinska, Y. Chen, T. Bradley, J. R. Hayes, Z. Li, S. U. Alam, F. Poletti, M. N. Petrovich, D. J. Richardson, E. Pelucchi, P. O'Brien, F. H. Peters, F. Gunning, and B. Corbett, **"40 Gb/s WDM Transmission over 1.15 km HC-PBGF Using an InP-Based Mach-Zehnder Modulator at 2 μm,"** **Journal of Lightwave Technology**, vol. 34, no. 8, pp. 1706–1711, 2016. doi:10.1109/JLT.2015.2508941

4. H. Zhang, **N. Kavanagh**, Z. Li, J. Zhao, N. Ye, Y. Chen, N. V. Wheeler, J.

P. Wooler, J. R. Hayes, S. R. Sandoghchi, F. Poletti, M. N. Petrovich, S. U. Alam, R. Phelan, J. O'Carroll, B. Kelly, L. Grüner-Nielsen, D. J. Richardson, B. Corbett, and F. C. Garcia Gunning, **"100 Gbit/s WDM transmission at 2 μm: transmission studies in both low-loss hollow core photonic bandgap fiber and solid core fiber,"** **Optics Express**, vol. 23, no. 4, pp. 4946–4951, 2015.
doi:10.1364/OE.23.004946

5. H. Zhang, M. Gleeson, N. Ye, N. Pavarelli, X. Ouyang, J. Zhao, **N. Kavanagh**, C. Robert, H. Yang, P. E. Morrissey, K. Thomas, A. Gocalinska, Y. Chen, T. Bradley, J. P. Wooler, J. R. Hayes, E. Numkam Fokoua, Z. Li, S. U. Alam, F. Poletti, M. N. Petrovich, D. J. Richardson, B. Kelly, J. O'Carroll, R. Phelan, E. Pelucchi, P. O'Brien, F. Peters, B. Corbett, F. Gunning, **"Dense WDM transmission at 2 μm enabled by an arrayed waveguide grating,"** **Optics Letters**, vol. 40, no. 14, pp. 3308–3311, 2015.
doi:10.1364/OL.40.003308

International conferences

1. **N. Kavanagh**, B. Murray, D. Goulding, P. E. Morrissey, R. Sheehan, B. Corbett, and F. C. Gunning, **"Enabling photonic technologies at 2 μm,"** **in 19th International Conference on Transparent Optical Networks (ICTON)**, pp. 1–4, 2017.
doi:10.1109/ICTON.2017.8024868

2. **N. Kavanagh**, K. Shortiss, H. Zhang, M. Sadiq, K. Thomas, A. Gocalinska, J. Zhao, E. Pelucchi, P. O'Brien, F. Peters, B. Corbett, and F. Gunning, **"Impact of DWDM at 50GHz spacing in the 2 μm waveband,"** **in 2016 Conference on Lasers and Electro-Optics (CLEO)**, CLEO 2016, (San Jose, California), p. SF1F.5, Optical Society of America, 2016.
doi:10.1364/cleo_si.2016.sf1f.5

3. **N. Kavanagh**, M. Sadiq, K. Shortiss, H. Zhang, K. Thomas, A. Gocalinska, J. Zhao, E. Pelucchi, P. O. Brien, F. H. Peters, B. Corbett, and F. C. G.

Gunning, **"Exploring a new transmission window for telecommunications in the 2 μm waveband," in 18th International Conference on Transparent Optical Networks (ICTON)**, pp. 1–4, 2016. ***Awarded Best Student Paper.***
doi:10.1109/ICTON.2016.7550279

4. E. Russell, **N. Kavanagh**, K. Shortiss, and F. C. G. Gunning, **"Development of thulium-doped fibre amplifiers for the 2 μm waveband," in SPIE Photonics Europe**, vol. 10683, p. 8, SPIE, 2018.
doi:10.1117/12.2306462

5. F. C. Garcia Gunning, **N. Kavanagh**, K. Shortiss, H. Zhang, M. Sadiq, K. Thomas, A. Gocalinska, J. Zhao, E. Pelucchi, P. O'Brien, F. H. Peters, and B. Corbett, **"Enabling technologies for a new wavelength window at 2microns," in IEEE Photonics Conference**, IPC 2016, pp. 546–547, 2016.
doi:10.1109/IPCon.2016.7831223

6. M. U. Sadiq, H. Zhang, M. Gleeson, N. Ye, B. Roycroft, **N. Kavanagh**, C. Robert, H. Yang, K. Thomas, A. Gocalinska, Z. Li, Y. Chen, N. V. Wheeler, J. R. Hayes, S. U. Alam, F. Poletti, M. N. Petrovich, D. J. Richardson, B. Kelly, J. O'Carroll, R. Phelan, E. Pelucchi, P. O'Brien, F. Peters, F. Gunning, and B. Corbett, **"40 Gbps WDM transmission over 1.15 km HC-PBGF using the first InP-based Mach Zehnder modulator at 2 μm," in European Conference on Optical Communication (ECOC)**, vol. 2015-November, pp. 1–3, 2015.
doi:10.1109/ECOC.2015.7341853

7. H. Zhang, Z. Li, **N. Kavanagh**, J. Zhao, N. Ye, Y. Chen, N. V. Wheeler, J. P. Wooler, J. R. Hayes, S. R. Sandoghchi, F. Poletti, M. N. Petrovich, S. U. Alam, R. Phelan, J. O'Carroll, B. Kelly, D. J. Richardson, B. Corbett, and F. C. Gunning, **"81 Gb/s WDM transmission at 2 μm over 1.15 km of low-loss hollow core photonic bandgap fiber," in European Conference on Optical Communication (ECOC)**, pp. 1–3, 2014.
doi:10.1109/ECOC.2014.6964083

National conferences

1. **N. Kavanagh**, D. Goulding, and F. C. Garcia Gunning, "**Injection Locking at 2 μm", in Photonics Ireland**, Cork, Ireland, 2018, Presentation.

2. **N. Kavanagh**, B. Murray, D. Goulding, P.E. Morrissey, R. Sheehan, B. Corbett, and F. C. Garcia Gunning, "**Injection Locking at 2 μm", in Photonics Ireland**, Galway, Ireland, 2017, Poster.

3. **N. Kavanagh**, K. Shortiss, H. Zhang, M. Sadiq, E. Pelucchi, P. O'Brien, F. H. Peters, B. Corbett, and F. C. Garcia Gunning, "**Opening a New Transmission Window for Telecommunications", in Institute of Physics Spring Meeting**, Belfast, Ireland, 2016, Poster. ***Awarded IOP Rosse Medal.***

4. **N. Kavanagh**, H. Zhang, J. Zhao, N. Ye, B. Corbett, and F. C. Garcia Gunning, "**Dense Wavelength Division Multiplexing at 2 μm", in Photonics Ireland**, Cork, Ireland, 2015, Poster.

Other technical publications

1. **N. Kavanagh**, and F. C. Garcia Gunning, "**Opening a new transmission window for optical communications", at the 69th Nobel Laureate Meeting**, Lindau, Germany, 2019, Poster.

2. **N. Kavanagh**, "**Opening a new window for communications", at the Conference on Lasers and Electro-Optics (CLEO)**, 2019, (San Jose, California), "Pride in Photonics: LGBTQI+ and Allies Workshop", Presentation.

3. **N. Kavanagh**, and F.C. Garcia Gunning, "**Opening a new transmission window at 2 μm for future optical communications", at the 4th LGBT**

STEMinar, Institute of Physics, London, UK, 2019, Presentation.

4. **N. Kavanagh**, "**Future of the internet? Hollow-core optical fibres could carry more information, even faster!**" **at the International Week of Scientific Young Talents**, Universcience, Paris, France, 2017, Presentation.

5. **N. Kavanagh**, "**The internet is not limitless**", **in the UCC Boolean Journal**, vol. 2015, pp. 81–86, 2015, Article.

Media publications

1. "**5 young scientists to represent Ireland at major Nobel prize meeting**", by Colm Gorey, siliconrepublic.com, 2nd May 2019.

   Siliconrepublic.com: >350,000 unique visitors generate >500,000 pageviews per month. Ireland's leading science and technology news service, with seven Irish Web Awards.

2. "**Five scientists to represent Ireland at Lindau Nobel Laureate Meeting**", by Kevin O'Sullivan, irishtimes.com, 2nd May 2019.

   Irishtimes.com: 10.8 million users per month and 58 million pageviews per month.

3. "**As people use the internet more and more we need to keep a step ahead**", by Claire O'Connell, irishtimes.com, 22nd December 2016.

4. **N. Kavanagh**, "**Making light work of the Internet**", **in Science Apprentice Book Series**, Series 1, Book 4: Computers and Data, pg.18-19, November 2016.

   Total distribution/circulation for the Science Apprentice Book series was

75,000 with a readership of >350,000. (The Science Apprentice project was funded by the Science Foundation Ireland (SFI) Discover Programme, also supported by the Environmental Protection Agency along with partners Irish Independent and SuperValu.)

5. "**20 incredible women leading the way to scientific advancement**", siliconrepublic.com, 14th November 2016.

6. "**The future of networks: lighting up the digital world**", by John Kennedy, siliconrepublic.com, 3rd October 2016.

7. "**Watch out for these 6 rising stars of Irish research**", siliconrepublic.com, 17th June 2016.

8. "**Shot Of Scientist | Niamh Kavanagh Famelab Winner**", by Nat Newman, headstuff.org, 3rd June 2016.

   Headstuff.org: 60,000 to 80,000 visitors per month. Arts and Culture Blog of the Year 2016.

9. "**Thesis in 3 finalists shine a spotlight on science**", by Claire O'Connell, siliconrepublic.com, 17th November 2015.

Appendix C

Awards

Technical

1. May 2019 - **69th Nobel Laureate Meeting in Lindau**: 580 young scientists were selected from 88 countries to meet with 40 Nobel Laureates in Physics. Applications were assessed by the Irish Research Council (IRC) and selected by the Lindau Nobel Laureate Foundation, following a rigorous and independent evaluation process.

2. July 2016 - **Awarded Best Student Paper** at an international technical conference (ICTON 2016): selected by conference committee, based on originality, technical excellence, scientific rigor, organization and clarity.

3. February 2016 - **Institute of Physics Rosse Medal Award winner**: for graduate research communication to a broad audience via poster and oral presentation at the national IOP spring meeting (38 entrants, 1 winner).

Non-technical

1. January 2017 - **Irish Representative at International Week of Scientific Young Talents** in Paris, France: 42 young scientists were selected from 26 countries. Success rate of 5% in Ireland (60

applications, 3 selected).

2. November 2016 - **Institute of Physics Early Career Physics Communicator Award winner**: recognising people who have encouraged excellent communication of physics, submission by written essay and oral presentation.

3. April 2016 - **1st place Famelab National Final**: Famelab is the world's leading science communication competition to explain a scientific concept to a panel of judges and a public audience in three minutes, evaluated on content, clarity and charisma (100 entrants, 1 winner).

4. November 2015 - **2nd Place Thesis in 3 National Final**: science communication competition to explain a scientific topic to a public audience in three minutes, judged on content, clarity and charisma (21 entrants, 3 winners).

Funding granted

1. January 2019 - **Corning Women in Optical Fiber Communications Travel Grant**: to cover travel costs to the Optical Fiber Communication Conference and Exposition (OFC), selected by The Optical Society (OSA).

2. July 2017 - **IOP Walton Fund**: Successful application for €3000 (maximum amount) from Institute of Physics Ireland for outreach equipment to be used in third level physics departments.

3. October 2014 - **Granted Irish Research Council Postgraduate Scholarship**: individual research excellence award for four years PhD funding (value €96,000) based on an objective selection process using international, independent expert peer review, with a success rate of 20% (1051 applications, 218 awardees).

References

[1] "Population and Migration Estimates April 2018, Central Statistics Office Ireland, CSO Statistical Release," 2018.

[2] OECD, "Data on Ireland, http://www.oecd.org/ireland/," 2018.

[3] Cisco, "Cisco visual networking index (VNI) global mobile data traffic," tech. rep., 2019.

[4] J. M. Senior and M. Y. Jamro, *Optical fiber communications : principles and practice*. Financial Times/Prentice Hall, 2009.

[5] I. Hayashi, M. B. Panish, P. W. Foy, and S. Sumski, "Junction lasers which operate continuously at room temperature," *Applied Physics Letters*, vol. 17, pp. 109–111, aug 1970.

[6] International Telecommunication Union, "TR-OFCS Optical fibres, cables and systems, http://handle.itu.int/11.1002/pub/80d239d3-en," 2015.

[7] G. P. Agrawal, "Optical communication: Its history and recent progress," in *Optics in Our Time*, pp. 177–199, Cham: Springer International Publishing, 2016.

[8] T. Miya, Y. Terunuma, T. Hosaka, and T. Miyashita, "Ultimate low-loss single-mode fibre at 1.55 μm," *Electronics Letters*, vol. 15, no. 4, pp. 106–108, 1979.

[9] E. Desurvire, C. R. Giles, J. R. Simpson, and J. L. Zyskind, "Efficient erbium-doped fiber amplifier at a 153-μm wavelength with a high output saturation power," *Optics Letters*, vol. 14, no. 22, p. 1266, 1989.

[10] R. J. Essiambre and R. W. Tkach, "Capacity trends and limits of optical communication networks," *Proceedings of the IEEE*, vol. 100, no. 5, pp. 1035–1055, 2012.

[11] C. H. Yeh, C. C. Lee, and S. Chi, "120-Nm Bandwidth Erbium-Doped Fiber Amplifier in Parallel Configuration," *IEEE Photonics Technology Letters*, vol. 16, pp. 1637–1639, jul 2004.

[12] J. Renaudier, "Recent Advances in Ultra-Wideband WDM Transmission based on Semiconductor Optical Amplifiers," in *Optical Fiber Communication Conference (OFC) 2019*, (Washington, D.C.), p. Tu3F.5, OSA, mar 2019.

[13] F. Hamaoka, M. Nakamura, S. Okamoto, K. Minoguchi, T. Sasai, A. Matsushita, E. Yamazaki, and Y. Kisaka, "Ultra-wideband WDM transmission in S-C- A nd L-bands using signal power optimization scheme," *Journal of Lightwave Technology*, vol. 37, pp. 1764–1771, apr 2019.

[14] Journal of Lightwave Technology, "Announcement of an IEEE/OSA Journal of Lightwave Technology Special Issue on: Ultra-Wideband WDM Systems 2020, http://ieee-jlt.org."

[15] S. Shibata, M. Horiguchi, K. Jinguji, S. Mitachi, T. Kanamori, and T. Manabe, "Prediction of loss minima in infra-red optical fibres," *Electronics Letters*, vol. 17, no. 21, pp. 775–777, 1981.

[16] R. Garnham, D. Cunningham, and W. Stallard, "34 Mbit/s optical fibre transmission system experiment at a wavelength of 2.4 μm," *Electronics Letters*, vol. 23, no. 20, p. 1063, 1987.

[17] F. C. Garcia Gunning, N. Kavanagh, E. Russell, R. Sheehan, J. O'Callaghan, and B. Corbett, "Key enabling technologies for optical communications at 2000 nm," *Applied Optics*, vol. 57, no. 22, p. E64, 2018.

[18] E. Russell, F. Gunning, K. Shortiss, and N. Kavanagh, "Development of thulium-doped fibre amplifiers for the 2um waveband," in *SPIE Photonics Europe*, vol. 10683, p. 97, SPIE, 2018.

[19] D. Atkin, T. Shepherd, T. Birks, P. Russell, and P. Roberts, "Full 2-D photonic bandgaps in silica/air structures," *Electronics Letters*, vol. 31, pp. 1941–1943, oct 2002.

[20] P. J. Roberts, F. Couny, H. Sabert, B. J. Mangan, D. P. Williams, L. Farr, M. W. Mason, A. Tomlinson, T. A. Birks, J. C. Knight, and P. S. J.

Russell, "Ultimate low loss of hollow-core photonic crystal fibres," *Optics Express*, vol. 13, no. 1, pp. 236–244, 2005.

[21] R. Slavik, M. N. Petrovich, N. Wheeler, J. Hayes, N. K. Baddela, D. R. Gray, F. Poletti, and D. Richardson, "1.45 Tbit/s, low latency data transmission through a 19-cell hollow core photonic band gap fibre," in *European Conference and Exhibition on Optical Communication*, p. Mo. 2. F. 2, Optical Society of America, 2012.

[22] C. M. Smith, N. Venkataraman, M. T. Gallagher, D. Müller, J. A. West, N. F. Borrelli, D. C. Allan, and K. W. Koch, "Low-loss hollow-core silica/air photonic bandgap fibre," *Nature*, vol. 424, no. 6949, pp. 657–659, 2003.

[23] P. P. Mitra and J. B. Stark, "Nonlinear limits to the information capacity of optical fibre communications," *Nature*, vol. 411, pp. 1027–1030, jun 2001.

[24] B. E. A. Saleh and M. C. Teich, *Fundamentals of Photonics , 2nd Edition*. Wiley-Interscience, 2007.

[25] R. Phelan, J. O'Carroll, D. Byrne, C. Herbert, J. Somers, and B. Kelly, "In 0.75Ga 0.25As/InP multiple quantum-well discrete-mode laser diode emitting at 2 μm," *IEEE Photonics Technology Letters*, vol. 24, no. 8, pp. 652–654, 2012.

[26] Z. Li, A. M. Heidt, N. Simakov, Y. Jung, J. M. O. Daniel, S. U. Alam, and D. J. Richardson, "Diode-pumped wideband thulium-doped fiber amplifiers for optical communications in the 1800 – 2050 nm window," *Optics Express*, vol. 21, no. 22, pp. 26450–26455, 2013.

[27] Z. Li, A. M. Heidt, J. M. O. Daniel, Y. Jung, S. U. Alam, and D. J. Richardson, "Thulium-doped fiber amplifier for optical communications at 2 μm," *Optics Express*, vol. 21, no. 8, p. 9289, 2013.

[28] F. Gunning and B. Corbett, "Time to Open the 2-μm Window?," *Optics and Photonics News*, vol. 30, no. 3, p. 42, 2019.

[29] N. V. Alexeeva and M. A. Arnold, "Near-Infrared Microspectroscopic Analysis of Rat Skin Tissue Heterogeneity in Relation to Noninvasive Glucose Sensing," *Journal of Diabetes Science and Technology*, vol. 3, no. 2, pp. 219–232, 2009.

[30] P. S. Jensen, J. Bak, and S. Andersson-Engels, "Influence of temperature on water and aqueous glucose absorption spectra in the near- and mid-infrared regions at physiologically relevant temperatures," *Applied Spectroscopy*, vol. 57, pp. 28–36, jan 2003.

[31] K. K. Chow, M. Short, S. Lam, A. McWilliams, and H. Zeng, "A Raman cell based on hollow core photonic crystal fiber for human breath analysis," *Medical Physics*, vol. 41, no. 9, p. 92701, 2014.

[32] N. Ye, M. R. Gleeson, M. U. Sadiq, B. Roycroft, C. Robert, H. Yang, H. Zhang, P. E. Morrissey, N. Mac Suibhne, K. Thomas, A. Gocalinska, E. Pelucchi, R. Phelan, B. Kelly, J. Ocarroll, F. H. Peters, F. C. Garcia Gunning, and B. Corbett, "InP-based active and passive components for communication systems at 2 μm," *Journal of Lightwave Technology*, vol. 33, no. 5, pp. 971–975, 2015.

[33] T. F. Refaat, S. Ismail, G. J. Koch, M. Rubio, T. L. MacK, A. Notari, J. E. Collins, J. Lewis, R. De Young, Y. Choi, M. N. Abedin, and U. N. Singh, "Backscatter 2-μm lidar validation for Atmospheric CO2 differential absorption lidar applications," *IEEE Transactions on Geoscience and Remote Sensing*, vol. 49, no. 1 PART 2, pp. 572–580, 2011.

[34] N. Sugimoto, N. Sims, K. Chan, and D. K. Killinger, "Eye-safe 2.1-μm Ho lidar for measuring atmospheric density profiles," *Optics Letters*, vol. 15, p. 302, mar 1990.

[35] N. Yamazoe and Y. Shimizu, "Humidity sensors: Principles and applications," *Sensors and Actuators*, vol. 10, pp. 379–398, nov 1986.

[36] K. Xu, H. Li, Y. Liu, Y. Wang, J. Tian, L. Wang, J. Du, Z. He, and Q. Song, "Optical Fiber Humidity Sensor Based on Water Absorption Peak Near 2-μm Waveband," *IEEE Photonics Journal*, vol. 11, no. 2, 2019.

[37] P. J. Winzer and R. J. Essiambre, "Advanced optical modulation formats," *Optical Fiber Telecommunications V1B*, pp. 23–93, jan 2008.

[38] N. Kavanagh, M. Sadiq, K. Shortiss, H. Zhang, K. Thomas, A. Gocalinska, Y. Zhao, E. Pelucchi, P. O'Brien, F. H. Peters, B. Corbett, and F. C. Garcia Gunning, "Exploring a new transmission window for telecommunications in the 2 μm waveband," in *International Conference on Transparent Optical Networks*, pp. 1–4, 2016.

[39] N. Kavanagh, K. Shortiss, H. Zhang, M. Sadiq, K. Thomas, A. Gocalinska, Y. Zhao, E. Pelucchi, P. O'Brien, F. H. Peters, B. Corbett, and F. C. Garcia Gunning, "Impact of DWDM at 50GHz spacing in the 2μm waveband," in *2016 Conference on Lasers and Electro-Optics, CLEO 2016*, (San Jose, California), p. SF1F.5, Optical Society of America, 2016.

[40] W. Cotter, D. Goulding, B. Roycroft, J. O'Callaghan, B. Corbett, F. H. Peters, J. O'Callaghan, B. Corbett, and F. H. Peters, "Investigation of active filter using injection-locked slotted Fabry-Perot semiconductor laser.," *Applied optics*, vol. 51, no. 30, pp. 7357–61, 2012.

[41] W. Cotter, *Photonic integrated circuit for the manipulation of coherent optical combs*. PhD thesis, UCC, 2014.

[42] L. Y. Chan, P. K. Wai, L. F. Lui, B. Moses, W. H. Chung, and H. Y. Tam, *Demonstration of All-Optical Packet Demultiplexing Using a Multi-Wavelength Mutual Injection-Locked Laser Diode*, vol. 86. Optical Society of America, 2003.

[43] N. Kavanagh, B. Murray, D. Goulding, P. E. Morrissey, R. Sheehan, B. Corbett, and F. C. Gunning, "Enabling photonic technologies at 2 μm," in *International Conference on Transparent Optical Networks*, pp. 1–4, 2017.

[44] N. Kavanagh, D. Goulding, and F. C. Garcia Gunning, " Stable injection locking with slotted Fabry–Perot lasers at 2 μ m ," *Journal of Physics: Photonics*, vol. 1, p. 015005, jan 2018.

[45] J. Hecht, *City of light : the story of fiber optics*. Oxford University Press, 2004.

[46] B. S. Finn, *City of Light: The Story of Fiber Optics (review)*, vol. 43. Oxford University Press, 2007.

[47] J. Ballato and P. Dragic, "Glass: The Carrier of Light - A Brief History of Optical Fiber," *International Journal of Applied Glass Science*, vol. 7, pp. 413–422, dec 2016.

[48] N. H. L. Wong, *Characterisation of Hollow-Core Photonic Bandgap Fibres and Other Multimode Fibres for Optical Communications*. PhD thesis, University of Southampton, 2017.

[49] C. Steinwender, "Real effects of information frictions: When the states and the Kingdom Became United," *American Economic Review*, vol. 108, pp. 657–696, mar 2018.

[50] M. J. Kelly and S. G. Radley, "Transatlantic communications: A historical resume," *Transactions of the American Institute of Electrical Engineers, Part I: Communication and Electronics*, vol. 75, no. 6, pp. 841–842, 2013.

[51] J. Tebo, "The early history of telecommunications: The first hundred years," *Communications Society*, vol. 14, pp. 12–21, jul 1976.

[52] K. Toker, "Visualization of airway," *Acta Clinica Croatica*, vol. 55, pp. 73–75, 2016.

[53] J. Hecht, "The "Lost Generation" of Fiber Optics," *Optics and Photonics News*, vol. 10, p. 26, nov 1999.

[54] T. H. Maiman, "Stimulated optical radiation in Ruby," *Nature*, vol. 187, pp. 493–494, aug 1960.

[55] A. J. Gross and T. R. W. Herrmann, "History of lasers," *World Journal of Urology*, vol. 25, pp. 217–220, jun 2007.

[56] K. Kao and G. Hockham, "Dielectric-fibre surface waveguides for optical frequencies," *Proceedings of the Institution of Electrical Engineers*, vol. 113, pp. 1151–1158, jul 1966.

[57] K. Ondrej, "Modern telecommunication optical fibers, http://www.posterus.sk/?p=6830," 2010.

[58] "Optical Fiber Attenuation – Fosco Connect, www.fiberoptics4sale.com/blogs/archive-posts/95052294-optical-fiber-attenuation, 2019."

[59] R. Olshansky, "Propagation in glass optical waveguides," *Reviews of Modern Physics*, vol. 51, pp. 341–367, apr 1979.

[60] D. Keck, "A future full of light," *IEEE Journal on Selected Topics in Quantum Electronics*, vol. 6, pp. 1254–1258, nov 2000.

[61] F. C. Garcia Gunning, N. Kavanagh, K. Shortiss, H. Zhang, M. Sadiq, K. Thomas, A. Gocalinska, Y. Zhao, E. Pelucchi, P. O'Brien, F. H. Peters,

and B. Corbett, "Enabling technologies for a new wavelength window at 2 μm," in *2016 IEEE Photonics Conference, IPC 2016*, pp. 546–547, 2017.

[62] Tingye Li, "Advances in Optical Fiber Communications: An Historical Perspective," *IEEE Journal on Selected Areas in Communications*, vol. 1, pp. 356–372, apr 2004.

[63] M. Ohashi, K. Shiraki, and K. Tajima, "Optical Loss Property of Silica-Based Single-Mode Fibers," *Journal of Lightwave Technology*, vol. 10, pp. 539–543, may 1992.

[64] E. Desurvire, C. Kazmierski, F. Lelarge, X. Marcadet, A. Scavennec, F. A. Kish, D. F. Welch, R. Nagarajan, C. H. Joyner, R. P. Schneider, S. W. Corzine, M. Kato, P. W. Evans, M. Ziari, A. G. Dentai, J. L. Pleumeekers, R. Muthiah, S. Bigo, M. Nakazawa, D. J. Richardson, F. Poletti, M. N. Petrovich, S. U. Alam, W. H. Loh, and D. N. Payne, "Science and technology challenges in XXIst century optical communications," *Comptes Rendus Physique*, vol. 12, no. 4, pp. 387–416, 2011.

[65] D. B. Keck, R. D. Maurer, and P. C. Schultz, "On the ultimate lower limit of attenuation in glass optical waveguides," *Applied Physics Letters*, vol. 22, pp. 307–309, apr 1973.

[66] P. C. Schultz, "Preparation of very low-loss optical waveguides," in *American Ceramic Society Bulletin*, vol. 52, p. 383, American Ceramic Society, 1973.

[67] D. Gloge, "Optical Fibers for Communication," *IEEE Journal of Quantum Electronics*, vol. 9, pp. 638–639, feb 1973.

[68] S. Abbott, "Review of 20 years of undersea optical fiber transmission system development and deployment since TAT-8," in *European Conference on Optical Communication, ECOC*, pp. 1–4, IEEE, 2008.

[69] L. J. Marra, "Sharkbite on the SL Submarine Lightwave Cable System: History, Causes, and Resolution," *IEEE Journal of Oceanic Engineering*, vol. 14, pp. 230–237, jul 1989.

[70] R. J. Mears, L. Reekie, I. M. Jauncey, D. N. Payne, and R. J. Mears, "Low-noise erbium-doped fibre amplifier operating at 1.54μm," *Electronics Letters*, vol. 23, no. 19, pp. 1026–1028, 1987.

[71] D. Manzani, J. L. Ferrari, F. C. Polachini, Y. Messaddeq, and S. J. L. Ribeiro, "1.5 μm and visible up-conversion emissions in Er 3+/Yb 3+ co-doped tellurite glasses and optical fibers for photonic applications," *Journal of Materials Chemistry*, vol. 22, pp. 16540–16545, jul 2012.

[72] A. E. White and S. G. Grubb, *Optical Fiber Telecommunications IIIB*. Academic Press, 1997.

[73] P. Trischitta, M. Colas, M. Green, G. Wuzniak, and J. Arena, "The TAT-12/13 cable network," *IEEE Communications Magazine*, vol. 34, no. 2, pp. 24–28, 1996.

[74] ITU-T, "Optical fibres, cables and systems, International Telecommunication Union Manual, http://handle.itu.int/11.1002/pub/8035a9bb-en," tech. rep., 2009.

[75] P. J. Winzer and R. J. Essiambre, "Advanced modulation formats for high-capacity optical transport networks," *Journal of Lightwave Technology*, vol. 24, pp. 4711–4728, dec 2006.

[76] T. Suhara, *Semiconductor Laser Fundamentals*. Marcel Dekker, 2004.

[77] R. E. Nahory, M. A. Pollack, W. D. Johnston, and R. L. Barns, "Band gap versus composition and demonstration of Vegard's law for InGaAsP lattice matched to InP," *Applied Physics Letters*, vol. 33, pp. 659–661, oct 1978.

[78] BATOPoptoelectronics, "Energy bandgap of InGaAs, www.batop.de/information/Eg_InGaAs.html, 2019."

[79] Sensors Unlimited, "What is InGaAs, or indium gallium arsenide?, http://www.sensorsinc.com/technology/what-is-ingaas, 2019."

[80] A. Baranov and E. Tournié, *Semiconductor lasers: Fundamentals and applications*. Woodhead Publishing, 2013.

[81] "Semiconductor Lasers BT - Fundamentals of Solid State Engineering," pp. 701–764, Boston, MA: Springer US, 2006.

[82] R. R. A. Syms and J. R. Cozens, *The optics of beams*. McGraw-Hill, 1992.

[83] M. N. Petrovich, F. Poletti, J. P. Wooler, A. Heidt, N. Baddela, Z. Li, D. Gray, R. Slavík, F. Parmigiani, N. Wheeler, J. Hayes, E. Numkam, L. Grűner-Nielsen, B. Pálsdóttir, R. Phelan, B. Kelly, J. O'Carroll,

M. Becker, N. MacSuibhne, J. Zhao, F. G. Gunning, A. Ellis, P. Petropoulos, S. Alam, and D. Richardson, "Demonstration of amplified data transmission at 2 μm in a low-loss wide bandwidth hollow core photonic bandgap fiber," *Optics Express*, vol. 21, no. 23, p. 28559, 2013.

[84] F. Poletti, M. N. Petrovich, and D. J. Richardson, "Hollow-core photonic bandgap fibers: technology and applications," *Nanophotonics*, vol. 2, no. 5-6, pp. 315–340, 2013.

[85] C. Cookson, "Time is money when it comes to microwaves," *Financial Times*, 2013.

[86] B. Crosignani, "Nonlinear effects in optical fibers," in *Fiber and Integrated Optics*, vol. 11, pp. 235–252, Springer, Dordrecht, 1992.

[87] M. Hirano, T. Haruna, Y. Tamura, T. Kawano, S. Ohnuki, Y. Yamamoto, Y. Koyano, and T. Sasaki, *Record low loss, record high fom optical fiber with manufacturable process*, vol. 17. 2013.

[88] R. F. Cregan, B. J. Mangan, J. C. Knight, T. A. Birks, P. S. J. Russell, P. J. Roberts, and D. C. Allan, "Single-mode photonic band gap guidance of light in air," *Science*, vol. 285, pp. 1537–1539, sep 1999.

[89] M. A. Duguay, Y. Kokubun, T. L. Koch, and L. Pfeiffer, "Antiresonant reflecting optical waveguides in SiO2-Si multilayer structures," *Applied Physics Letters*, vol. 49, pp. 13–15, jul 1986.

[90] N. M. Litchinitser, A. K. Abeeluck, C. Headley, and B. J. Eggleton, "Antiresonant reflecting photonic crystal optical waveguides," *Optics Letters*, vol. 27, p. 1592, sep 2002.

[91] P. Russell, "Photonic crystal fibers," *science*, vol. 299, no. 5605, pp. 358–362, 2003.

[92] I. Jamnik, "Artificial Opals, http://mafija.fmf.uni-lj.si/seminar/files/2006_2007/ARTIFICIAL_OPALS.pdf," in *Faculty of Mathematics and Physics Seminar*, (Ljubljana), Department of Physics, University of Ljubljana, 2006.

[93] M. Ziemienczuk, *Coherent Gas-Laser Interactions via Stimulated Raman Scattering in Hollow-Core Photonic Crystal Fibers*. PhD thesis, University of Erlangen-Nürnberg, jun 2012.

[94] P. Vukusic and J. R. Sambles, "Photonic structures in biology," *Nature*, vol. 424, pp. 852–855, aug 2003.

[95] V. N. Bogomolov, S. V. Gaponenko, I. N. Germanenko, A. M. Kapitonov, E. P. Petrov, N. V. Gaponenko, A. V. Prokofiev, A. N. Ponyavina, N. I. Silvanovich, and S. M. Samoilovich, "Photonic band gap phenomenon and optical properties of artificial opals," *Physical Review E - Statistical Physics, Plasmas, Fluids, and Related Interdisciplinary Topics*, vol. 55, pp. 7619–7625, jun 1997.

[96] N. Mac Suibhne, Z. Li, B. Baeuerle, J. Zhao, J. Wooler, S.-u. Alam, F. Poletti, M. Petrovich, A. Heidt, N. Wheeler, N. Baddela, E. R. Numkam Fokoua, I. Giles, D. Giles, R. Phelan, J. O'Carroll, B. Kelly, B. Corbett, D. Murphy, A. D. Ellis, D. J. Richardson, and F. Garcia Gunning, "WDM Transmission at 2μm over Low-Loss Hollow Core Photonic Bandgap Fiber," in *Optical Fiber Communication Conference/National Fiber Optic Engineers Conference 2013*, (Anaheim, California), p. OW1I.6, Optical Society of America, 2013.

[97] D. Richardson, "Emerging fibers and amplifiers for next generation communications and laser applications," in *6th International Symposium on Ultrafast Photonic Technologies (ISUPT 2013)*, (Rochester, United States), p. 52, 2013.

[98] F. Poletti, "Nested antiresonant nodeless hollow core fiber," *Optics Express*, vol. 22, p. 23807, oct 2014.

[99] Y. Chen, N. V. Wheeler, N. K. Baddela, J. R. Hayes, S. R. Sandoghchi, E. N. Fokoua, M. Li, F. Poletti, M. N. Petrovich, and D. J. Richardson, "Understanding wavelength scaling in 19-cell core hollow-core photonic bandgap fibers," in *Conference on Optical Fiber Communication, Technical Digest Series*, (Washington, D.C.), p. M2F.4, OSA, mar 2014.

[100] H. Zhang, M. Gleeson, N. Ye, N. Pavarelli, X. Ouyang, J. Zhao, N. Kavanagh, C. Robert, H. Yang, P. E. Morrissey, K. Thomas, A. Gocalinska, Y. Chen, T. Bradley, J. P. Wooler, J. R. Hayes, E. Numkam Fokoua, Z. Li, S. U. Alam, F. Poletti, M. N. Petrovich, D. J. Richardson, B. Kelly, J. O'Carroll, R. Phelan, E. Pelucchi, P. O'Brien, F. Peters, B. Corbett, and F. Gunning, "Dense WDM transmission at 2 μm enabled by an arrayed waveguide grating," *Optics Letters*, vol. 40, no. 14, p. 3308, 2015.

[101] H. Sakr, T. D. Bradley, Y. Hong, G. T. Jasion, J. R. Hayes, H. Kim, I. A. Davidson, E. N. Fokoua, Y. Chen, K. R. H. Bottrill, N. Taengnoi, P. Petropoulos, D. J. Richardson, and F. Poletti, "Ultrawide Bandwidth Hollow Core Fiber for Interband Short Reach Data Transmission," in *Optical Fiber Communication Conference Postdeadline Papers 2019*, (Washington, D.C.), p. Th4A.1, OSA, mar 2019.

[102] F. Poletti, "Advances in Hollow Optical Fiber Technologies and Applications," in *Optical Fiber Communication Conference (OFC) 2019*, (Washington, D.C.), p. Th3E.1, OSA, mar 2019.

[103] J. H. L. Voncken, "The Rare Earth Elements—A Special Group of Metals," pp. 1–13, Springer, Cham, 2015.

[104] Y. Jaouën, E. Lucas, G. Canat, L. Lombard, and S. Bordais, "1 kW peak power, 110 ns single-frequency thulium doped fiber amplifier at 2050 nm," *Applied Optics*, vol. 53, p. 4413, jul 2014.

[105] V. A. Kamynin, S. A. Filatova, I. V. Zhluktova, and V. B. Tsvetkov, "Holmium doped fiber amplifier in the spectral region 2-2.15 um," in *Proceedings - 2016 International Conference Laser Optics, LO 2016*, p. S117, Institute of Electrical and Electronics Engineers Inc., aug 2016.

[106] R. E. Tench, C. Romano, J. M. Delavaux, T. Robin, B. Cadier, and A. Laurent, "Broadband High Gain Polarization-Maintaining Holmium-Doped Fiber Amplifiers," in *European Conference on Optical Communication, ECOC*, vol. 2018-Septe, pp. 1–3, IEEE, sep 2018.

[107] R. E. Tench, C. Romano, G. M. Williams, J. M. Delavaux, T. Robin, B. Cadier, and A. Laurent, "Two-Stage Performance of Polarization-Maintaining Holmium-Doped Fiber Amplifiers," *Journal of Lightwave Technology*, vol. 37, pp. 1434–1439, feb 2019.

[108] S. S. Haykin, *Communication systems*. Wiley, 2001.

[109] G. P. Agrawal, *Fiber-Optic Communication Systems*. Wiley, 2007.

[110] G. P. Agrawal, *Lightwave Technology*. Wiley-Interscience, 2005.

[111] OpenLearn-OpenUniversity, "Exploring communications technology: 1.4 Amplitude-shift keying (ASK) TM355_1, www.open.edu/openlearn/science-maths-technology/exploring-

communications-technology/content-section-1.4,
2019."

[112] M. U. Sadiq, M. R. Gleeson, N. Ye, J. O'Callaghan, P. Morrissey, H. Y. Zhang, K. Thomas, A. Gocalinska, E. Pelucchi, F. C. G. Gunning, B. Roycroft, F. H. Peters, and B. Corbett, "10 Gb/s InP-based Mach-Zehnder modulator for operation at 2 μm wavelengths," *Optics Express*, vol. 23, no. 9, p. 10905, 2015.

[113] M. U. Sadiq, H. Zhang, J. O'Callaghan, B. Roycroft, N. Kavanagh, K. Thomas, A. Gocalinska, Y. Chen, T. Bradley, J. R. Hayes, Z. Li, S. U. Alam, F. Poletti, M. N. Petrovich, D. J. Richardson, E. Pelucchi, P. O'Brien, F. H. Peters, F. Gunning, and B. Corbett, "40 Gb/s WDM Transmission over 1.15-km HC-PBGF Using an InP-Based Mach-Zehnder Modulator at 2 μm," *Journal of Lightwave Technology*, vol. 34, no. 8, pp. 1706–1711, 2016.

[114] Photonics.ixblue.com, "Mach-Zehnder Modulators, photonics.ixblue.com/store/lithium-niobate-electro-optic-modulator/intensity-modulators,
2019."

[115] SaorView, "Digital Television Transmission Network Main Stations Site County, http://www.2rn.ie/wp-content/uploads/2013/11/2RN-DTT-Television-Transmission-Network-Nov-2013.pdf," tech. rep., 2013.

[116] W. J. Tomlinson and G. D. Aumiller, "Optical multiplexer for multimode fiber transmission systems," *Applied Physics Letters*, vol. 31, pp. 169–171, aug 1977.

[117] W. J. Tomlinson, "Wavelength multiplexing in multimode optical fibers," *Applied Optics*, vol. 16, p. 2180, aug 1977.

[118] H. Ishio and T. Miki, "A preliminary experiment on wavelength division multiplexing transmission using LED," in *International Conference on Integrated Optics and Optical Fiber Communication*, vol. 77, pp. 3–7, Institute of Electronics and Communication Engineers of Japan, 1977.

[119] H. Ishio, J. Minowa, and K. Nosu, "Review and Status of Wavelength-Division-Multiplexing Technology and Its Application

(Invited Overview)," *Journal of Lightwave Technology*, vol. 2, no. 4, pp. 448–463, 1984.

[120] *Cisco Systems Internetworking Technologies Handbook*. Cisco Press, 3rd ed., 2000.

[121] A. H. Gnauck, R. W. Tkach, A. R. Chraplyvy, and T. Li, "High-capacity optical transmission systems," *Journal of Lightwave Technology*, vol. 26, pp. 1032–1045, may 2008.

[122] K. Fukuchi, T. Kasamatsu, M. Morie, R. Ohhira, T. Ito, K. Sekiya, D. Ogasahara, and T. Ono, "10.92-Tb/s (273 x 40-Gb/s) triple-band/ultra-dense WDM optical-repeatered transmission experiment," in *Optical Fiber Communication Conference and International Conference on Quantum Information*, (Washington, D.C.), p. PD24, OSA, mar 2001.

[123] M. N. Petrovich, F. Poletti, J. P. Wooler, A. M. Heidt, N. K. Baddela, Z. Li, D. R. Gray, R. Slavík, F. Parmigiani, N. V. Wheeler, J. R. Hayes, E. Numkam, L. Grűner-Nielsen, B. Pálsdóttir, R. Phelan, B. Kelly, M. Becker, N. MacSuibhne, J. Zhao, F. G. Gunning, A. D. Ellis, P. Petropoulos, S. U. Alam, and D. J. Richardson, "First Demonstration of 2μm Data Transmission in a Low-Loss Hollow Core Photonic Bandgap Fiber," in *European Conference and Exhibition on Optical Communication*, p. Th.3.A.5, 2012.

[124] N. MacSuibhne, Z. Li, B. Baeuerle, J. Zhao, J. Wooler, S. Alam, F. Poletti, M. Petrovich, A. Heidt, I. Giles, D. Giles, B. Pálsdóttir, L. Grüner-Nielsen, R. Phelan, J. O'Carroll, B. Kelly, D. Murphy, A. Ellis, D. Richardson, and F. G. Gunning, "Wavelength Division Multiplexing at 2μm," in *European Conference and Exhibition on Optical Communication*, (Amsterdam), p. Th.3.A.3, Optical Society of America, 2013.

[125] Z. Liu, Z. Li, Y. Chen, J. P. Wooler, B. Kelly, R. Phelan, J. O'Carroll, N. V. Wheeler, A. M. Heidt, F. Poletti, M. N. Petrovich, S. Alam, D. J. Richardson, and R. Slavik, "Up to 64QAM (30 Gbit/s) directly-modulated and directly-detected OFDM at 2 μm wavelength," 2014.

[126] H. Zhang, N. Kavanagh, Z. Li, J. Zhao, N. Ye, Y. Chen, N. V. Wheeler, J. P. Wooler, J. R. Hayes, S. R. Sandoghchi, F. Poletti, M. N. Petrovich,

S. U. Alam, R. Phelan, J. O'Carroll, B. Kelly, L. Grüner-Nielsen, D. J. Richardson, B. Corbett, and F. C. Garcia Gunning, "100 Gbit/s WDM transmission at 2 μm: transmission studies in both low-loss hollow core photonic bandgap fiber and solid core fiber," *Optics Express*, vol. 23, no. 4, p. 4946, 2015.

[127] EblanaPhotonics, "Laser packaging, www.eblanaphotonics.com/packaging.php," 2019.

[128] M. R. D. Rodrigues and I. Darwazeh, "Fast OFDM: A proposal for doubling the data rate of OFDM schemes," in *Proceeding of the International Conference on Telecommunications*, pp. 484–487, 2003.

[129] J. Zhao and A. D. Ellis, "A novel optical fast OFDM with reduced channel spacing equal to half of the symbol rate per carrier," in *Optics InfoBase Conference Papers*, OSA Technical Digest (CD), (San Diego, California), p. OMR1, Optical Society of America, 2010.

[130] H. Zhang, Z. Li, N. Kavanagh, J. Zhao, N. Ye, Y. Chen, N. V. Wheeler, J. P. Wooler, J. R. Hayes, S. R. Sandoghchi, F. Poletti, M. N. Petrovich, S. U. Alam, R. Phelan, J. O'Carroll, B. Kelly, D. J. Richardson, B. Corbett, and F. C. Gunning, "81 Gb/s WDM transmission at 2μm over 1.15 km of low-loss hollow core photonic bandgap fiber," in *European Conference on Optical Communication, ECOC*, pp. 1–3, 2014.

[131] J. Zhao, S. K. Ibrahim, D. Rafique, P. Gunning, and A. D. Ellis, "Symbol synchronization exploiting the symmetric property in optical fast OFDM," *IEEE Photonics Technology Letters*, vol. 23, no. 9, pp. 594–596, 2011.

[132] X. Ouyang, J. Jin, G. Jin, Z. Wang, and Y. Park, "Interleaved Multiplexing Optical Fast OFDM Without the Interference Between Subchannels," *IEEE Photonics Technology Letters*, vol. 25, pp. 378–381, feb 2013.

[133] X. Ouyang, H. Zhang, Y. Chen, S. Alam, M. N. Petrovich, F. Poletti, D. J. Richardson, F. C. Gunning, and J. Zhao, "Experimental Demonstration of Improved Equalization Algorithm for IM/DD Fast OFDM," *IEEE Photonics Technology Letters*, vol. 27, pp. 1780–1783, aug 2015.

[134] X. Ouyang, W. Jia, P. Gunning, P. D. Townsend, and J. Zhao, "Experimental Demonstration and Field-Trial of an Improved Optical

Fast OFDM Scheme Using Intensity-Modulation and Full-Field Detection," *Journal of Lightwave Technology*, vol. 33, pp. 4353–4359, oct 2015.

[135] J. Zhou, Y. Qiao, T. Zhang, E. Sun, M. Guo, Z. Zhang, X. Tang, and F. Xu, "FOFDM Based on Discrete Cosine Transform for Intensity-Modulated and Direct-Detected Systems," *Journal of Lightwave Technology*, vol. 34, pp. 3717–3725, aug 2016.

[136] X. Ouyang, *Digital signal processing for fiber-optic communication systems*. PhD thesis, University College Cork, 2017.

[137] J. P. Wooler, S. R. Sandoghchi, D. Gray, F. Poletti, M. N. Petrovich, N. V. Wheeler, N. Baddela, and D. J. Richardson, "Overcoming the Challenges of Splicing Dissimilar Diameter Solid-Core and Hollow-Core Photonic Band Gap Fibers," in *Workshop on Specialty Optical Fibers and their Applications*, (Washington, D.C.), p. W3.26, OSA, aug 2013.

[138] N. V. Wheeler, M. N. Petrovich, N. K. Baddela, J. R. Hayes, E. N. Fokoua, F. Poletti, and D. J. Richardson, "Gas Absorption between 1.8 and 2.1 μm in Low Loss (5.2 dB/km) HC-PBGF," in *Conference on Lasers and Electro-Optics 2012*, (San Jose, California), p. CM3N.5, Optical Society of America, 2012.

[139] I. E. Gordon, L. S. Rothman, C. Hill, R. V. Kochanov, Y. Tan, P. F. Bernath, M. Birk, V. Boudon, A. Campargue, K. V. Chance, B. J. Drouin, J. M. Flaud, R. R. Gamache, J. T. Hodges, D. Jacquemart, V. I. Perevalov, A. Perrin, K. P. Shine, M. A. Smith, J. Tennyson, G. C. Toon, H. Tran, V. G. Tyuterev, A. Barbe, A. G. Császár, V. M. Devi, T. Furtenbacher, J. J. Harrison, J. M. Hartmann, A. Jolly, T. J. Johnson, T. Karman, I. Kleiner, A. A. Kyuberis, J. Loos, O. M. Lyulin, S. T. Massie, S. N. Mikhailenko, N. Moazzen-Ahmadi, H. S. Müller, O. V. Naumenko, A. V. Nikitin, O. L. Polyansky, M. Rey, M. Rotger, S. W. Sharpe, K. Sung, E. Starikova, S. A. Tashkun, J. V. Auwera, G. Wagner, J. Wilzewski, P. Wcisło, S. Yu, and E. J. Zak, "The HITRAN2016 molecular spectroscopic database," *Journal of Quantitative Spectroscopy and Radiative Transfer*, vol. 203, pp. 3–69, dec 2017.

[140] J.-P. Laude, *DWDM Fundamentals, Components, and Applications*. Norwood, MA: Artech House, 1 ed., jan 2002.

[141] Agiltron, “Manual Grating-Based Fiber Optic Tunable Filter, agiltron.com/product/manual-grating-based-fiber-optic-tunable-filter, 2019.”

[142] T. Hertsens, “Measuring diode laser characteristics,” Tech. Rep. 2, ILX Lightwave, 2005.

[143] X. J. M. Leijtens, B. Kuhlow, and M. K. Smit, “Arrayed Waveguide Gratings,” in *Wavelength Filters in Fibre Optics*, pp. 125–187, Springer Berlin Heidelberg, 2006.

[144] R. Phelan, J. O’Carroll, D. Bryne, R. Lennox, K. Carney, L. P. Barry, and B. Kelly, “Low linewidth discrete mode lasers for coherent communications applications,” in *European Conference on Optical Communication, ECOC*, pp. 1–3, IEEE, sep 2014.

[145] M. Sadiq, *Design and characterization of InP based Mach-Zehnder modulators at 2μm wavelength*. PhD thesis, University College Cork, 2016.

[146] R. K. Sinha, M. Wan, S. K. Bag, and S. K. Varshney, “Design and Fabrication of Microring Resonator Array for mid-IR Filter Applications,” in *Frontiers in Optics / Laser Science*, (Washington, D.C.), p. JTu3A.19, OSA, sep 2018.

[147] T.-H. Xiao, Z. Zhao, W. Zhou, C.-Y. Chang, S. Y. Set, M. Takenaka, H. K. Tsang, Z. Cheng, and K. Goda, “Mid-infrared high-Q germanium microring resonator,” *Optics Letters*, vol. 43, p. 2885, jun 2018.

[148] J. Haas, P. Artmann, and B. Mizaikoff, “Mid-infrared GaAs/AlGaAs micro-ring resonators characterized: Via thermal tuning,” *RSC Advances*, vol. 9, no. 15, pp. 8594–8599, 2019.

[149] M. U. Sadiq, H. Zhang, M. Gleeson, N. Ye, B. Roycroft, N. Kavanagh, C. Robert, H. Yang, K. Thomas, A. Gocalinska, Z. Li, Y. Chen, N. V. Wheeler, J. R. Hayes, S. U. Alam, F. Poletti, M. N. Petrovich, D. J. Richardson, B. Kelly, J. O’Carroll, R. Phelan, E. Pelucchi, P. O’Brien, F. Peters, F. Gunning, and B. Corbett, “40 Gbps WDM transmission over 1.15 km HC-PBGF using the first InP-based Mach Zehnder modulator at 2 μm,” in *European Conference on Optical Communication, ECOC*, vol. 2015-Novem, pp. 1–3, 2015.

[150] K. Kikuchi, C. E. Zah, and T. P. Lee, "Amplitude-modulation sideband injection locking characteristics of semiconductor lasers and their application," *Journal of Lightwave Technology*, vol. 6, no. 12, pp. 1821–1830, 1988.

[151] O. Gough, C. Silva, S. Bennett, and A. Seeds, "Zero frequency error DWDM channel synthesis using optical injection-locked comb line selection," *Electronics Letters*, vol. 35, no. 23, p. 2050, 2002.

[152] C. Silva, A. Seeds, and P. Williams, "Terahertz span >60-channel exact frequency dense WDM source using comb generation and SG-DBR injection-locked laser filtering," *IEEE Photonics Technology Letters*, vol. 13, pp. 370–372, apr 2001.

[153] H. D. Kim, S. G. Kang, and C. H. Lee, "Low-cost WDM source with an ASE injected Fabry-Perot semiconductor laser," *IEEE Photonics Technology Letters*, vol. 12, pp. 1067–1069, aug 2000.

[154] Sang-Mook Lee, Ki-Man Choi, Sil-Gu Mun, Jung-Hyung Moon, and Chang-Hee Lee, "Dense WDM-PON based on wavelength-locked Fabry–Pérot laser diodes," *IEEE Photonics Technology Letters*, vol. 17, pp. 1579–1581, jul 2005.

[155] S. K. Mondal, B. Roycroft, P. Lambkin, F. Peters, B. Corbett, P. Townsend, and A. Ellis, "A multiwavelength low-power wavelength-locked slotted Fabry-Pérot laser source for WDM applications," *IEEE Photonics Technology Letters*, vol. 19, pp. 744–746, may 2007.

[156] S. H. Strogatz and I. Stewart, "Coupled Oscillators and Biological Synchronization," *Scientific American*, vol. 269, pp. 102–109, dec 1993.

[157] T. Wang, "Sub-harmonic Injection Locking in Metronomes," *arXiv preprint arXiv:1709.03886*, 2017.

[158] J. Buck and E. Buck, "Mechanism of rhythmic synchronous flashing of fireflies. Fireflies of Southeast Asia may use anticipatory time-measuring in synchronizing their flashing.," *Science (New York, N.Y.)*, vol. 159, pp. 1319–27, mar 1968.

[159] R. Meier and A. Gwerder, "Synchronicity, a film produced by Audemars Piguet Art Commission, Le Brassus," 2015.

[160] T. J. Walker, "Acoustic synchrony: two mechanisms in the snowy tree cricket.," *Science (New York, N.Y.)*, vol. 166, pp. 891–4, nov 1969.

[161] A. Pikovsky, M. Rosenblum, and Jürgen Kurths, *Synchronization A universal concept in nonlinear sciences*, vol. 53. Cambridge University Press, 2013.

[162] R. Adler, "A Study of Locking Phenomena in Oscillators," *Proceedings of the IRE*, vol. 34, no. 6, pp. 351–357, 1946.

[163] W. H. Steier and H. L. Stover, "Locking of Laser Oscillators by Light Injection, 1," *IEEE Journal of Quantum Electronics*, vol. 2, pp. 111–112, feb 1966.

[164] C. Buczek, R. Freiberg, and M. Skolnick, "Laser injection locking," *Proceedings of the IEEE*, vol. 61, no. 10, pp. 1411–1431, 1973.

[165] S. Kobayashi and T. Kimura, "Injection locking in AlGaAs semiconductor laser," *IEEE Journal of Quantum Electronics*, vol. 17, no. 5, pp. 681–689, 1981.

[166] S. Kobayashi and T. Kimura, "Optical Phase Modulation in an Injection Locked AIGaAs Semiconductor Laser," *IEEE Transactions on Microwave Theory and Techniques*, vol. 30, pp. 1650–1657, oct 1982.

[167] R. Lang, "Injection locking properties of a semiconductor laser," *IEEE Journal of Quantum Electronics*, vol. 18, no. 6, pp. 976–983, 1982.

[168] F. Mogensen, H. Olesen, and G. Jacobsen, "Locking conditions and stability properties for a semiconductor laser with external light injection," *IEEE Journal of Quantum Electronics*, vol. 21, no. 7, pp. 784–793, 1985.

[169] C. H. Henry, N. A. Olsson, and N. K. Dutta, "Locking Range and Stability of Injection Locked 1.54 μ m InGaAsP Semiconductor Lasers," *IEEE Journal of Quantum Electronics*, vol. 21, no. 8, pp. 1152–1156, 1985.

[170] E. K. Lau, L. J. Wong, and M. C. Wu, "Enhanced modulation characteristics of optical injection-locked lasers: A tutorial," *IEEE Journal on Selected Topics in Quantum Electronics*, vol. 15, no. 3, pp. 618–633, 2009.

[171] J. Appl and G. Csp, "Contribution of spontaneous emission to the line width of an injection-locked semiconductor laser," *Electronics Letters*, vol. 21, no. 14, pp. 626–628, 1985.

[172] K. Iwashita and K. Nakagawa, "Suppression of Mode Partition Noise by Laser Diode Light Injection," *IEEE Transactions on Microwave Theory and Techniques*, vol. 30, pp. 1657–1662, oct 1982.

[173] X. Jin and S. L. Chuang, "Bandwidth enhancement of Fabry-Perot quantum-well lasers by injection-locking," *Solid-State Electronics*, vol. 50, no. 6, pp. 1141–1149, 2006.

[174] K. Kobayashi, H. Nishimoto, and R. Lang, "Experimental observation of asymmetric detuning characteristics in semiconductor laser injection locking," *Electronics Letters*, vol. 18, no. 2, p. 54, 1982.

[175] L. Goldberg, H. Taylor, and J. Weller, "Locking bandwidth asymmetry in injection-locked GaAlAs lasers," *Electronics Letters*, vol. 18, no. 23, p. 986, 1982.

[176] D. P. Goulding, *Non-Linear Dynamics of Optically Injected Quantum Dot Lasers*. PhD thesis, University College Cork, 2011.

[177] T. B. Simpson, J. M. Liu, K. F. Huang, and K. Tai, "Nonlinear dynamics induced by external optical injection in semiconductor lasers," *Quantum and Semiclassical Optics: Journal of the European Optical Society Part B*, vol. 9, pp. 765–784, oct 2002.

[178] D. Labukhin, C. A. Stolz, N. A. Zakhleniuk, R. Loudon, and M. J. Adams, "Modified Fabry-Perot and rate equation methods for the nonlinear dynamics of an optically injected semiconductor laser," *IEEE Journal of Quantum Electronics*, vol. 45, pp. 864–872, jul 2009.

[179] I. Petitbon, P. Gallion, G. Debarge, and C. Chabran, "Locking bandwidth and relaxation oscillations of an injection-locked semiconductor laser," *IEEE Journal of Quantum Electronics*, vol. 24, no. 2, pp. 148–154, 1988.

[180] A. Bogris, D. Syvridis, A. Fragkos, T. Nikas, H. Simos, and W. Elsäßer, "Optical injection in semiconductor lasers: Physics and applications," in *International Conference on Transparent Optical Networks*, vol. August, pp. 1–4, 2016.

[181] A. Daly, B. Roycroft, and B. Corbett, “Stable locking phase limits of optically injected semiconductor lasers,” *Optics Express*, vol. 21, no. 25, pp. 30126–30139, 2013.

[182] A. D. Bristow, N. Rotenberg, and H. M. van Driel, “Two-photon absorption and Kerr coefficients of silicon for 850–2200nm,” *Applied Physics Letters*, vol. 90, p. 191104, may 2007.

[183] J. Leuthold, C. Koos, and W. Freude, “Nonlinear silicon photonics,” *Nature Photonics*, vol. 4, p. 535, 2010.

[184] A. Rahim, E. Ryckeboer, A. Z. Subramanian, S. Clemmen, B. Kuyken, A. Dhakal, A. Raza, A. Hermans, M. Muneeb, S. Dhoore, Y. Li, U. Dave, P. Bienstman, N. Le Thomas, G. Roelkens, D. Van Thourhout, P. Helin, S. Severi, X. Rottenberg, and R. Baets, “Expanding the Silicon Photonics Portfolio with Silicon Nitride Photonic Integrated Circuits,” *Journal of Lightwave Technology*, vol. 35, pp. 639–649, feb 2017.

[185] D. Liu, H. Wu, and D. Dai, “Silicon Multimode Waveguide Grating Filter at 2 μm,” *Journal of Lightwave Technology*, vol. 37, no. 10, pp. 2217–2222, 2019.

[186] E. J. Stanton, N. Volet, and J. E. Bowers, “Silicon arrayed waveguide gratings at 2-μm wavelength characterized with an on-chip resonator,” *Optics Letters*, vol. 43, no. 5, p. 1135, 2018.

[187] W. Cao, D. Hagan, D. J. Thomson, M. Nedeljkovic, C. G. Littlejohns, A. Knights, S.-U. Alam, J. Wang, F. Gardes, W. Zhang, S. Liu, K. Li, M. S. Rouifed, G. Xin, W. Wang, H. Wang, G. T. Reed, and G. Z. Mashanovich, “High-speed silicon modulators for the 2 μm wavelength band,” *Optica*, vol. 5, no. 9, p. 1055, 2018.

[188] J. Li, Y. Liu, Y. Meng, K. Xu, J. Du, F. Wang, Z. He, and Q. Song, “2-μm Wavelength Grating Coupler, Bent Waveguide, and Tunable Microring on Silicon Photonic MPW,” *IEEE Photonics Technology Letters*, vol. 30, no. 5, pp. 471–474, 2018.

[189] R. Soref, “Group IV photonics: Enabling 2 μm communications,” *Nature Photonics*, vol. 9, pp. 358–359, jun 2015.

[190] D. Liu, H. Wu, and D. Dai, “Silicon-based add-drop optical filter at 2 μm,” *Asia Communications and Photonics Conference, ACP*, vol. 2018-Octob, 2018.

[191] T. F. Refaat, U. N. Singh, J. Yu, M. Petros, S. Ismail, M. J. Kavaya, and K. J. Davis, "Evaluation of an airborne triple-pulsed 2 μm IPDA lidar for simultaneous and independent atmospheric water vapor and carbon dioxide measurements," *Applied Optics*, vol. 54, no. 6, p. 1387, 2015.

[192] S. Moro, A. Danicic, N. Alic, N. G. Usechak, and S. Radic, "Widely-tunable parametric short-wave infrared transmitter for CO2 trace detection," *Optics Express*, vol. 19, no. 9, pp. 8173–8178, 2011.

[193] A. Khan, D. Schaefer, L. Tao, D. J. Miller, K. Sun, M. A. Zondlo, W. A. Harrison, B. Roscoe, and D. J. Lary, "Low power greenhouse gas sensors for unmanned aerial vehicles," *Remote Sensing*, vol. 4, pp. 1355–1368, may 2012.

[194] J. J. Scherer, J. B. Paul, H. J. Jost, and M. L. Fischer, "Mid-IR difference frequency laser-based sensors," *Applied Physics B: Lasers and Optics*, vol. 110, pp. 271–277, feb 2013.

[195] S. Ishii, K. Mizutani, H. Fukuoka, T. Ishikawa, B. Philippe, H. Iwai, T. Aoki, T. Itabe, A. Sato, and K. Asai, "Coherent 2 μm differential absorption and wind LIDAR with conductively cooled laser and two-axis scanning device," *Applied Optics*, vol. 49, no. 10, pp. 1809–1817, 2010.

[196] R. J. De Young and N. P. Barnes, "Profiling atmospheric water vapor using a fiber laser LIDAR system," *Applied Optics*, vol. 49, no. 4, pp. 562–567, 2010.

[197] S. Wills, "Gravitational Waves: The Road Ahead," *Optics and Photonics News*, vol. 29, p. 44, may 2018.

[198] B. Chen, L. Thomsen Sharon, J. Thomas Robert, J. Oliver, and J. Welch Ashley, "Histological and modeling study of skin thermal injury to 2.0 μm laser irradiation," *Lasers in Surgery and Medicine*, vol. 40, no. 5, pp. 358–370, 2008.